An Investigation to Determine the Adsorption of Water And Simple Organic Molecules on Anodised Aluminium Oxide Thin Film

Thesis submitted in accordance with the requirements of the University of St. Andrews for the degree in Doctor of Philosophy
by:

Mohammed Nawaz Khan
September 1999

The adsorption of water and simple organic molecules on aluminium oxide thin film

Abstract

The interaction of simple organic molecules to probe the adsorption behaviour of aluminium oxide thin film in UHV has been studied using a variety of surface sensitive techniques. Importance given to Scanning Electron Microscopy (SEM) was used in a straightforward way to determine any changes in the surface structure brought about by deposition of a Post Anodic Treatment (PAT) liquor. PAT is a chemical conversion process which forms an insoluble precipitate on the surface of the anodic film (particularly at the pore mouths where the concentration of Al^{3+} is the highest). Atomic Force Microscopy (AFM) provides information on the surface topography without destroying the surface. Transmission Electron Microscopy (TEM) provided information on the morphology of the porous anodic films showing the development of a duplex film comprising an inner barrier film and overlying layer. The barrier layer consisits of many parallel porous twisting channels. Secondary Ion Mass Spectroscopy (SIMS) provided chemical information on the surfaces. X-Ray Photoelectron Spectroscopy (XPS) was used to determine the elemental composition of the STD PAT and NON PAT surfaces.

The adsorption of aniline, phenol, ethanol, methanol, xylene and hexane acting as probe molecules on alumina surface has been studied by TPD. Each sample produced a different desorption spectrum (fingerprint). Aniline and phenol (aromatic molecules) showed to be the most favoured probe molecules showing very similar but different TPD spectra. Anodising resulted in the emergence of an intermediate state, increasing in exposure. The PAT process is seen to preferentially block the intermediate adsorption site on the STD PAT substrate.

Information has been gained about molecular interaction of water with alumina substrate. This is extremely important in determining the ability of a substrate to take up water, giving information about the hydrophilicity of the substrate and the

role of water at the interface. Simultaneous dosing of H_2O and D_2O yielded high temperature desorption features that are largely isotope independent and exhibit extensive H/D exchange. H_2O followed by D_2O yields more complex desorption with strong isotope effects and reduced H/D exchange. D_2O desorption proceeds H_2O desorption with HDO features appearing as a superposition of the non-exchange features. When modelling the adsorption-desorption behaviour the direct adsorption path into the high temperature adsorption states all molecules forced to pass through the physisorption state before chemisorption. With this constraint within the model the effect of adsorption temperature could be modelled very successfully.


بسم الله الرحمن الرحيم

Acknowledgements

All Praise and thanks are due to Allah. We Praise and give thanks to him. We seek his aid and ask for his forgiveness. Whomsoever Allah guides then none can misguide him, and Whomsoever he misguides then none can guide him. I bear witness that none has the right to be worshipped except Allah, alone, having no partner, and I testify that Muhammad (may Allah peace and blessing be upon him) is his final messanger to all of mankind.

As is, I dare say, the normal state of affairs in the act of completing an extended body of work such as this, there are a great many people who, in varying ways, varying degrees, and indeed at many different stages of my life, have contributed to this thesis. I cannot therefore name them individually here, but my thanks goes out to all of them.

Instead let me first thank my supervisor Prof. Neville Richardson, for giving me the opportunity to study at Liverpool and St.Andrews University *"the home of golf"*. His expertise has provided a constant supply of inspiration and much help and advice throughout my research is greatly appreciated. I am grateful to Dr.S.M.Francis my "other" supervisor for his encouragement, understanding and positive attitude. He has not only been a colleague but also a friend to "talk" to throughout the three years. With their support, I have learned not only the fundamental surface science, but also the professional way as a scientist. I would also like to Kodak-Polychrome (Horsell Graphics Ltd) for their tremendous help and direction especially Peter Blum, Harjit Bhambra and Sarah Mattin for their advice and cooperation and making me feel part of a team during my frequent visits at the company and Nick Sawyer for the SEM images and everyone who made my time there very hospitable. Funding from the Engineering and Physical Sciences Research Council (EPSRC) and Kodak Polychrome to carry out this work is acknowledged.

I would like to thank the current, and past members of the group for their needed words of encouragement: Dr.Brian Frederick, Dr.Myoung-Bok Lee, Dr.Sam Haq, Dr.Thomas Bitzer, Dr.Qiao Chen, Dr.Chris Perry, Mrs Stacey Wilkie, Daz Dillinger,

the Klix and *The Dogg Pound* (you know who you are !!!!).

I guess throughout the three years I have learnt about surface science and its applications, and about methods for continuing to learn. But more than that, I have learnt about myself and my possible role as a scientist. Ken Keyes wrote, "Everyone and everything around you is your teacher", and I believe this is the embodiment of what science has to offer.

Last in chronology, but formost in my mind, are the people closet to me, my family and friends. I wish to thank my parents especially my mother who has been the "wind beneath my wings" for such a long time. So I dedicate this thesis to her for helping me over the years, for her unconditional love and her unwavering faith in me has never ceased to provide a great source of strength. A big thank you goes out to the crew and last but not least my sister who was there when I needed her through thick and thin, your help will never be forgotten "Thanks".

The Perfectionist

His organisational skills are second to none
One can be sure it will be done
There's never any need to fear
There's never any mishaps here

His's a stickler for neatness and cleanliness too
A haphazard fashion will never do
Everything has to be just so
Nearly clean would never go

His every fibre oozes creativity
It's here we realise his naivete
For simple attitudes nuture beauty and wonder
For us perhaps a moment to ponder

His faults it appears (at first) he hasn't any
But like everyone else he has a few - but not many
He strives to be in tune with his perfect environment
He's still be trying when he reaches retirement

His moods are sombre like the thundery sky
No one would say this was a lie
But he comes smiling through in his usual way
And tries again to perfect another day.

Nas (1999)

Declarations

I, Mohammed Nawaz Khan, hereby certify that this thesis, which is approximately 45,000 words in length, has been written by me, that is the record of work carried out by me and that it has not been submitted in any previous application for a higher degree.

Date: 4/4/00 Signature of candidate:

I was admitted as a research student in October 1996 and as a candidate for the degree of PhD in October 1996 at the University of Liverpool. I transferred to the University of St. Andrews on 21 September 1998; the higher study for which this is a record was carried out in the Universities of Liverpool and St. Andrews between 1996 and 1999.

Date: 4/4/00 Signature of candidate:

I hereby certify that the candidate has fulfilled the conditions of the Resolution and Regulation appropriate for the degree of PhD in the University of St. Andrews and that the candidate is qualified to submit this thesis in application for that degree.

Date: 4/4/00 Signature of supervisor:

In submitting this thesis to the University of St. Andrews I understand that I am giving permission for it to be made available for use in accordance with the regulations of the University Library for the time being in force, subject to any copyright vested in the work not affected therby. I also understand that the title and abstract will be published, and that a copy of the work may be made and supplied to any bona fide library or research worker.

Date: 4/4/00 Signature of candidate:

CONTENTS

Chapter 1

General Introduction

1.1 Technological Significance

Surface science is an interdisciplinary activity encompassing many areas of technology [1]. In the last few years, there has been increased research activity in the atmospheric, high pressure, or aqueous solution environments with the development of new surface analysis instrumentation [2]. There is particular interest in the use of organic materials that can be used as electronic devices. The development of science and technology has significantly reduced the gap between fundamental research and application in industry. It becomes possible to design a basic research project to achieve not only the understanding of chemistry and physics, but also leading to the development of new materials, based on the technology of designing, constructing, testing and commercialising, on the molecular and atomic scale.

1.2 Lithography and the use of Aluminium

The properties of aluminium such as low relative density, i.e. one third of that of steel or copper-based alloys, the possible improvement in mechanical properties (tensile strength, hardness, rigidity) by addition of relatively small amounts of other elements like Si, Cu, Mn, Mg and the relative small abundance of aluminium have been made it an attractive metal for many aspects of engineering and construction.

Lithography printing is a mature technology having been invented in 1796 by Aloes Senfelder. It has probably been the most widely studied of all the printing processes. Despite this, many questions remain and a total understanding of the lithographic process still eludes us. This is largely due to the complex interactions which occur on press between the ink and the dampening solution.

Lithographic printing process is possible because ink and water are immiscible. The printing plates are designed to enhance the separation of ink and water in a thin film on the plate surface. The separation is achieved by creating an oleophilic (oil loving) areas and an hydrophilic (water loving) areas on the plate surface (medium). In present technology, the image is transferred onto the lithographic sheet by coating it with a photosensitive chemical, and exposing the sheet to actinic light (UV light) through the negative (or positive) of the image required. Further chemical treatments are performed to remove the chemicals from the unexposed areas, and finally the image is inked. This is illustrated in Figure 1 [3].

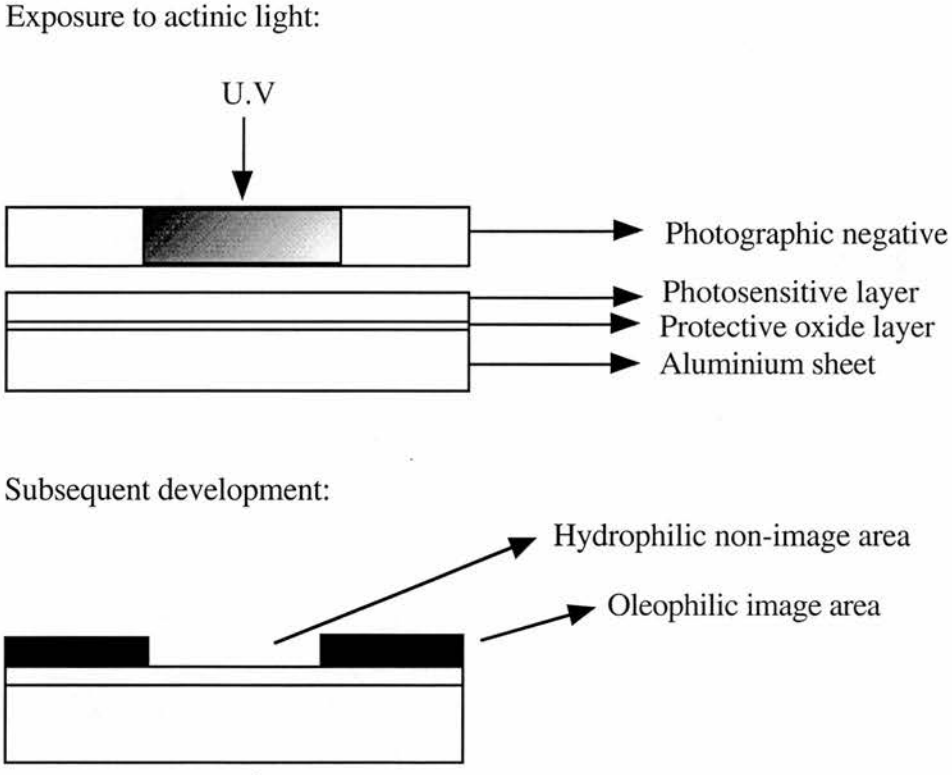

Figure 1. Schematic diagram of the Photo-lithographic process on aluminium sheet [3].

Removal of light source (UV) the aluminium is then developed. This leaves oleophilic areas where the chemical remains and hydrophic areas where it is removed.

1.3 Importance of the Interface

It is generally agreed that the processes that occur at an adhesion interface are complex. The wettability of the surface is known to be of major importance for good adhesion, as shown by the contact angle measurements by Zisman [4], but there is debate as to the state of the adhesive bond that finally forms. Four main mechanisms [5] within the literature are the mechanical theory, the diffusion theory, the electronic theory and the adsorption theory. Each proposed mechanism of adhesion is appropriate for certain adhesive systems. Organic adhesives on metal or oxide surface systems are usually described using the mechanical or adsorption theory [5], so these two theories will be discussed in detail.

(i) Mechanical Theory

This suggests that all the intrinsic adhesion is caused by mechanical interlocking of the adhesive and the substrate. Kinloch [5] states that it has been shown to occur in a few cases, but in most cases, the surface pre-treatment does not create a morphology that could support mechanical interlocking. The increase in joint strength observed with increased surface roughness/pore structure e.g. from anodisation in alumina adhesion, has been associated with improved interfacial contact and enhanced energy dissipation within the adhesive, rather than the physical difficulty of removing the glue from the pores. Hence, surface morphology is important even if mechanical interlocking does not occur.

(ii) Adsorption Theory

This is the most widely applicable theory. It is based on the premise that, provided intimate molecular contact takes place at the interface, interatomic and intermolecular forces will cause adhesion between the adhesive and the substrate. These forces [6] are usually described as primary forces, donor-acceptors bonds or secondary (physical) bonds. Primary bonds include covalent, ionic or metallic bonds. Donor acceptor bonds

are Brønsted or Lewis acid-base interactions and secondary bonds include hydrogen bonds and van der Waals' forces. Kinloch [5] suggests that there is evidence that secondary bonding alone could account for the force holding an adhesive bond together. In contrast, Fowkes [7] argues that the formation of acid-base interactions forms the major type of intrinsic adhesion.

It is thought by Kinloch [5] that particular systems are best described by one of these theories or a mixture of them, though the mechanical theory does not appear to be able to stand alone. However, the chemical and physical bonds between the surface, are considered to be important for wetting the surface whether or not they are dominant in the final adhesion mechanism. The failure of the bond is almost always associated with the effect of environmental conditions. The most important environmental factor is water [8] and it is thought that disruption of the secondary (or physical) bonds of the joint may cause the failure. Thus, an understanding of the chemical (primary, donor-acceptor) and physical (hydrogen, van der Waals') bonds, between the organic polymer and the aluminium, would be important for the understanding of the adhesion process.

1.4 Importance of the modelled molecules

By far the vast majority of colour change dyes depend on their action on the generation of an acidic species in the coating on exposure, so it is appropriate to consider here how this can be achieved. Several types of acid release agents are known which are either inherently sensitive to UV light, or may be sensitised to the correct wavelength. The dye molecules shown in Figure 2. perform two function: firstly, it imparts a suitable colour to the coating and secondly, it provides a strong visible image after development. Pigments are often used because of their resistance to leaching by the developer [9]. The phenolic resins used is shown in Figure 3.

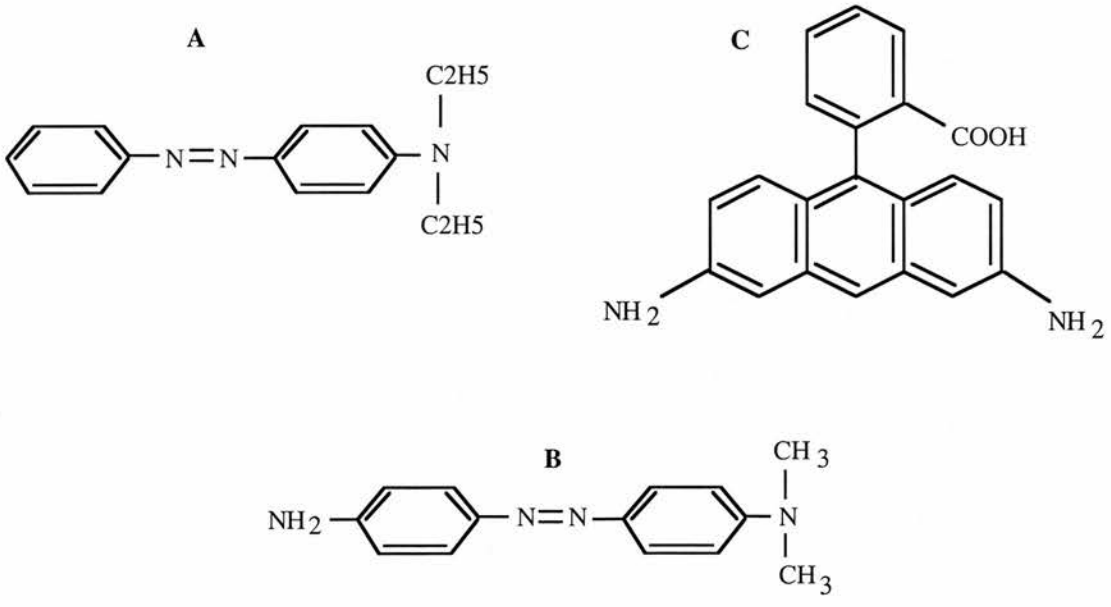

Figure 2. The above diagram shows various model dye compounds studied [9].

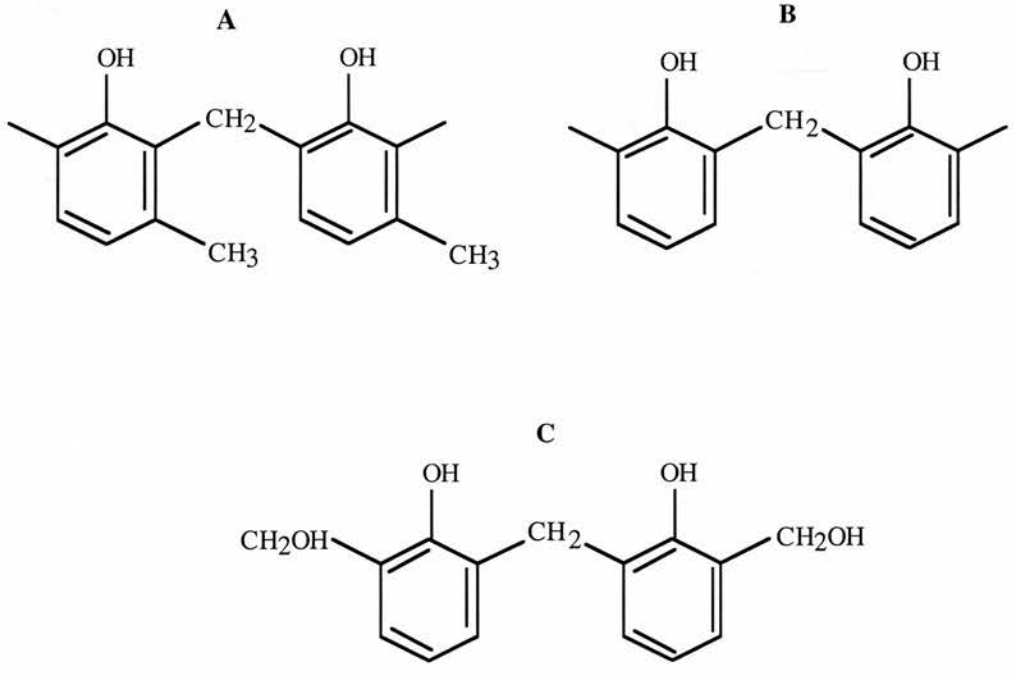

Figure 3. The above diagram shows various model phenolic resin compounds studied [9].

1.5 Analysis of substrate manufacture

A series of chemical processes takes place before printing can commence. These can consist of degrease, clean, or etch clean desmut, grain, a second desmut, anodising and Post Anodic Treatment (PAT).

1.5.1 Clean/Degrease Process

Aluminium alloy produced by the cold rolling process is coated with roller oil and this needs to be removed from the surface. This is achieved by cleaning in an alkaline solution containing chelating agents. The chelating agents reduce repreciptiation of etchants and oil back onto the aluminium. After cleaning the oil and debris are removed and smoothing of the surface has occured due to etching by the alkaline solution. An etching product consisting of aluminium hydroxide remains loosely bound to the surface. Much of it is removed in the water rinse. Further removal of this "smut" as it is called is carried out in the desmutting process. Figures 4 and 5. shows an electron micrograph of a typical as-received surface. The direction of rolling is clearly visible.

Figure 4. Low magnification SEM image of aluminium as received [10]

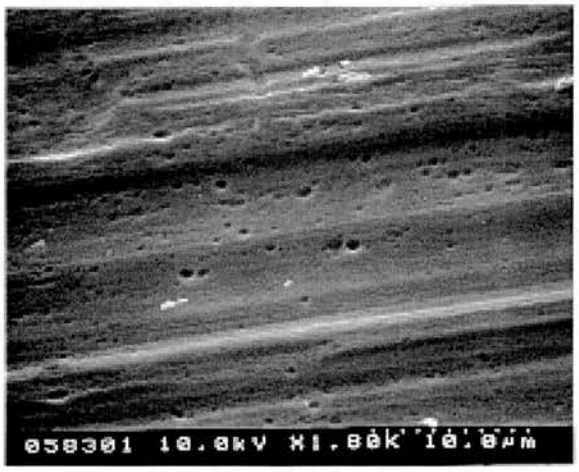

Figure 5. High magnification SEM image of aluminium as received [10]

1.5.2 Desmutting Process

This process removes etch product produced on the aluminium in the previous alkali clean that was not removed by the water rinse. The aluminium surface is made acidic and remains passive so it is unaffected.

1.5.3 Electrograining Process

Electrograining is carried out electrochemically in an acidic solution which causes local breakdown of the protective oxide layer. The aluminium metal exposed to the acid starts to dissolve at the breakdown sites, and pits grow. This is illustrated in Figure 6. The surface of the aluminium is roughened electrochemically to give it a greater surface area and surface volume. (Increased surface volume is thought to increase water retention on the plate and allow the photocoat on image areas to be protected during printing. High surface area is also believed to increase adhesion of the photocoat to the substrate. It is also generally observed that the finer the roughness the better the resolution of the printed matter.

Figure 6. Low magnification SEM image of an electrograined surface [10].

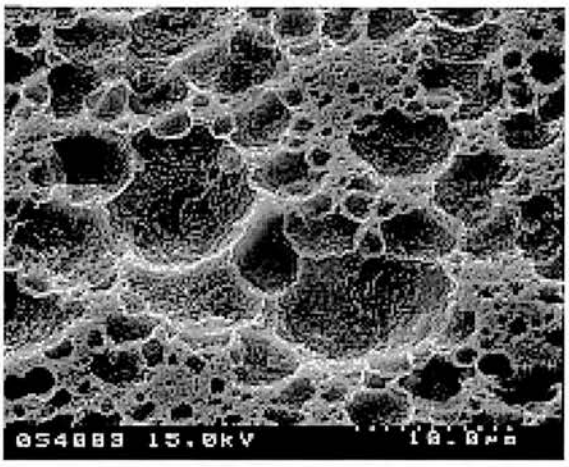

1.5.4 Electrochemical Desmut Process

A resilient surface, better able to withstand the friction and the chemical attack experienced on the press is applied. This is done electrochemically by growing an anodic oxide film on the surface of the pitted aluminium. Hydrogen is evolved on the surface of the aluminium and during its evolution it removes the smut from the surface helping to clean it.

1.5.5 Anodic Tank Process

Anodising is generally carried out in sulphuric acid. The acid promotes the growth of a porous oxide film. The film is grown via ionic conduction of O^{2-} and Al^{3+} through film already present. Applying a positive current through to the aluminium, Al forms Al^{3+} and attracts O^{2-} to the metal, growing the film. Figures 7 and 8. shows an SEM image of the anodic pores of the oxide layer. While the oxide layer increases the surface area of the plate which is thought to improve its water holding properties it introduces the problem of dye staining. This occurs when the dye molecules present in the photocoat are retained by the anodic film. To prevent this undesirable occurance the plates are given a post anodic treatment (PAT).

Figure 7. Low magnification SEM image of a typical oxide film [10].

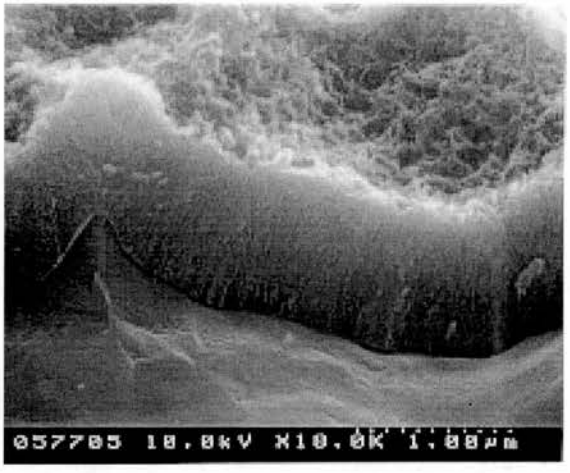

Figure 8. High magnification SEM image of the anodic pores [10].

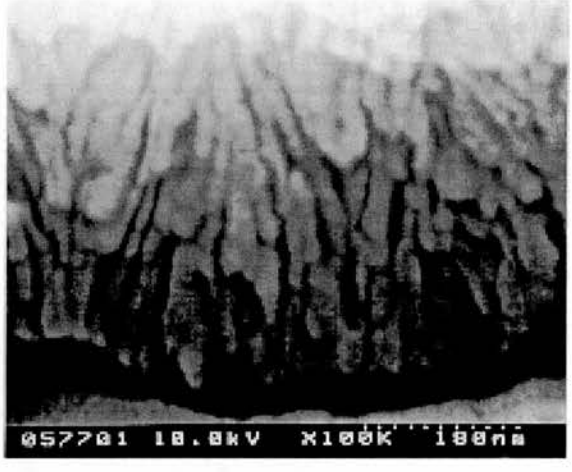

1.5.6 Post Anodic Treatment Process

PAT has several functions including prevention of dye staining by changing the anodic film structure. The PAT improves the corrosion resistance and modifies adhesion of the photocoat to the substarte easing its removal during developing. However, this reduction in bonding can lead to a shortening of the life time of the plate as the photocoat image is more readily removed from the substrate.

As the anodised aluminium is immersed in the PAT, the electrolyte in the pores becomes saturated in Al^{3+} ions and dissolved hydroxide. The aluminium start to diffuse out of the pores and as they reach the PAT solution, Al^{3+} ions react with the phosphate to become insoluble aluminium-phosphates which is precipitated onto the surface of the anodic film. This is illustrated in Figure 9. This precipitate blocks the pore mouths and, on application of the photocoat, stops the small dye molecules from becoming trapped.

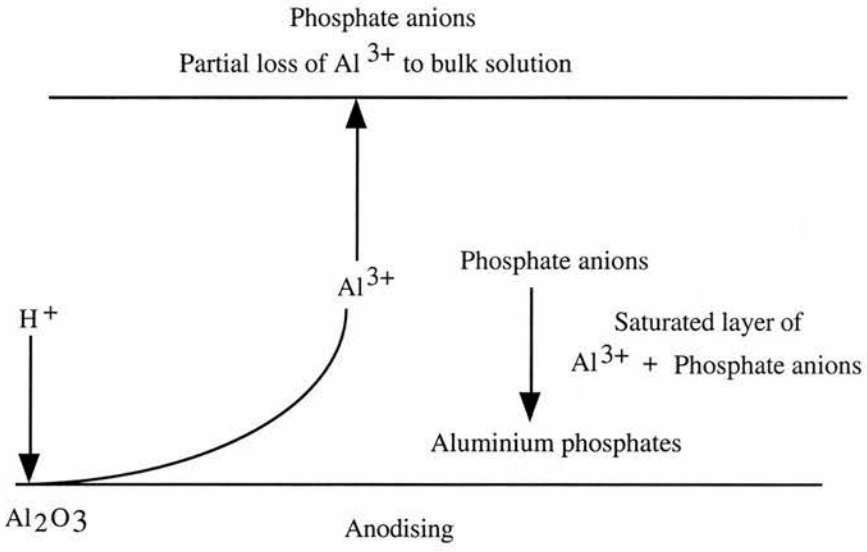

Figure 9. Illustration of the chemical conversion process [11].

1.6 Scope of this Thesis

The theme of this thesis is to develop an understanding of molecular interactions between lithographic substrate and photocoating through the thermal adsorption/desorption characteristics of simple organic molecular probes. The molecular adsorption of the light sensitive coating influences properties such as staining, developability, abrasion resistance and run length. The understanding gained on the interaction of the substrate with molecules which represent the light sensitive coating will be extended to include examination of the interaction of the substrate with water. This will provide the following

benefits:

. Molecular level understanding of the interaction of photo-coating with the substrate.

. Determination of the effect of different photo-coating components.

. Information on the effect of PAT on adhesion.

. A basis for manipulation of the substrate to give improved press performance.

1.7 References

[1] G.A.Somorjai, Introduction to Surface Chemistry and Catalysis, John Wiley & Sons, New York (1994).

[2] G.A.Somorjai, Prog.Surf.Sci., **50** (1995).

[3] R.M.Organ, PhD Thesis, University of Cambridge (1991).

[4] W.A.Zisman, Influence of Constitution on Adhesion. Ind.Eng.Chem., **55** (1963) 19-38.

[5] A.J.Kinloch, In Adhesion and Adhesives, Science and Technology, N.Y.Chapman and Hall (1987).

[6] L.Pauling, The Nature of the Chemical Bond, Ithaca, NY: Cornell University Press (1960).

[7] F.W.Fowkes, Physico-chemical aspects of Polymer Surfaces. ed. K.L.Mittal.Vol.2, N.Y Plenum Press (1983).

[8] A.J.Kinloch, Environmental factors in the failure of adhesive bonds, in Polymer Interfaces and Surfaces, W.J.Feast and H.S.Munro, John Wiley & Sons Ltd, London (1987).

[9] M.J.Pratt, Horsell Graphics Industries (1997).

[10] Nick Sawyer, Horsell Graphic Industries.

[11] H.Bhambra, Horsell Graphics Industries (1998).

Chapter 2

Alumina structure and chemistry

2.1 Introduction

This chapter reviews areas of literature that are most relevant to this thesis. The first is a discussion of the work that has been done on alumina surfaces, planar oxides and powdered oxides and what is known about their structure, phase and defects. This is followed by a discussion of the weak interactions of molecules with alumina surfaces. The modern literature available concerning the electrochemistry of aluminium is vast. By necessity, therefore, this review is highly selective and focuses on key issues most pertinent to the processing of lithographic substrate material.

2.2 Alumina: bulk structure, surface structure and defects

There is only one stoichiometric form of aluminium oxide - Al_2O_3 or alumina. However, this is made up of a number of polymorphs and hydrated states in which alumina can exist. The formation of these different forms is very much dependent on the conditions of preparation. In α-alumina, the oxide ions form a distorted hexagonal close packed (hcp) array with aluminium ions distributed symmetrically in two thirds of the octahedral interstices [1].

The structure of γ-alumina is often regarded as a defect spinel structure [2]. A spinel structure is a cubic close packed (ccp) array of oxygen ions with an eighth of its tetrahedral interstices and half of its octahedral interstices filled with cations. γ-alumina has a deficit of cations in this spinel structure with a ratio of two occupied octahedral sites for every tetrahedral aluminium ion. The oxide that occurs on aluminium metal has a different structure [2]. It takes up a structure with aluminium and oxygen ions in the rock salt structure with every third aluminium ion missing. Studies [3,4] of amorphous oxides

suggest that the structure of alumina can be described in terms of being part of a continuum of structure from α-alumina to γ-alumina. The amorphous oxide structure is a dense randomly packed oxygen ion lattice with aluminium ions tetrahedrally coordinated to oxygen ions. With increased ordering, aluminium ions organise their environments to create sites for cations that have spinel-type cation-cation correlations. More long range order on the oxygen ion lattice creates more octahedral interstices. This allows the cation-cation correlations to approach the spinel lattice of η and γ-alumina. Between α-alumina γ-alumina more octahedral interstices are occupied until there is a restructuring of the oxygen ion lattice from fcc to hcp.

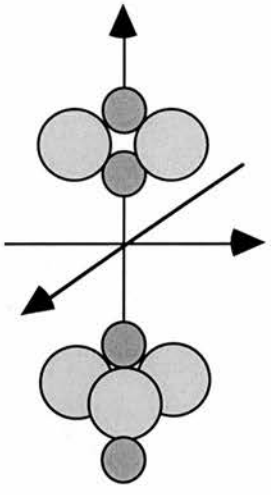

Figure 1. The bulk structure of α-alumina as discussed in Wyckoff's Crystal Structures [1]. A side view of a rhombohedral unit cell with the positions of the aluminium in black and oxygen in grey.

Low energy electron diffraction (LEED) studies [5-7] have revealed that the α–alumina (0001) surface is bulk-like and stable up to 1250°C. Above this temperature, the surface reconstructs with desorption of oxygen to give a ($\sqrt{31}$ x $\sqrt{31}$) rotated by $\tan^{-1}$ ($\sqrt{3}/11$). The aluminium ions in the high temperature surface structure are found to exist in a reduced oxidation state. The surface model proposed by Chang [5] for the (0001) α-alumina is shown in Figure 2. The diagram shows the outermost Al-O-Al unit. The large

circles represent the oxygen lattice in the ideal hcp positions. The arrows show how the oxygen ions are slightly displaced so that the oxygen periodicity becomes the same as that of the aluminium lattice. The dark circles are the upper layer aluminium ions.

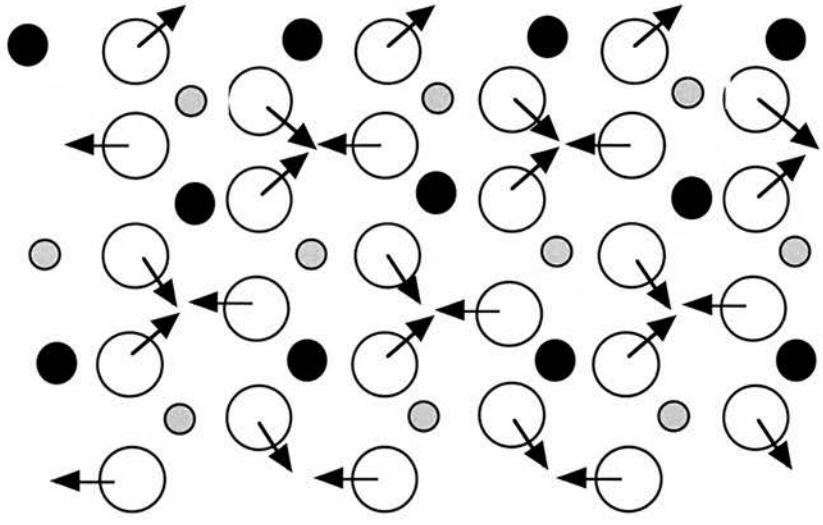

Figure 2. The model of the (0001) surface of α-alumina as proposed by Chang [5] from LEED studies. The large spheres represent the oxygen ion lattice in their ideal hcp positions with arrows indicating the slight displacement that occurs to make the oxygen periodicity the same as the aluminium lattice. The small dark circles indicate the positions of the lower aluminium ions and the lighter small circles shows the positions of the upper aluminium ions.

The structure of the (111) γ-alumina surface can also be thought of as the truncated bulk defect spinel structure. This means that the oxygen ion lattice would be in a ccp array and the aluminium ions fill tetrahedral and octahedral sites in a 1:2 ratio. The actual termination of the surface could be with aluminium or oxygen ions or a mixture of the two. A surface terminated by just oxygen would have the structure shown in Figure 3. Here, groups of three coplanar oxygen ions of the upper Al_2O_3 group of the unit cell almost totally cover the surface. The tetrahedral aluminium sites in the layer below are just visible and may or may not be occupied by coordinately saturated aluminium ions (represented by black dots). A surface that was terminated by just aluminium ions would

appear quite different. Here, aluminium ions can either occupy either the tetrahedral or octahedral interstices of the oxygen lattice. Figure 4(a). shows the aluminium terminated surface with all the tetrahedral sites filled and diagram 4(b). shows all the octahedral sites filled to illustrate the different sites more clearly on the real surface, these would be filled in a ratio of two octahedral to one tetrahedral in a symmetrical array. The aluminium ions on these surfaces are coordinately unsaturated and are expected to be more reactive than aluminium ions that were coordinately saturated. Figure 5. shows how the real (111) γ-alumina surface might look with random filling of the tetrahedral and octahedral holes with aluminium ions.

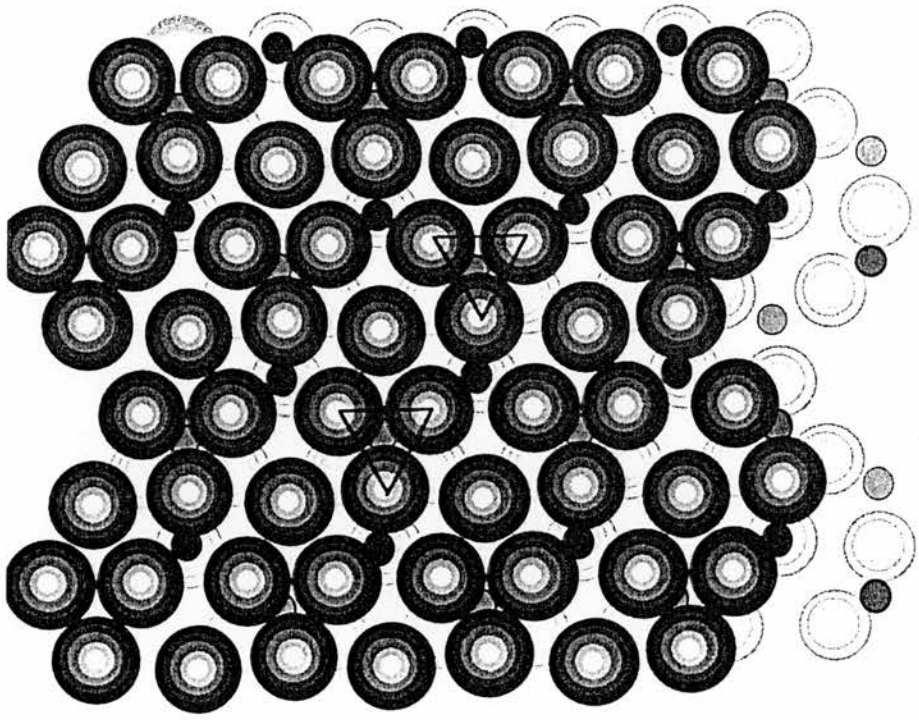

Figure 3. The bulk-truncated, oxygen-terminated surface structure of the (111) face of γ-alumina [5].The large spheres represent the oxygen ion (O^{2-}) lattice; the dark layer is the top layer and the light layer is the next layer below. The small spheres represent aluminium ions (Al^{3+}); the black spheres are Al^{3+} in the upper tetrahedral interstices, the dark grey spheres are the octahedral Al^{3+} and the light grey spheres are the lower tetrahedral Al^{3+}. All tetrahedral and octahedral interstices of the ccp O^{2-} lattice of the lower level have been filled with Al^{3+} to show different sites. However, in the real structure there would be a deficit of these cations and there would be two octahedral interstices filled for every tetrahedral site.

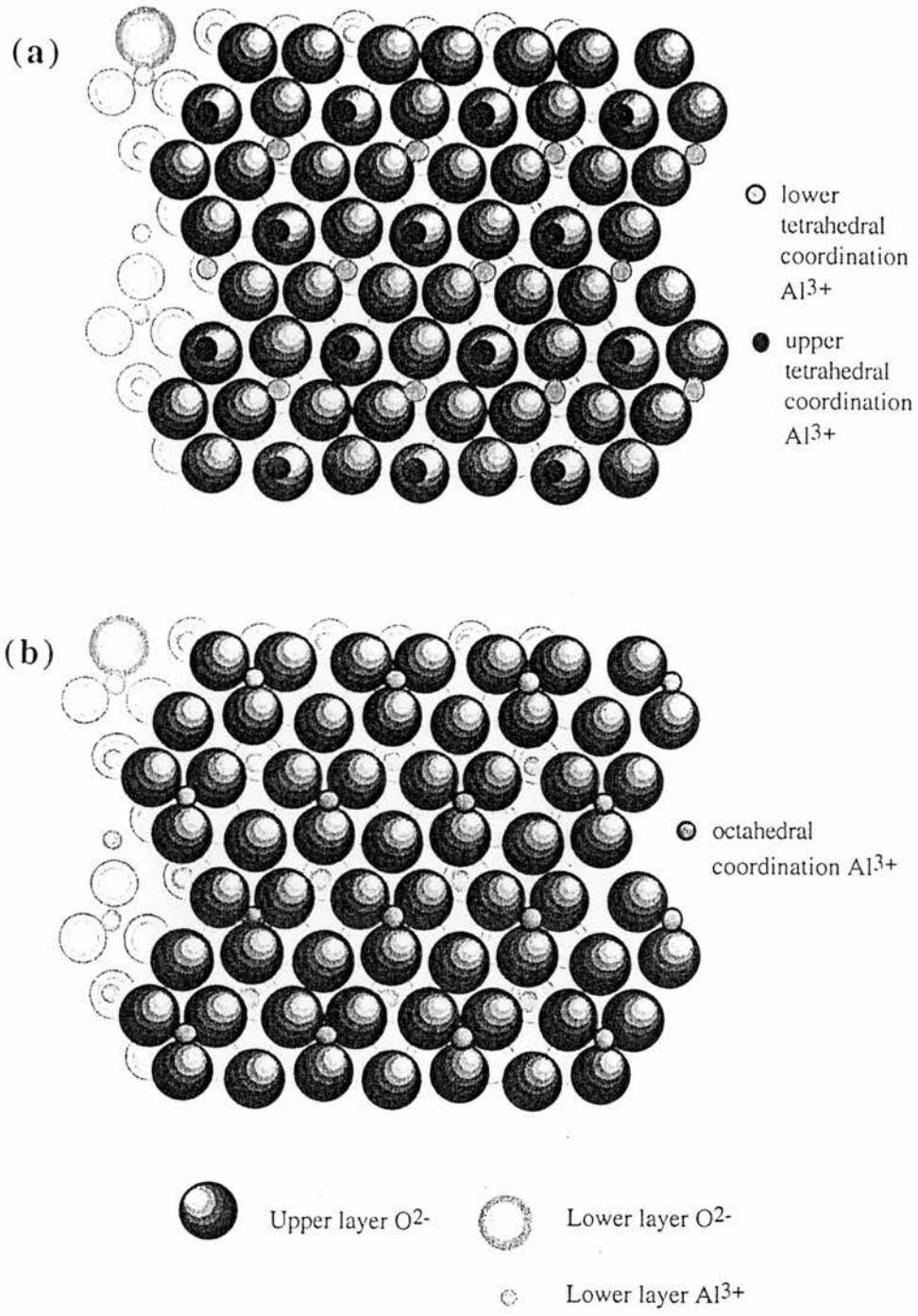

Figure 4. The bulk-truncated, aluminium γ-terminated surface structure of the (111) face of γ-alumina. (a) This shows only aluminium ions (Al^{3+}) in the tetrahedral interstices of the ccp oxygen ion (O^{2-}). (b) This shows only Al^{3+} in the octahedral interstices. The large spheres represent the O^{2-} lattice; the dark layer is the top layer and the lighter layer is the next layer below. The small spheres represent the Al^{3+}. The Al^{3+} coordination is shown in the key beside each diagram [5].

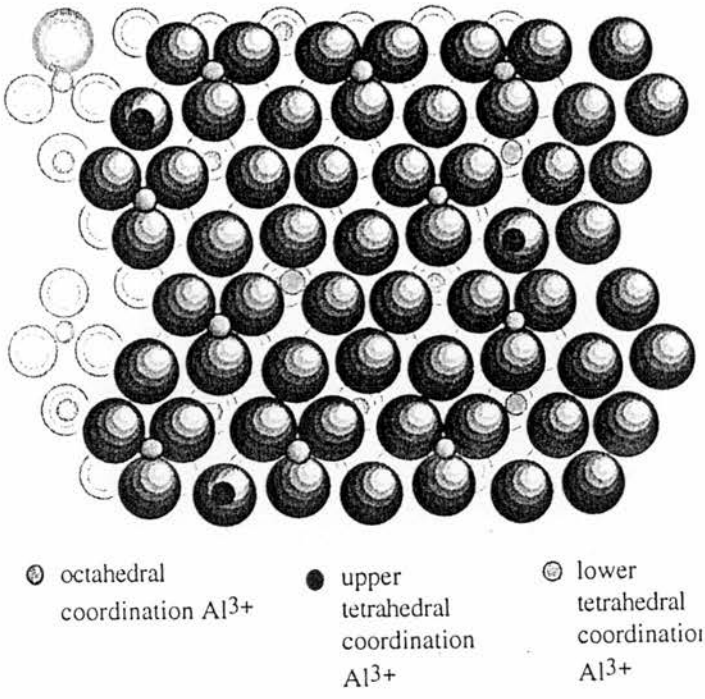

Figure 5. The aluminium terminated surface structure of the (111) face of γ–alumina with random inclusion of aluminium ions. This shows aluminium ions (Al^{3+}) in the tetrahedral (Th) and octahedral (Oh) interstices of the ccp oxygen ion lattice (O^{2-}) in the ratio found in bulk γ–alumina (Oh to Th 2:1). The large spheres represent the O^{2-} lattice; the dark layer is the top layer and the lighter layer is the next layer below. The small spheres represent the Al^{3+} ions, with coordination as indicated below the diagram [5].

The surface of an amorphous alumina prepared in a dry atmosphere would be expected to have aluminium ions tetrahedrally coordinated with oxygen ions. The amount of oxygen present during the preparation would dictate whether the surface was totally oxygen terminated or there were coordinately unsaturated aluminium ions in the top layer of the oxide. As such an oxide is heated, it becomes more like γ-alumina surface with more aluminium ions in octahedral coordination. If the oxide forms in a wet atmosphere then a surface covered in hydroxyls would form a different type of oxide. A review of hydroxylated powder aluminas is given by Knozinger and Ratnasamy [8].

2.3 Interactions of molecules with alumina surfaces

The interaction of molecules with alumina can be divided into five categories. These include: **(i)** Van der Waals' and related interactions [9], **(ii)** Hydrogen bonding interactions [10,11], **(iii)** Lewis acid-base interactions [12], **(iv)** Brønsted acid-base interactions [12] and **(v)** Ionic or covalent chemical bonds [2]. Van der Waals' interactions can be on the order of 0-8 $kJmol^{-1}$ (or 0-2 $kcalmol^{-1}$) [13] between the molecule and the alumina surface. These interactions are not specific to any part of the molecule or oxide, though the force will be stronger for larger molecules, easily polarised molecules or ones with a permanent dipole [9]. Hydrogen bonding requires the sharing of a hydrogen atom between two electronegative centres, usually oxygen or nitrogen. As the alumina surface will contain oxygen ions, any molecule containing a hydrogen attached to an amine group, alcohol group, thiol, halogen or similar functional groups will be attracted to the surface via hydrogen bonds. These bonds can be as large as 50 $kJmol^{-1}$ (or 12 $kcalmol^{-1}$) [11]. There is evidence from work by Frederick *et al* [14] that, at low temperatures (140K), methanol forms a weakly chemisorbed species that has a desorption activation energy of about 28 $kJmol^{-1}$ (7 $kcalmol^{-1}$). This type of bond is intermediate between dipole-dipole van der Waals' bonding and hydrogen bonding in energy. Lewis acid-base interactions involve the transfer of electrons from an electron rich atom to an electron deficient atom, where the electron donor is defined as the base and the electron acceptor is defined as the acid [12]. On an alumina surface, aluminium ions that are coordinately unsaturated are Lewis acids and will accept electron donation from lone pairs on, e.g., amine nitrogen atoms. This type of interaction is shown in Figure 6(i). The energy of this bond can be as much as 160 $kJmol^{-1}$ (40 $kcalmol^{-1}$) [15]. Brønsted acid-base interactions require the transfer of a hydrogen ion. The hydroxyl groups on alumina surface can behave as Brønsted acids. Interaction with amine groups can give an alkyl ammonium ion, which bonds ionically to the oxygen ion derived from the hydroxyl. The defect sites of alumina powders have been studied using weak Lewis acids, such as

carbon monoxide (CO), with infrared spectroscopy [16-19]. Morterra *et al* [18] showed that, on α-alumina powder, there are two defect sites. The first defect site is a coordinatively unsaturated aluminium ion (Al^{3+}) in octahedral coordination and the second is associated with a surface OH group. In 1994, Morterra *et al* [19] showed that there are three defect sites on γ-Al_2O_3 and δ,θ-Al_2O_3 powders. Two of these were assigned to sites formed by dehydroxylation. The coverage and interaction energies have been determined; however, more specific microscopic structural information would be desirable but requires better defined surfaces. Working using amines [20], particularly pyridine [21], has also been used to probe the defect sites of alumina powders. This type of work confirms the existence of Lewis and Brønsted acid sites. Covalent and ionic bonds are much stronger than all the other bonds mentioned in this section. For example, the oxygen-hydrogen bond, which is covalent, has a bond enthalpy of 483 $kJmol^{-1}$ and the enthalpy of formation ($\Delta_f H^o$) for the ionic compound α-alumina is -1675.7 $kJmol^{-1}$ [9].

Amines are used as probes for Brønsted and Lewis sites on alumina surfaces. One of the reasons for their utility is their reversible adsorption, simplifying the experiment [20]. However, ammonia is known to form ion pairs on alumina shown in Figure 7 [21].

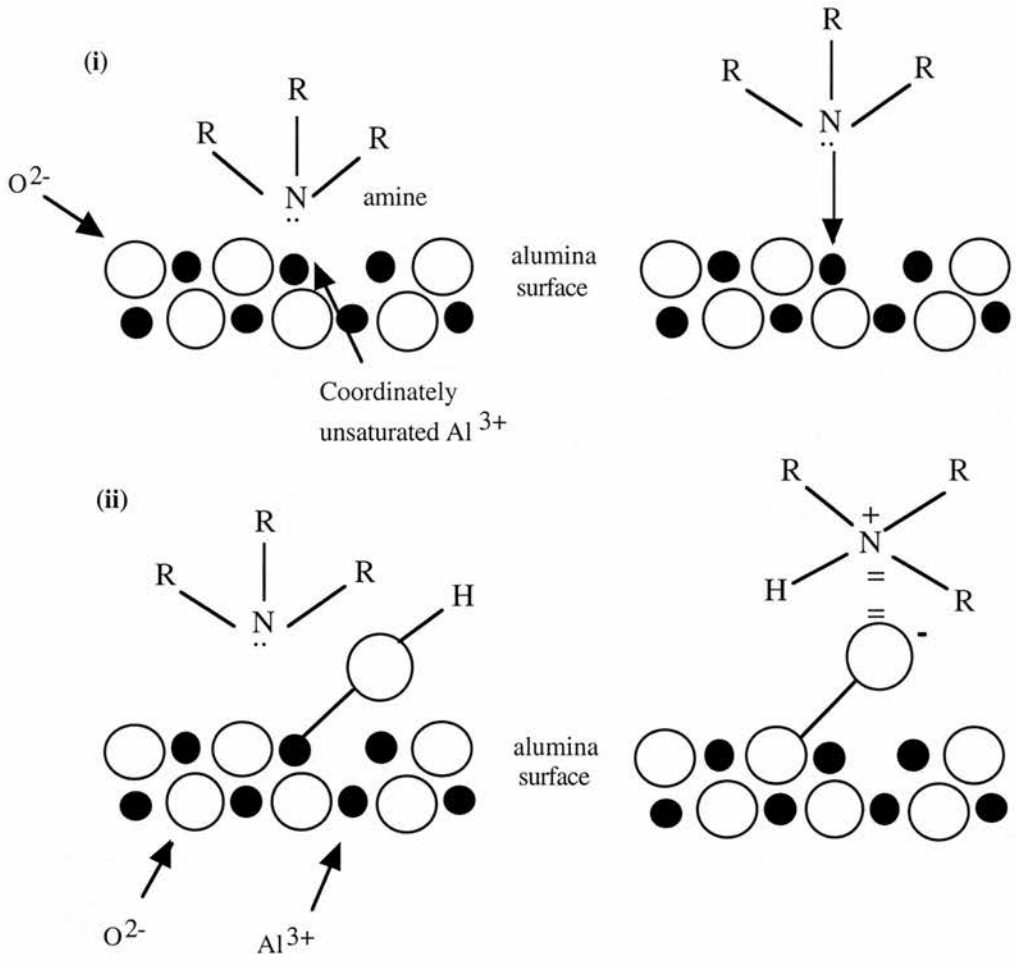

Figure 6. The BrØnsted and Lewis sites on alumina surfaces illustrating how an amine would interact with them.

(i) A Lewis site shown as a coordinately unsaturated aluminium ion. The lone pair of the amine nitrogen donates electron density to the aluminium ion to form a dative bond.

(ii) A BrØnsted acid site shown as a hydroxyl group on the alumina surface. The hydrogen of this hydroxyl group transfers to the nitrogen when the interaction occurs. The proton transfer causes a positive charge on the nitrogen and leave a negative charge on the hydroxyl oxygen. An ionic bond holds the alkyl ammonium ion on the surface.

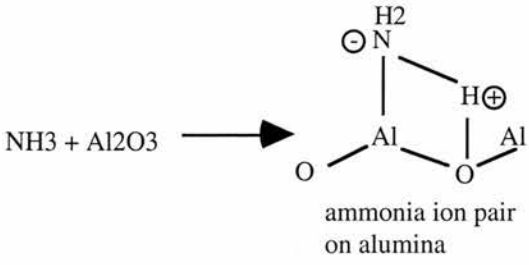

Figure 7. The structure of an ion pair for ammonia on alumina as proposed by Peri [21].

Methanol is known [22-24] to react with aluminium metal to form a surface oxide and methane in the first instance. Further reaction with the oxide surface leads to a surface methoxy species. These two stages are shown in Figure 8.

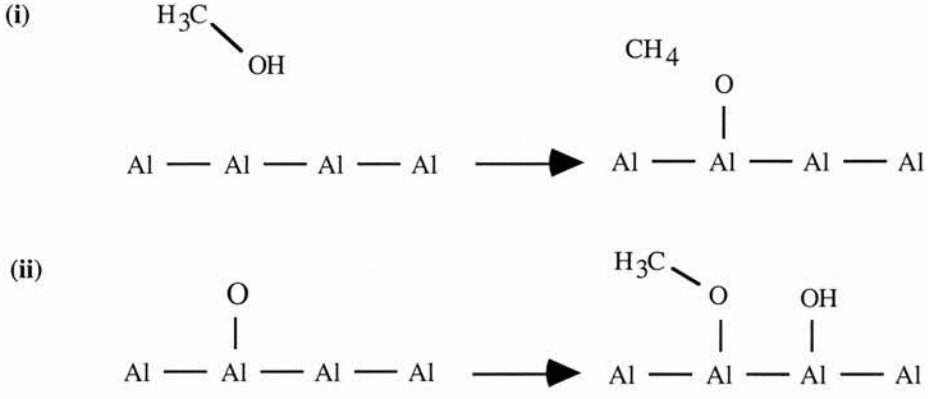

Figure 8. A summary of the reaction of methanol with aluminium metal as described by Tindall and Vickerman [22]. (i) The reaction of methanol with the clean aluminium surface to form an oxide and methane. (ii) The reaction with oxidised aluminium to form a methoxy species and a surface hydroxyl.

2.3.1 Interaction of substituted benzenes with metal surfaces

The interaction of aromatic molecules with metal surfaces has recently been the subject of several investigations [25]. Much of this interest is derived from the importance of aromatic molecules such as fuels, chemicals and lubricants that are produced and utilised

by technologies where surface phenomena play a dominant role. For example, phenolic groups are used as adhesion promoters of polymers and aniline is the monomer for the conducting polyaniline; both molecules are subunits in the aromatic polyimides. For phenol on Cu (110) the HREELS spectrum shows an intense CH out-of-plane bending mode at 770 cm^{-1}, and its presence led Richardson and Hofmann [26] to deduce a parallel orientation of the aromatic ring, whereas the absence of OH stretch was taken to indicate the formation of phenoxide species at the surface. The removal of phenolic hydrogen to form surface phenoxide has also been suggested for phenol adsorption on Mo (110) at around 360K [27], and Pd (110) below room temperature.

2.4 Nature of acidic sites and acidic solids

Alumina surfaces exhibit a remarkable chemical heterogeneity and can be considered as typical amphoters. Their chemical properties may be illustrated by comparing their surface chemical activity with the activity of water as shown below.

Amphoteric nature of water [28] and alumina:

Acids:

$$xH_2O + :Cl^- \longrightarrow Cl:(H_2O)_x$$

$$Al + :NH_3 \longrightarrow Al:NH_2$$

Bases:

$$yH_2O + Mg^{2+} \longrightarrow Mg(H_2O:)y^{2+}$$

$$Al\text{-}O^{2-} + CO_2 \longrightarrow Al\text{-}O\text{-}CO_2{}^{2-}$$

Oxidants:

$$2H_2O + 2Na \longrightarrow 2Na^+ + 2OH^- + H_2$$

Reductants:

$$2H_2OF_2 \longrightarrow 4H^+ + 4F^- + O_2$$

These reactions indicate that the acidity is not the only important chemical property of alumina surfaces. Two important types of active sites which exist on alumina surfaces are surface hydroxyls and aluminium cations embedded in a specific neighbourhood. The existence of these sites depends on the calcination temperature of the aluminium hydroxide or oxide. Models for alumina surface hydration were proposed by Peri [29] and by Knozinger and Ratnasamy [8]. Our subsequent discussion of the acidic properties of alumina will be based mainly on the latter model. Knozinger and Ratnasamy [8] discriminated between 5 different types of surface hydroxyls assuming that, on the surfaces of η-alumina and γ-alumina, the dominant planes are (111) and (100), respectively, and that there exist two possible distributions of aluminium cations in the spinel lattice of both aluminas. In η-alumina, two types of OH group configurations are connected with the so called anionic layer A which possesses 24 cationic positions. Cations linked with this layer occupy octahedral interstices and the other 16 cations occupy tetrahedral cationic positions. The remaining three types of OH group configurations in η-alumina correspond to the "B-layer" in which all 24 aluminium cations are in octahedral coordination. The possible configurations of hydroxyls [8] are shown in Figure 9. The terminal OH group **(Ia)** is linked with only one tetrahedral aluminium cation, while the OH group of **(IIa)** type is bridging an Al^{3+} cation in tetrahedral configuration with one in octahedral configuration. Both types of OH groups **(IIb)** and **(III)** are bridges connecting octahedral aluminium cations. Hydroxyl of type (III) coordinates simultaneously three cations. The OH group termed **(Ib)** links only one Al^{3+} cation of octahedral configuration.

During calcination above 300°C, the alumina surface undergoes intensive dehydration. Up to a temperature of about 430°C, dehydration occurs by the reaction of two neighbouring hydroxyls to form a water molecule. After release of H_2O, an anionic vacancy and a naked O^{2-} ion remain on the surface. The defects formed have a weakly acidic and basic character, respectively. At temperatures higher than 430°C, significant irregularities begin

to appear in the dehydration process [30,31]. Surface protons and aluminium cations become mobile and start to change their positions in the lattice. Under these conditions, new defects are generated, which have been termed "surface configurations of low probability" [31]. These defects are: multiple anionic vacancies (three or more Al^{3+} cations in close neighbourhood), oxygen ion clusters, and defects being a combination of the former defects. The multiple anionic vacancy possesses a strong Lewis acidic character; the cluster of oxygen ions is of strong basic character; and the combined defects form sites which possess ion pair character: strong acid-strong base properties (termed acid-base sites). The local defects of oxygen-ion-deficient type are the source for the Lewis acidity exhibited by alumina. As shown above, the naked aluminium cations formed during the regular dehydration and the multiple anionic vacancies originating during calcination at high temperatures are the most important potential electron acceptors.

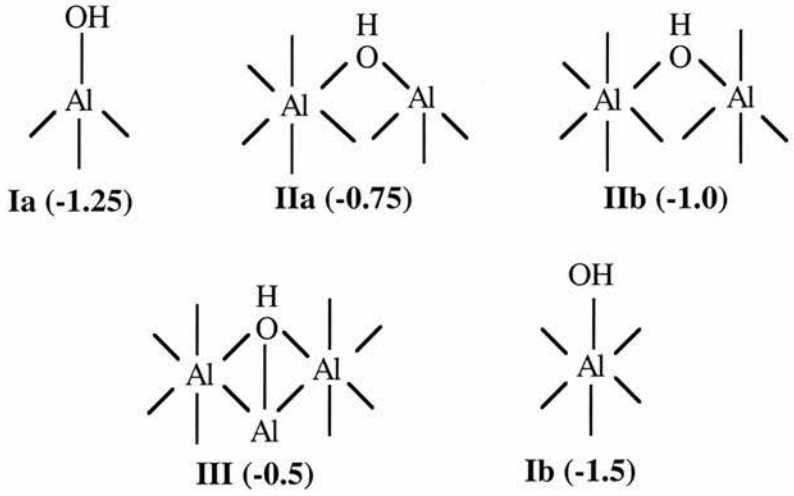

Figure 9. Schematic representation of the superficial OH groups (the charge on the oxygen is represented by negative numbers).

The insignificant activity of alumina calcined at low temperature found by many investigators [32-35], and the remarkably higher negative charge deficit in the sphere of a multiple vacancy, indicate that the latter is the surface site active as electron acceptor. In a

more general sense, we can state that the principle origin of acidic properties of simple oxides are surface OH groups (Brønsted acidity) and overexposed metal cations (Lewis acidity). The temperature range of their existence can be different depending on the solid. In general, acidic activity of electron deficient defects on the metal oxide surfaces depends on the position of the particular metal in the periodic system of elements, i.e. on the electronegativity of the metal cation.

2.5 Properties of Zeolites

This section compares the pore structure of zeolites to alumina surfaces. Zeolites encompass a broad range of porous crystalline solids comprising of alumino-silicates. The framework consists of an infinitely extended three-dimensional network of corner-sharing SiO_4^- and AlO_4^{5-} tetrahedra (T). The void volume consists of regular micropores and cages which may amount to 50% of the crystal by volume. The zeolite framework should be viewed as somewhat flexible. The size and shape of the pore system responds to changes in temperature and interaction with guest molecules. As a result of the physical and chemical nature of zeolites a number of properties and characteristics arise [35] such as:

- Reversible water loss,
- Thermal framework stability,
- Cationic exchange capabilities,
- Brønsted and Lewis acidity,
- Adsorption of gases and vapours,
- Conductiometric abilities.

2.5.1 Zeolite Classification and Structure

Over 100 topologically distinct, naturally occurring and synthesised zeolites are known [36]. They exhibit pore sizes from 0.3 to 1.5 nm. Breck [37] first proposed a method of

classifying zeolite frameworks based on common subunits. The primary building unit (PBU) is a tetrahedron, centred on either a silicon or aluminium with bonds to four oxygen atoms located at the vertices. In turn each oxygen is bonded to two T atoms. Secondary building units (SBUs) are generated when a specific array of T units are linked through T-O-T bridges as shown in Figure 10. Meier postulated eight key SBUs as the smallest number of subunits to describe zeolite framework [38].

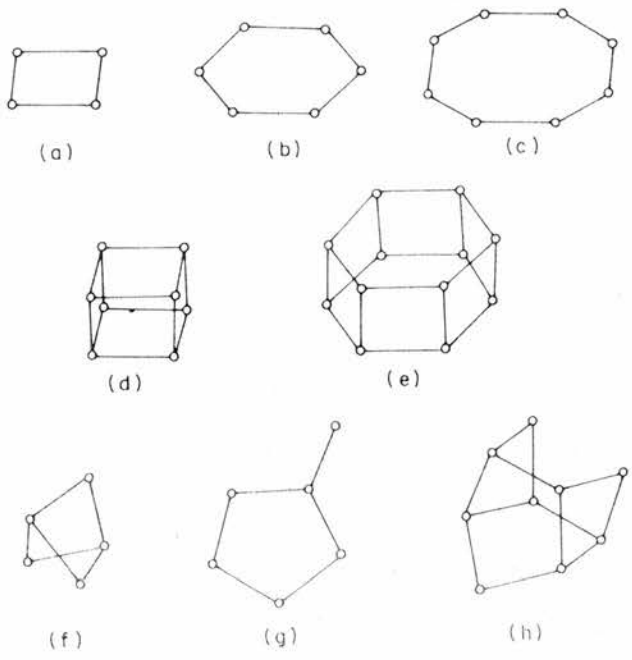

Figure 10. SBUs: SR-single ring, DR-double ring (a) S4R, (b) S6R, (c) S8R, (d) D4R, (e) complex 4-1 (T_5O_{10} unit), (f) complex 5-1 (T_8O_{16} unit), (g) complex 4-4-1 ($T_{10}O_{20}$ unit) and (h) D6R.

2.5.2 The structure of ZSM-5 and ZSM-11

ZSM-5 and ZSM-11 have been defined as the structure types MFI and MEL, respectively [39]. They form the end members of a series of high-silica zeolites known as Pentasils. Crystallographic studies [40] have shown that both structures are composed of 96 T atoms and based upon identical basic building units made up of 8-and 5-MRs joined along [001] as depicted in Figure 11. These form chains which pack laterally along [010] generating a pentasil sheet as shown in Figure 12. The structure of ZSM-5 is generated

when adjacent [100] planes or sheets are related to one another by inversion (i) symmetry. In contrast, the structure of ZSM-11 is formed when the [100] sheets are associated by mirror symmetry (σ). In ZSM-5, two orthogonal sets of intersecting 10-MR aperture channels or pore systems occur. The channels, that run along [010] are straight with nearly circular diameter of 5.5 Å, whilst those along [100] follow a sinusoidal course and possess an elliptical cross-section of approximately 5.1x5.5 Å. The unit cell dimensions of ZSM-5 based on orthorombic (Pnma) sysmmetry are a=20.02 Å, b=19.90 Å and c=13.38 Å. For ZSM-11 the two orthogonal sets of channels are equivalent, straight and elliptical about 5.1x5.5 Å in diameter. The unit cell dimensions of ZSM-11 based on tetragonal (I4m2) symmetry are a=20.07 Å, b=20.07 Å and c=13.41 Å.

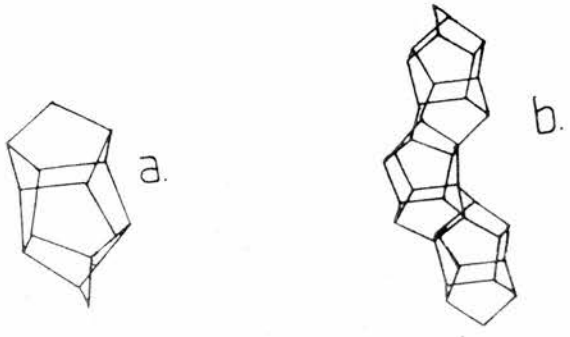

Figure 11. Basic pentasil building unit (a) and chain (b).

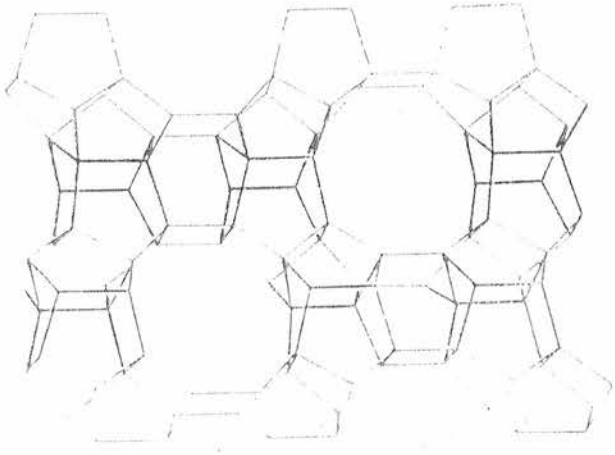

Figure 12. Characteristic pentasil layer.

All cavities formed at the intersections of the channels in ZSM-5 are equivalent. In ZSM-11 there are two distinct types [41], one similar to that found in ZSM-5, the other larger by approximately 30%. The net result is a decrease in the channel tortuosity and an increase in the volume available within the intra-crystalline pore structure of ZSM-11 compared to ZSM-5. This duality of cavity geometry is of particular significance in determining the precise nature of the shape-selective catalytic characteristics of the two materials [42]. Kokatailo and Meier [41] suggested that due to the subtle differences in the framework nature of ZSM-5 and ZSM-11 an almost infinite variety of related compounds could be synthesised, intermediate in structure between ZSM-5 and ZSM-11. By a regular and random sequencing of the σ and i planes intergrowth materials are generated as depicted in Figure 13. A schematic representation of the pore systems of ZSM-5, ZSM-11 are given in Figure 14.

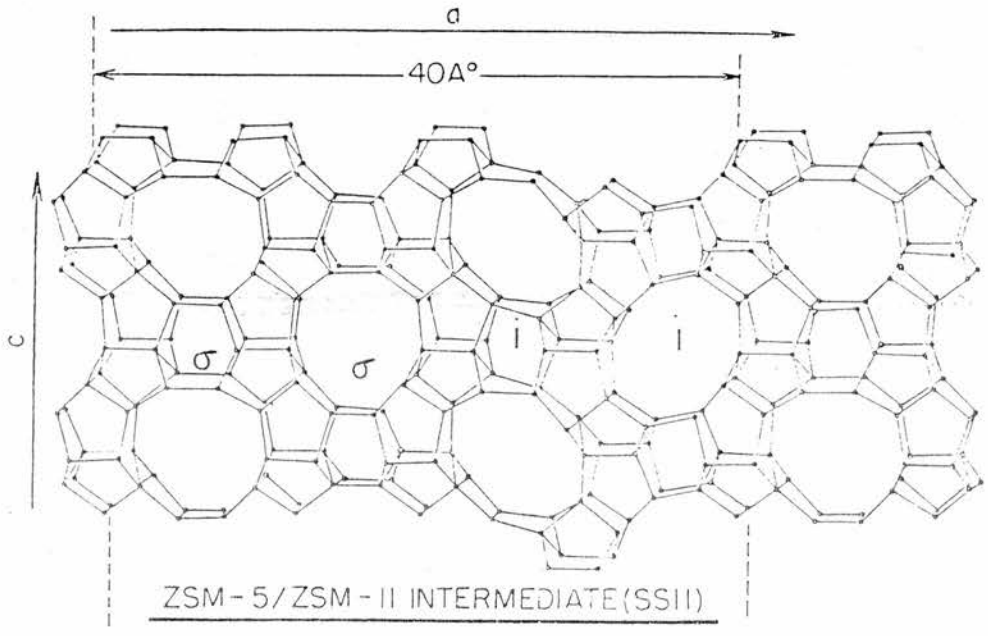

Figure 13. Skeletal framework diagram of a (σσii) pentasil intergrowth and subsequent pore system projected along the [010].

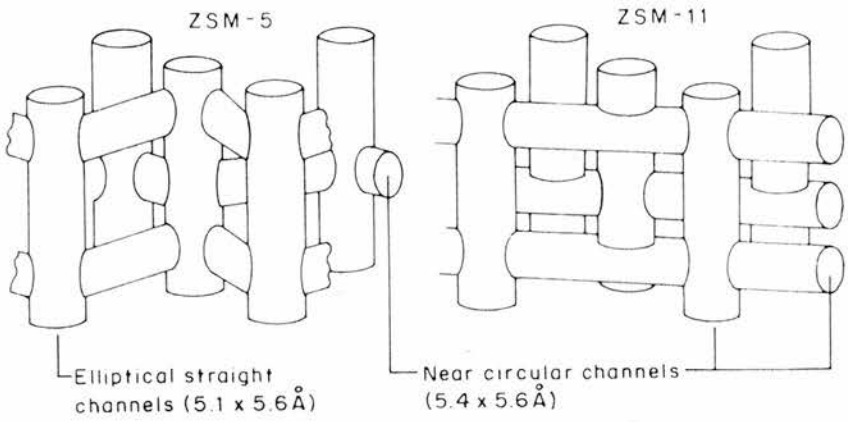

Figure 14. The pore sysytem of (a) ZSM-5 and (b) ZSM-11.

2.5.3 Acidity of Zeolites

Although reactions do occur on the surface of the zeolite crystal, the majority of the reactants are transformed at the active sites within the intra-crystalline void system. Access to the interior of the zeolite crystals is controlled by the aperture size of the pore system. The reactant molecule, typically organic, enters the zeolite and is then subjected to the geometry environment of the pore system. In the case of ZSM-5 and ZSM-11 the internal pore system consists of channel linked by channel intersections. The pore geometry has important consequences for the diffusion and shape-selective catalysts in zeolites.

The majority of zeolite catalytic processes involves acid-catalysed hydrocarbon transformation. It is generally accepted that the hydroxyls groups associated with the framework aluminium provide the Brønsted sites [43]. Such framework acidity is usually introduced by the thermal decomposition of the ammonium ion-exchanged form of the zeolite [43]. The hydroxyl groups may be regarded as protons bonded to negatively charged framework oxygen associated with the AlO_4^- tetrahedra. At reaction temperatures above 200°C the protons are mobile and move between sites [44]. The presence of

another type of acid site, namely a true Lewis site, have been identified. Such sites are thought to be composed of alumino-hydroxyl species, thermally dislodged from the framework at temperatures above 500°C [43]. Although still open to speculation, several workers have suggested the presence of super-acid sites [45]. These are believed to be enhanced BrØnsted acid sites arising from the synergism between dislodged alumino-hydroxyl species and framework hydroxyls such as:

$$TO_n(OH)_m \ldots (AlO)^+_p$$

where T represents Si and Al atoms and n, m and p are integral numbers. Hence, the acidic properties of zeolites as a consequence of framework composition, depends on the number and concentration of acid sites as well as their relative strengths [46].

The matching the size and configuration of reacting molecules, intermediates and products with the geometry and tortuousity of the zeolite channel or cavity provides the basis for controlled shape selectivity [43]. Reactant selectivity is observed when only a fraction of the reactants has access to the active sites because of the molecular sieving effects. Product selectivity occurs when only some of the products species with the correct dimensions or configuration can diffuse out of the zeolite intra-crystalline volume. Restricted transition state selectivity takes place when certain transitions states cannot be formed due to steric restrictions.

2.6 Morphology of anodic films

The metallurgical properties of aluminium such as low relative density, hardness and rigidity by the addition of relatively small amounts of Si, Cu, Mn have made it an attractive metal for many aspects of engineering and construction. Anodising is a well accepted surface treatment for aluminium and its alloys before applying a primer or an adhesive. Anodic films on aluminium are generally classified as barrier-type or porous type. Barrier-type films develop usually in so-called non-aggressive electrolytes (environments with little or no reactivity to the anodic alumina), e.g. neutral borate solutions. The resultant film thickness is proportional to the forming voltage and is

usually limited to less than one micron because of the onset of dielectric breakdown. A porous film is formed in electrolytes with some solvent action on, or reactivity with, the anodic alumina, e.g. phosphoric acid. Anodising conditions such as current density, potential, electrolyte concentration and temperature have a significant effect on the morphology, composition and thickness of the resultant porous film. Thickness ranges from fractions of a micron to tens, or hundreds, of microns, depending on anodising conditions.

2.6.1 Barrier films

Barrier films are relatively thin and, if formed at high efficiency, they are considered to be essentially non-porous. The films are relatively uniform, compact and show little electronic conduction. Barrier films are formed in electrolytes with little or no solvent effect of the electrolyte on the alumina film material; tartrates and phosphate solutions, and several organic electrolytes including citric and maleic acids. During anodising, the film thickens as the voltage rises with time in an approximately linear manner. Such thickening is terminated at a relatively high value at which dielectric breakdown occurs. The resultant thickness of the barrier film is dependent upon the formation voltage and is usually expressed in terms of the "anodising or forming ratio" (nm/V). In summary, barrier films appear relatively featureless in the TEM, though they do contain minute flaws. Film thickness is relatively uniform. Barrier films formed at ambient temperatures are amorphous or have been considered to consist of microcrystalline γ -Al_2O_3, the relative extent of crystalline material depending on forming conditions. Barrier film growth is believed to occur by two simultaneous processes[47,48]:

1. Growth by ionic migration through an existing film occurs i.e. both Al^{3+} and O^{2-}/ OH^- ions form new oxide at the metal/film interface.

2. Solid state film formation occurs at the film/solution interface by solid state mechanisms involving Al^{3+} egress. Al^{3+} egress has been inferred for both barrier films and porous anodic film.

2.6.2 Porous films

Porous films are also called duplex films due to their characteristic morphology. Anodising of aluminium in electrolytes in which the film is slightly soluble produces a porous film. Porous anodic films are formed readily in acid electrolytes including phosphoric [47], chromic [48], sulphuric [49] and oxalic acids [50]. Porous anodic films on aluminium are morphologically well characterised, with the characteristic major pores seen to pass normally to the macroscopic aluminium substrate, but separated from it by a barrier layer of scalloped appearance. The porous layer consists of continuous columns of cell material with pores at their centres; the pore base is separated from the metal by the barrier layer. Variations in the film can occur, for instance, as the pores on occasion branch, merge and terminate due to local variations in the pore base situation. To maintain growth perpendicular to the metal surface, new pores form by branching in the oxide above concave surfaces and pores terminate in the oxide above convex surface and ridges. It is recognised [49] that steady-state porous anodic films consist of an approximately hexagonal close packed arrangement of anodic alumina cells, with a major pore at the centre of each cell. The size of the cells increases with increasing voltage [50]. The pore population density shows an inverse relationship to the forming voltage. A major characteristic of porous anodic films is the "whiskers" at the film surface. These are formed by dissolution of the film surface. Dissolution can proceed by two mechanisms, field assisted and chemical dissolution. Field assisted dissolution involves stretching and breaking of aluminium-oxygen bonds under the field during anodising. This aids solvation of Al^{3+} ions and proceeds at a much faster rate than chemical dissolution of the film material, and, by definition, is influenced by the presence of the field and local Joule heating effects generated in the barrier layer during film growth.

2.6.3 Barrier film growth

Despite numerous investigations, the nature of ion transport is still not clear; this is a crucial factor in determining where new material is "deposited" and in deciding how fine pores, nucleating on the outside of a film, develop eventually into steady-state or major pores. It is known that barrier-type anodic films on aluminium develop by high field ionic conduction across the initial air-formed film present on the substrate. The transport of ionic species is stimulated by the relatively high field strength across the thickening film. The exact mechanism of transport is subject to some uncertainty; however, it is generally considered that Al^{3+} and O^{2-}/OH^- are mobile species during anodising. A model for initial film growth has been proposed which involves two simultaneous processes [62,63]:

1. Growth by ionic migration through an existing film occurs, i.e. both Al^{3+} and OH^-/O^{2-} are mobile and form new oxide at the metal/film interface.
2. Growth by a deposition process occurs at the film/electrolyte interface, that is Al^{3+} ions are ejected at this interface to form hydrated ions in solution.

2.6.4 Pore initiation and growth

Pores are initially formed in the barrier layer by dissolution of the film by the electrolyte. Current passing raises the temperature of the solution contacting the substrate and thus further increases the rate of chemical dissolution. This process leads to the penetration of pores, as the current flows through a single pore, a cylindrical cell with a roughly hemispherical end is built up in accordance with the electric field, which in turn finishes up in contact with six surrounding cylinders and ultimately gives a hexagonal prism shape. A popular concept in film growth was that it was due to aluminium ions migrating outwards and reacting with oxygen containing ions near the outside of the barrier layer, resulting in the formation of anhydrous alumina. This has been developed so growth involves two major simultaneous processes [63]:

1. Growth by ionic migration through an existing film occurs i.e. Al^{3+} and O^{2-}/OH^- are

mobile and form oxide at the metal/film interface.

2. Solid film formation occurs at the film/solutions interface by solid state mechanism and/or by dissolution/precipitation. In the initial stages of film growth, this corresponds to a linear rise of voltage in the voltage-time curve, the film develops relatively uniformly to a thickness dependent on the voltage. After the initial uniform film growth where the current is relatively uniformly distributed for a transient period, the current is greatest at the regions above the metal ridges which consequently develop a locally thicker film and tend to flatten the metal/film interface.

2.6.5 Steady state film growth

The initial non-uniform film growth and pore development lead to the formation of the relatively regular porous anodic film, which thickens coulombically in the steady-state region. At this stage of the growth process, there is a dynamic equilibrium between film growth and film assisted dissolution. As a result of steady state porous anodic film growth, aluminium ions are detected in the electrolyte which arise from distinctly different processes. Chemical dissolution of the film material, generally at a relatively slow rate, is one source and direct ejection due to the film growth process is another. Additionally, loss of aluminium from the film material also occurs as a result of field assisted dissolution at the pore base.

2.7 Composition of porous anodic films

2.7.1 General structural and compositional features

It is generally agreed [59] that anodic films consist of mainly anhydrous alumina which is either amorphous or microcrystalline alumina. There is considerable disagreement regarding the degree of crystallinity of the film and, although various attempts have been made to quantify this, it is still uncertain whether the material comprising the barrier layer and cell walls is amorphous, microcrystalline or glassy in nature, and whether such forms of alumina co-exist. However it would appear that at least part of the film is probably a

relatively open array of alumina microcrystallites. It has been inferred that the extent of crystalline material depends upon the electrolyte and tends to increase with increasing voltage, thickness, temperature and in anodising at higher acid concentration. There is considerable disagreement [70] to the degree of crystallinity of films. Within one film, for instance, formed in sulphuric acid, the outer layer was considered to comprise a mixture of crystalline γ-Al_2O_3 and boehmite, α-AlO(OH), whereas the inner layer was amorphous. A freshly prepared anodic film is considered to be a relatively open array of amorphous, largely anhydrous, alumina microcrystallites, the surfaces of which carry hydroxyl groups or ions. Regions between microcrystallites contain molecular water and probably the acid anion. A cell boundary band of relatively pure alumina is effectively separated from the electrolyte in the pores by a phosphate incorporated film region in the case of phosphoric acid anodisation. The grain sizes of anodic films have been estimated, and although the values vary considerably e.g. sulphuric acid 1.2 nm, oxalic acid 0.5-1.0 nm, phosphoric acid 2.4 nm, they support the concept of microcrystallites in the anodic film.

2.7.2 Water content of anodic films

The quantities of water found in anodic films vary considerably, probably due to the different forming conditions. Most of the evidence available indicates that the water is in the form of either hydroxide, free hydrated alumina or both. Water incorporation into a film slowly converts the amorphous film material to the monohydrate. Little hydration has been found in barrier films formed in tartrate electrolytes. Thermogravimetric analysis (TGA) on freshly prepared chromic acid anodising (CAA) films showed the mass of the specimen remained practically unchanged throughout heating, indicating the films contain no appreciable amounts of water or structural anions [72]. Quantities of water in anodic films have shown wide variations, probably due to different film forming conditions, handling and measuring techniques. Values for films formed in sulphuric acid have ranged from 1-15% water, whereas films found in chromic acid have been stated to be

anhydrous.

2.7.3 Acid anion incorporation into anodic films

The literature shows reasonable agreement with respect to the levels of anion incorporation within the bulk films. The highest anion incorporation is reported for sulphuric acid, decreasing in the order phosphoric acid > oxalic acid > chromic acid. Anion incorporation occurs in both barrier films and porous films [63]. With barrier films, in almost every case, incorporation of species from the electrolyte occurs to give a contaminated outer region of the barrier film and an inner anion free region, probably of relatively pure alumina, adjacent to the metal/film interface. The thickness of the inner region appears to be related to the electrolyte anion of the solution in which the film was formed. Phosphorus is widely reported [69] to be found in the outer two thirds of barrier film material with a phosphate-free region adjacent to the substrate. However, a separate study detected phosphate species initially throughout the film, only at a certain thickness is there an anion free layer. Barrier films formed in other electrolytes show broadly similar behaviours. Boron has been found in the outer half of the alumina film, tungsten in the outer one-third, chromium in the outer one-fifth and carbon, from nickel acatate electrolyte, has been found by SIMS depth profile. It is widely accepted [72] that porous anodic films are contaminated by acid anion species. The literature shows reasonable agreement with respect to levels of acid anion incorporation within the bulk films. In films produced by anodizing in sulphuric acid sulphur has been found in the film as SO_4^{2-} and as sulphides by XPS; the distribution of species is non-uniform throughout the film. Carbon is present in the oxide layer in a measurable concentration, incorporated from the solution. The carbon concentration shows a maximum at the surface, a slow decrease through the oxide, and no signal from the very thin oxide region adjacent to the metal. Other work using dissolution and chemical analysis techniques divides the film into three regions [63]:

1. Pore walls with extensive (9%) oxalate incorporation.

2. An intermediate region with higher (12%) oxalate incorporation.

3. Inner region where the acid anion incorporation content decreases significantly to a relatively low level .

In the same work, films formed in sulphuric and phosphoric acids gave qualitatively similar results.

2.8 Electrochemistry of Aluminium-Water system

2.8.1 General Principles

Whether a metal will corrode or not is a question best answered by carrying a suitably designed experiment. However, an acceptable substitute, bearing in mind the limitation can be obtained by considering the equilibrium thermodynamics of the metal/environment system. The limitations referred to are that the reactions considered are under equilibrium conditions, whereas corrosion is a non-equilibrium process. The thermodynamic consideration give no indication of reaction rates (kinetics), they apply only to pure metals, not alloys, are temperature dependant and do not predict the behaviour of metals in contact with certain aggressive media such as chlorides. Electrochemical reactions which involve the release of electrons are oxidation and are referred to as anodic reactions. Those which consume electrons are reduction or cathodic reactions [51]. If we consider [52] a reaction between a clean metal surface immersed in an aqueous solution such that metal dissolves from the electrode surface, then as the metal dissolves there occurs an increasing separation of electric charge. These charges lend to line up opposite to each other, in a similar manner to the plates of a capacitor.

2.8.2 The aluminium-water potential-pH diagram

The potential-pH diagram for the aluminium-water system at 298K is presented in Figure 15. as derived by Pourbaix *et al* [53]. At low values of pH and above the potential where the metal itself is the stable phase, the diagram indicates Al^{3+} as the thermodynamically stable species. Pourbaix indicated some tendency for the formation of Al^{3+}, but stated

that the conditions under which it formed were not at that stage established.

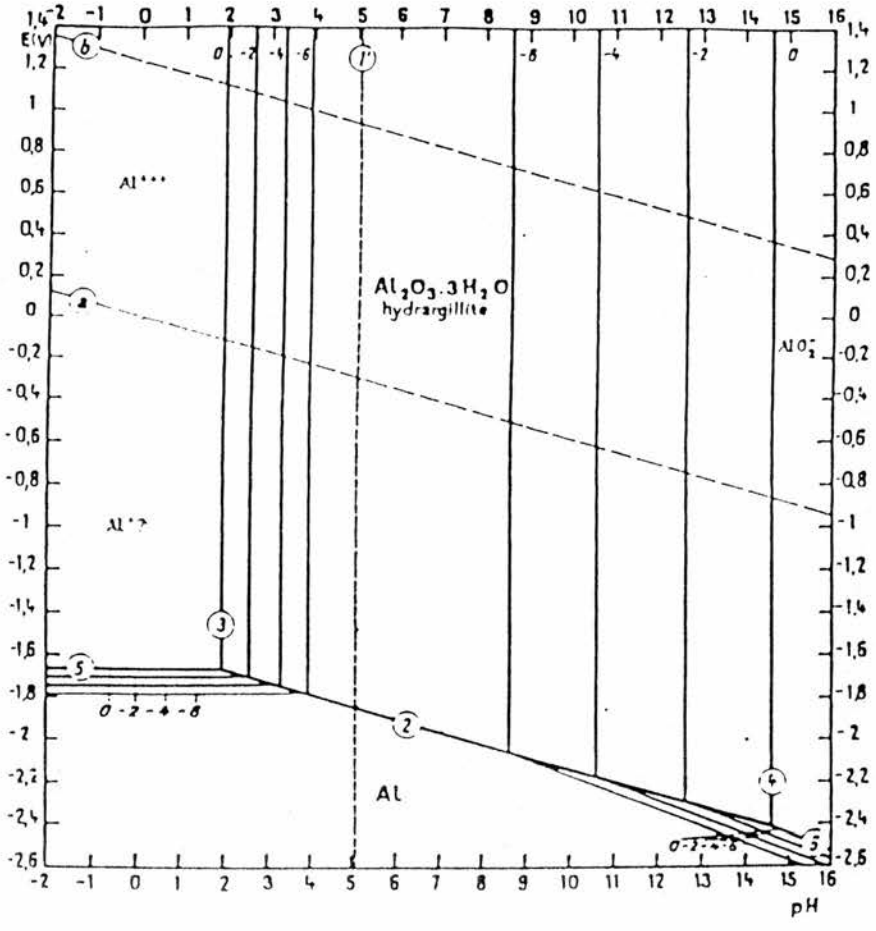

Figure 15. Potential - pH diagram for the aluminium-water system [53].

The modern view is to consider Al^{3+} as stable [54] forming by the reaction:

$$Al \text{ ---> } Al^{3+} + 3e^-$$

This reaction can only occur directly in regions where the overlying tenaceous oxide film has been breached. Consideration of anodic reaction at such flaw sites form the basis of one of the important theories of pit initiation and will be dealt in more detail later in this review. Hoar and Jacob [55] and Pryor [56] considered the anodic reaction to take place at the oxide/solution interface. Hoar and Jacob described the process as involving a

specific number of halide ions adsorbing onto the oxide surface around a lattice cation and forming a transitional complex of high energy. Upon formation, this readily and immediately separates from the oxide lattice, the cation dissolving in solution more readily than adjacent cations in the oxide surface not subjected to the influence of chloride. Pryor considered the reaction to be:

$$Al^{3+} + Cl^- + 2H_2O \dashrightarrow AlO_2H + 3H^+ + Cl^-$$

In neutral pH range, resulting in a reduction in pH at the electrode/solution interface. Oxidation states other than Al^{3+} are considered to be unstable due to solvation sheath instability, and there is no evidence that they exist in solution at ordinary temperatures, although Al^+ and Al^{2+} ions are claimed to be present during high current density anodic oxidation of aluminium but these states are empheral [54]. In solution, Al^{3+} ions are rapidly solvated [54] and exist as octahedral moderately acidic anions, i.e.

$$Al^{3+} + 6H_2O \dashrightarrow Al(H_2O)_6{}^{3+}$$

The hydrolysis of the aluminate aquo-ion occurs by the reaction:

$$Al(H_2O)_6{}^{3+} \dashrightarrow Al(OH)_2{}^+ + OH^-$$

In alkaline solution at pH values > 9 and potentials greater than that at which metal is the stable phase, the stable ion is written as AlO^{2-} conventionally formed by the reaction below [53]:

$$Al + 2H_2O \dashrightarrow Al(OH)_2{}^- + 4H^+ + 3e^-$$

In reality, solvation on solution occurs [54] to form either 4 or 6 coordinated species such as $Al(OH)_4^-$ or $[Al(OH)_4 (H_2O)_2]^-$. At intermediate pH values, the diagram predicts reaction between clean metal surface and solution to form $Al_2O_3.3H_2O$, (hydrargillite), considered by convention to be present as solid on the metal surface which forms an inert barrier between solution and metal. The barrier reduces the corrosion rate significantly since any dissolution reactions must occur by diffusion through the film or breaching at weak spots or flaws. This phenomenon is known as passivation. Experiments in aqueous solution by Pourbaix and co-workers established that hydrargillite forms initially as a hydroxide gel, corresponding closely to $Al(OH)_3$, which is unstable and passes through several crystallographic changes, i.e.

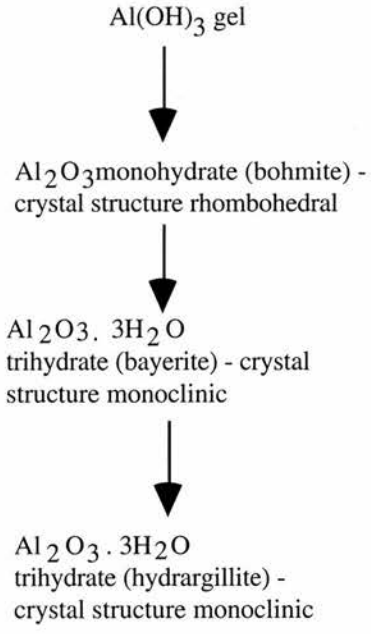

The aluminium/water diagram also exhibits equlibria which refer to the stability of the H^+, OH^- and also oxygen dissolved in water. The diagram portrays the thermodynamically derived regions of stability of water. Below line (b), any oxygen in solution might be expected to be reduced by the reaction:

$$O_2 + 4H^+ + 4e^- \text{ ---> } 2H_2O$$

in acid and neutral solution, and according to the reaction:

$$O_2 + 2H_2O + 4e^- \text{ ---> } 4OH^-$$

in alkaline solution. Similarly, below line (a), any hydrogen ions in solution would tend to be reduced by the reduction:

$$2H^+ + 2e^- \text{ ---> } H_2$$

Thus, the diagram also describes the thermodynamic properties of the two common cathodic reactions. A further reaction which may occur [53] particularly with aluminium and zinc, but of limited extent, is the reduction of oxygen dissolved in the water by hydrogen ions to form hydrogen peroxide.

The above electrochemical reactions on aluminium electrode do not occur uniformly over the metal surface except under very carefully contrived conditions as elegantly demonstrated by Hagyard *et al* [57,58,59,60]. Aluminium surfaces are covered by a tenaceous oxide film, which is effectively an insulator and prevents dissolution over a large part of the electrode surface in the neutral pH range. The oxide film is either air-formed and/or thickened as a result of thermal treatment during fabrication of the material sheet. In the neutral pH range in the absence of aggressive ions dissolution is thermodynamically predicted to be terminated by passivation of metal exposed at any defects in the oxide.

2.9 The anodisation of aluminium in pore forming electrolyte

Porous films are formed in electrolytes in which the oxide has sparing solubility, e.g. sulphuric, chromic, phosphoric and oxalic acids at most concentrations. The most widely accepted general model of porous film structure, with certain reservations is the Keller, Hunter and Robinson model [61]. Work by Keller *et al* [61], O'Sullivan [62] and Wood's review [63] have all described these porous systems in some detail. In this model the porous film is a close packed array of cells of oxide which are basically hexagonal in shape. Each cell contains a single pore, the size of which was claimed to depend on the electrolyte used and was independent of forming voltage. Figure 16. shows a schematic diagram of the porous film. Pore wall and barrier layer thickness are a function of the forming-voltage although electrolyte type does have an effect. The model proposed that in the ideal case the pore section would be star-shaped due to dissolution effects caused by cell geometry. Such star-shaped pores have not been observed in isolated cases [64]. Murphy and Michelson [65] suggested that pores seen in electro-micrographs could be partly due to drying of the porous anodic film during vacuum preparation techniques and that so-called thin spots in the film were contrast effects caused by regions of low density in the oxide material. They proposed the presence of three regions in the film, being:

1. A compact anhydrous inner alumina layer made up of microcrystallites less than 1nm across.
2. A transition region in which hydration of the intercrystallite region increases from the anhydrous state to the state of hydration of the porous layer.
3. A porous layer containing regions of different hydration and density of oxide, distinguishable physically as pores.

Wood *et al* came to certain general conclusions based on an electron optical study of such film:

1. The classical model of Keller *et al* is largely confirmed but some of derivations are not exact.

2. Barrier thickness is proportional to applied voltage with a unit barrier layer thickness of 1nm/V.

3. Cell size is proportional to the applied voltage, although there is still disagreement over proportionality constants.

4. The calculated pore diameter of 30 nm in 4% H_3PO_4 is much lower than values obtained from direct measurement which are in the range 70-80 nm.

Later work by O'Sullivan and Wood's indicated that the barrier layer thickness and pore diameter were directly proportional to forming voltage. When sectioned along their length the pores appeared to be trumpet shaped rather than the truncated cone predicted.

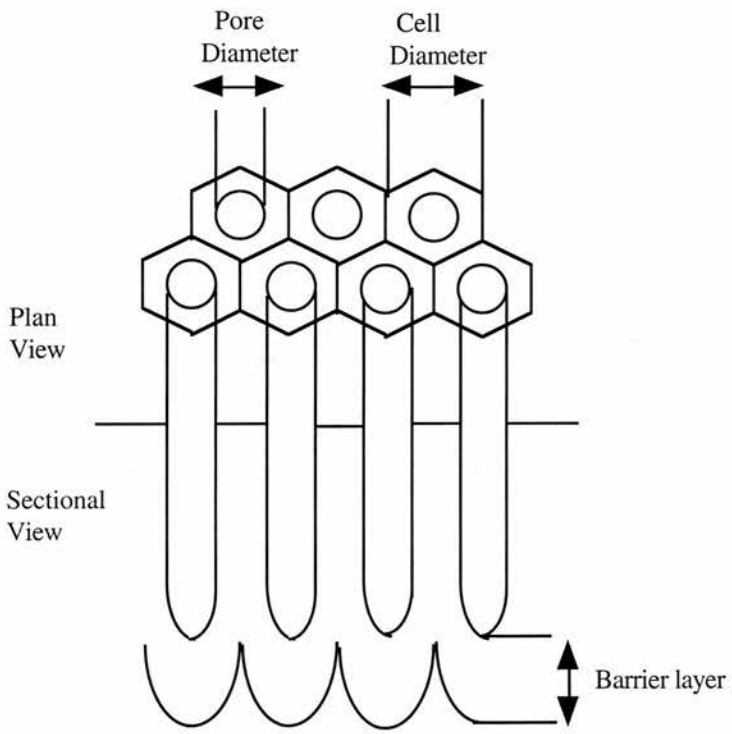

Figure 16. Duplex oxide film on aluminium [66].

2.9.1 Theories of Pit Initiation

Several mechanisms for the action of chloride ions in initiating pitting corrosion have been suggested in the literature. These include:

1. Cl^- penetration of the protective oxide film which covers the metal surface through pores or other weak places [67,68,69].

2. Competitive adsorption of Cl^- and oxygen or OH^- for sites on the metal surface [70,71].

3. Migration of ions inward through the oxide lattice [72].

4. Peptization of the oxide film by a strong negative charge resulting from the presence of adsorbed ions [73].

These processes where the oxide film composition is affected, are considered to promote a change in the conductivity of the oxide film. Work by Augustynski and co-workers [74,75,76,77,78] can be cited to demonstrate an apparent incorporation of chloride into the air formed film. Painot and Augustynski [75] considered this to be an aluminium oxychloride of the type AlOCl, and is further supported by the evidence of Heine, Keir and Pryor [79] claiming a decrease in ionic resistance with immersion time of oxide covered aluminium. However, Abd Rabbo, Wood, Richardson and Jackson [80] in their SIMS work on anodic films reported Cl^- to be present on the outer surface only and found no evidence of chloride incorporation within the oxide film. Sputtering revealed that the metal substrate had been attacked at localised sites, which prior to removal of the oxide showed no evidence of Cl^- contamination. They concluded that attack had occurred at flaws in the anodic film, undermining it. Transport of metal ions and chloride ions through the oxide film is only possible under a high electric field; without such a field, migration will be very much smaller or negligible in the solid film at room temperature.

2.9.2 Local action at oxide film flaws

Metals contain non-metallic inclusions, second phase particles, impurity segregation and grain boundaries. Such sites are considered likely to induce defects in the overlying passive film. Richardson, Wood and Sutton [81] categories flaws as either residual, or mechanical as a result of defects in the underlying metal substrate such as inclusions, second phase particles, etc. Davydov and co-workers [82,83] investigated the importance of defects in air-formed passivating films using the method of local determination of pitting potential, Enp. The pitting potential as originally observed by Brennert [84] was described as a potential in the passive range Enp, at which the passive state became transpassive, the potential being lower than that expected for such behaviour, and being due to the onset of pitting in the presence of an aggressive species. The surface of aluminium is covered by an air-formed film up to 10 nm thick depending on conditions [85], rapidly developed on exposure of bared metal to oxygen in air or dissolved in solution [57,58,59,60] and modified by exposure to solution. Films on aluminium are electronically speaking insulators. If the film are formed in solution, then their composition may depend on environment. Hydrogen profiles have been detected in aluminium barrier type anodic film [86], and surface active ions such as chromate and phosphate may slowly enter the film though is not observed for chlorides [87]. Moreover, such compositional change appears to be too slow to account for breakdown of passivity. Flaws have been demonstrated to be present by TEM of barrier type films [88]. When aluminium is anodised at steady state to form a porous film which is subsequently stripped by dissolution in CrO_3/H_3PO_4 solution, further anodising to produce an oxide replicas yields evidence of apparent defects present at many triple points [89,90]. Alvarez, Galvele and collaborators working on zinc [91] and in a further discussion paper by Galvele of generalised content [92], postulated that transport processes can be further developed to explain pit initiation as well as propagation. They invoke the idea that the length of the diffusion path in a fissure (or flaw), i.e. the base to mouth distance,

determines effectively whether the pH within the fissure falls below a critical value necessary for propagation of that fissure as a pit. Galvele confirmed that such fissure sizes as the 10 nm quoted for aluminium could easily be provided by flaws in oxide films. Flaws breaching is envisaged to be followed by chloride accumulation, metal dissolution, hydrolysis and solution acidification. It may be that complex formation with oxide at the flaw base or revealed metal is possible by some means. Work by Foroulis and Thubrikar [93], Foroulis [94], Dallek and Foley [95] and Bogar and Foley [96] imply the possibility of complex such as $AlCl_4^-$, Al_2Cl_8, $Al(OH)_2Cl_2^-$ which may take part in a cyclic reaction.

2.9.3 Electrochemical conditions leading to pitting

The onset of pitting is considered by many workers [85] to require that the following conditions be fulfilled.

(a) Aggressive ions specific to the metal under consideration must be present at concentrations higher than a critical value, e.g. in the case of aluminium - chloride, fluoride, bromide and iodide are all classed as aggressive species.

(b) The electrochemical potential must be higher than the potential required for pit nucleation, the so-called Enp potential.

(c) An induction period must be exceeded.

The critical aggressive ion concentration for pitting is derived during induction time measurements made after the methods of Engell and Stolica [97] and Hoar and Jacob [55]. In this technique, the metal electrode is held potentiostatically in the passive potential range in an electrolyte which supports passivation, e.g. H_2SO_4 solution.

2.9.4 Development of pits beyond the initiation stage

It has been the convention to regard pitting as taking place by stages, designated initiation, propagation or development and termination. The theory of Wood *et al* [98] makes no

distinction between stages of pit development, but it is considered relevant to mention here the currently widely accepted theory of pit propagation, particularly in view of the ideas of Galvele [92] concerning the possible role of mass transport at flaws or fissure sites in initiating pits. The presence of propagation is viewed as being auto-catalytic [51] and is envisaged as follows in Figure 17.

1. Metal dissolution within the pit.

2. Migration of chloride in the bulk solution under the influence of the corrosion current through the cell and the charge on the anion.

3. The generation of an acid solution within the pit by the hydrolysis of metal ions with water and chloride, for example:

$$Al^{3+} + H_2O + Cl^- \rightarrow H^+ + AlOHCl^-$$

$$Al^{3+} + 3H^+ + 2Cl^- \rightarrow 3/2H_2 + AlCl_2^+$$

4. A consequently high conductivity in the concentrated salt solution in the pit.

5. A limited oxygen solubility in the concentrated salt solution, leading to limited oxygen supply.

6. The formation of a crust or membrane of corrosion product of hydrate $Al(OH)_3$ restricting the dilution of the solution by diffusion and convention.

7. Cathodic protection around the pit by the corrosion current, preventing general corrosion.

8. Passivation by alkali formed in the cathode reaction.

9. Deposition of any noble metal cations in solution onto the cathode surface, increasing cathodic efficiency.

2.9.5 Alternating voltage electrochemical etching of aluminium

The etching of aluminium to provide a hydrophilic surface on aluminium lithographic plates is the subject of various British patents [99,100] and has been in use for at least twenty years [101]. Despite this, very little has been published concerning the pitting behaviour of aluminium under alternating current conditions. The conventional process, and industrially, involves electrograining using an alternating current density of about 200-1000 Am^{-2} for times of between ten seconds and ten minutes in aqueous solutions containing 0.5-2.5% hydrochloric acid. The intention is to produce a uniform array of fine pits and cause fine sub microscopic roughening of the surface, the combination of which imparts exceptional mattness to the aluminium surface.

Thompson and Wood [102] found the pit population density on electropolished and subsequently electrograined aluminium to be in the range $4x10^{13}m^{-2}$. It was noted that growth of pits was non-uniform with preferential growth of pits at certain sites where the anodic current was deduced to be concentrated. Thompson and Woods [102] found a correlation between the number density of these larger pits and the flaw population density quoted by Richardson *et al* [81]. After longer electrograining times, a film formed which did not hinder dissolution of the aluminium substrate suggesting it might be porous or discontinuous in nature. Thompson and Woods considered the film to have been formed by a dissolution/precipitation mechanism on the negative half cycle of the alternating voltage treatment, brought about by a local pH increase due to hydrogen evolution, or by protonation of the initially present air formed film. Dowell's work [101] included half and full wave rectification experiments.

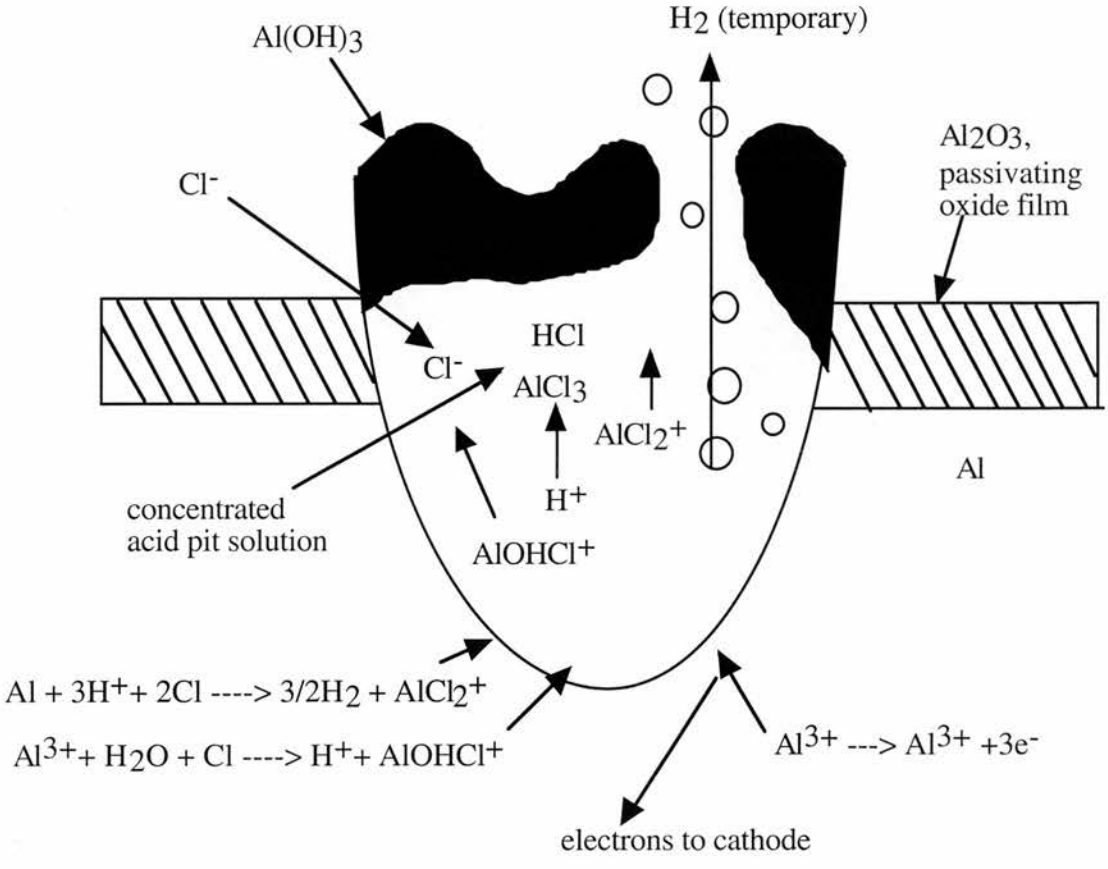

Figure 17. An active pit chloride electrolyte on aluminium [103].

2.10 References

[1] R.W.G.Wykoff, Crystal Structure. Vol.2. (1964), New York: Wiley Interscience.

[2] F.A.Cotton and G.Wilkinson, Advanced Inorganic Chemistry. 5th edition ed. (1988), New York: John Wiley & Sons Interscience.

[3] R.Manaila, A.Devenyi, and E.Candet, Structural order in amorphous aluminas. Thin Solid Films (Preparation and Characterisation), (1984). **116**: p.289-299.

[4] H.J.van Beek and E.J.Mittenmeijer, Amorphous and crystalline oxides on aluminium. Thin Solid Films (Preparation and Characterisation), (1984) **122**: p.131-151.

[5] C.C.Chang, LEED studies of the (0001) face of α-alumina. J.Appl.Phys., (1968) **39** (12): p.5570-5573.

[6] J.M.Charing, Low-energy electron diffraction observations of α-alumina. Appl.

Phys.Let., (1967) **10**: p.139-140.

[7] T.M.French and G.A.Somorjai, Composition and Surface Structure of the (0001) Face of α-Alumina by Low-Energy Electron Diffraction. J.Phys.Chem., (1970) **74**: p: 2489-2495.

[8] H.Knozinger and P.Ratnasamy, Catalytic Aluminas: Surface Models and Characterisation of Surface Sites. Catal. Ref. -Sci. Eng., (1978), **17** (1): p.31-70.

[9] P.W.Atkins, Physical Chemistry. 3rd ed. (1987): Oxford University Press.

[10] G.A.Jeffrey and W.Saenger, Hydrogen bonding in Biological Stuctures. (1991), Heidelberg: Springer-Verlag. 51.

[11] A.S.N.Murthy and C.N.R.Rao, ed. Spectroscopic studies of the Hydrogen Bond. Applied Spectroscopy Reviews, ed. E.G.Brame. Vol.2. (1969), Marcel Dekker, Inc.: London. 69-192.

[12] H.L.Finston and A.C.Rychtman, A New View of Current Acid-Base theories. (1982), Chichester: John Wiley & Sons.

[13] H.Margenau and N.R.Kestner, Theory of intermolecular forces. 2nd ed. (1971), Oxford: Pergamon Press.

[14] B.G.Frederick, G.Apai, and T.N.Rhodin, Defect structure of clean and chlorinated aluminium oxide films probed by methanol chemisorption. Surf.Sci., (1992), **277**: p. 337-350.

[15] P.Hirva and T.A.Pakkanen, The interaction of amine bases on the Lewis acid sites of aluminium oxide - a theoretical study. Surf.Sci., (1992), **277**: p.389-394.

[16] T.H.Ballinger and J.T.Yates, Jr., IR Spectroscopic Detection of Lewis acid sites on Al_2O_3 Using Adsorbed CO. Correlation with Al-OH Group Removal. Langmuir, (1991), **7**: 3041-3045.

[17] M.I.Zaki and H.Knozinger, Characterisation of oxide surfaces by adsorption of carbon monoxide-a low temperature infrared spectroscopy study. Spectrochem. Acta, (1987), **43A** (12): p.1455-1459.

[18] C.Morterra, G.Magnacca, and N.D.Favero, IR Study of CO Adsorption at ~77K on α-Al_2O_3. Langmuir, (1993), **9:** p.642-645.

[19] C.Morterra, V.Bolis, and G.Magnacca, IR Spectroscopic and Microcalorimetric Characterisation of Lewis Acid Sites on (Transition Phase) Al_2O_3 Using Adsorbed CO. Langmuir, (1994), **10**: p.1812-1824.

[20] M.H.Healy, L.F.Wieserman, E.M.Arnett, and K.Wefers, Infrared Spectroscopy and Microcalorimetric investigation of α-alumina using basic probe molecules: Acetonitrile, Pyridine, 2,6-Lutidine, and n-Butylamine. Langmuir, (1989), **5**: p.114-123.

[21] E.P.Parry, An Infrared Study of Pyridine Adsorbed on Acidic Solids. Characterisation of Surface Acidity.J.Catal., (1963), **2**: p.371-379.

[22] I.F.Tindall and J.C.Vickerman, The adsorption and reactions of methanol on clean and oxidised aluminium surfaces. Surf.Sci., **149** (1985) 577.

[23] J.W.Rogers, Jr.R.L.Hance and J.M.White, An electron spectroscopic investigation of the interaction of methanol with polycrystalline aluminium. Surf.Sci., **100** (1980) 388.

[24] G.D.Waddille and L.L.Kesmodel, Identification of methoxide on Al (110) by High-Resolution EELS. Surf.Sci., **182** (1987) L248-252.

[25] F.P.Netzer and J.U.Mack, Langmuir, in press.

[26] N.V.Richardson and P.Hofmann., Vacuum, **33** (1983) 793.

[27] J.G.Serafin and C.M.Friend., Surf.Sci., **209** (1989) L163.

[28] W.Jensen, Chem.Rev., **78,** 1 (1978).

[29] J.B.Peri, J.Phys.Chem., **69**, 221, (1965).

[30] F.H.van Cauwelaert, W.K.Hall, Trans. Faraday Soc., **66**, 454, (1970).

[31] F.H.van Cauwelaert, W.K.Hall, Trans. Faraday Soc., **66**, 477, (1970).

[32] W.K.Hall, H.P.Leftin, F.J.Cheselske and D.E.O'Reilly, J.Catal., **2** (1963) 506.

[33] H.Dunken and P.Fink, J.Chem, **6** (1966) 194.

[34] J.L.Carter, P.J.Luccesi, P.Corneil, D.J.C.Yates and J.H.Sinfelt, J.Phys.Chem.,

69 (1965) 3070.

[35] C.L.Thomas, Ind.Eng.Chem., **41** (1965) 2645.

[36] E.M.Flanigen in Proc.5th Int Zeolite Science and Practice, Stud.Surf.Sci.Catal. **58**, (Eds.van Bekkum, Flanigen & Jansen, Elsevier) **13** (1991).

[37] D.W.Breck, Zeolite Molecular Sieve (Wiley Interscience, 1974).

[38] W.M.Meier in Molecular Sieves, Soc. Chem.Int., London, **12** (1968).

[39] R.von Ballmoos & J.B.Higgins, Collection of Simulated X-Ray Powder Patterns for Zeolites, IZA Special Publication, (Butterworth, 1990).

[40] G.T.Kokotailo & W.M.Meier, Chem.Soc.Special Publ., **33** (1980) 33

[41] H.van Koningsveld, J.C.Jansen & H.van Bekkum, Zeolites, **10**, (1990) 235

[42] P.A.Jacobs & J.A.Martens, Pure Appl.Chem., **58**, No.10, 1329 (1986).

[43] J.Dwyer, Chem.Ind., 258 (1984).

[44] M.M.Mestdach, E.E.W.Stone and J.J.Fripiat, J.Chem.Soc.Farad.Trans.1, **72** (1976) 154.

[45] A.G.Ashton, J.Dwyer, I.S.Elliot, F.R.Fitch, G.Qin, M.Greenwood and J.Speakman in Proc.6th Int.Zeolite Conf., (Eds.Olson and Bisio, Butterworths) Reno, USA 704 (1983).

[46] A.F.H.Wielers, M.Vaarkamp and M.F.M.Post, J.Catal., **127**, 51 (1991).

[47] J.P.O'Sullivan and G.C.Wood, Proc.Roy.Soc.London A, **317** (1970) 511.

[48] D.J.Arrowsmith and D.A.Moth, Trans.Inst.Met.Finish., **64** (1986) 91.

[49] G.C.Wood and J.P.O'Sullivan, Electrochim.Acta, **15** (1970) 1865 .

[50] G.Tu, PhD.Thesis, University of Manchester (1981).

[51] G.Wranglen, Introduction to corrosion and protection of metals, printed in Britain by Butler and Tanner Ltd., (1972).

[52] J.D.A.Miller: Microbial Aspects of Metallurgy, Medical and Technical Publishing Co., Ltd (1971).

[53] M.Pourbaix: Atlas of Electrochemical Equilibria in Aqueous Solutions (1966).

[54] F.A.Cotton and G.Wilkinson, Advanced Inorganic Chemistry, Interscience Publishers (1962).

[55] T.P.Hoar and W.R.Jacob, Nature, **216** (1967) 1299.

[56] M.J.Pryor, Electrochem., **62** (1958) 782.

[57] T.Hagyard and J.R.Williams, Trans.Fraday Soc., **57** (1961) 2288.

[58] T.Hagyard and M.J.Pryor, Trans.Fraday Soc., **57** (1961) 2295.

[59] T.Hagyard and W.B.Earl, J.Electrochem.Soc., **114** (1967) 694.

[60] T.Hagyard and K.M.Chapman, J.Electrochem., **113** (1966) 961.

[61] F.Keller, H.S.Hunter and D.L.Robinson, J.Electrochem.Soc., **100** (1953) 411.

[62] J.P.O'Sullivan and G.C.Wood, Proc.Roy.Soc.Lond.A., **317** (1970) 511.

[63] G.C.Wood, In Oxides and Oxides Film Vol.2, p.167, ed J.W.Diggle, Marcel Dekker, Inc., New York (1973).

[64] G.C.Wood, Planary Lecture to 5th Int. Congr. on Metallic Corrosion, Sydney (1975).

[65] J.F.Murphy and C.E.Michelson, Proceedings of Symposium of Anodising Aluminium, Nottingham University, September 1961, Published by the Aluminium Development Association, London (1962).

[66] V.Willard, PhD Thesis, University of Cambridge (1995).

[67] U.R.Evans, L.C.Bannister and S.C.Britton, Proc.Royal Soc., Series A, **131** (1931) 366.

[68] T.P.Hoar and U.R.Evans, J.Electrochem.Soc., **99** (1952) 212.

[69] M.Streicher, J.Electrochem.Soc., **103**, (1956) 375.

[70] H.P.Leckie and H.H.Uhlig, J.Electrochem.Soc., **113** (1966) 1262.

[71] L.M.Kolotyrkin, Corrosion, **19** (1963) 261.

[72] H.P.Hoar, D.C.Mears and G.P.Rothwell. Corr.Sci., **5** (1965) 279.

[73] T.P.Hoar, J.Electrochem.Soc., **7** (1967) 431.

[74] J.Augustynski, Passivity of Metals, Edited by R.P.Frankenthal and J.Kruger,

J.Electrochem.Soc., 989 (1978).

[75] J.Painot and J.Augustynski, Electrochem Acta, **20** (1975) 747.

[76] J.Painot and J.Augustynski, Electrochem Acta, **123** (1976) 841.

[77] M.Koudelkova and J.Augustynski, J.Electrochem.Soc., **126** (1979) 1659.

[78] M.Koudelkova and J.Augustynski and H.Berthou, J.Electrochem.Soc., **124** (1977) 1165.

[79] M.A.Heine, D.S.Keir and M.J.Pryor, J.Electrochem.Soc., **112** (1965) 24.

[80] M.F.Abd Rabbo, G.C.Wood, J.A.Richardson and C.K.Jackson, Corr.Sci. **14** (1974) 645 and **16** (1976) 677.

[81] J.A.Richardson, G.C.Wood and W.H.Sutton, Thin Solid Films, **16** (1973) 99.

[82] A.D.Davydov, A.N.Kamkin and T.N.Roskichina, Electrochemija (Russ)., **14** (1978) 901.

[83] A.D.Davydov, Electrochemija (Russ)., **14** (1978) 979.

[84] S.Brennert, J.I.S.I., **35** (1937) 101.

[85] M.Janik-Czachor, G.C.Wood and G.E Thompson (1978).

[86] M.F.Abd Rabbo, J.A.Richardson and G.C.Wood, Electrochim Acta, **22** (1977) 1375.

[87] G.C.Wood and J.P.O'Sullivan, Electrochim Acta, **15** (1970) 1865.

[88] G.E.Thompson, R.C.Furneaux, G.C.Wood and R.Hutchings, J.Electrochem.Soc., 125 (1978).

[89] P.E.Doherty, The Pitting of Aluminium by Chloride Attack (1979).

[90] M.J.Pryor, Corr.Sci., **11** (1971) 463.

[91] M.G.Alvarez and J.R.Galvele, Corrosion, **32** (1976) 285.

[92] J.R.Galvele, J.Electrochem.Soc., **123** (1976) 464.

[93] Z.A.Foroulis and M.J.Thubrikar, J.Electrochem.Soc., **122** (1975) 1296.

[94] Z.A.Foroulis, J.Electrochem.Soc., **113** (1966) 532.

[95] S.Dallek and R.T.Foley, J.Electrochem.Soc., **123** (1976) 1775.

[96] F.D.Bogar and R.T.Foley, J.Electrochem.Soc., **119** (1972) 462.

[97] H.Engell and N.Stolica, Z.Physik, Chem. N.F., 20 (1959) 113.

[98] G.C.Wood, W.H.Sutton, J.A.Richardson, T.N.K.Riley and A.C.Malherbe: NACE; Proceedings of the U.R.Evans Conference on Localised Corrosion; Williamsburg, Virginia, December 1971. Published 1974.

[99] British Patent 1, 392, 191.

[100] British Patent 902, 827.

[101] A.J.Dowell, Trans. Int.Met.Finish., **57** (1979) 138.

[102] G.E.Thompson and G.C.Wood, Corr.Sci., **18** (!978) 128.

[103] V.Willard, PhD Thesis, University of Cambridge (1995).

Chapter 3

Experimental Techniques

To understand the structure and dynamics of the organic/substrate interface in ultra-high vacuum (UHV), requires the multi-technique approach in solving problems. With the availability of many surface analysis techniques, it is important to understand the advantages of each technique. This chapter summaries the principles behind the experimental techniques, and sample preparation procedures, used in this thesis.

3.1 Sample preparation in surface science studies

The preparation of alumina substrates was carried out in Leyabold-Heraus stainless steel ultra high vacuum (UHV) chambers with surface preparation facilities and in-situ characterisation tools including Auger Electron Spectroscopy (AES) and Temperature Programmed Desorption (TPD). Low pressures were required to reduce sample contamination during the experiment and because the spectroscopic technique used (see 3.2) requires at least a vacuum of $2x10^{-7}$ mbar. The stainless steel chambers used for this work were kept under UHV conditions using various combinations of turbo molecular pumps, ion pumps and titanium sublimation pumps, all of which are described in Chambers *et al* [1]. The attainment of UHV conditions requires that the whole system be baked to 150°C for 15 hours. This increases the desorption rate of gases, notably water on the inside of the chamber, thus decreasing the time to achieve UHV. Reviews about the use of vacuum chambers in surface science can be found in Woodruff and Delchar [2] and Riviere [3].

The substrates used for this investigation were named STD PAT and NON PAT alumina substrates. The difference in the process between STD PAT and NON PAT is the chemical treatment which results in a change in the surface area, surface volume and

surface chemistry of the STD PAT. The STD PAT substrate is treated in what is referred to as a PAT-liquor. This consists of sodium-dihydrogen-phosphate, sodium fluoride and water as a solvent. The PAT liquor results in controlled blocking of the anodic pores which run throughout the alumina. This chemical treatment is absent in the NON PAT. A third set of aluminium substrates plates were made up in the laboratory with different stages of preparation: electrograining, anodising and PAT, where the shape of the oxide pores had been controlled by the preparation. The substrates received no further chemical treatment prior to analysis.

The chambers used for desorption experiments were equipped with a sample manipulator to mount and control the position of the sample. In addition to the X,Y and Z translation, the manipulator is fully rotatable around the vertical through the centre of the chamber for surface preparation and angular dependent spectroscopic measurements. Two stainless steel, molecular beam dosers (used to minimise background effects), a liquid nitrogen tank which allowed the substrate temperature to be reduced to around -120°C, a quadrupole mass spectrometer was used for detection of desorbed species in the gas phase and for dose monitoring and a computer controlled heating supply delivering a linear temperature ramp to the sample. Figure 1a. illustrates the schematic drawing of the TPD instrumentation.

A square of side 1 cm by 1 cm was cut from an aluminium substrate. A 0.9 mm diameter hole was drilled at each corner of the sample and the sample attached to the end of the manipulator using 0.125 mm diameter tantalum support wire. A fifth 0.9 mm diameter hole was drilled and a K-type thermocouple attached directly to the sample, allowing its temperature to be measured directly. Figure 1b. illustrates the schematic drawing of the sample preparation.

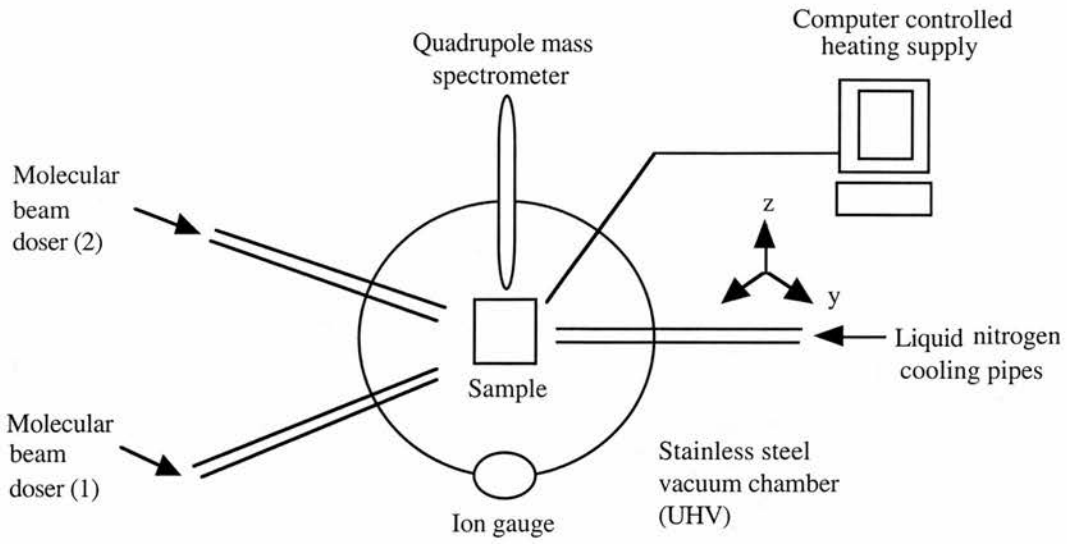

Figure 1a. Schematic illustration of the TPD instrumentation.

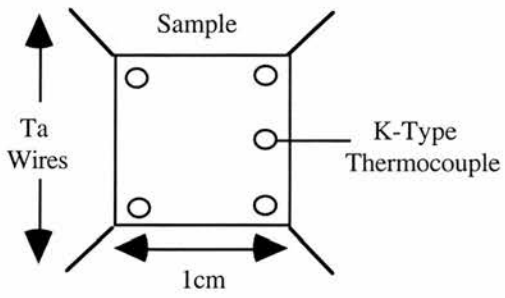

Figure 1b. Sample preparation.

3.1.1 Experimental Procedure

The surface of the substrate was first cooled to a temperature of -120°C. This was the minimum temperature achievable by conduction, as the liquid nitrogen does not make intimate contact with the substrate. The substrate was then heated to the maximum desorption temperature typically 350-400°C. The maximum temperature must be limited to avoid structural damage to the sample. This initial pre-heating step was carried out to remove any molecules (predominantly water) that had adsorbed onto the substrate from the background. The substrate was then allowed to cool to -120°C prior to dosing. The

oxide surface was exposed to the relevant organic molecules by dosing from a glass tube, connected to the gas handling manifold. The sample of organic material was frozen whilst under vacuum then a freeze-pump-thaw process was repeated three times to outgas the organic sample. The tube was allowed to return to room temperature before dosing. The dosing tube used was a simple 0.25mm diameter stainless steel tube. It had the advantage that it exposed only the sample to significant amounts of the molecule and major contamination of the whole system was avoided. The pressure inside the chamber, measured by the ion gauge, was allowed to increase to a specific value for a specific length of time. This was typically $2x10^{-8}$ mbar for 600 seconds (10 minutes). An integration of the pressure/time curve over a dosing period allowed a precise measure of exposure by allowing for the rise and delay times at the start and the end of dosing.

After dosing, the sample was allowed to stand for 43 minutes (determined experimentally as the maximum time required under these dosing conditions for the pressure to recover to the normal baseline). By standardising on a constant pump down time, any variation caused by kinetic effects such as diffusion within the pore is also kept constant. A measure of the amount of organic vapour introduced into the chamber was made using the quadrupole mass spectrometer. The substrate was rotated to face the mass spectrometer and a current passed through the substrate under a heating controller which was programmed to heat the sample at a rate of 1°C sec^{-1}. The mass spectrometer can be programmed to record up to ten different masses simultaneously. The resulting temperature programmed spectrum consists of a plot of pressure versus temperature. When the pressure of the chamber had recovered the process was repeated using a different dose. The dose could be varied by changing the pressure or the time of the dose. Usually pressure variation was used, again to standardise diffusion effects.

Note

It should be recognised that the exact amount of organic vapour dosed onto the sample cannot be measured by this method, because of the geometry of the instrument. The sample is situated directly in front of, and only a few cms away from the molecular beam dosers. The mass spectrometer is approximately 10 cm from the dosers. The effect of the sample being closest to the dosers is that during dosing, the local vapour pressure at the sample is greater (by some unknown factor) than the pressure measured at the mass spectrometer. The result of this is that the sample receives a larger dose than that indicated by either the ion gauge or mass spectrometer. However, a reproducible dose (albeit of unknown amount) can be given to the sample if the pressure increase, its duration, the relative positions of the dosers, sample and mass spectrometer are kept constant. There is a linear relationship between sample coverage and dose time, so it is possible to vary the dose received by the sample by changing the exposure time.

3.1.2 Validation of Dose Procedure

The first experiment performed was to determine the reliability of the dose procedure. The NON PAT sample was exposed for 10 minutes to a range of exposures of water. The thermal desorption spectra were obtained and the area under the mass curve was determined by the integration.

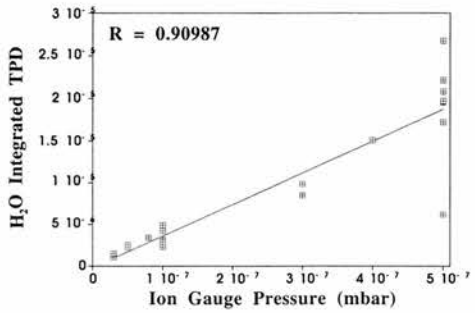

Figure 2. Integrated area mass 18 TPD spectra against ion gauge dose pressure for a NON PAT sample.

As mentioned in the experimental section it is possible to obtain a measure of the relative amount of water dosed by using the mass spectrometer to record the mass 18 signal during dosing. A plot of integrated area under the mass TPD spectra against the integrated area under the mass 18 dose curve is shown in Figure 3.

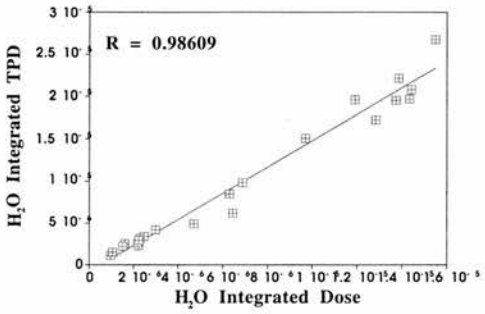

Figure 3. Integrated area mass 18 TPD spectra against integrated area, mass 18 dose curve for a NON PAT sample.

Both graphs show a linear relationship between the amount of water dosed and the amount desorbed from the sample. However, the regression analysis for Figure 2. is 0.90987 whereas for Figure 3. it is 0.98609. This indicates that a more reliable measure of the relative amount of water dosed to the sample is achieved by plotting the integrated dose area against integrated TPD area rather than ion gauge pressure against integrated TPD area. Using the mass spectrometer to monitor the species introduced into the UHV chamber gives a more reliable measure than the ion gauge for the following reasons. The ion gauge is being used to set the pressure of the water in the chamber but adjustments have to be made manually using the leak valve to maintain the chosen pressure. This necessarily leads to fluctuations in the water pressure about the chosen value so the actual water dosed will not be exactly the intended one. The mass spectrometer on the other hand samples only those water molecules introduced into the chamber. So, regardless of any fluctuations in the flow from the leak valve, the mass spectrometer is able to give an accurate integrated measure of the amount of water dosed.

Another contributing factor is that the ion gauge measures the pressure increase in the chamber due to all species introduced. If the water has not been fully degassed, then the dissolved gases remaining in the water will contribute to the pressure increase in the chamber, although it is not expected that these gases interfere with the water adsorption process. The small amount of dissolved gas evolved from the water will not be a constant from day to day, so a falsely low and variable, dose of water will be delivered. The mass spectrometer is unaffected by changes in dissolved gas content of the dose water because it measures specifically the partial pressure due to mass 18 in the chamber during dose and desorption.

3.2 Spectroscopic Techniques

There are many ways to obtain information on the physico-chemical properties of materials. For example, one can irradiate a catalyst with X-rays and study how the X-rays are diffracted (X-Ray Diffraction, XRD), or one can study the energy distribution of electrons that are emitted from the catalyst due to the photoelectric effect (X-ray Photoelectron Spectroscopy, XPS).

3.2.1 Thermal Desorption Spectroscopy (TDS)

TDS does not provide the same analytical information afforded to such techniques as XPS and AES, but rather is employed as an adjunct to other fundamental surface science techniques such as these and UPS and LEED. Any species adsorbed on a surface must be bound to the surface with some specific amount of energy and will desorb at a rate determined by a Boltzmann factor. Heating the surface will increase this desorption rate, and the desorbing species may be detected in the gas phase by a pressure gauge or better by a mass spectrometer. Evidently, a study of the temperature dependence of the desorption rate leads to information on the binding energy states of the adsorbate (or, more strictly, on the desorption energies). Of course, the binding energy states investigated will relate to those occupied at the temperature at which the desorption rate is

substantial; these need not be the same states occupied at lower temperatures. One particular feature of thermal desorption spectroscopy is that it is totally destructive; at the end of a heating cycle one has by the final temperature desorbed all those surface species which can be desorbed in this way, and thus the technique is more simple when heating returns the surface to a 'clean' state. Also, it is important to state that fragmentation of the adsorbed species can leave a tightly bound fragment which contaminants the surface at the end of the heating cycle.

When a metal oxide sample is heated rapidly in a vacuum, gas is desorbed from the surface. Experimentally, it is observed that the rate of gas evolution changes with temperature and, in addition, there may be several temperatures for which the evolution rate goes through a relative maxima. Since the initial work of Urbach (1920), rate measurements at continuously changing temperatures have been widely applied, not only in the study of surfaces, but in other unrelated areas such as thermoluminescence, chemical transformation in solids, and annealing of defects. As the temperature of the surface increases, the rate of evolution of gas increases as well, resulting in a rise of instantaneous gas density. From this increase it should be possible, in principle, to derive information on the nature and number of adsorbed species as well as on the kinetics of their evolution. The experiment may be carried out either of two distinct ways:

1. The temperature rise may be carried out rather rapidly, typically in less than half a second, so that the desorption rate is very much greater than the rate at which gas is pumped out of the system. This procedure is commonly called Flash Desorption and the analysis is the same as if the desorption were carried out in a closed system with no pumping.

2. The temperature rise may be carried out rather slowly, over a period of perhaps 15 seconds to a few minutes and here the gas evolved rapidly at a particular temperature is removed by pumping as the temperature continues to rise. The desorption of a particular binding state now results in a peak in the pressure-temperature curve rather than a step.

This type of curve is called Temperature Programmed Desorption (TPD). Although flash and thermal desorption are simple in concept their execution is fraught with difficulties which can invalidate quantitative and even qualitative conclusions, but before these problems can be understood a general analysis is required to derive the rate law of the rate of desorption from evolution curves and indicate the effects to be expected when different binding states are present at a surface. Figures 4a and 4b. shows the difference in spectra obtained experimentally for the two methods when CO is desorbed from W according to the work carried out by Goymour and King [4] then Ehrlich [5]. TPD has been used extensively by those interested in catalysis to study the kinetics and thermodynamics of surface interactions. A review of how it can be used in this way is given by King [6]. However, in this work TPD was only used to monitor the products of surface reactions. The technique required cooling the sample to produce a physisorbed layer of molecules, then heating the sample under computer control while monitoring fragments that desorbed using a quadrupole mass spectrometer.

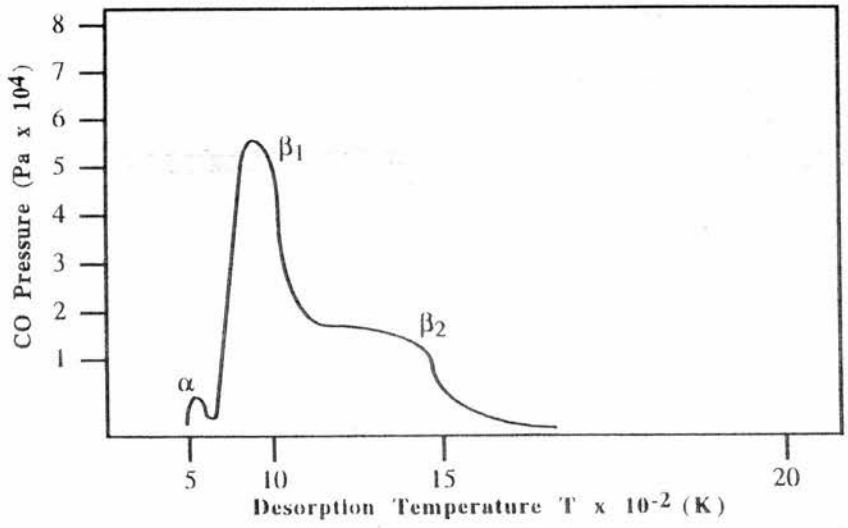

Figure 4a. Curves obtained for the CO/W system by (a) Thermal Desorption showing α, β_1 and β_2 states [4].

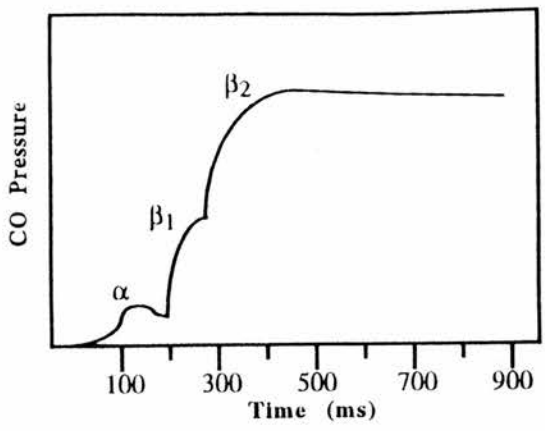

Figure 4b. Curves obtained for the CO/W system by Flash Desorption showing α, β_1 and β_2 states [5].

3.2.2 Theoretical Interpretation and Quantification

The rate of evolution of adsorbed material from a surface is dependent on the temperature as given by the general Arrhenius equation.

$$-\partial N/\partial t = k_m N^m \exp(-E_d/RT)$$

where; **N** is the surface concentration of adsorbed particles per unit area, $\mathbf{k_m}$ is the frequency factor, **m** is the order of the desorption process, $\mathbf{E_d}$ is the activation energy of the desorption process and **T** is the absolute temperature. It is possible to derive forms of the equation relevant to a first order reaction in which the particles desorb independently of each other, second order reactions in which the particles combine before desorption (being rate determining), and fractional orders for complex desorption processes [3]. Since for TPD there is always sufficient pumping speed in relation to the desorption rate, the increase in pressure is proportional to the latter. By differentiating these equations, the parameters can be limited with the maxima in the desorption rate described by a temperature value, T_{max}. For a first order reaction, the surface concentration is not involved and T_{max} is not coverage-dependent. This is seen in the work by Kirstein *et al* [6] who adsorbed different amounts of CO at 105K onto a Cu (111) surface and obtained three desorption maxima α, β_1 and β_2. The β_2 maxima develops first with increasing

coverage, followed by β_1 and α respectively. When the heating rate is known and the pre-exponential factor can be estimated, or determined from experiments using different heating rates, activation energies can be obtained. This simple derivation assumes E_d and k are independent of coverage. For second-order reactions T_{max} does vary according to the concentration of adsorbed species. This is illustrated in the work by Surnev and co-workers [7] who measured TDS as a function of increasing coverage of O_2 on Ru (001) at 880K. There is a downward shift in T_{max} with desorption peaks characteristic of second-order kinetics as exposure is increased up to 2L. Above this value, second-order characteristics do remain but a more complex desorption curve suggests there is a multi-state desorption process taking place. This may result from various surface processes including reaction with surface contaminants or oxide formation and desorption, but in this case the authors attribute the change in peak shape to oxygen diffusion into the Ru lattice. These example are relatively easy thermal desorption spectra to analyse and imply that the rate constant k is independent of the coverage. This is in fact not necessarily the case and k and E_d may vary with coverage due to lateral interactions as the number of surface species increases. Additional structure in a desorption peak may imply desorption from another surface site with different binding energy but in fact has been shown to be possible for desorbing molecules from equivalent sites [8]. These more complex traces may arise from repulsive lateral interactions between adsorbed species. The desorption peak shape also gives useful information. Redhead [9] showed the relationship between T_{max} and E_d to have a good linear approximation for first order reactions, and that a peak shape is indicative of reaction order. A schematic illustration based upon this study is shown in Figure 6. according to the work of Madix [10].

Ideally, desorption peaks should show no background effects due to inhomogeneity of the surface, heating rate or any other experimental artifacts to be of value in this respect. The shapes for first and second order reactions are in good agreement with the experimental observations of Kirstein *et al* [6] and Surnev *et al* [7]. A particularly good

example showing zero order kinetics is the work carried out by Zhou *et al* [11] for the desorption of Fe layers from W, which has two peaks in the spectra, β_1 corresponding to multilayers and β_2 with that of monolayer desorption. The calculated desorption energy (80 kcalmol^{-1}) is close to the heat of sublimation of bulk Fe (84 kcalmol^{-1}). In addition the spectra obtained for low coverage CO adsorbed onto Ni (110) at room temperature by Falconer and Madix [12] show pure first order behaviour in terms of shape and coverage dependance. Desorption of multilayers is usually characterised by zero order kinetics. In addition to information regarding binding site and reaction kinetics, TDS can be used to determine the amount of substance adsorbed on a surface. This is achieved by increasing the temperature sufficiently that all adsorbed species being investigated are desorbed and, with the mass spectrometer recording the number of such ions leaving the surface, the area under the individual desorption peaks correspond to the concentration of each species. The areas of the peaks are integrated for the partial pressure of the species as a function of time after the start of desorption. Accuracy is only achieved if the peak is well resolved from neighbouring peaks. In the work carried out by Paul [13] for the adsorption of hydrogen and deuterium on Al (100), straightforward integration of the resultant single peak is possible for all but very low coverages where there is poor signal-to-noise. TDS is not an effective direct measure to determine saturation coverage as in reality without information on ionisation cross sections and pumping speeds, the mass spectrometer is unable to record the absolute amount of gas adsorbed. As a result, calibration is required using such techniques as AES, XPS, LEED or using indirect means such as monitoring an alternative reaction involving the species under investigation. In further studies made by Paul and Hoffmann [14] for the determination of the total hydrogen or deuterium desorbed from Al, coadsorption with sodium and potassium and then the subsequent decomposition of the hydrides and deuterides was carried out. Also Cameron and Dwyer investigated the effect of small quantities of potassium on Fe (100) to the adsorption of CO [15].

In conclusion, TDS can be used to study binding, estimate the quantity and follow the surface reaction of an adsorbed species. However, it should be noted that the nature of binding may be altered when the temperature is increased during the experiment. There could be changes in surface structure from a change in crystal phase or ordering and the desorption may actually result from an intermediate state. Therefore, TDS needs to be used in conjunction with other techniques to yield the most accurate information.

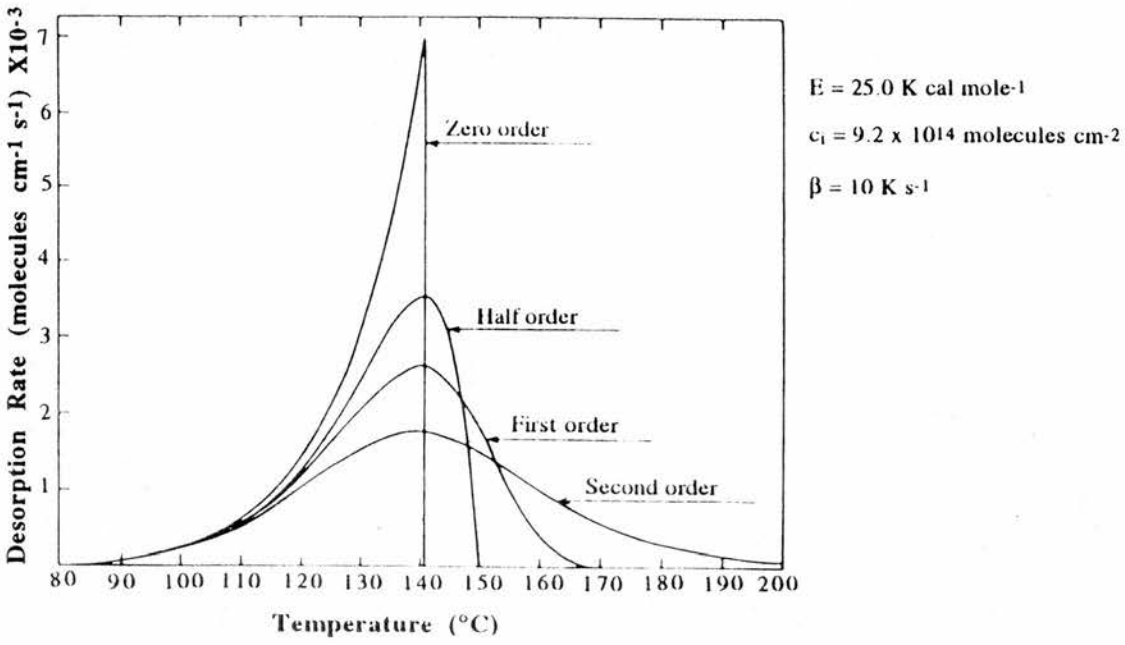

Figure 6. Desorption peak in relation to the order of reaction [12].

3.2.3 Adsorption-Desorption Theory

The most widely applicable theory is based on the premise that, provided intimate molecular contact takes place at the interface, interatomic and intermolecular forces will lead to bonding between the adsorbate and the substrate.

As a molecule approaches a surface, it initially "feels" an attractive interaction due to van der Waals' forces and is drawn towards the surface by these comparatively weak, long range forces. This process leads to Physisorption. As the molecules approaches more closely to the surface, in order of a molecular diameter, it may experience a much

stronger, chemical type (covalent or ionic) interaction and therefore may become bound to the surface via a chemical bond. This is termed Chemisorption. As a molecule approaches even closer to the surface, the interaction becomes strongly repulsive due to coulombic interaction of electrons within the molecule and those of the surface. The point at which the physisorption potential curve crosses the chemisorption curve determines whether the overall adsorption process is activated or not. If the crossover of the two potential energy curves is above the zero on the potential energy axis then the adsorption process is activated as there is a energy barrier for the molecule to overcome when going from the physisorption into the chemisorption well. This is shown in Figure 7.

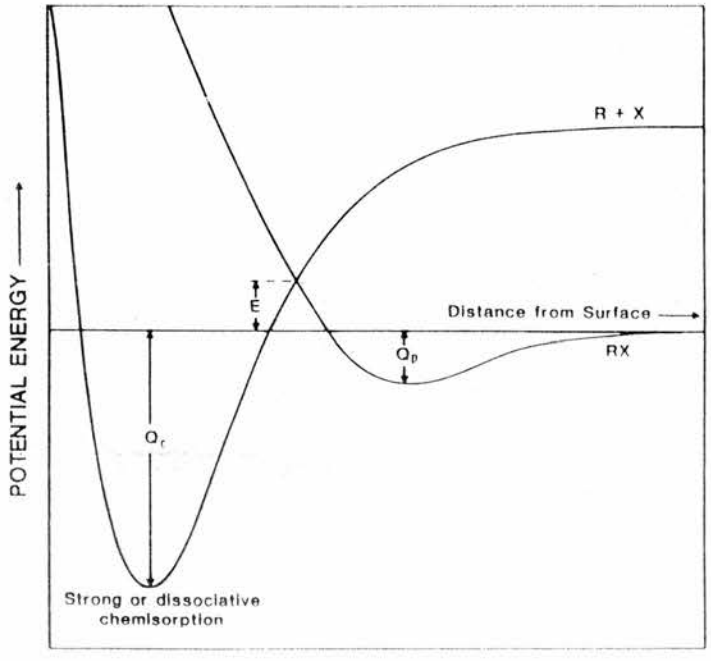

Figure 7. A simple potential energy diagram for desorption. The shapes of the curves are schematic (Qc = Chemisorption and Qp = Physisorption).

The binding energy of the physisorption well is typically below 20 $kJmol^{-1}$, with little lateral variation and therefore the molecule is able to diffuse relatively freely across the surface in order to find a suitable surface site onto which to chemisorb. This diffusion is relatively distant from the surface. During diffusion on the surface the molecule within the

physisorption well may pick up sufficient energy to re-enter the gas phase and thus not all molecules impringing on the surface remain bound to it. The average time the molecule spends in this state is termed the surface "residence time".

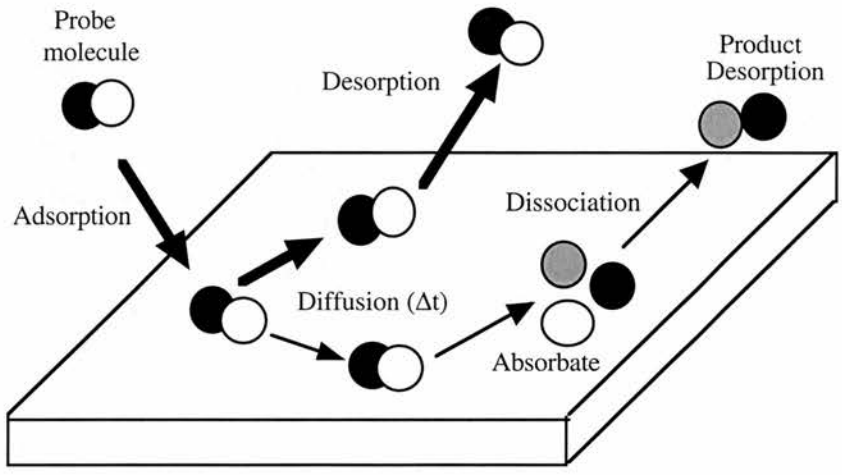

Figure 8. Schematic illustration of the possible routes in the adsorption-desorption process on a metal surface.

All the surface processes occurring here, adsorption, diffusion and desorption shown in Figures 8 and 9. can be modelled using a simple calculation of impringment rate and standard rate equation as shown in the equation below:

$$\mathbf{d(x)/dt = k(x) = A.exp - [Ea/KT].(x)}$$

Where, **k** is the reaction constant, **A** is pre-exponential (frequency) factor for a particular step in the reaction, $\mathbf{E_a}$ is the activation energy for a particular step in the reaction, **T** is temperature in Kelvin and **[x]** is the concentration of species x. In this simple analysis, A and E_a are assumed to be independent of [x]. A model for the adsorption-desorption process showing the importance of the physisorbed state will be discussed in chapter 8.

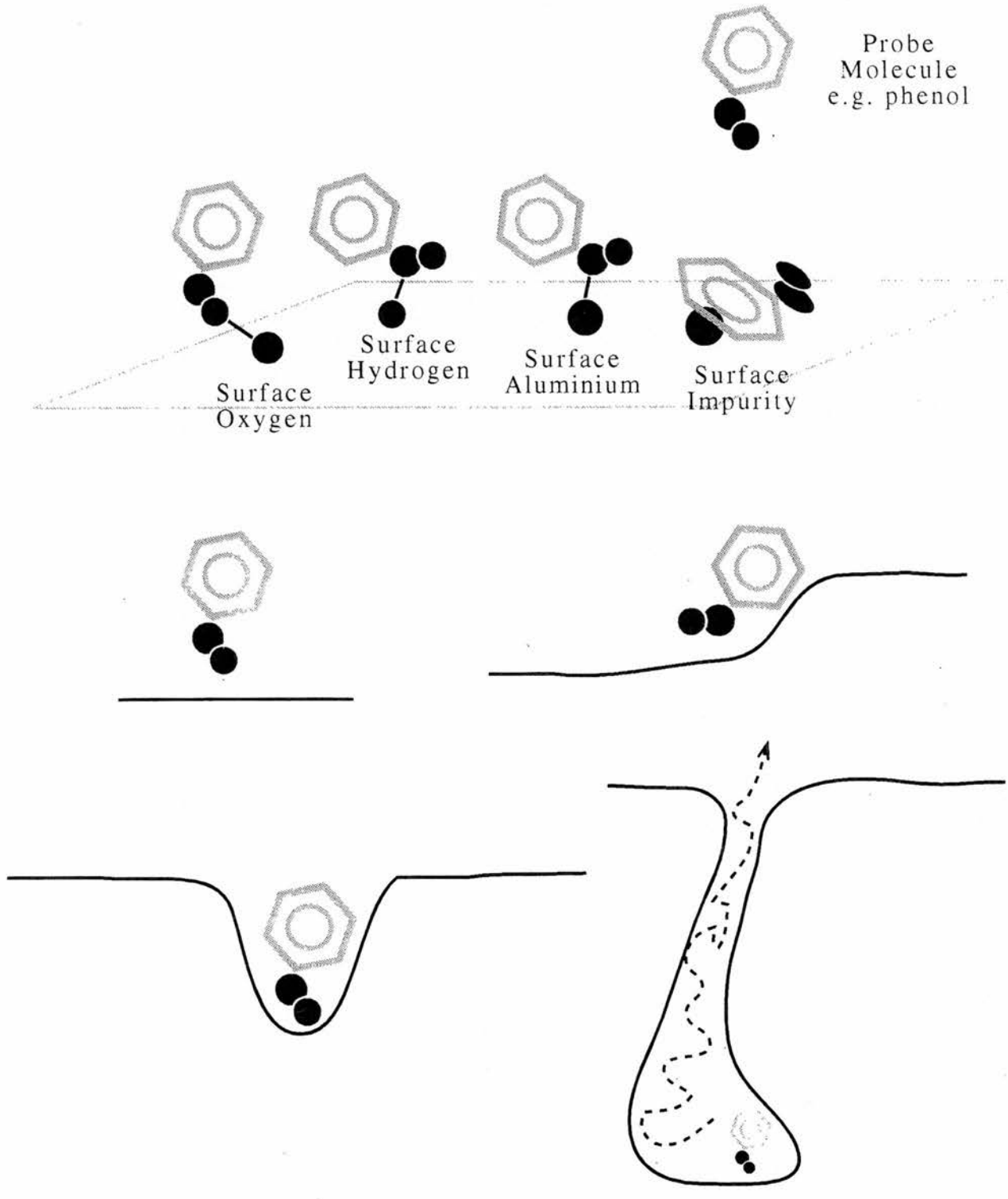

Figure 9. Showing the possible routes for the interaction of a probe molecule on a metal oxide surface.

Pumping capacity is an important consideration in thermal desorption. The pumping speed should be sufficiently high to prevent re-adsorption of the desorbed species back onto the surface. This effect leads to broadening of the spectrum towards higher desorption temperatures. For example, studies of H_2 desorption in UHV systems pumped by turbo molecular pumps with their unfavourable compression factors for light gases will certainly suffer from readsorption features. For heavier gases, the situation becomes less critical. If the pumping speed is sufficiently high, re-adsorption may be ignored, and the relative rate of desorption as the change in adsorbate coverage per unit time, is given by [16]:

$$\mathbf{r = - d\theta/dt = K_{des}\ \theta^{n} = \nu\ (\theta)\ \theta^{n}\ exp\ [-E_{des}(\theta)/RT]}$$

$$\mathbf{T = T_0 + \beta t}$$

Where, **r** is the rate of desorption, θ is the coverage in monolayers, **t** is time, $\mathbf{K_{des}}$ is the reaction rate constant for desorption, **n** is the order of desorption, ν is a pre-exponential factor of desorption, $\mathbf{E_{des}}$ is the activation energy of desorption, **R** is gas constant, **T** is temperature in kelvin, $\mathbf{T_0}$ is the temperature at which the experiment starts and β is the heating rate, equal to dT/dt.

3.3 Secondary Ion Mass Spectrometry (SIMS)

In a SIMS analysis, the sample is bombarded with a beam of charged positive ions with energies in the 1-25 KeV range. These incoming particles are called primary ions and, in the "Chemical Microscope" [25], the energy of this primary ion beam is about 7 KeV. The primary ions deposit energy into the surface layers. Around the impact site and to a depth of ~3nm, many bonds are broken and there is much random displacement and movement of atoms. This region is called the collision cascade region. Collisions which result in translational energy being directed back to the surface lead to ejection of material. This process is termed sputtering of the surface. The sputtered material is mostly ejected

as neutral fragments, but 1% is ejected in the form of charged particles. These are known as secondary ions and the vast majority are singly charged. This is illustrated in Figure 10. Both positive and negative ions are emitted and they range in size from single atoms to very large clusters of atoms (molecular ions and fragments). Sputtered ions can leave the surface some distance (up to ~5nm) from the impact site. As a generalisation, as this distance increases the more likely is the desorption of the larger fragment ions since these need to have the minimum of internal energy to prevent disintegration. Typically, secondary ions have kinetic energies of the order of 20 KeV, but different ions have different energy distributions. In particular, the molecular/cluster ions have significantly narrower distributions than atomic ions and they peak at slightly lower energy. Under typical SIMS conditions most of the sputtered material (>95%) emanates from the two uppermost atomic layers, so the sampling depth can be taken to be ~1nm. Large organic fragments are more likely to come predominantly from the surface monolayer, whilst the most energetic atomic fragments may come from significantly deeper layers. Primary ion bombardment also leads to emission of low energy electrons and these can be detected to provide sample visualisation (topographic information) in a manner analogues to Scanning Electron Microscopy (SEM). The secondary mass spectrum is obtained by collecting the secondary ions and subjecting them to mass filtration prior to detection. Three types of mass filter (or mass analyser) are used in SIMS - magnetic sector, quadrupole and time-of-flight; the Chemical Microscope uses a quadrupole mass filter. Since this device cannot filter ions with high kinetic energy, it requires an energy filter to select the appropriate fraction of the secondary ion energy distribution prior to mass analysis. Positive and negative secondary ion mass spectra are obtained in sequential experiments by switching the polarity of the whole mass spectrometer. The mass filter must be capable of separating secondary ions which differ in mass by one atomic mass unit (amu or dalton) over the whole mass range. The mass resolution or resolving power **(R)** of the mass spectrometer is defined by:

$$R = m/\Delta m$$

where **m** is the mass of the detected species and Δ**m** is the peak width. Δm is often quoted as the full width at half peak height but in the case of the quadrupole it is more useful to quote Δm_b, the full width at 10% maximum peak height i.e. the width at the base of the peak.

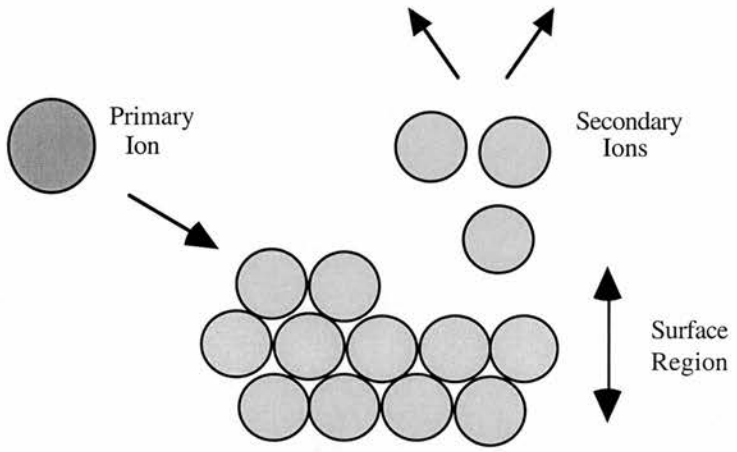

Figure 10. Schematic representation of the SIMS process.

3.3.1 Theory of SIMS

The signal intensity I_S (expressed as a rate) of an elemental positive or negative ion is given by:

$$I_s = I_p \, Y \, R \, c^{surf} \, T$$

where; I_p is the flux of primary ions, **Y** is the sputter yield of the element, equal to the number of atoms ejected per incident ion, R is the probability that the particle leaves the surface as positive or negative ions, c^{surf} is the fractional concentration of the element in the surface layer (a number between 0 and 1) and **T** is the transmission of the mass spectrometer, typically 10^{-3} for a quadrupole.

The essential quantities that determine the yield of secondary ions in a SIMS spectrum are the sputter yield Y and the ionisation probability R. Sputtering is a reasonably well

understood phenomenon [17]. Sputter yields depends on the properties of the sample as well as those of the incident ions. Sputter yields of an element vary between 1 and 10, with a few exceptions to the low side, such as bismuth with a sputter yield around 0.1 under SIMS conditions, and to the high side such as zinc, which has a sputter yield of around 15 under 5 KeV argon bombardment. For a given element, the sputter yield depends on the surface morphology: Surfaces that are rough on the scale comparable to the dimensions of sputter cascade give higher yields of secondaries than flat surfaces [18]. For single crystals, sputter yields have been observed to vary with the plane exposed [19]. The sputter yields depends furthermore on the mass of the primary ion, its energy, and the angle of incidence. The trends are quantatively easy to understand.

- **Mass**: A heavy ion such as xenon deposits more energy into a surface and sputters more efficiently than a lighter ion such as argon.

- **Energy**: Initially, increasing the energy of the primary ions increases the sputter yield. At high energy, however, ions penetrate deeper into the solid and dissipate their energy further away from the surface. The result is that fewer collisions cascades reach the surface and the sputter yield decreases at high energy. Thus the sputter yield goes through a maximum.

- **Angle**: The penetration depth of primary ions with a certain energy into the sample will be at maximum when the angle of incidence is perpendicular to the surface (if we include channelling phenomena). Hence, the sputter yield will increase when the angle of incidence,θ_i measured with respect to the surface normal, increases.

Sputtering can be done with ions, but also with atoms (**F**ast **A**tom **B**ombardment **S**pectroscopy, **FABS**). An incident ion neutralises rapidly when it enters the metal and hence, there is no difference in the sputtering effect of argon atoms and argon ions.

3.4 X-Ray Photoemission Spectroscopy (XPS)

The use of XPS to solve problems in surface technology [20] is widespread, with many industrial establishments owning an Electron Spectroscopy for Chemical Analysis (ESCA) instrument. For example, Brewis and Briggs [21] showed in 1981 that the technique of XPS could be used to resolve some controversies concerning the changes observed in polymer surfaces during various pretreatments. When a sample is irradiated with X-Rays, core level electrons are ejected from the atoms within it. These photoelectrons are characteristic of the elements in the sample. Figure 11. illustrates this process.

The kinetic energy of these electrons ($\mathbf{E_{ke}}$) is related to the X-ray energy ($\mathbf{h\nu}$), the binding energy of the electron ($\mathbf{E_b}$) relative to the Fermi level ($\mathbf{E_f}$) and the work function of the sample ($\mathbf{\emptyset}$), assuming that the sample work function is greater than that of the spectrometer. The relationship is below:

$$E_{ke} = h\nu - E_b - \emptyset$$

The binding energy described in this way depends on the initial state intrinsic to the chemical environment of the atom through its orbital energy ($\mathbf{E_i}$) and relaxation effects ($\mathbf{E_r}$) accompanying the excitation processes.

$$E_b = E_i + E_r$$

Chemical shifts occur because the precise initial energy of the photoelectron depends on the bonding interactions of the valence band electrons. The chemical environment of the atom therefore changes the binding energy of the electron. This can be seen for carbon [22], where its binding energy is 288eV when it is bound to an oxygen atom in an ether compound and 285eV when bound to a hydrogen in a hydrocarbon. The final state effects include the relaxation of the electrons around the core-ionised hole, which changes the electric field that the photoelectron moves through. The source of the X-rays can be an X-

ray anode, often made of aluminium or magnesium although synchrotron sources are also used. The electron energies are scanned using either a hemispherical or cylindrical electron analyser. Figure 12. shows the principle of this technique. A review of the instrumentation and data analysis is given by Riviere [3].

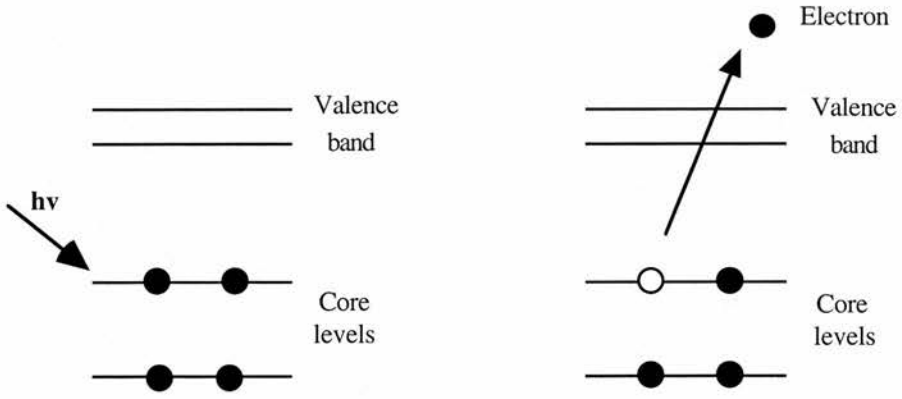

Figure 11. X-rays can be used to excite core level electrons whose kinetic energy is characteristic of the element from which they were emitted. The final state is a core-ionised state.

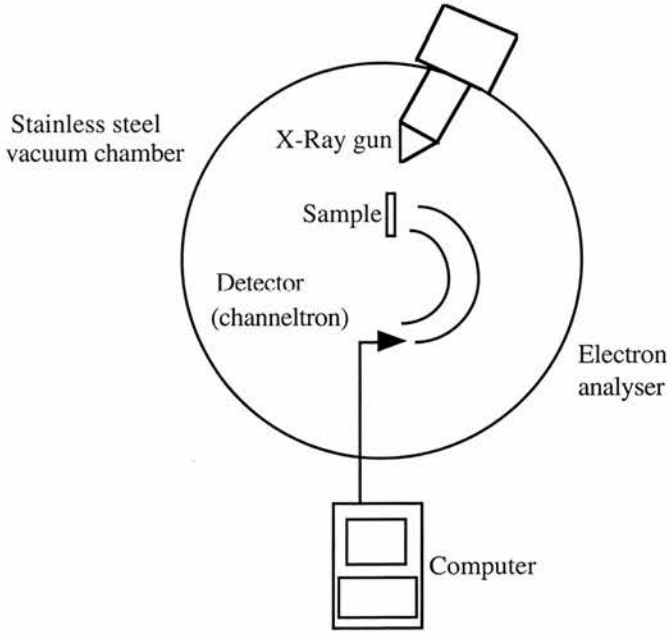

Figure 12. Schematic illustration of the instrumentation required for X-Ray Photo-emission Spectroscopy (XPS).

X-rays are generated by electron impact at energies of 10-15 keV on an aluminium or magnesium target. The X-rays impinge on the sample and cause emission of photoelectrons. The photoelectrons are energy analysed using an electrostatic deflector, an electron multiplier, together with pulse counting electronics, is utilised for electron detection.

3.5 Auger Electron Spectroscopy (AES)

This technique is similar to XPS where a sample is bombarded with electrons of a suitable energy. Irradiation of a sample by electrons with energy in the range 2-5eV can result in ejection of a core electron which is illustrated in Figure 13. Relaxation of the excited core hole state can occur by Auger electron emission.

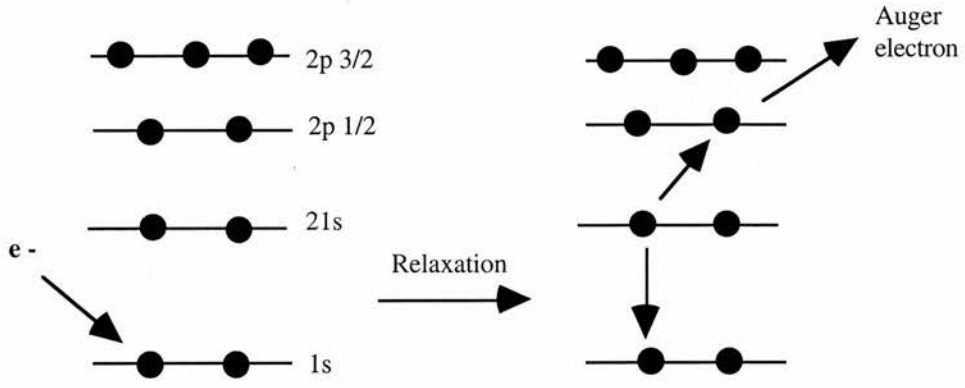

Figure 13. The excited ion relaxes by filling the core hole with an electron from a higher shell. The energy released by this transition is taken up by another electron, the Auger electron, which leaves the sample with an element specific kinetic energy.

It should be noted that the sampling depth is comparable to XPS, as elastically emitted electrons originating within tens of Angstroms of the surface are detected.

3.6 Atomic Force Microscopy (AFM)

Atomic force microscopy (AFM) is based on the minute but detectable forces, in the order of magnitude nanoNewtons, between a sharp tip and the atoms in the surface. The tip is mounted on a flexible arm, called a cantilever, and is positioned at subnanometer distance from the surface. If the sample is scanned under the tip in the x-y plane, it feels the attractive or repulsive force from the surface atoms and hence it is deflected in the z-direction. Various methods exist to measure the deflection, as described by Sarid [23, 24].

3.6.1 Theoretical Aspect of AFM

Atomic force microscopy can be applied in two ways. In the contact mode, the tip is within a few Ångstroms of the surface and the interaction between them is determined by the interaction between the individual atoms in the tip and on the surface. The description of atomic force interactions in the contact mode is highly complex. It requires a molecular dynamics simulation of the Coulomb interaction between the charges or charge distribution, polarisation due to induced dipole moments and quantum mechanical forces when electron orbitals start to interact, for each pair of atoms from the tip and the surface [23].

Let us simplify the situation to the one indicated in Figure 14a. where we consider the interaction between the atom at the apex of a tip and the atom directly underneath in the surface in terms of a Lennard-Jones potential. The force between the two atoms is given by the negative derivative of the potential. As indicated in the figure, one can work with an attractive or repulsive force within the contact mode. The contact mode is the usual choice of operation for surface morphology and the only one if one requires atomic resolution is required.

The second mode of operation is the non-contact mode, in which the distance between tip and sample is much larger, between 2 and 30 nm. Figure 14b. gives an example in which

the sample has a flat surface and the tip is a spherical particle. Several forces may play a role: Electrostatic in case of a potential difference between the tip and the sample, magnetostatic if the sample is magnetic, and the always present van der Waals' forces due to fluctuating or induced dipoles in the tip and the sample. Forces in the non-contact mode are typically 2-4 orders of magnitude smaller than in the contact mode.

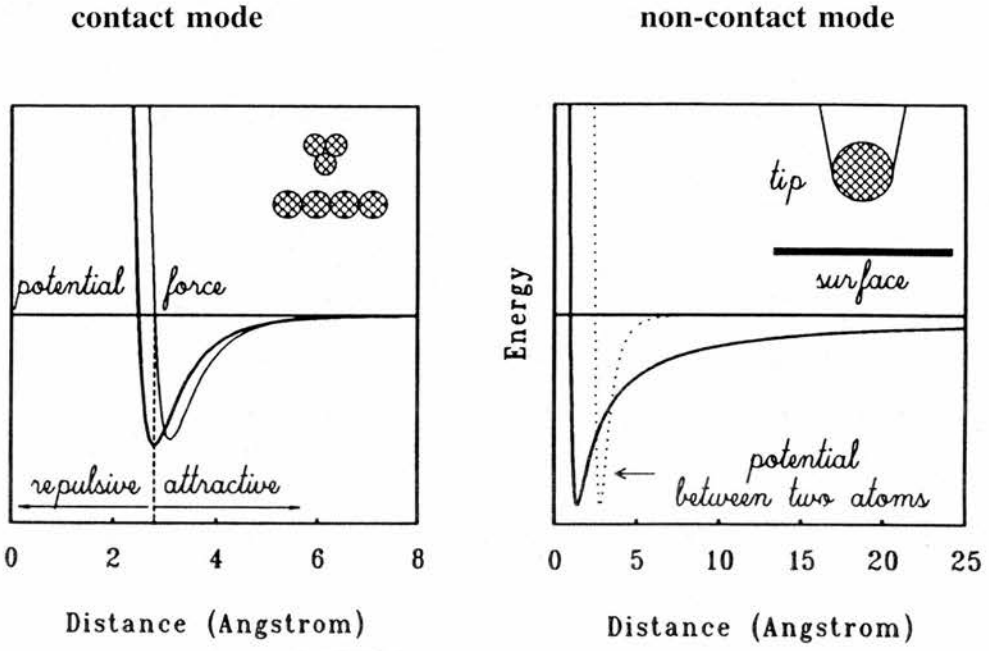

Figure 14. (a) Interaction potential and force between an atom at the apex of the tip and an atom in the surface. Tip-surface can be described by a summation of these potentials over all combinations of atoms from the tip and the surface. (b) Interaction potential between the tip, approximated as a sphere, and a plane surface, valid in the non-contact mode of force microscopy. To stress the long range character of the non contact-potential, the Lennard-Jones interaction potential between two atoms has been included as well (dotted line).

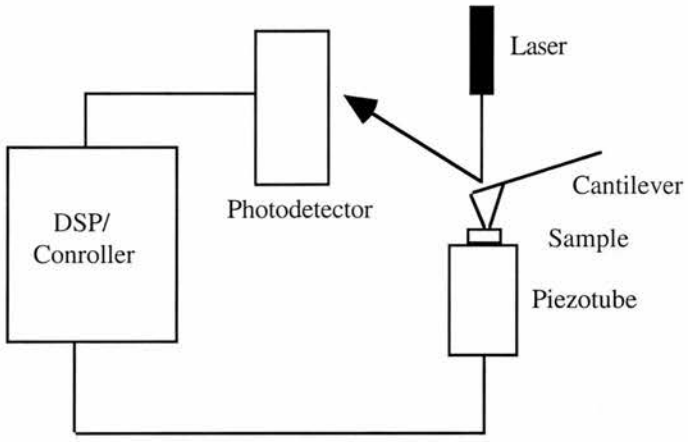

Figure 15. Schematic diagram of an Atomic Force Microscopy (AFM).

3.7 References

[1] A.Chambers, R.K.Fitch, and B.S.Halliday, Basis Vacuum Technology, ed. A.Hilger. Bristol: IOP Publishing Ltd (1989).

[2] D.P.Woodruff and T.A.Delcher, Modern Techniques of Surface Science, Cambridge: Cambridge University Press (1990).

[3] J.C.Riviere, Surface Analytical Techniques, Oxford: Oxford University Press (1990).

[4] C.G.Goymour and D.A.King, Trans.Faraday Soc., **69** (1973) 736.

[5] G.Erlich, J.Chem.Phys., **34** (1961) 39.

[6] W.Kirstein, B.Kruger and F.Thieme, Surf.Sci., **176** (1986) 505.

[7] L.Surnev, G.Rangelov and G.Bliznakov, Surf.Sci., **159** (1985) 299.

[8] T.E.Madley and J.T.Yates, Actes Colloq. Int.Structure Properties Surface Solids (Paris, 1970).

[9] P.A.Readhead, Vacuum **12** (1962) 203.

[10] R.J.Madix, Cat. Rev.- Sci.Eng., **15** (1977) 293.

[11] X.L.Zhou, C.Yoon, and J.M.White, Surf.Sci., **203** (1988) 53.

[12] J.L.Falconer and R.J.Madix, Surf.Sci., **48** (1975) 393.

[13] J.Paul, Phy.Rev.B **37** (1988) 6164.

[14] J.Paul and F.M.Hoffmann, Surf.Sci., **194** (1988) 419.

[15] S.D.Cameron and D.J.Dwywe, Surf.Sci., **198** (1988) 315.

[16] R.T.K.Baker, Catal.Rev. - Sci.Eng., **19** (1979) 161.

[17] P.Sigmund, In Sputtering by Particle Bombardment, I.R.Behrisch (Ed.), Topics in Applied Physics, **47** (1981) 9, Phys.Rev. **184** (1969) 383.

[18] J.C.Vickermann, A.Brown and N.M.Hercules (Eds.), Secondary Ion Mass Spectrometry (SIMS), Principles and Applications, Clarendon, Oxford (1989).

[19] H.E.Roosendaal, In Sputerring by Particle Bombardment I.R.Behrisch (Eds.), Topic in Applied Physics, **47** (1981) 219.

[20] D.Briggs, The Impact of Surface Science on Technology. Surf.Sci., **189/190** (1975), 801-822.

[21] D.M.Brewis and C.Briggs, Polymer, **22** (1981) 7.

[22] T.A.Carlson, Photoelectron and Auger Spectroscopy, New York, USA, Plenum Press (1975).

[23] D.Sarid, Scanning Force Microscopy with Applications to Electric, Magnetic and Atomic Forces, Oxford University Press, New York (1991).

[24] D.Sarid and V.Elings, J.Vac.Sci. Technology. **B9** (1991) 431.

[25] Millbrook Instrument Ltd, The Chemical Microscope User Manual (1998).

Chapter 4

Surface analysis techniques of aluminium oxide thin film

The major experimental techniques used to analyse and quantify the surface structure of aluminium oxide thin film will be discussed in this chapter.

4.1 Introduction

The principal substrates used in the thermal desorption experiments were, STD PAT and NON PAT aluminium oxide thin films. The chemical and structural differences between the two substrates form the basis of this chapter. The ideal techniques used for surface analysis are, SEM, TEM, AFM, SIMS, XPS and AES. Scanning Electron Microscopy (SEM) was used in a straightforward way to determine any changes in the surface structure brought about by deposition of the PAT liquor. Atomic Force Microscopy (AFM) provides information on the surface topography without destroying the surface. Transmission Electron Microscopy (TEM) provided information on the morphology of the porous anodic films. Secondary Ion Mass Spectroscopy (SIMS) provided chemical information on the surfaces. X-Ray Photoelectron Spectroscopy (XPS) was used to determine the elemental composition of the STD PAT and NON PAT surfaces.

Auger Electron Spectroscopy (AES) was used for depth profiling providing information about the distribution of elements in the anodic layer. Auger experiments were carried out by C.Mair at Liverpool University, however the interpretation of these results is entirely my own.

4.2 SEM Images

The SEM images were carried out at Horsell Graphics Industries, using a Hitachi scanning electron microscope, Model 4100 instrument.

Figure 1. Low magnification SEM image from a NON PAT surface [1]

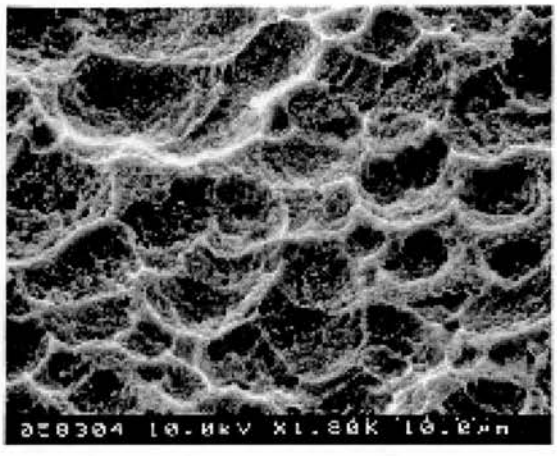

Figure 2. High magnification SEM image of a single hemispherical pit from a NON PAT surface [1]

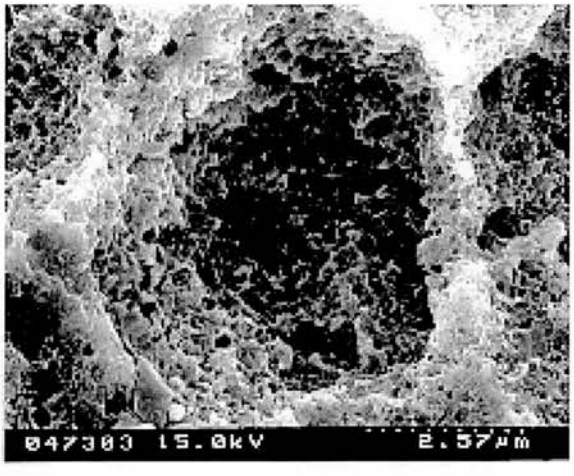

At low magnification the surface is evidently uniformly pitted, giving an apparently rough appearance. The SEM images illustrated in Figures 1 and 2. reveal large hemispherical pits ranging from 2 µm to 10 µm in diameter. The hemispherical pits are broader than they are deep. Each of these large pits is composed of many smaller

pits, ~0.2 μm in diameter, illustrated in Figure 3. It is not possible to determine whether the shape of the pits has a crystallographic origin.

Figure 3. High magnification SEM image from a NON PAT surface [1]

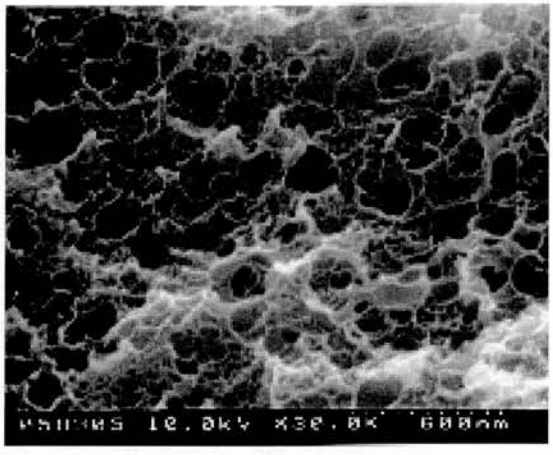

Figure 4. High magnification SEM image of the oxide layer from a NON PAT surface [1]

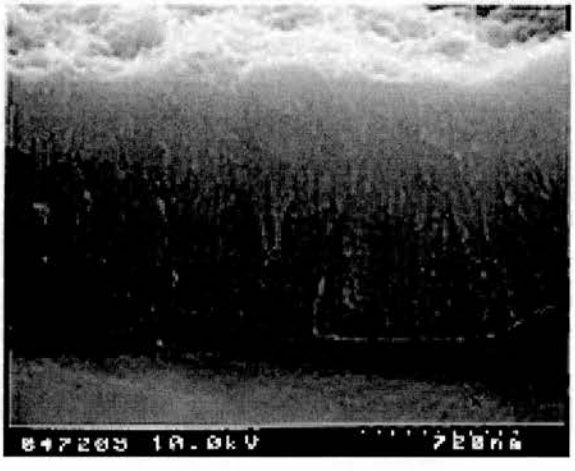

Anodising the aluminium surface results in the formation of a barrier film followed by the formation of a porous film. Closer examinination of the porous film reveals clearly the pores running parallel to each other as illustrated in Figure 4. The diameter of the pores and the thickness of the barrier film is discussed in the next section using TEM analysis.

Figure 5. Low magnification SEM image from a STD PAT surface [1]

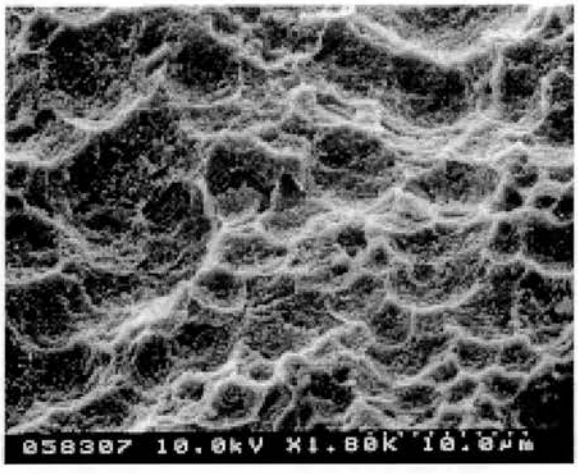

Figure 6. High magnification SEM image from a STD PAT surface [1]

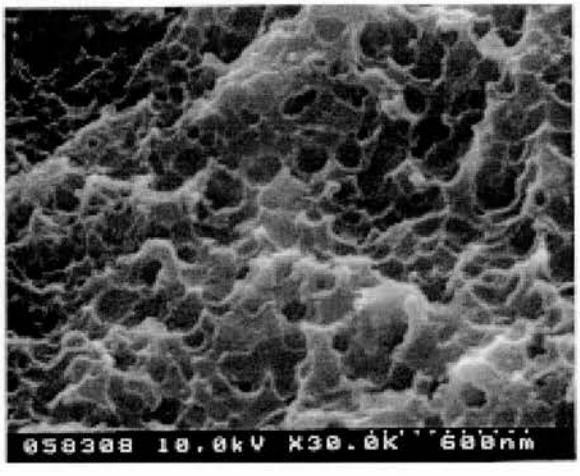

The STD PAT surface illustrated in Figures 5 and 6. shows a smoother surface in appearance and the large hemispherical pits are much more well defined as a result from the PAT treatment. The micropits illustrated in Figure 6. are not seen clearly on the STD PAT surface. This is a direct result of the PAT liquor blocking the pores.

4.2.1 Discussion

The SEM images of the STD PAT and the NON PAT surfaces reveals two changes as a direct result from the chemical treatment.

(i) Change in the Surface Area:

Smaller surface features such as the anodic pores and micropits make a significant contribution to the total surface area. As a result of the PAT treatment, we can conclude that there are far fewer anodic pores available on the surface of the STD PAT surface.

(ii) Change in the Surface Volume:

Physical or mechanical keying of the photocoat to the substrate plays a significant part in adhesion. Deposition of PAT decreases the mechanical interlocking by applying phosphate which penetrates the porous anodic structure and the micropit surface. A relatively non-porous outer surface is formed with which the photocoat can no longer effectively interlock. Mechanical interlocking on a micro scale has been recently suggested [2] to be a major mechanism in increasing interface stability for aluminium substrates. For example, on phosphoric acid anodised surfaces of aluminium the adhesive penetrates virtually to the bottom of the pores. This has led some workers to believe that micro-mechanical interlocking will be established and represent a major reason for the interface strength and durability [2].

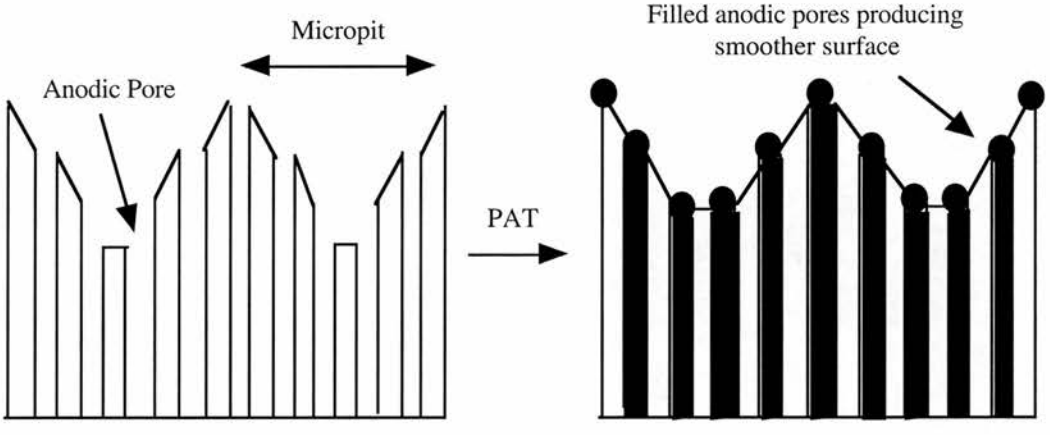

Figure 7. Cross sectional illustration of a sample with PAT (right) and without PAT (left).

The surface area for STD PAT and NON PAT was attempted using the BET measurements. Due to instrument failure these results were not obtained.

4.3 Transmission Electron Microscopy (TEM)

Porous anodic films, formed on pure aluminium by anodising in acid electrolyte, have attracted considerable attention owing to their importance in surface finishing aluminium [3-7]. Transmission electron microscopy of stripped porous anodic films formed on pure aluminium has provided information on the porous oxide film structure and the pore initiation stage [2,3,8]. The aim of the TEM experiments was to investigate the morphology of porous anodic films formed on aluminium in sulphuric acid.

4.3.1 Experimental Procedure

The majority of the anodic films were examined in a Philips 430 transmission electron microscope, operated at 300 KV. The preparation of the specimens had two stages. First a mechanical polishing of the aluminium strips, which were glued to a copper grid, to a thickness of 10-15 μm and then an ion beam thinning from both sides on a rotating specimen, at an angle of 30°. The argon ion energy was 5 KeV. The thinning procedure was completed after 15 hours.

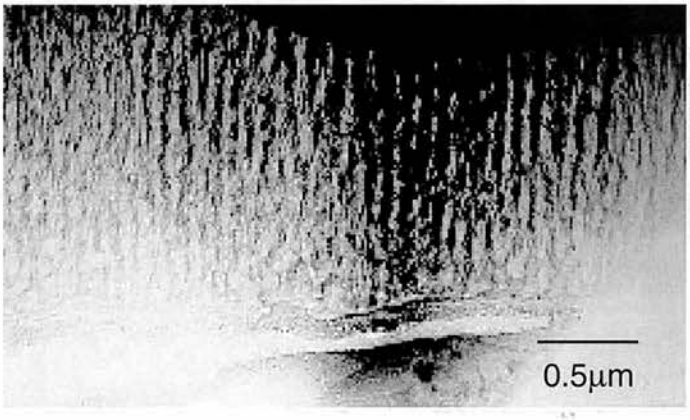

Figure 8. TEM image of a NON PAT substrate, illustrating the anodic pores structure which are parallel to the barrier layer.

The TEM film illustrated in Figure 8. shows a cross sectional view of the NON PAT sample prepared according to the procedure described. The total thickness of the film is approximately 760 nm, with the barrier layer being identifiable as the barely

resolved dark line at the bottom of the image; the barrier layer is approximately 10 nm thick. The film overlying the barrier layer consisits of many parallel porous twisting channels, the diameter ranging from 5 nm to 20 nm. Previous work [6] has shown that the film formed by anodising aluminium shows a regular pore structure. The pores in the oxide are straight and parallel to each other. Figure 9. shows a cross section of the anodic pores from an aluminium oxide film [9].

Figure 9. TEM image of a cross section of the film formed in sulphuric acid showing both top and bottom sections of the film with open pores [9].

4.3.2 Cell material packing and cell sub-structure of porous anodic film on aluminium

Previous work [9] relating to observations of film material sub-structure and morphology of porous films, formed in sulphuric acid is illustrated below. The films were formed under constant voltage conditions to obtain relatively uniform porous anodic films. The various anodising voltages, covering a relatively wide voltage range, were chosen to determine any morphological or substructural changes with applied voltage.

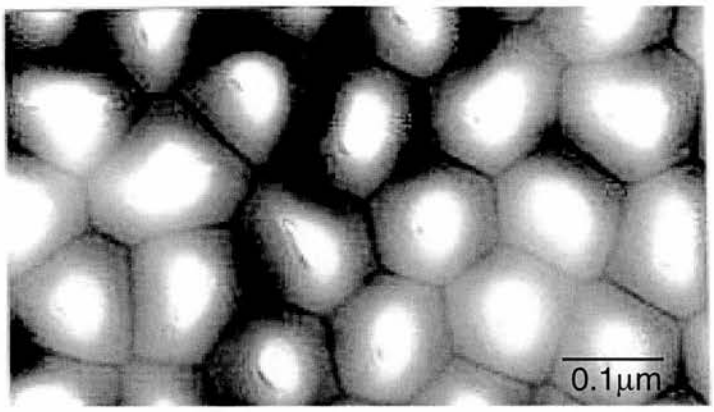

Figure 10. Transmission electron micrograph of ion beam thinned films formed in 0.25M sulphuric acid at constant 60 V. Films were exposed to the electron beam for 5 minutes [9].

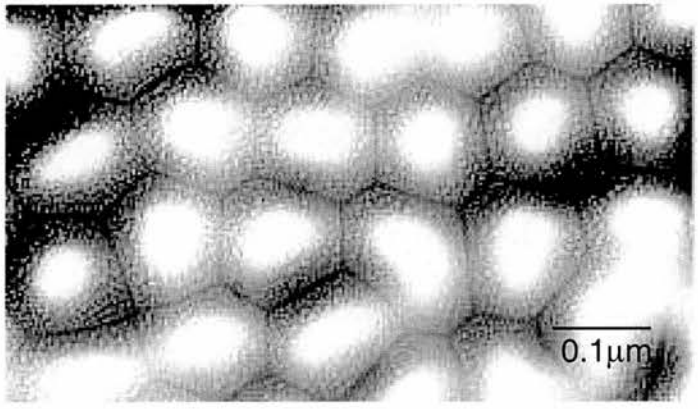

Figure 11. Transmission electron micrograph of ion beam thinned films formed in 0.25M sulphuric acid at constant 60 V. Films were exposed to the electron beam for 15 minutes [9].

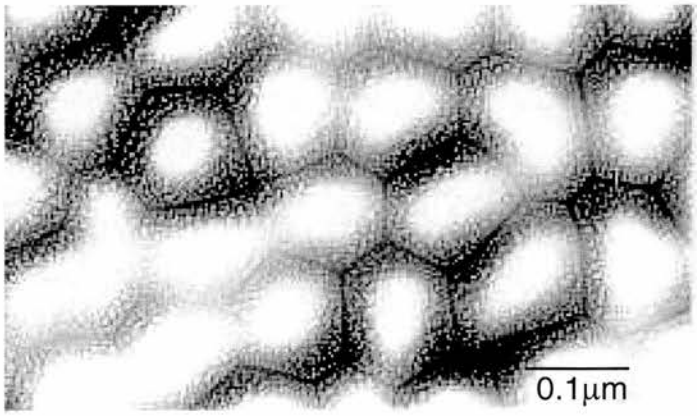

Figure 12. Transmission electron micrograph of ion beam thinned films formed in 0.25M sulphuric acid at constant 60 V. Films were exposed to the electron beam for 20 minutes [9].

The transmission electron micrograph of Figures 10-12. shows suitably prepared ion beam thinned films formed in sulphuric acid; generally the pores appeared as approximately circular or elongated holes present in the centre of the cell material which was arranged in approximately pentagonal or hexagonal packing. The shapes of the pores followed the morphology of the cells; for example, where the cells have equal sides, the pores were circular and where the cells were elongated, the pores also had an elongated shape. This consistent observation, confirms that the shapes of the pores are genuine.

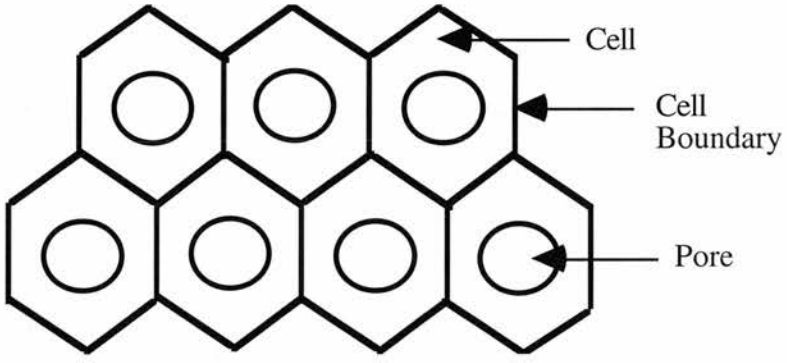

Figure 13. Schematic plan view of an ion beam thinned film, showing the idealised cell, pore and cell boundary.

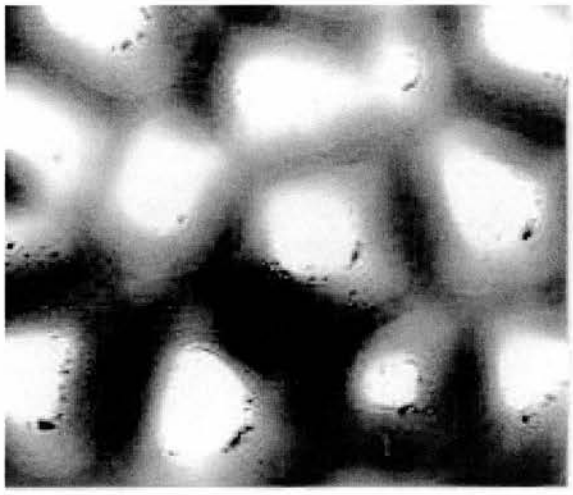

Figure 14. Transmissiom electron micrograph of ion beam thinned films formed in 0.4M phosphoric acid at constant 30 V [9].

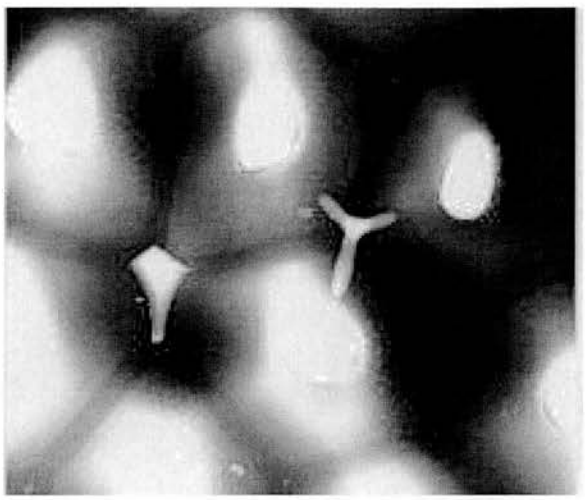

Figure 15. Transmissiom electron micrograph of ion beam thinned films formed in 0.4M phosphoric acid at constant 30 V [9].

Figures 14 and 15. shows that the film formed at 30 V is composed of cells of different shapes, mostly pentagonal and hexagonal with relatively few square-shaped cells. The pore shapes appear to be large pentagonal cells surrounding smaller square or pentagonal cells. The average cell diameter is about 49 to 112 nm.

4.3.3 Discussion

The regular morphology of the porous anodic film has fascinated fundamental investigators for many years, this is because the mechanism of pore and cell formation represents an almost unique situation in the field of anodic processes, in addition to the importance of the films in the surface finishing of aluminium. The literature survey reported earlier has shown that current knowledge of the steady-state film morphology suggests an arrangement of parallel sided pores passing normal to the macroscopic aluminium substrate, the pore and cell diameters of the anodic films being directly proportional to the film forming voltage.

It is very clear from the TEM images that the anodic pores of the NON PAT sample consists of many "twisting" parallel porous channels, the diameter of these pores ranging from 5 nm to 20 nm. Earlier work [9] with anodised alumina in sulphuric acid and phosphoric acid shows the pore shape to be circular or elongated holes arranged in approximately pentagonal or hexagonal packing.

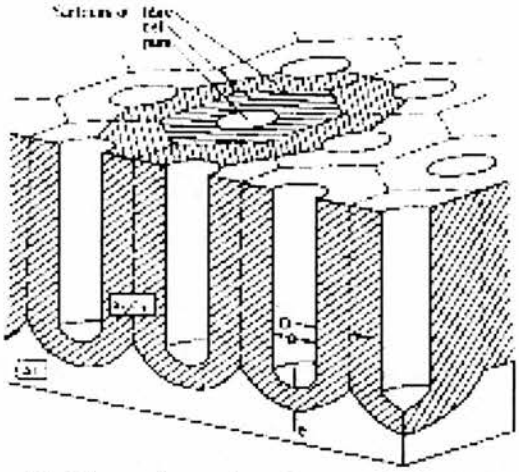

Figure 16. Schematic section of a porous Al_2O_3 layer [4].

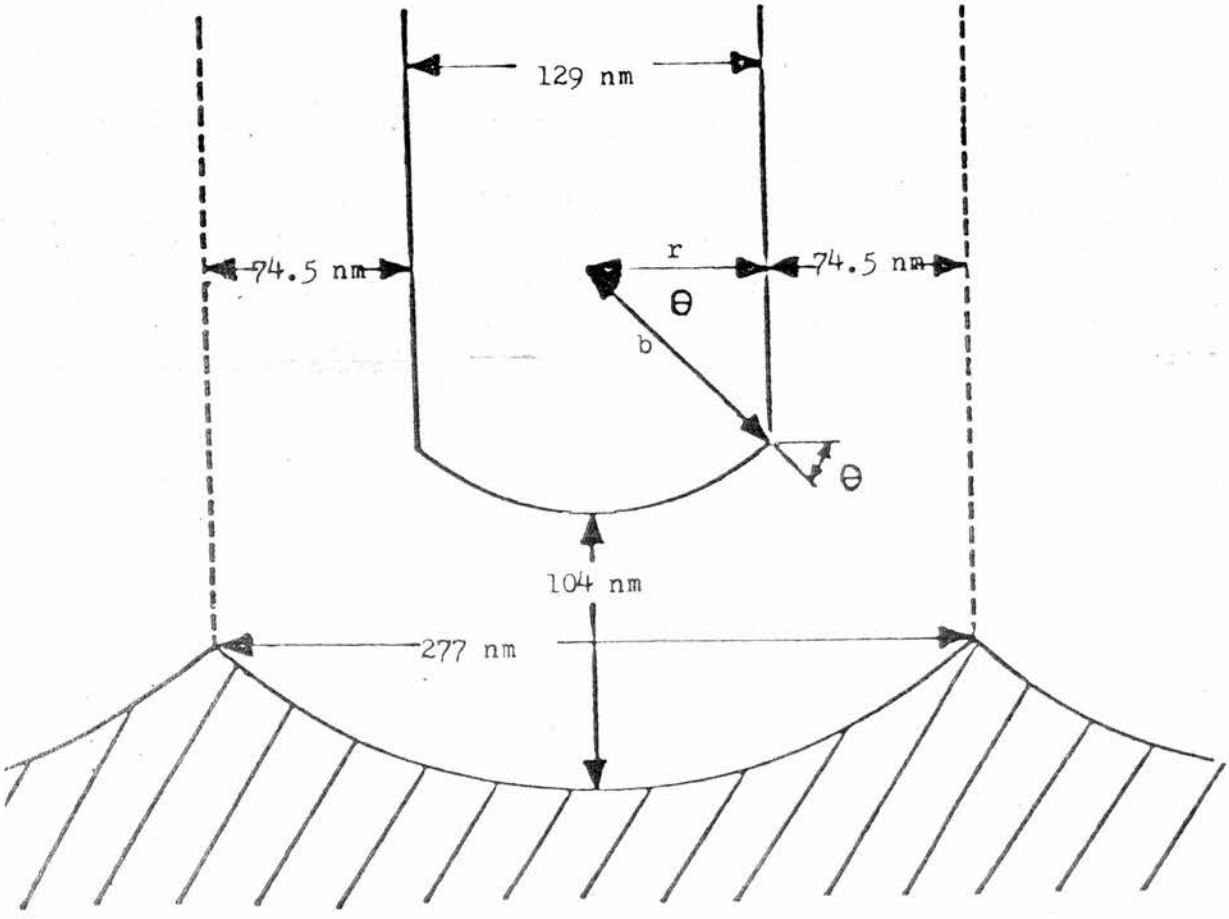

Figure 17. Schematic representation of the barrier later, cell material and the pore of a steady-state porous anodic film developed on aluminium at 100 V in phosphoric acid [9] r = pore diameter; b = pore base radius of curvature, cos = r/b = cell thickness/barrier layer thickness.

Figure 16. gives a schematic sectional drawing of a porous later as first described by Keller *et al* [4]. The pores are vertical channels in the oxide layer, closed towards the metal. In a porous layer cells are defined such as to attribute walls to each pore. Pore diameter ***p***, bottom layer thickness ***e***, and cell wall thickness ***D***, are generally found to be proportional to the anodising voltage ***U***.

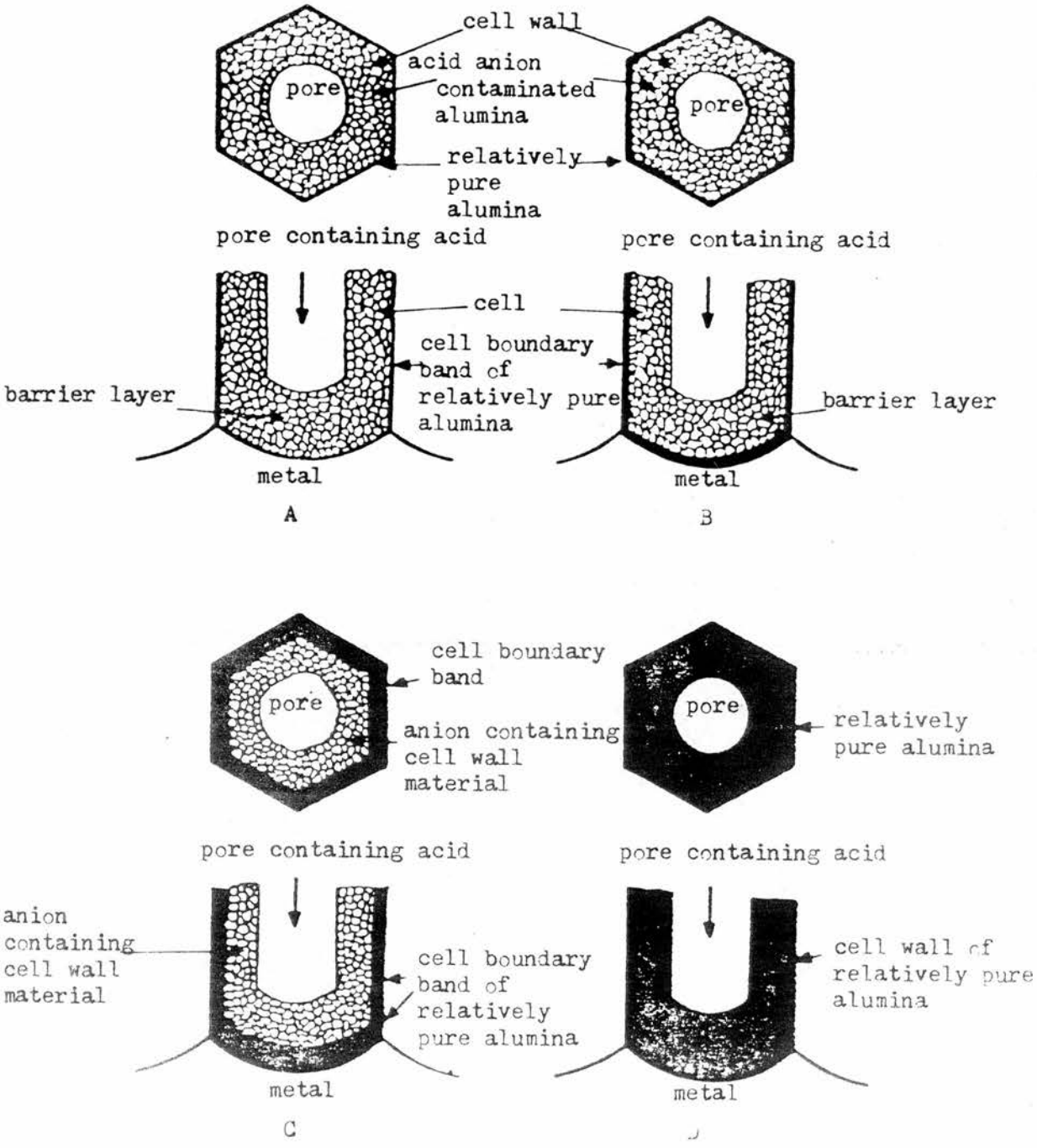

Figure 18. The plan and sectional views of a pore and adjacent cell for films formed in each of the major acid; (a) sulphuric acid; (b) oxalic acid; (c) phosphoric acid and (d) chromic acid. The cell wall comprises acid anion contaminated film material adjacent to the pore and relatively pure alumina remote from it [9].

4.4 Atomic Force Microscopy (AFM)

Atomic Force Microscopy allows non-destructive scanning of any surface morphology on a nanometer scale. The aim of the AFM experiments was to investigate the topography of the alumina surfaces.

4.4.1 Experimental Procedure

Contact mode AFM was used, where the surface is scanned underneath the tip at constant applied force. The cantilever is deflected by structure on the surface. This deflection is detected by means of a laser beam reflected off the back of the cantilever onto a photodetector. The tip sample separation is then adjusted to maintain a constant force on the sample. The surface was imaged using a Nanoscope III Multimode Scanning Probe Microscope, manufactured by Digital Instruments, Inc. The cantilevers used were standard silicon nitrides probes, with a radius of curvature ~30 nm, and spring constant ~0.12 N/m [10]. The cantilevers have a square pyramidal tip structure, orientated parallel to the cantilever axis, and are 4 μm across at the base and 2 μm at the apex of the pyramid.

The angle between parallel faces is 70° and across the diagonal from corner to corner, 90°. The angle between the 70° face and the sample, when the z axis of the tip is perpendicular to the sample, is 55°. However, when mounted in the AFM, the cantilevers are tilted by 10°; this creates angles of 45° on one side and 65° on the other side with respect to the surface. The precise structure and size of the tip at its apex remains unknown. It has been generally accepted, however, to be parabolic and about 25-50 nm in diameter.

Figure 19. AFM image of a NON PAT surface

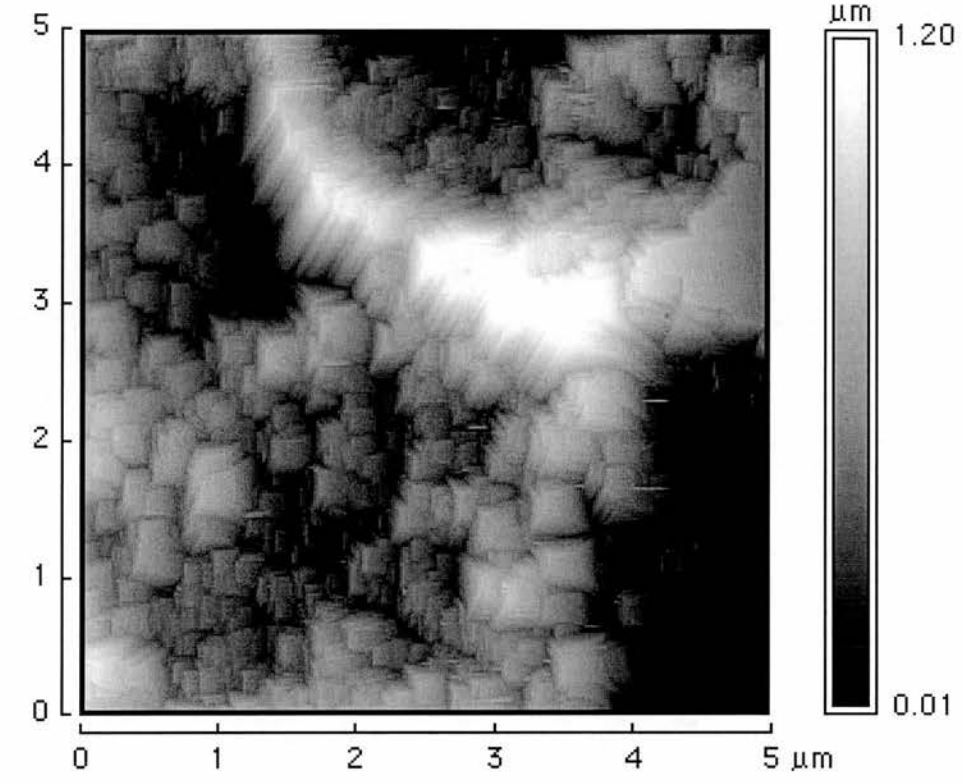

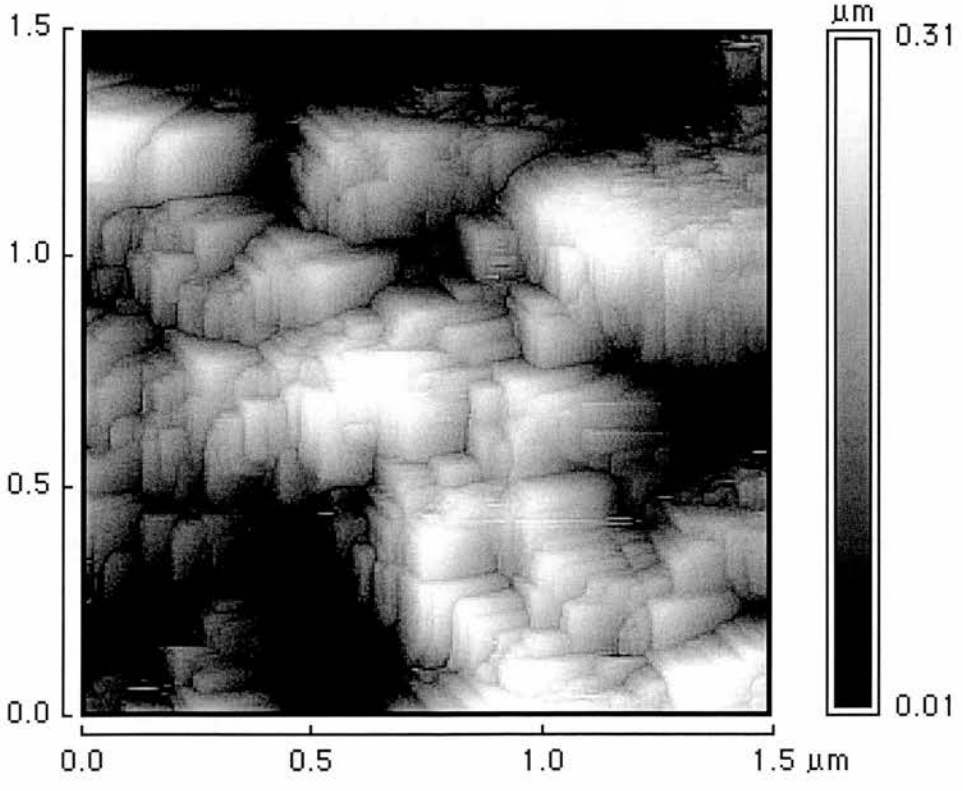

Figure 20. AFM image of a STD PAT surface

4.4.2 General Description

The surface of both the NON PAT and STD PAT shows large areas of crystalline cubodial structures distributed across the surface.

4.5 Secondary Ion Mass Spectrometer (SIMS)

The critical point to remember is that SIMS is extremely surface sensitive. Wearing disposable gloves is essential for this stage. All care must be taken to avoid surface contamination. The sample was fixed to a stub using double-sided adhesive tape which is low in volatiles and which does not involve a silicone release agent. The experiments were carried out using a Millbrook Chemical Microscope [11].

4.5.1 Positive Ion analysis

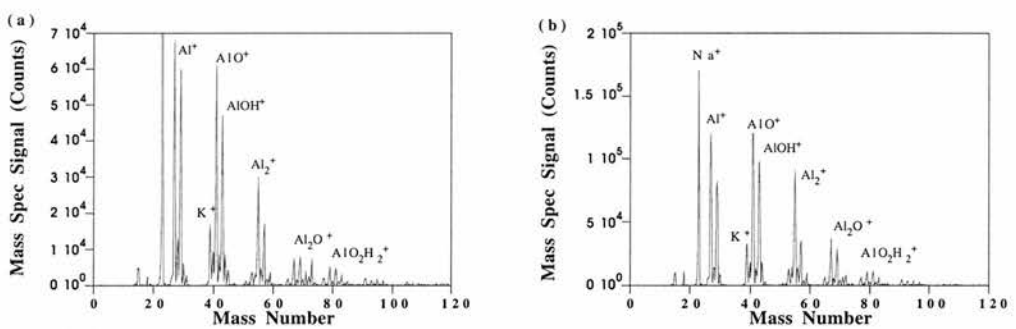

Figure 21. Showing a Positive Ion Spectra for (a) NON PAT and (b) STD PAT substrate.

4.5.2 General Description

All positive ion spectra for the NON PAT and STD PAT were dominated by peaks at m/z = 27 due to the Al^+ ion. The spectra did not contain the typical clusters of hydrocarbon peaks observed on untreated aluminium surfaces that are associated with the presence of residual rolling lubricants and additives [12]. The spectra in Figure 21. highlight the principal difference in the surface chemistry of the two substrates. In both spectra, peaks at m/z = 39 peak can be derived from potassium, but observation of the m/z = 41, 43 and 45 suggests that the peaks can be attributed to aliphatic hydrocarbons. Some contribution to the m/z = 43 peak was associated with the AlO^+ fragment, and peaks at m/z = 44 and 61 were associated with $AlOH^+$

and $AlO_2H_2^+$ fragments, respectively. Similarly, peaks at m/z = 70 and 86 were associated with Al_2O^+ and $Al_2O_2^+$ fragments respectively. The main difference in the two spectra were the loss in intensity of the hydrocarbon-derived fragments, the decrease in intensity of the m/z = 43 peak and an increase in the intensities of the $AlO_2H_2^+$ and Al_2O^+ peaks for the STD PAT, shown in Figure 21b. Above m/z = 100, positive ion spectra contained only very low intensity peaks at m/z values characteristic of traces of aromatic hydrocarbons.

4.5.3 Negative Ion analysis

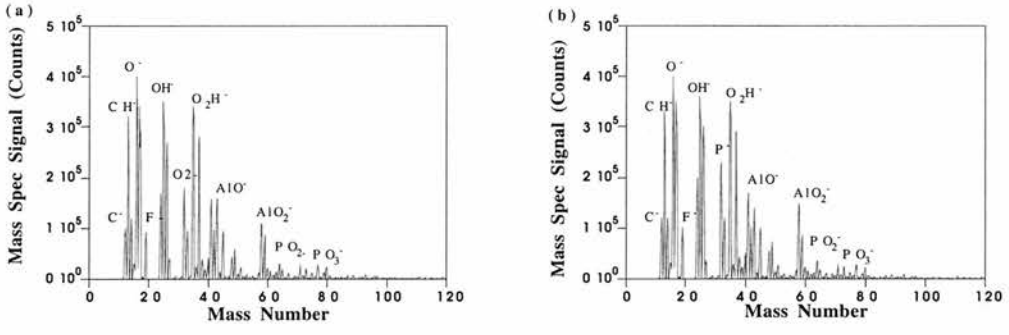

Figure 22. Showing a Negative Ion Spectra for (a) NON PAT and (b) STD PAT substrate.

4.5.4 General Description

The negative ion spectra for the the NON PAT and STD PAT contained intense O^- and OH^- peaks, together with low intensity C^- and C_2^- peaks illustrated in Figure 22. represents low levels of organic contamination. Peaks at m/z = 32 and 33 corresponding to O_2^- and O_2H^-, respectively, and peaks at m/z = 43, 59, 63 and 79 correspond to the AlO^-, AlO_2^-, PO_2^- and PO_3^- fragments, respectively. The low intensity peaks of P^-, PO_2^- and PO_3^- shown in the STD PAT sample implies that there may be changes in the surface chemistry of the aluminium; clearly this could also affect the adhesive properties of the surface.

4.5.5 Discussion

The treatment of the alumina surface with phosphate in PAT treatment changes the chemical interactions which can occur between the substrate and the photocoat. The phosphate formed when aluminium is immersed in a phosphate containing solution is difficult to determine. A large number of aluminium phosphates exist, of different forms and stoichiometries, depending on the exact experimental conditions. Although compounds with Al_2O_3:P_2O_5 molar ratios of 1:2 have sometimes been observed, those most frequently encountered have been found to have ratios 1:1 and 1:3 [13]. Compounds of the 1:1 variety are most commonly obtained by direct reaction of alumina powder with phosphoric acid at 60°C [14], yielding a precipitate of $AlPO_4.2H_2O$. Aluminium dihydrogen phosphate $Al(H_2PO_4)_3$ is formed, however, if the temperature of the phosphoric acid is raised to 100°C [15], a condensation reaction occurs, as shown in Figure 23.

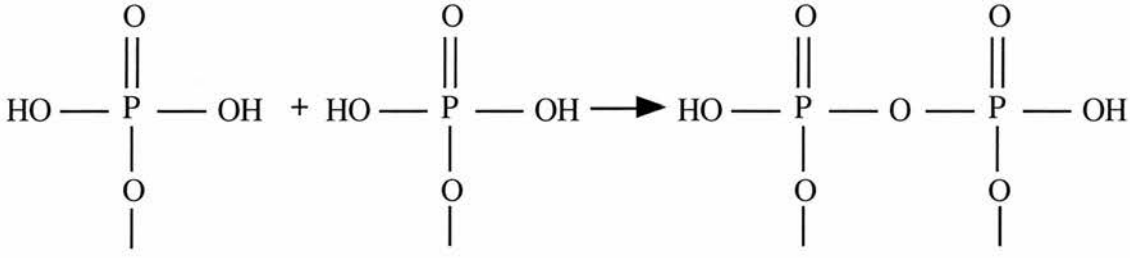

Figure 23. Illustrating a reaction scheme showing the formation of a condensation polymer during dehydration of an hydrated phosphate [16].

4.6 X-Ray Photoelectron Spectroscopy (XPS)

The aim of the XPS experiments was to demonstrate the elemental difference between the NON PAT and STD PAT after chemical treatment.

4.6.1 Experimental Procedure

A 1cm square sample of STD PAT or NON PAT was mounted in an XPS instrument which had a base pressure of $5x10^{-9}$ mbar and was heated to 150°C during the bakeout procedure. The analysis chamber was fitted with an X-ray gun

(AlKα and MgKα radiation). The preparation chamber was fitted with a quadrupole mass spectrometer (Spectra-Tech) and an ion sputter gun (VG).

4.6.2 XPS Analysis of STD PAT substrate

Figure 24. shows a widescan of the XPS data of an STD PAT surface as received, after bakeout. Initially, there are small traces of aluminium and carbon peaks. With heating the surface at variable temperatures up to 400°C, several trace elements such as sodium, sulphur, phosphorus, fluorine, calcium and chlorine are observed, which are present in the manufacturing process. Carbon contaminant on the surface suggests foreign species are predominantly present at the surface, not within the oxide layer. In technological applications, these species may significantly affect adhesion.

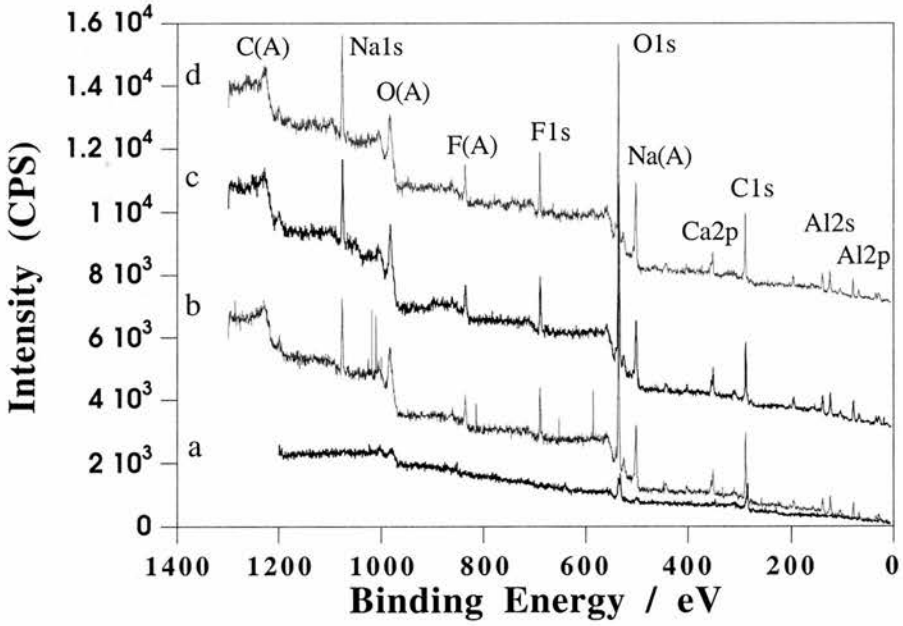

Figure 24. Overall AlKα XPS spectra of a STD PAT substrate (a) as received, (b) substrate heated to 100°C (c) substrate heated to 300°C and (d) substrate heated to 400°C, for 15 minutes.

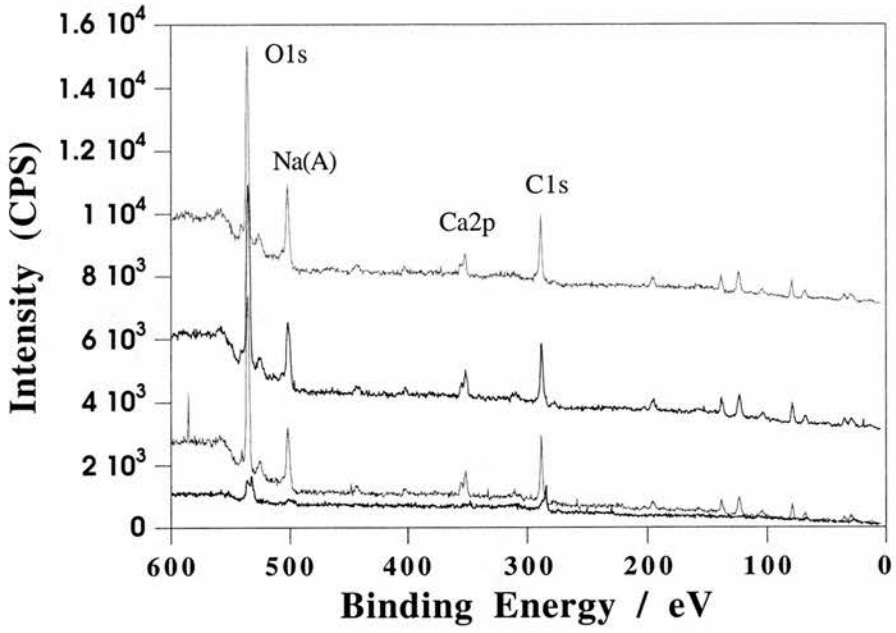

Figure 25. An enlargement of the low region (600-0 eV) of figure 24.

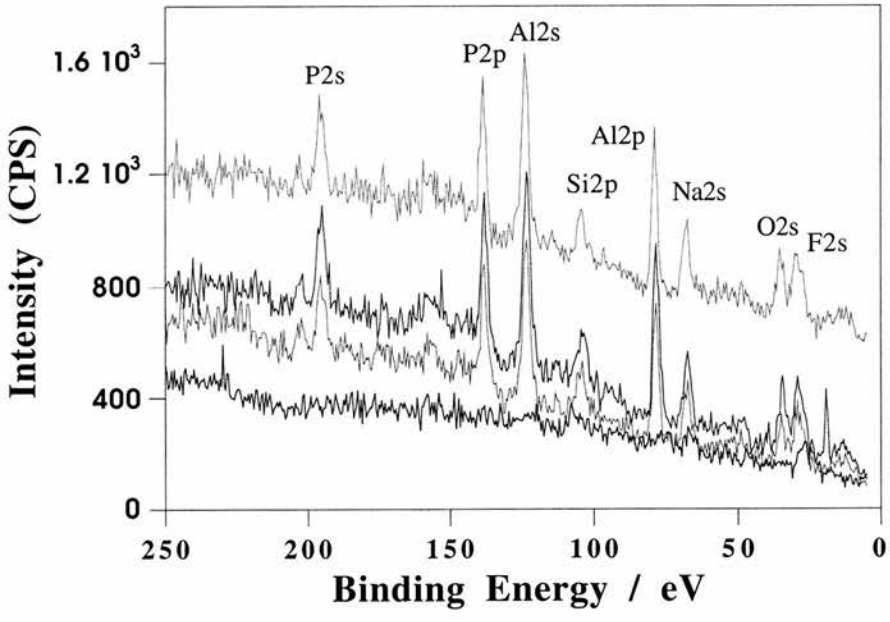

Figure 26. An enlargement of the low energy region (250-0 eV) of figure 25.

4.6.3 XPS Analysis of NON PAT substrate

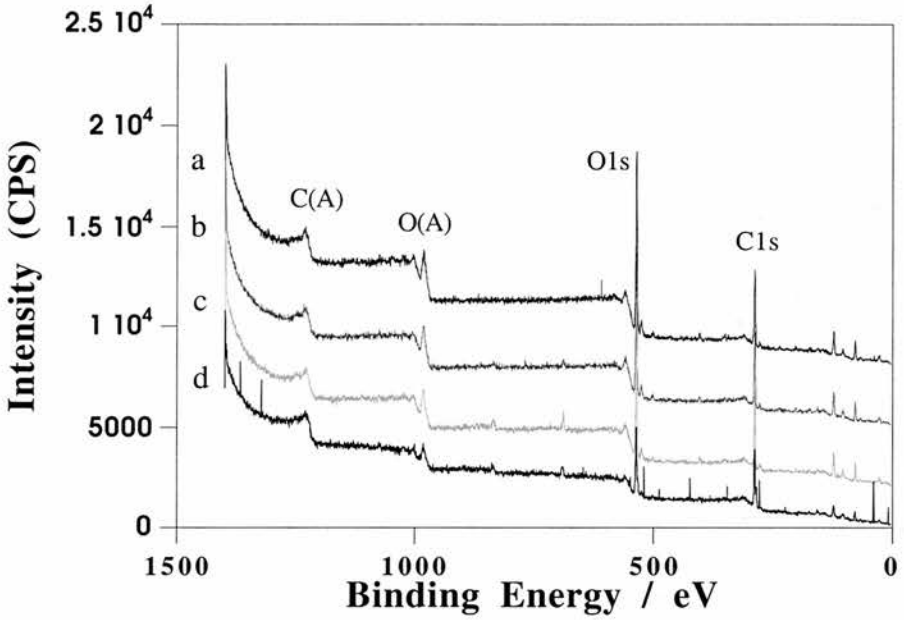

Figure 27. Overall AlKα XPS spectra of a NON PAT sample (a) as received, (b) sample heated to 200°C (c) sample heated to 300°C and (d) sample heated to 400°C for 10 minutes.

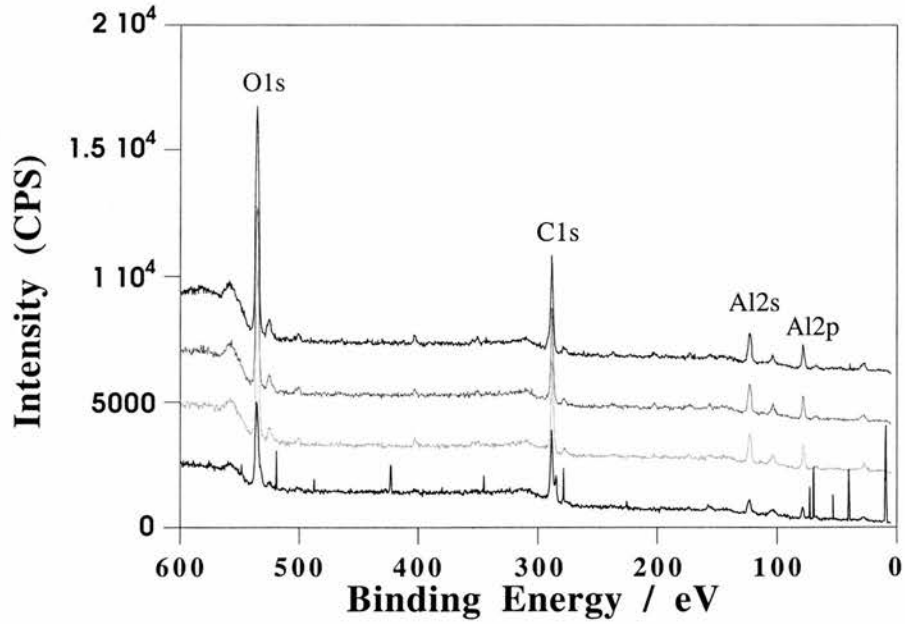

Figure 28. An enlargement of the low energy region (600-0 eV) of figure 27.

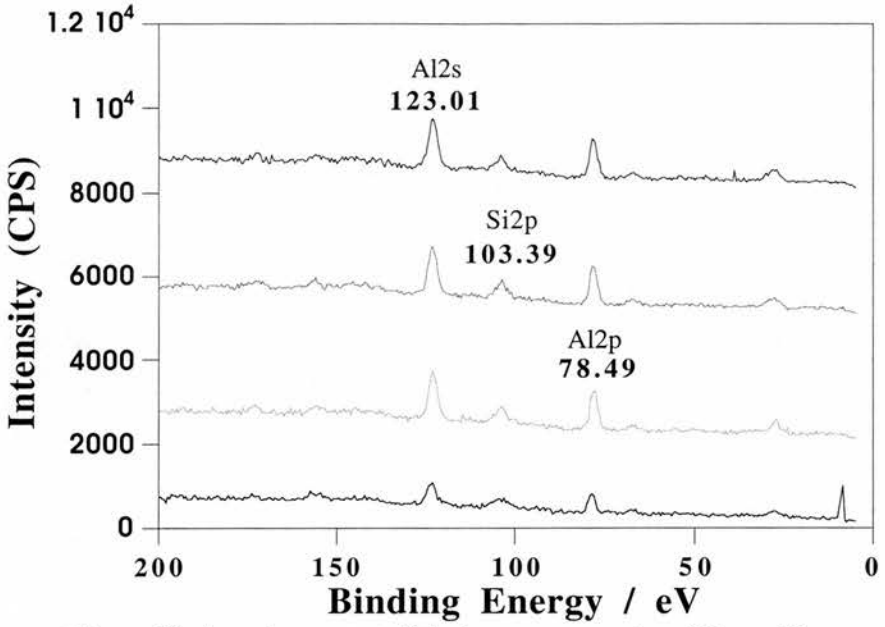

Figure 29. An enlargement of the low energy region of figure 28.

XPS experiments on the NON PAT revealed the presence of carbon, aluminium oxygen and silicon peaks as the only detectable surface constituents. The silicon is believed to originate from the interleaving paper used to package the plates. Table 1. shows the elemental differences between the NON PAT and the STD PAT substrate.

Table 1. XPS analysis of NON PAT and STD PAT substrate (+ means identified)

SAMPLE	Na	Cl	P	F	Si	Ca	N	C	Al	O
NON PAT					+			+	+	+
STD PAT	+	+	+	+	+	+		+	+	+

Table 2. Information regarding the manufacture of the samples supplied by Horsell Graphic Ltd [1]

SAMPLE	Clean NaOH	Electrograin HCl	Anodised H2SO4	PAT NaH2PO4, NaF, NaSi
NON PAT	+	+	+	
STD PAT	+	+	+	+

Table 3. Assignment of the principal peaks to particular electrons within the surface of the STD PAT and NON PAT sample. Standard binding energies for these electrons are included for comparison [17]

Observed Binding Energy[eV]	Assigned Electron	Standard Value of Binding Energy [eV]
29	O (2s)	23
65	Na (2s)	64
76	Al (2p)	74
121	Al (2s)	119
136	P (2p)	134
193	P (2s)	191
287	C (1S)	287
500	Na (Auger)	497
533	O (1s)	531
688	F (1s)	686
833	F (Auger)	832
979	O (Auger)	976
1073	Na (1s)	1072

4.6.4 Discussion

XPS reveals key differences between the STD PAT and NON PAT substrate. It is a surface sensitive technique suitable for studying the surface elemental composition of an aluminium substrate. The slight differences in the binding energies shown in

Table 3. were due to the charging of the sample. Both samples shows considerable carbon contamination.

4.7 Auger Electron Spectroscopy (AES)

This technique is similar to XPS where a sample is bombarded with electrons of a suitable energy. Irradiation of a sample by electrons with energy in the range 2-5eV can result in ejection of a core electron.

An advantage of AES is that it provides a quick assessment of the surface composition (depth profile analysis). Owing to the short data collection times (seconds per scan per peak), AES can be combined with sputtering to measure concentrations as a function of depth.

4.7.1 Depth Profile information from a STD PAT sample

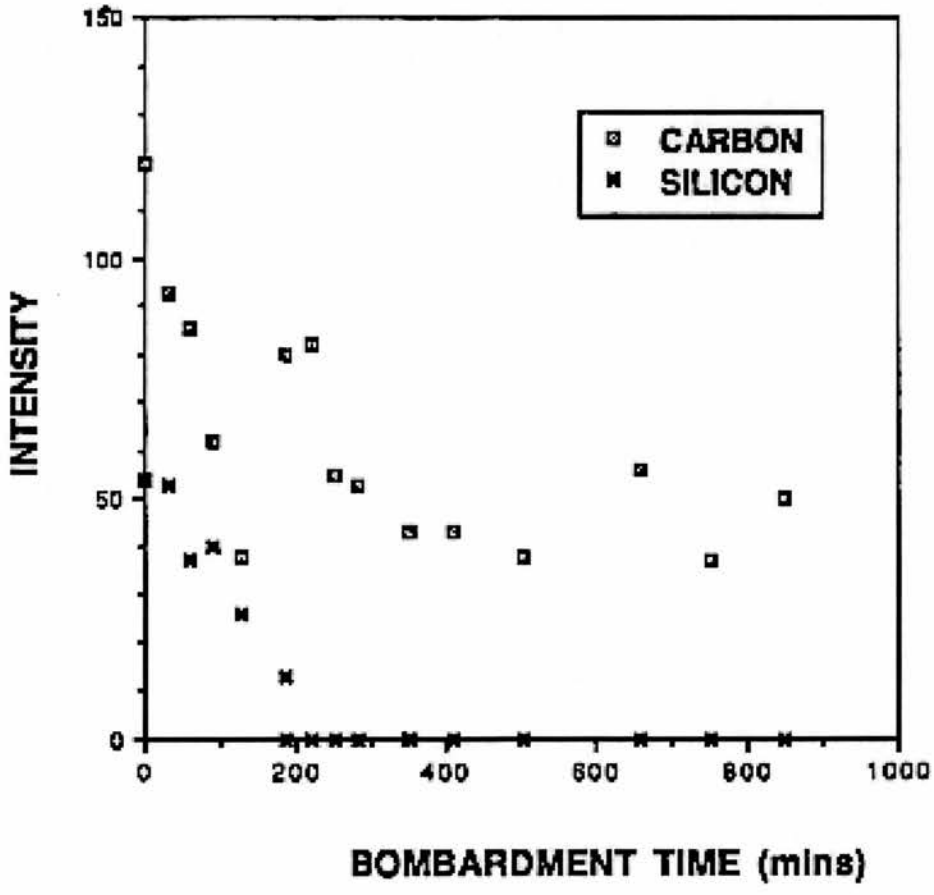

Figure 30. Showing Depth profile of Carbon and Silicon

Figure 30. illustrates a higher concentration of carbon is present on the surface of the sample than the bulk. Carbon is a common contaminant in UHV systems. The intensity of the carbon signal was relatively small immediately after sputtering, but it increased with time. Although sputtering removes much of the surface contamination the sample quickly readsorbs hydrocarbons once sputtering has ceased. In order to minimise this effect, the AES measurements were made as quickly as possible after sputtering.

After 200 mins of argon ion bombardment the silicon intensity has been reduced to zero. This suggests that the depth penetration of sodium silicate PAT is small.

Figure 31. Showing Calcium Depth Profile

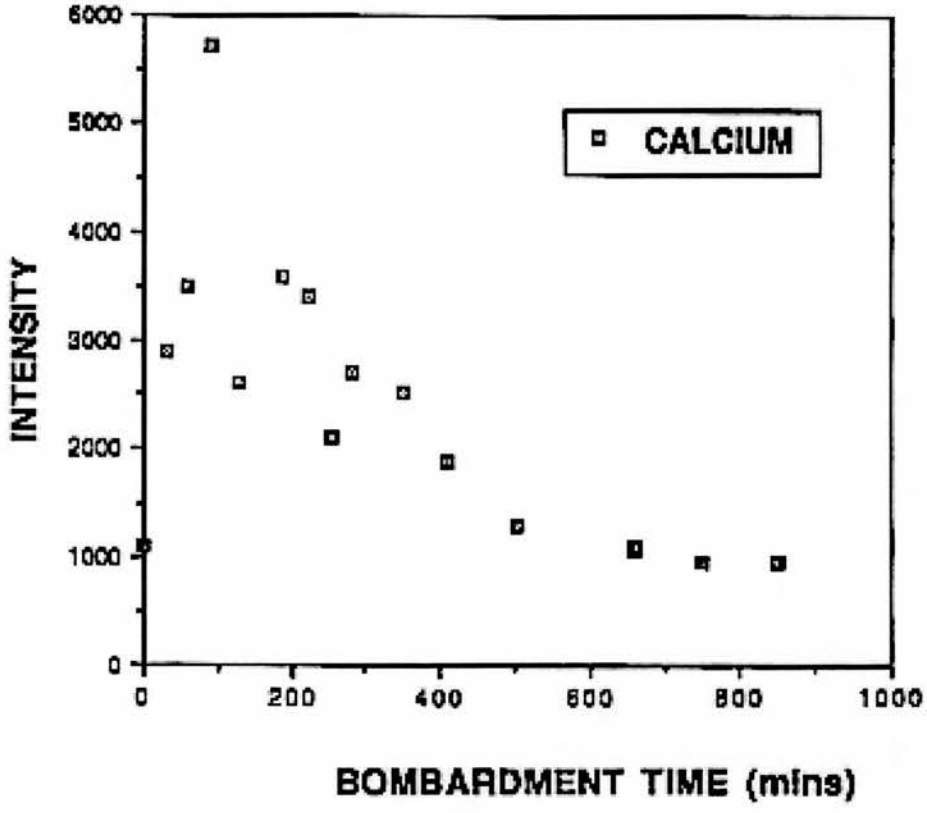

Figure 32. Showing Nitrogen Depth Profile

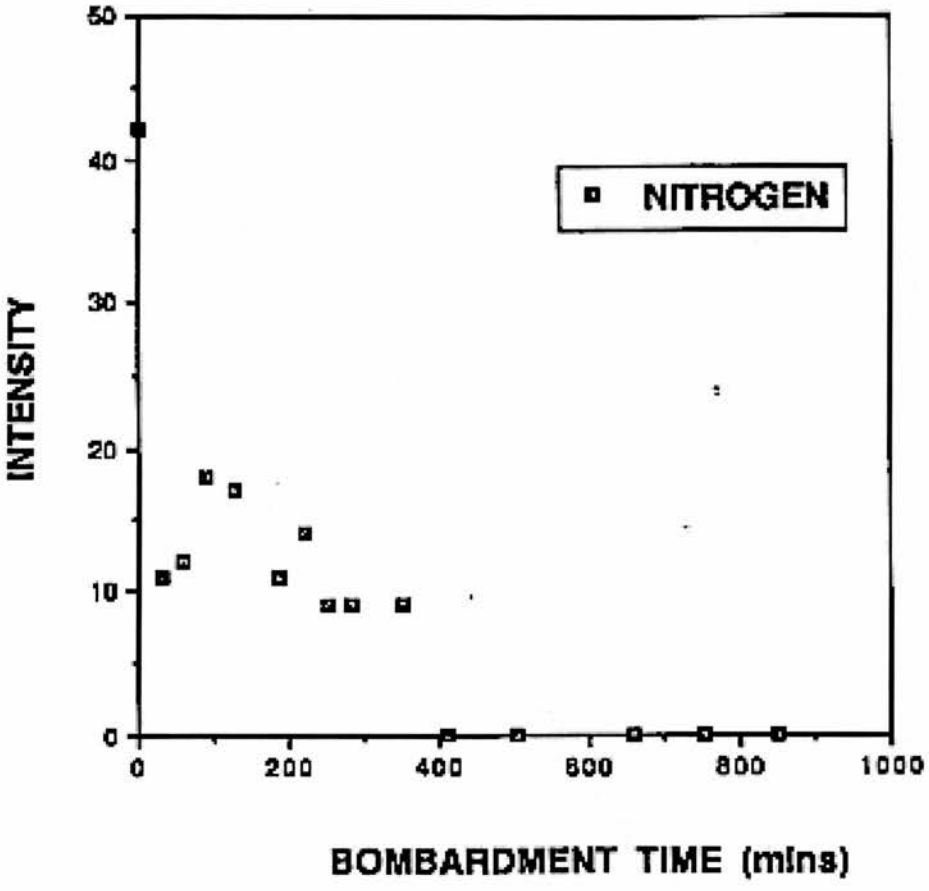

Calcium depth profile illustrated in Figure 31. shows calcium concentrated in the uppermost region, but even after 900 minutes of sputtering, it is still detectable. Nitrogen is concentrated in the uppermost region and after 400 minutes it could no longer be detected.

Figure 33 and 34. Showing Sulphur and Oxygen/AluminiumDepth Profile

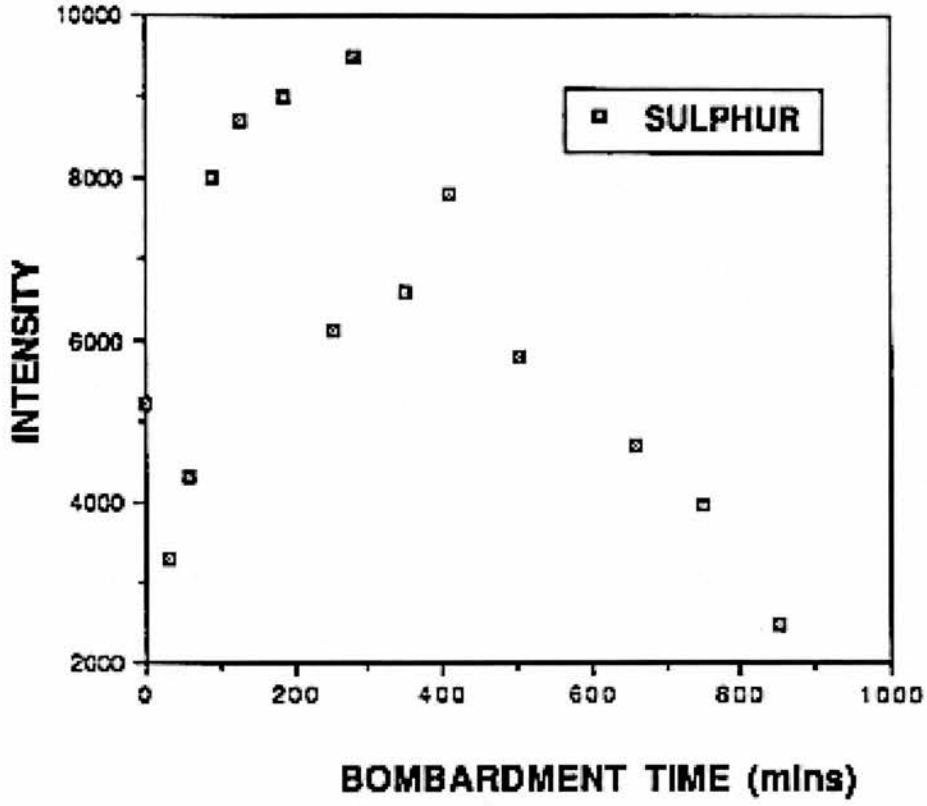

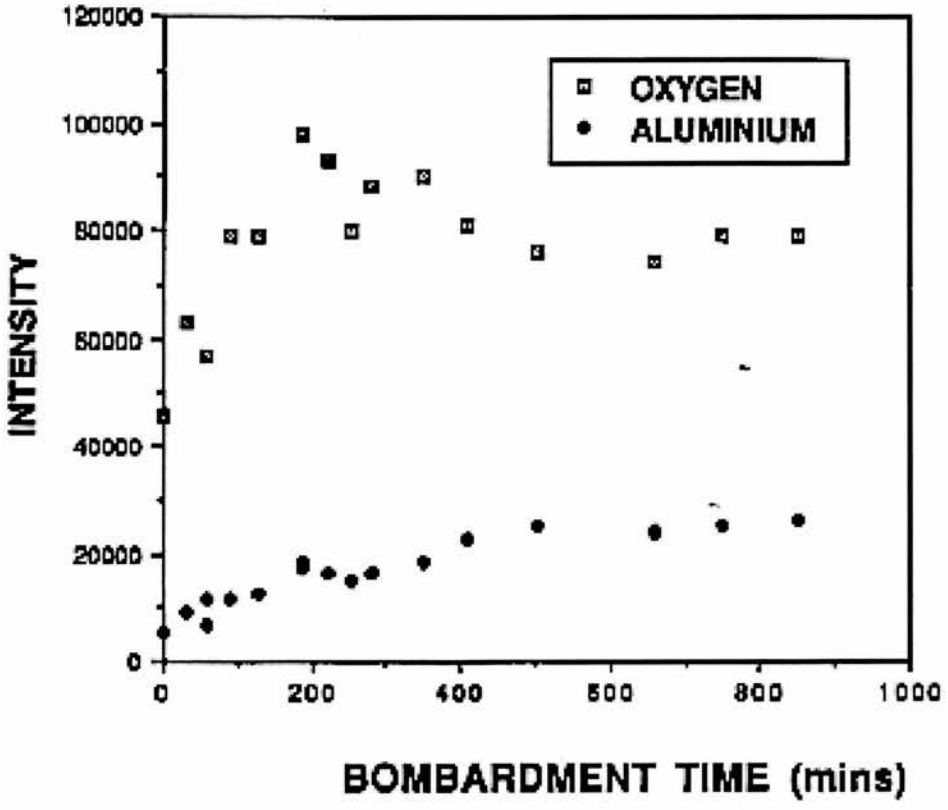

Some sulphur is detected on the surface. However, the highest concentration resides in the bulk after 250 minutes of sputtering.

Both the oxygen and aluminium signals increased initially due to the removal of surface contamination to expose the purer alumina. After about 400 minutes the intensities of aluminium and oxygen level off.

Table 4. Elements detected by AES and XPS from a STD PAT substrate (+ means detected, - means not identified)

TECHNIQUE	Na	Cl	P	F	Si	Ca	N	C	Al	O	S
AES	+	-	-		+	+	+	+	+	+	+
XPS	+	+	+	+	+		+	+	+	+	

4.7.2 Discussion

AES is a surface sensitive technique suitable for elemental analysis of Al_2O_3. The results obtained for a STD PAT substrate are in good agreement with those from XPS data. However, AES did not confirm the presence of P and Cl. The use of ion sputtering in surface analysis is not without its problem. In particular it is difficult to determine the depth of erosion into the material for the following reasons:

1. The rate of surface erosion is difficult to determine.
2. The process does not simply lead to sequential removal of atomic layers but substantial damage occurs in the sub-surface region including atomic mixing.
3. Surface morphology may be changed eg. the second layer begins to be eroded whilst the first layer is partially complete.
4. In a multi-component system, such as Al_2O_3, preferential sputtering of one species may occur relative to another leading to a change in surface composition.

These four effect lead to problems in calibration and depth resolution of depth profiling. Until they can be addressed the results quoted in this experiment are given as a function of argon ion bombardment time. Although this is not ideal, it should allow for comparisons to be made between samples.

4.8 References

[1] N.Sawyer, Horsell Graphic Industries (1999).

[2] A.J.Kinloch, Durability of Structural Adhesives, Applied Science Publishers (1983).

[3] J.P.O'Sullivan and G.C.Wood, Proc.Roy.Soc. Lond., A, **317** (1970) 511.

[4] F.Keller, M.S.Hunter and D.L.Robinson, J.Electrochem. Soc., **100** (1953) 411.

[5] G.E.Thompson, Y.Xu, P.Skeldon, K.Shimizu, S.H.Han and G.C.Wood, Philos. Mag.B, **55** (6) (1987) 651.

[6] J.W. Diggle, T.C.Downie and C.W.Goulding, Chem.Rev., **69** (1969) 356.

[7] K.Yokoyama, H.Konno, H.Takahashi and M.Nagayama. PATing and Surface Finishing, **44** (1982) 62.

[8] G.E.Thompson, R.C.Furneaux, J.S.Goode and G.C.Wood, Tran. IMT, **56** (1978) 159.

[9] S.H.Tan, PhD Thesis, Manchester (1982)

[10] T.R.Albrecht, S.Akamine, T.E.Carver, C.F.Quate: J.Vac.Sci.Tech., A8 (1990) 3386.

[11] Millbrook Instrument Ltd, The Chemical Microscope User Manual, (1998).

[12] J.A.Treverton and M.P.Thomas, Int.J.Adhes. Adhes., **9** (1989) 211.

[13] J.C.Brosheer, F.A.Lenfsty and J.F.Anderson, J.Amer.Chem.Soc., **76** (1954) 5951.

[14] F.d'Yvoire, Bull.Soc.Chim. France, (1962) 1762.

[15] F.d'Yvoire, Bull.Soc.Chim. France, (1961) 2277.

[16] M.Sychev, Ress. J.Appl.Chem., **44** (1971) 1740.

[17] C.D.Wagner, W.M.Riggs, L.E.Davis, J.F.Moulder and J.E.Mullenber,

Handbook of XPS, Perkinelmer Cooperation, Physical electronic division 6509, Prairie, Minnesota (1978) 55344.

Chapter 5

A Thermal Desorption study of the adsorption of simple organic molecules on aluminium oxide thin film

The experimental methods used to study chemisorption on metal-oxide surfaces fall into two categories: those that determine what is on the surface, and those that determine what comes off the surface. The major experimental techniques that are used to determine what is on the surface have already been discussed in chapter 4. The techniques used to study the interaction of organic molecules with metal-oxide surfaces are thus somewhat different. This chapter discuses how thermal desorption is used to measure species that desorb after a particular molecule has been adsorbed onto a surface at low temperature. This technique does not provide any direct measure of the species actually adsorbed on the surface, but it is often possible to infer those species from the distribution of desorption products. In some cases XPS and UPS have been used to monitor the adsorbed species, but the determination is often not unique due to the complexity of the species. A general feature of oxide surfaces (which is important in selective oxidation catalysis) is the rather facile breaking of the C-H, but not of the C-C, bonds. Molecular adsorption on oxide surfaces has been studied extensively [1-18]. One reason of course has been the eminent importance of oxide substrates as a support for dispersed metal catalysts as well as active catalysts themselves [19]. For surface studies three strategies have been applied:

1. Adsorption and reaction studies on micro-crystalline materials [15,16].
2. Adsorption studies of single crystal oxides by a number of groups including the groups from Yale [1], Copenhagen [7,8], Manchester [9,10] and Tubingen [11,12].

3. Adsorption and reaction studies on oxide films grown on metallic substrates [13,14].

The third strategy has proven to be particularly relevant to this investigation.

5.1 Introduction

The organic probe molecules of particular interest in this study were Aniline, Phenol, Methanol, Ethanol, Xylene and Hexane. These organic molecules represent the constituents of the light sensitive coating or their close analogue which, when applied to the substrate, form the image areas on the substrate. Analysis of the TPD spectra was made using Redhead's analysis [11], assuming first order kinetics with well identified parameters:

$$E_d/RT_{max} = \ln (\nu_d T_{max}/\beta - 3.64]$$

$$E_d = RT_{max} [\ln(\nu_d T_{max}/\beta - 3.64]$$

where T_{max} is the peak maximum temperature, β is the experimental heating rate ($1°C\ s^{-1}$). The pre-exponential (ν_d) for the desorption process is assumed to be $10^{-13} s^{-1}$ for all absorbates studied.

Aniline, a Lewis base was chosen to model the dye molecules. Phenol, a Lewis acid was used to model the phenolic base resin of between 8 and 25 repeating units. Aniline and phenol are interesting molecules in the field of polymer-metal interface chemistry: Aniline is the monomer for the conducting poly-aniline, and both molecules are subunits in poly-imides; in addition, phenolic groups are used as adhesion promotors, that is to improve adhesive bonding between organic films/substrates bonding [20]. Ethanol and methanol as weak acids were used to model the constituents of the phenolic resin. Methanol can be regarded as a model molecule well suited for surface chemistry studies because it is relatively simple and yet contains C-H, C-O and O-H bonds. Hexane is a simple saturated molecule with no functional groups: it is a good reference molecule against which other molecules with functional groups can be compared. Xylene was investigated to show the effect of aromaticity on adhesion compared to non-aromatic molecules such as hexane.

The experiments were carried out using TPD as previously described in chapter 4.

5.2 Desorption of Aniline from a NON PAT and STD PAT substrate

Three of the largest cracking fractions of aniline, m/q = 39, 66 and 93, the last being the parent ion, were followed during the dosing experiments illustrated in Figure 1. A typical desorption pattern from a NON PAT substrate is illustrated in Figure 2. Although the desorption of other fragments was not recorded, the respective intensities of the desorption signals for these indicate that the only product desorbing is aniline.

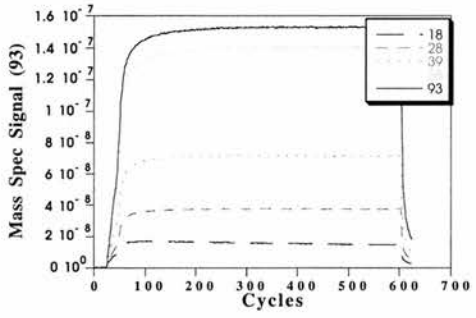

Figure 1. Integrated spectra of the principal cracking fractions of Aniline during dosing at $1.5x10^{-7}$mbar onto a NON PAT substrate.

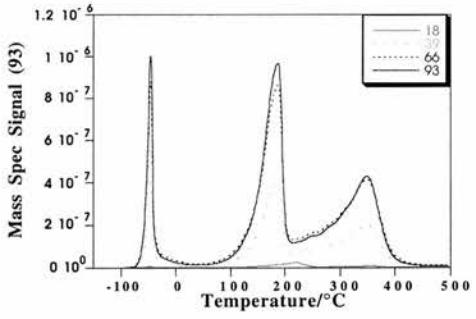

Figure 2. TPD spectra of Aniline from a NON PAT substrate.

The pertinent question concerning the chemical identity of aniline in the monolayer is whether the surface species consist of intact molecules or whether H abstraction occurs from the aniline. The latter process might be suspected on chemical grounds. Since no

water is observed on the surface, shown in Figure 2, it appears that no N-H bonds are broken.

5.2.1 TPD Analysis of Aniline Desorption

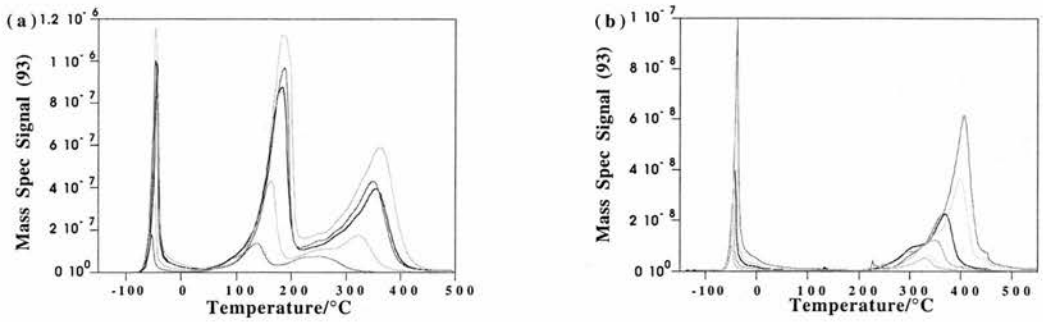

Figure 3. Desorption spectra of Aniline from (a) NON PAT and (b) STD PAT substrate as a function of exposure.

The parent ion 93 amu (atomic mass units), the strongest fragment in the cracking pattern of aniline was used to follow the desorption for both spectra. The first set of desorption peaks are known as the ice peak, extending from -60°C (60 $kJmol^{-1}$) to 0°C for both spectra. This region corresponds to the desorption of aniline ice. It does not give information on surface bonding. The ice peak maximum for both the NON PAT and STD PAT substrate increases in temperature in accordance to zero-order desorption kinetics, indicated by the common leading edge which is typical of the desorption of weakly-bound multilayers. The NON PAT spectrum reveals two broad, higher temperature desorption peaks starting at ~80°C (100 $kJmol^{-1}$) and 250°C increasing in exposure to ~350°C. The low temperature desorption peak at 80°C appears to follow first-order kinetics. It is difficult to assess the order of the high temperature desorption peak starting at 250°C. The two broad desorption peaks indicates aniline molecules are bound to the surface on two distinctly different adsorption sites. The shift of the spectra to a higher temperatures with increasing exposure suggests that the interaction between adjacent adsorbed aniline molecules is strong and attractive.

The STD PAT spectrum reveals only one high temperature desorption peak starting at 250°C (130 kJmol^{-1}) increasing in exposure to ~400°C and appears to follow first-order desorption kinetics. The shift of the spectra to higher temperatures with increasing exposure suggests that the intermolecular interactions are again strong and attractive. For both subtrates aniline is completely desorbed at around 500°C. The two spectra are very similar in appearance except that the NON PAT has an extra "intermediate" peak between ~100°C and 200°C. It would seem the PAT process has preferentially blocked the intermediate adsorption site on the STD PAT substrate.

5.3 Desorption of Phenol from a NON PAT and STD PAT substrate

Two of the largest cracking fractions of phenol exist at m/q = 66 and 94, the latter is the parent ion. Both were followed during the dosing experiments are shown in Figure 4. A typical desorption pattern from a NON PAT substrate is illustrated in Figure 5. Although the desorption of other fragments was not recorded, the respective intensities of the desorption signals for these indicates that the only product desorbing is phenol.

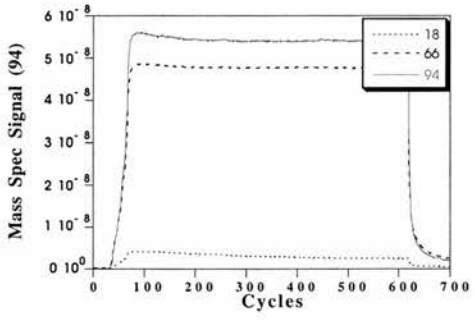

Figure 4. Integrated spectra of the principal cracking fractions of Phenol during dosing at 5.5x10^{-8} mbar onto a NON PAT substrate.

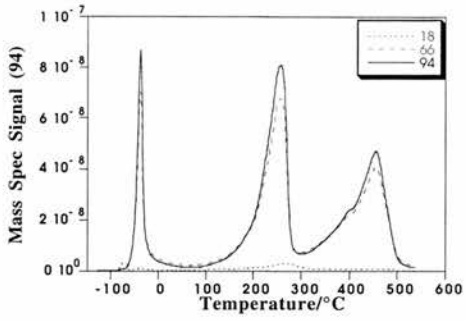

Figure 5. TPD spectra of Phenol on NON PAT substrate.

5.3.1 TPD Analysis of Phenol Desorption

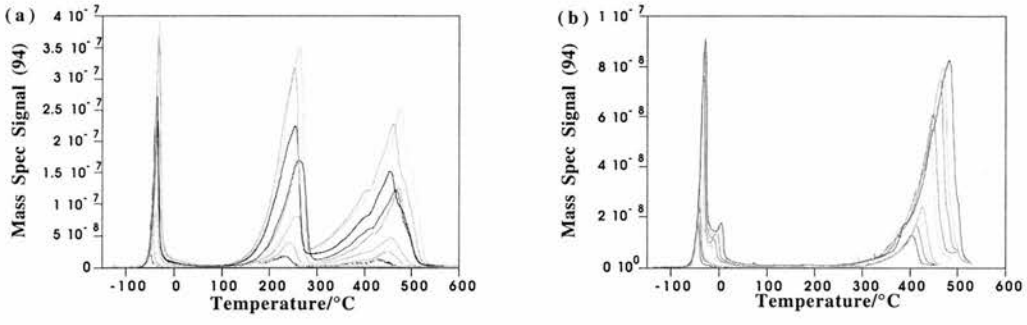

Figure 6. Desorption spectra of Phenol from (a) NON PAT and (b) STD PAT substrate as a function of exposure.

The parent ion 94 amu, the strongest fragment in the cracking pattern of phenol was used to follow the desorption for both spectra. The ice peak temperature for both substrates extends from -60°C (60 kJmol^{-1}) to 0°C. The peak maximum increases in temperature in accordance to zero-order desorption kinetics, indicated by the common leading edge. The NON PAT spectrum reveals two broad higher temperature desorption states starting at 150°C (120 kJmol^{-1}) and 350°C (170 kJmol^{-1}). The presence of the two higher desorption peaks indicates phenol molecules are bound to the surface on two distinctly different adsorption states. The high temperature desorption peak arises from chemisorbed phenol. The symmetric peak shape about T_{max} and its shift to lower temperature with increasing exposure suggest that the desorption process is governed by

second order kinetics, while the low temperature peak shifts to higher temperatures with increasing exposure suggests that the process is governed by first order kinetics and assuming interaction between adjacent adsorbed phenol molecules is strong and attractive. The STD PAT spectrum reveals one high temperature broad desorption peak at 350°C (200 $kJmol^{-1}$). The desorption temperature of this state increases with exposure and appears to follow first order desorption kinetics. The shift of the spectra to higher temperatures with increasing exposure suggests that the intermolecular interactions are again strong and attractive. For both substrates, desorption is completed around 510°C. The two spectra are very similar in appearance except that the NON PAT has an extra "intermediate" peak between 100°C and 300°C. It would seem the PAT process has preferentially blocked the intermediate adsorption site on the STD PAT substrate. Aniline and phenol show very similar desorption spectra. However, the desorption temperatures for phenol are slightly higher than those of aniline desorption.

In terms of reactivity, phenol is more reactive than aniline, which may explain the higher desorption energies for phenol. The hydrogen bonding ability is in general, greater than that of amines. An indication of the increased hydrogen bonding in phenol is its melting point of 41°C, while aniline melts at -5°C, even though the molecular weight of aniline is similar to that of phenol. It would seem from both aniline and phenol desorption that the PAT process has preferentially blocked the intermediate adsorption site on the STD PAT substrate.

5.4 Desorption of Ethanol from NON PAT and STD PAT substrate

Two of the largest cracking fractions of ethanol are m/q = 31and 45, with the mass 31 being the parent ion, were followed during the dosing experiments, illustrated in Figure 7. A typical desorption spectrum from a NON PAT surface is illustrated in Figure 8.

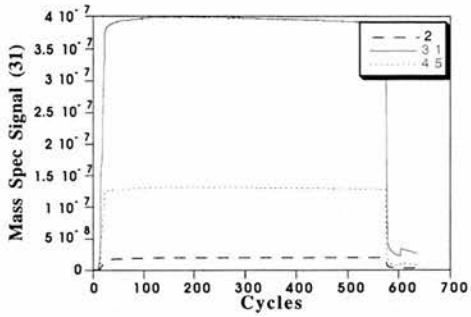

Figure 7. Integrated spectra of the principle cracking fractions of Ethanol during dosing at $4x10^{-7}$ mbar onto a NON PAT substrate.

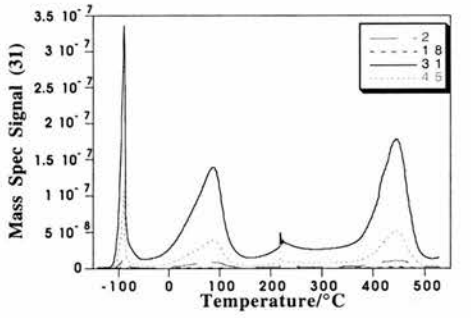

Figure 8. TPD spectra of Ethanol from a NON PAT substrate.

5.4.1 TPD Analysis of Ethanol Desorption

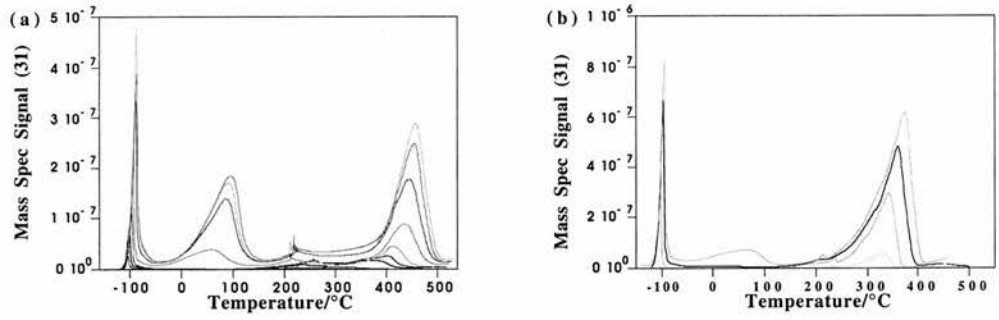

Figure 9. Desorption spectra of Ethanol from (a) NON PAT and (b) STD PAT substrate as a function of exposure.

The parent ion 31amu, the strongest fragment in the cracking pattern of ethanol was used to follow the desorption of ethanol. The ice peak for both substrates starts at -110°C (50 $kJmol^{-1}$). The NON PAT spectrum shows a low temperature desorption peak starting at 20°C and high temperature desorption peak starting at 400°C. The symmetric peak shape about T_{max} suggest that the desorption process is governed by first order kinetics and its shift to higher temperature with increasing exposure. The ethanol, detected in the TPD spectra, can only be the result of non-dissociative (molecular) adsorbed ethanol, desorbing from two different molecular adsorption states on the surface. The shift of the spectra to a higher temperature with increasing exposures suggests that the interactions between adsorbed ethanol are attractive. The two broad desorption peaks indicates ethanol molecules are bound to the surface on two distinctly different adsorption sites. The shift of the spectra to higher temperatures with increasing exposure suggests that the interaction between adjacent adsorbed ethanol molecules is strong and attractive. An attractive interaction could be due to the hydrogen bonding between adsorbed ethanol molecules.

The STD PAT spectrum reveals only one desorption peak starting at 250°C (150 $kJmol^{-1}$). The shift of the spectra to a higher temperatures with increasing exposure suggest that the interaction between adjacent adsorbed ethanol are strong and attractive. The shape of the curve again represents first-order desorption kinetics. It would seem the PAT process has preferentially blocked the intermediate adsorption site on the STD PAT substrate.

5.5 Desorption of Methanol from a NON PAT and STD PAT substrate

Three of the largest cracking fractions of methanol are m/q = 30, 31 and 32, with mass 31 being the parent ion, were followed during the dosing experiments, illustrated in Figure 10. A typical desorption pattern from a STD PAT substrate is illustrated in Figure 11. Although the desorption of other fragments was not recorded, the respective intensities of the desorption signals for these indicates that the only product desorbing is methanol.

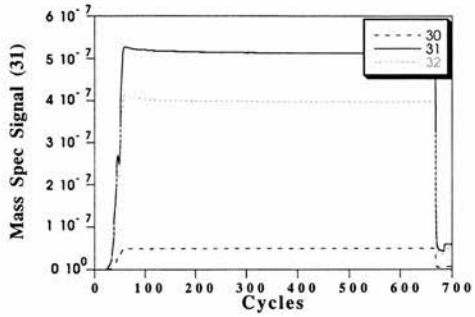

Figure 10. Integrated spectra of the principal cracking fractions of Methanol during dosing at $5x10^{-7}$ mbar onto a STD PAT substrate.

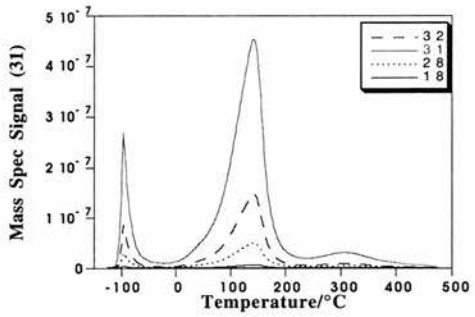

Figure 11. TPD spectra of Methanol on STD PAT substrate.

5.5.1 TPD Analysis of Methanol Desorption

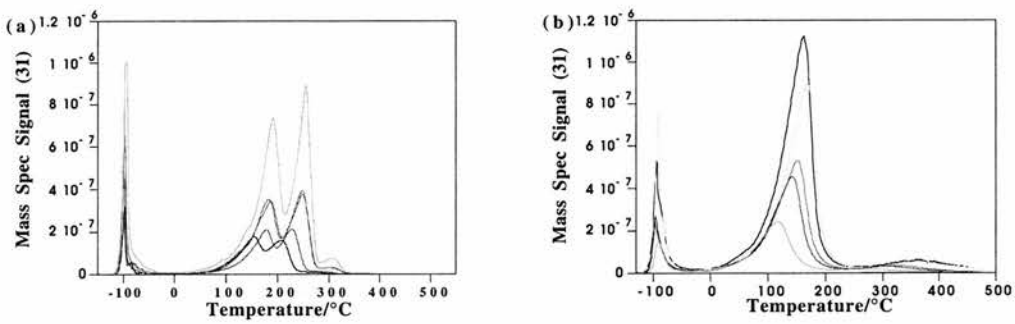

Figure 12. Desorption spectra of Methanol from (a) NON PAT and (b) STD PAT substrate as a function of exposure.

The parent ion 31 amu, the strongest fragment in the cracking pattern of methanol was used to follow the desorption of methanol. The ice peak maxima for STD PAT and NON PAT started at -110°C (50 $kJmol^{-1}$). The NON PAT spectrum reveals two higher temperature desorption peaks starting at ~100°C (100 $kJmol^{-1}$) and another starting at ~200°C (130 $kJmol^{-1}$). The peak maximum for both of these states increases with exposure. The shift of the spectra to a higher temperatures with increasing exposure suggest that the interaction between adjacent adsorbed methanol are attractive. It is difficult to assess the order of the reaction for the two higher desorption states.

The STD PAT spectrum reveals only one broad high temperature desorption peak, starting at ~50°C (70 $kJmol^{-1}$) extending to ~150°C and increasing with exposure; it appears to follow first-order desorption kinetics.

Ethanol and methanol shows very different TPD spectra. From the results gathered on previous molecules it is assumed the PAT process would preferentially block the intermediate adsorption site on the STD PAT substrate. However, with methanol this is not the case.

5.6 Desorption of Xylene from a NON PAT and STD PAT substrate

Two of the largest cracking fractions of ethanol are xylene, m/q = 91 and 106, with mass 91 being the parent ion, were followed during the dosing experiments, illustrated in Figure 13. A typical desorption pattern from a STD PAT substrate is illustrated in Figure 14. Although the desorption of other fragments was not recorded, the respective intensities of the desorption signals for these indicates that the only product desorbing is xylene.

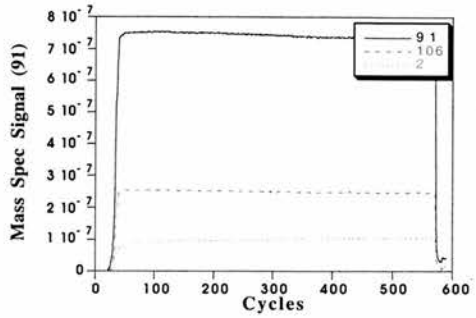

Figure 13. Integrated spectra of the principal cracking fractions of Xylene during dosing at $7.5x10^{-7}$ mbar onto a STD PAT substrate.

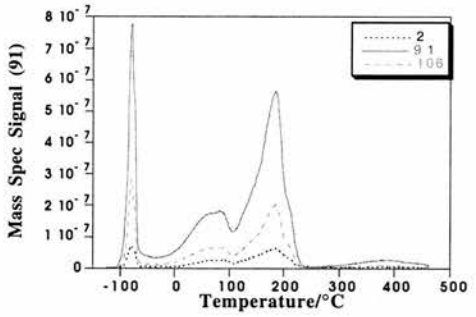

Figure 14. TPD spectra of Xylene from a STD PAT substrate.

5.6.1 TPD Analysis of Xylene Desorption

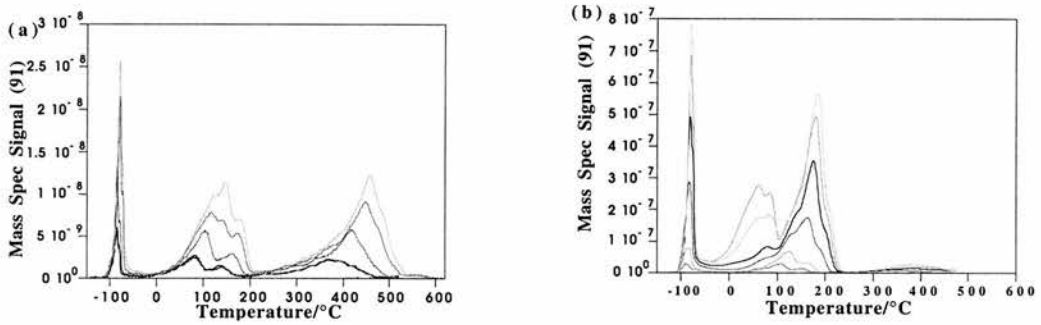

Figure 15. Desorption spectra of Xylene from (a) NON PAT and (b) STD PAT substrate as a function of exposure.

The parent ion 91amu, the strongest cracking fragment in the cracking pattern of xylene, was used to follow the desorption for both spectra. Both spectra shows an ice peak temperature starting at -100°C (50 $kJmol^{-1}$). The NON PAT sample shows two broad higher temperature desorption peaks starting at around 50°C and 350°C increasing in exposure to 450°C. The low temperature peak at 0°C shows multiple desorption states increasing with exposure. The STD PAT shows two high temperature desorption peak starting at 0°C and 100°C increasing in exposure. It is difficult from the above spectra to determine the order of the peaks. It seems xylene is more strongly bonded to the STD PAT than the NON PAT substrate.

5.7 Desorption of Hexane from a NON PAT and STD PAT substrate

Two of the largest cracking fractions of hexane m/q = 43 and 57, the last being the parent ion, were followed during the dosing experiments are shown in Figure 16. A typical desorption pattern from a STD PAT substrate is illustrated in Figure 17. Although the desorption of other fragments was not recorded, the respective intensities of the desorption signals for these indicates that the only product desorbing is hexane.

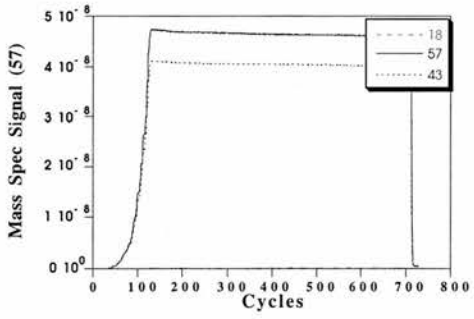

Figure 16. Integrated spectra of the principal cracking fractions of Hexane during dosing at $5x10^{-8}$ mbar onto a STD PAT substrate.

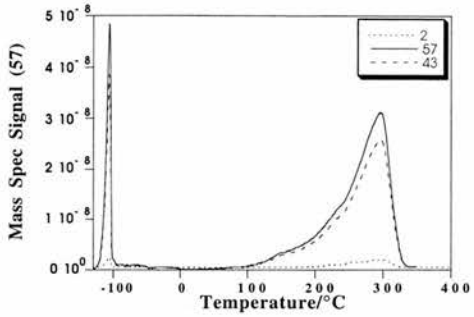

Figure 17. TPD spectra of Hexane on STD PAT substrate.

5.7.1 TPD Analysis of Hexane Desorption

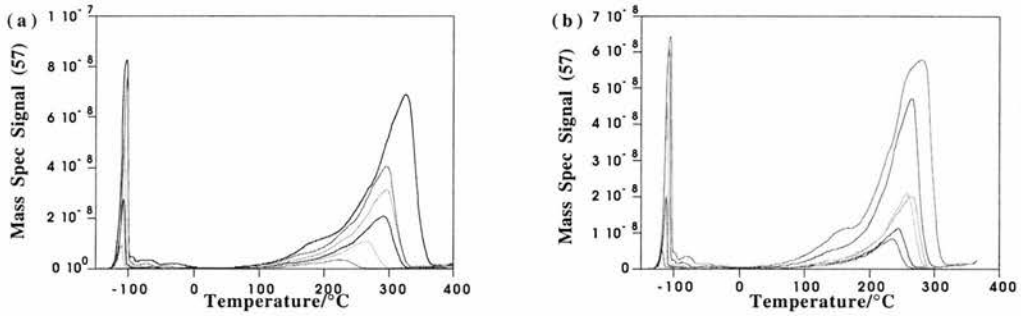

Figure 18. Desorption spectra of Hexane from (a) NON PAT and (b) STD PAT substrate as a function of exposure.

The parent mass 57 amu, the strongest cracking fraction in the cracking pattern of hexane, was used to follow the desorption for both spectra. The ice peak temperature for both substrates starts at -110°C (50 kJ mol^{-1}). The NON PAT and STD PAT spectra reveal only one broad high temperature desorption peak starting at 150°C (100 $kJmol^{-1}$) increasing in exposure. On both substrates hexane is completely desorbed at around 300-350°C. The absence of an intermediate peak is common in both substrates. Hexane is an unlikely molecule to distinguish bewteen NON PAT and STD PAT.

Table 1. Showing desorption temperatures of the organic probe molecules from a NON PAT substrate.

Probe Molecule	Peaks	Ice Peak/°C	Peak 1 Desorption/°C	Peak 2 Desorption/°C
Aniline	3	-60	80	250
Phenol	3	-60	150	350
Methanol	3	-110	100	200
Ethanol	3	-110	20	400
Xylene	3	-100	50	350
Hexane	2	-120	150	-

Table 2. Showing desorption temperatures of the organic probe molecules from a STD PAT substrate.

Probe Molecule	Peaks	Ice Peak/°C	Peak 1 Desorption/°C	Peak 2 Desorption/°C
Aniline	2	-60	-	250
Phenol	2	-60	-	350
Methanol	2	-110	50	-
Ethanol	2	-110	-	250
Xylene	3	-100	0	100
Hexane	2	-120	150	-

5.8 Comparing Phenol uptake ratio for NON PAT and STD PAT substrates

Each surface was exposed to a well defined pressures of organic vapour. This was determined by the integration of the area under the parent mass dose curve. Similarly, the amount of organic vapour desorbing during thermal desorption, was determined by the integration of the area under the parent mass thermal desorption spectra. From this it is possible to gain a measure of the amount of molecules actually adsorbed on the surface. Combination of these two integrals leads to a crude measure of the relative uptake ratios (sticking probability) for each organic probe molecule.

The uptake ratio can be defined as, the probability of a molecule being adsorbed after a collision with the surface. This is determined by (i) the presence of active sites on the surface, (ii) the orientation of the molecule when approaching the surface, (iii) the surface temperature, (iv) surface coverage, (v) translational/rotational energies etc. Figure 19. illustrates the relative uptake ratio of phenol on a STD PAT and NON PAT substrate. This suggest a constant uptake ratio with coverage.

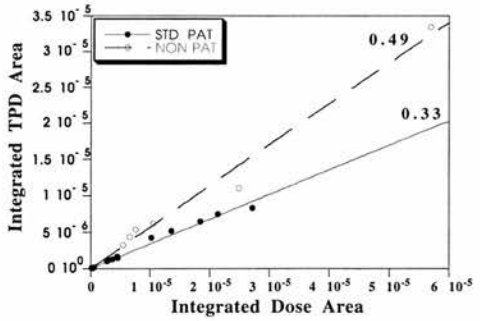

Figure 19. Shows a plot of TPD area against dose area for a STD PAT and NON PAT substrate, illustrating the relative uptake ratio (sticking probability) of Phenol.

Given an equivalent phenol exposure both the NON PAT and STD PAT adsorb different quantities of phenol. Phenol has an average uptake ratio of 0.49 on NON PAT and 0.33 on STD PAT. This is further illustrated in Table 3. showing the uptake ratios for different

organic probe molecules on the NON PAT and STD PAT substrate.

Table 3. Relative uptake ratios for the organic molecules of STD PAT and NON PAT substrate.

Probe Molecule	Uptake Ratio (%) for NON PAT	Uptake Ratio (%) for STD PAT
Aniline	0.49	0.32
Phenol	0.49	0.33
Ethanol	0.42	0.40
Methanol	0.43	0.36
Hexane	0.38	0.35
Xylene	0.48	0.38

The higher percentage of probe molecules adsorbed onto the surface of a NON PAT, may be due to the substrate having a large surface area which has been discussed in chapter 5, and as a result of this there is an increase in interfacial interaction (active sites). When a molecule interacts with a surface, prior to bonding, it can be mobile across the surface. It may be trapped by the surface but, it can diffuse (hop) across it until it reaches a more reactive site with which it bonds, either as an intact molecule or as a dissociate species. Under normal circumstances, if a surface has several different binding sites, the most energetically favourable is occupied first (i.e. highest adsorption potential according to a Boltzmann distribution of their binding energies), diffusion permitting, followed by the next favourite. Equilibrium is attained by: (i) the preferential desorption of the molecules from sites of low adsorption potential and their subsequent random re-adsorption at unoccupied sites having a wide range of binding energies; and (ii) the migration of molecules from lower range and subsequent capture at an unoccupied site having the highest adsorption potential.

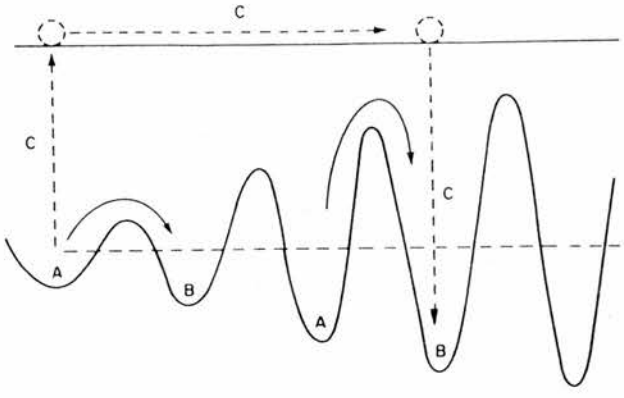

Figure 20. Establishment of adsorption equilibrium on a surface. A. Initial random occupation; B. Migration of a molecule to sites of higher adsorption; C. Desorption from a lower energy site and subsequent random adsorption at an unoccupied higher energy site.

5.9 Discussion

The thermal-desorption spectrum reflects the binding energy of the adsorbed species. Because its value and, therefore, the heats of adsorption may change from site to site on the surface, TPD can be used as a "fingerprint" of the surface structure. The spectra can be split into two distinct regions. The first desorption state, is centred at temperatures of -110°C/-60°C indicating only a weakly bound adsorption state. The abrupt leading edge of this peak and its narrow width suggest a zero order desorption process which is typical of the desorption of weakly bound multilayers. The ice peak kinetics is also characterised by a peak maximum temperature which shifts gradually to higher temperatures as the exposure was increased. As the temperature of the sample is increased the next most weakly bound states desorb, followed by the next most. By contrast the multilayer peak does not saturate with increasing exposure because, in theory, there can be an infinite number of layers which will continue to grow in a process analogous to condensation, as long as dosing continues. The bonding energy, and therefore the desorption temperature, of molecules bonded directly to the substrate will be greater than that of the multilayers.

As more molecules adsorb onto the surface, they not only form an interaction with the substrate, but they interact with neighbouring molecules. If this interaction is attractive, then more energy is required to remove them from the surface, because both the surface/adsorbate and the adsorbate/adsorbate interactions have to be broken. Therefore, the features in the spectra shift to higher temperatures with increasing exposure. Aniline and Phenol TPD spectra shows similar forms but important differences. The chemical identity of aniline and phenol in the chemisorbed state is uncertain. However, since no water is observed on the surface, shown in Figures 2 and 5. it appears that no N-H and O-H bonds are broken and we can assume aniline and phenol molecules follows path (i) and remains intact on the surface. The NON PAT substrate shows an intermediate peak moving to higher temperatures with increasing exposure. The STD PAT doesn't show the presence of the intermediate peak and it would seem the PAT process has preferentially blocked the intermediate site in the STD PAT substrate.

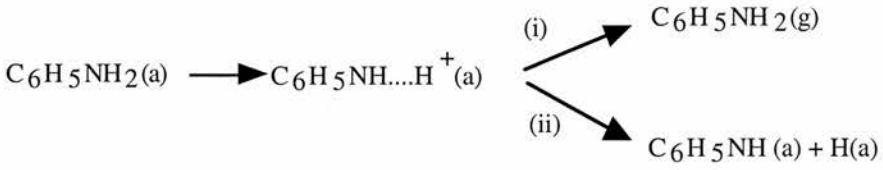

The interaction of the aniline and phenol with a metal oxide surfaces is governed by the chemistry of the benzene ring and the lone pair of electrons on the amine and hydroxyl group. The behaviour of benzene and amine can be used to predict how the aniline might interact. Benzene is known to chemisorb onto metal surfaces [21,22] in a parallel configuration; illustrated in Figure 21. It is bound via interaction between the π-orbitals of the ring and orbitals of the surface metal atoms or the lone pair of electrons from the nitrogen group. Aniline has a gas-phase basicity of 203 kcal/mol [23] and is also a good Lewis base. For gas-phase aniline, the angle between the plane of the -NH_2 group and the plane containing the aromatic ring is 37.5° [24]. The angle between the lone pair

electrons and direction of the π^* orbitals (perpendicular to the ring) is then approximately 19° ($1/2$ of 37.5°). If the lone pair were directed towards the surface and completely responsible for orientating the molecule, the tilt angle would be 19°. However, the van der Waals repulsion between adjacent rings and the attractive interaction of the lone pair with the surface may explain the greater tilt angle. For gas-phase phenol the -OH group lies in a plane with the aromatic ring [25]. The lone pair is, therefore, also contained in the ring, and would not orient the ring on the surface in the observed fashion. However, the hydrogen bonding ability of alcohols is in general greater than that of the amines. The heat of vaporisation of phenol is 11.89 kcal/mol which is slightly higher than aniline which has a heat of vaporisation of 11.30 kcal/mol [26]. The crystal structure of phenol is bound together by hydrogen bonds between the oxygen atoms [27]. Therefore, the intermolecular bonds between phenol molecules are significant in the ordering the structure.

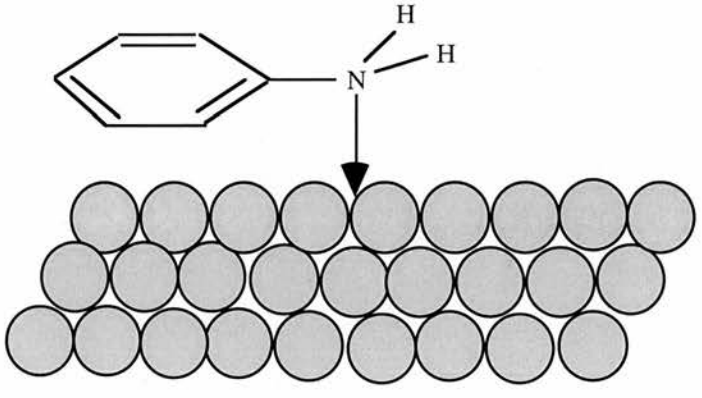

Figure 21. The interaction of aniline with a metal surface.

Alumina surfaces contains various kinds of surface sites including Lewis acid sites (coordinatively unsaturated aluminium atoms), associated basic Al-O sites and at least five kinds of surface hydroxyl groups. However, concerning the amine base interaction on the surface, the Lewis acid sites are the most important adsorption centres. A model devised [28] to represent the tetrahedral and octahedral Lewis acid sites on a spirel type aluminium

oxide is illustrated in Figure 21. The models T1 and T2 represent the tetrahedral coordination of the aluminium atoms and models O1 and O2 the octahedral coordination.

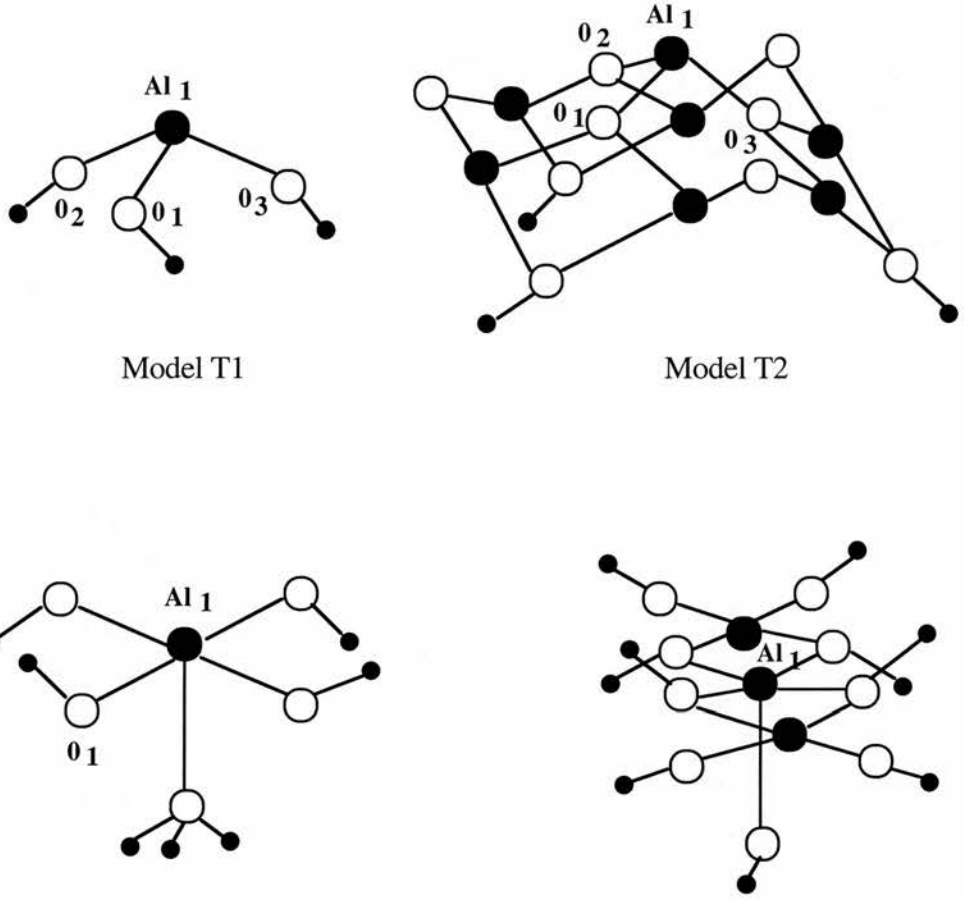

Figure 21. Cluster models for the tetrahedral (T1, T2) and octahedral (O1 and O1) Lewis acid sites on aluminium oxide surfaces. The tetrahedral sites have a larger Lewis acidity than the octahedral sites and the adsorption of ammonia shows higher interaction energies with the tetrahedral sites [28].

The ethanol desorption spectra on NON PAT and STD PAT is similar to aniline and phenol desorption. The intermediate peak shown in the NON PAT is absent in the STD PAT substrate and it would seem the PAT process has again preferentially blocked the intermediate adsorption site on the STD PAT substrate.

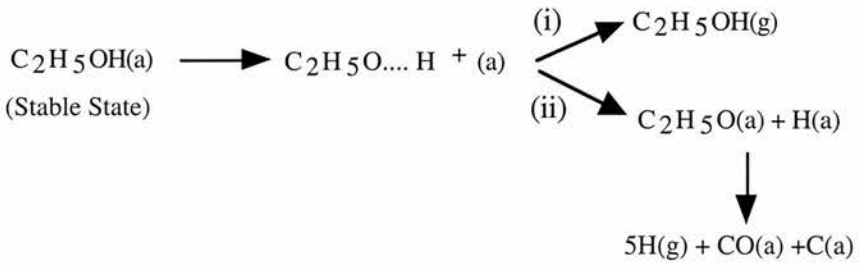

Ethanol absorbs molecularly through its hydroxyl group via its oxygen atom, with the lone pair electrons involved in the process. The shift of the spectra to a higher temperature with increasing exposures suggests that the interactions between adsorbed ethanol molecules are attractive. An attractive interaction could be due to the hydrogen bond between adsorbed ethanol molecules.

Methanol interaction with metal surfaces has been the subject to several studies. An interesting characteristic of this interaction is that it produces a very stable methoxy species on Cu (110) [29], Ag (110) [30] and Ag(110) [31]. The interaction of methanol with Ru (001) had shown two reaction pathways for dissociation. In the first, the O-H is split and methoxy species are formed. In the second C-O bond cleavage ultimately produce water, hydrogen and surface carbon. The methoxy species, identified as intermediates of the first reaction channel, are found to be orientated perpendicularly to the surface. Upon heating of the surface the methoxy recombines with hydrogen and desorbs as methanol shown in Figure 22.

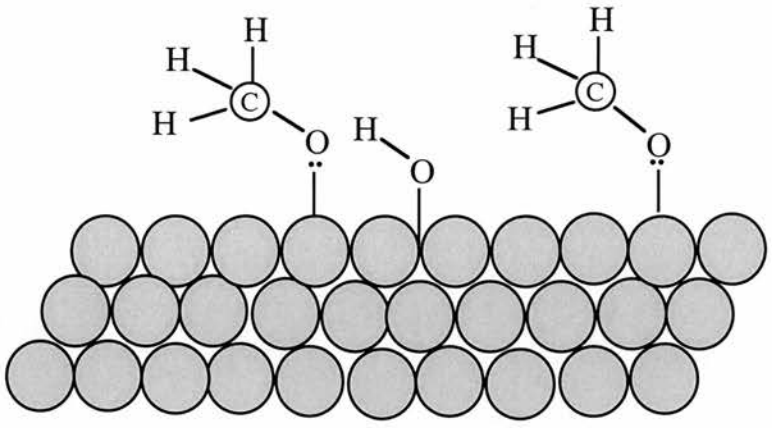

Figure 22. Schematic representation of the reaction of methanol with a metal oxide surface.

Hexane is an unlikely molecule to determine the difference between STD PAT and NON PAT. The adsorption bond strength of saturated alkane molecules on metal surfaces is weak and the interactions barely exceed those of physisorptive coupling. This was previously recognised in the early IR study of ethane on Cu (110) by Horn and Prichard [32], and confirmed more recently by Chesters [33] for ethane on Cu (111) using RAIRS. In both studies it was concluded that the molecules physisorbed in the first monolayer are arranged with the C-C bond parallel to the surface. The monolayers of normal alkanes C_3 to C_8 on Pt (111) have been investigated by LEED by Firment and Somorjai [34], and a number of ordered LEED structures has been observed. Some of the molecules grow epitaxially on top of the ordered monolayers to form organic crystals. These multilayers structures were found to be very sensitive to electron beam damage, much more than the molecular monolayers [34]. The adsorption of n-alkanes from n-butane to n-decane on Cu (100) has been studied by Sexton and Hughes [35]. The heats of adsorption were estimated from the thermal desorption peak temperatures, and values comparable to the heats of sublimation were obtained. From this it was concluded that the alkanes are physisorbed in their monolayer phases. The NEXAFS spectra of ethane on Cu (100) and Ag (100) [36,37] are also consistent with weak adsorption in that the

molecular σ^* resonance occured at the same energy on both substrates as in the gas phase, thus indicating no alteration of the C-C bond. The structures of adsorbed alkanes are therefore essentially true replicas of their molecular structures in the gas phase, and their arrangement at metal surfaces is presumably governed by packing density effects rather than molecular-surface interactions. The first xylene molecules to diffuse into the pores are generally the last to finally desorb because they have the opportunity to diffuse the farthest and hence have a greater distance travel to ultimately desorb. Clearly this simple minded model does not explain the multi-peaked nature of the high temperature features. This probably is determined by the strength of the interaction of the molecules with the solid surface of the pore. Multiple binding sites give rise to multiple peaks.

Comparing this work with zeolites porous channels of ZSM-11 which gives rise to two types of porous intersection. One has the same volume as those in ZSM-5, while the other has a volume which is 30% greater [38]. The kinetic size of m-xylene (6.8 Å) appears to be too large to penetrate the channels (5.2-5.5 Å). It has been suggested that the molecule enters the zeolite pores by undergoing isomerisation to the smaller para isomer. Such processes occur on the crystal outer surface site [39]. Alternatively, via steric juggling or by being compressed by the steric field experienced within the pore network, m-xylene invades the zeolite pore system [40].

It can be seen in Figure 23. that transition state A cannot "fit" in the channels and so this precludes the production of molecules arising from scission of this transition state. On the other hand transition state B can be accommodated within the pores and so its breakdown products are the ones which form. Shape selectivity can be induced by altering other zeolite parameters for instance crystalline size variation. Larger crystals provide longer diffusion path lengths and this can be used to modify catalysis product because product selectivity is a function of a diffusion-limited process.

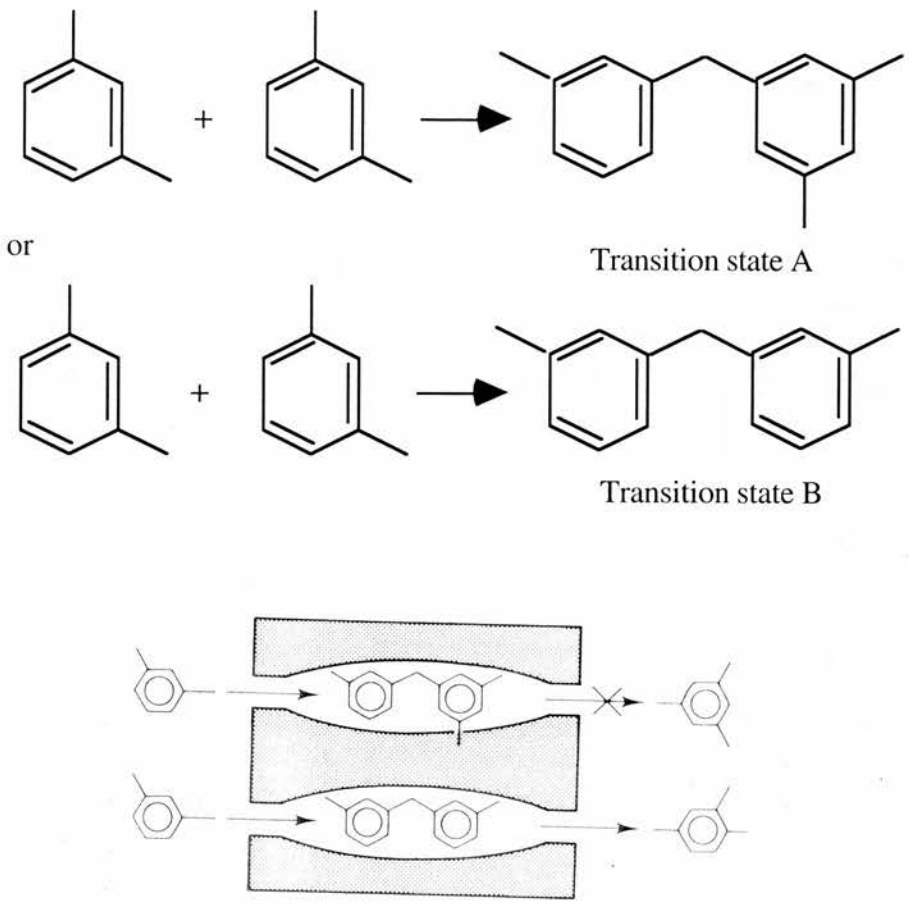

Figure 23. Transition state shape selectivity in zeolite channels [41].

Table 4. Showing differences of the probe molecules on NON PAT and STD PAT substrate.

Organic Molecule	NON PAT	STD PAT
Aniline	Ice Peak temperature starting at -60°C. Two desorption states at 80°C and 250°C moving to higher temperature for a given exposure	Ice Peak temperature starting at -60°C. One desorption state at 250°C moving to higher temperature for a given exposure
Phenol	Ice Peak temperature starting at -60°C. Two desorption states at 150°C and 350°C moving to higher temperature for a given exposure	Ice Peak temperature starting at -60°C. One desorption states at 350°C moving to higher temperature for a given exposure
Ethanol	Ice Peak temperature starting at -110°C. Two desorption states at 20°C and 400°C moving to higher temperature for a given exposure	Ice Peak temperature starting at -110°C. One desorption state at 250°C moving to higher temperature for a given exposure
Methanol	Ice Peak temperature starting at -110°C. Two desorption states at 100°C and 200°C moving to higher temperature for a given exposure	Ice Peak temperature starting at -110°C. One desorption state at 50°C moving to higher temperature for a given exposure
Xylene	Ice Peak temperature starting at -100°C. Two desorption states at 50°C and 350°C moving to higher temperature for a given exposure	Ice Peak temperature starting at -100°C. Two desorption states at 0°C and 100°C moving to higher temperature for a given exposure
Hexane	Ice Peak temperature starting at -120°C. One desorption state at 150°C moving to higher temperature for a given exposure	Ice Peak temperature starting at -120°C. One desorption state at 150°C moving to higher temperature for a given exposure

Aniline and Phenol (aromatic molecules) proved to be the most favoured probe molecules showing very similar but different TPD spectra. This is further investigated in chapter 6. on a range of aluminium oxide substrates prepared under controlled conditions to determine the desorption peaks in relation to the change in the substrate morphology.

5.10 References

[1] V.E.Henrich and P.A.Cox, The Surface Science of Metal Oxides, Cambridge University Press (1994).

[2] H.J.Freund and E.Umbach (Fds), Adsorption on ordered surfaces of ionic solids and thin films, Surf.Sci., **33** (1993).

[3] H.H.Kung, Transition Metal Oxide: Surface Chemistry and Catalysis (1989).

[4] A.A.Davidov, Infrared Spectroscopy of Adsorbed Species on the Surface of Transition Metal Oxide (1990).

[5] H.J.Freund, H.Kuhlenbeck and V.Staemmler, Rep.Prog.Phys., in press.

[6] H.J.Freund, Ber.Bunsenges, Phys.Chem., (1995).

[7] M.C.Wu and P.J.Moller, Surf.Sci., **221** (1989) 250; P.J.Moller and M.C.Wu, Surf.Sci., 224 (1989) 265; M.C.Wu and P.J.Moller, Surf.Sci., **235** (1990) 228.

[8] P.J.Moller and J.Nerlov, Surf.Sci., **307-309** (1993) 591.

[9] P.W.Murry, F.M.Leibsle, H.J.Fischer, C.F.J.Flipse, C.A.Muryn and G.Thornton, Phys.Rev.B, **46** (1992) 12877.

[10] N.G.Condon, P.W.Murrey, F.M.Leibsle, G.Thornton, A.R.Lemic and D.J.Vanghan, Surf.Sci., **310** (1994) L609.

[11] W.Gopel, Progr.Surf.Sci., **20** (1985) 9.

[12] W.Gopel, J.A.Anderson, D.Frenkel, M.Jaehnig, K.Philips, J.A.Schafer and G.Rocker, Surf.Sci., **139** (1984) 333.

[13] (a) M.Ch.Wu, C.A.Estrada and D.W.Goodman, Phy.Rev.Lett., **67** (1991); (b) M.Ch.Wu, Ch.Truong and D.W.Goodman, In Adsorption on Ordered Surfaces of Ionic Solids and Thin Film, H.J.Freund and E.Umbach, Surf.Sci., **33** (1993).

[14] P.J.Chen and D.W.Goodman, Surf.Sci.Lett., **312** (1994) L767.

[15] (a) L.Marchese, S.Coluccia, G.Martra and A.Zecchina, Surf.Sci., **269** (1992) 135.

[16] (a) M.I.Zaki and H.Knozinger, J.Catal., **119** (1989) 311; (b) G.Mestl, H.Knozinger and J.H.Lundsford, Ber.Bunsenges, Phy.Chem., **97** (1993) 319.

[17] W.Weiss, A. Barbieri, M.A.van Hove and G.A.Somorjai, Phys. Rev. Lett., **71** (1993) 1848.

[18] A.Barbieri, W.Weiss, M.A.van Hove and G.A.Somorjai, Surf.Sci., **302** (1994) 259.

[19] G.A.Somorjai, Introduction to Surface Chemistry and Catalysis, Wiley, New York (1994).

[20] J.Robins, In Structural Adhesives: Chemistry and Technology, Plenum, New York (1986).

[21] J.C.Bertolini, G.Dalamai-imelik, and J.Rousseau, Benzene adsorption on nickel (100) and (111) faces studied by LEED and High Resolution Electron Energy Loss Spectroscopy. Surf.Sci., **67** (1977) 478.

[22] F.P.Netzer and M.G.Ramsey, Structure and orientation of organic molecules on metal surfaces. Crit.Rev.Sol.St.Mat.Sci., **17** (1992) 397.

[23] D.H.Aue and M.T.Bowers, in: Gas Phase Ion Chemistry, Vol. 2, Ed. M.T.Bowers Academic Press, New York (1979) p.1.

[24] D.G.Lister, J.K.Tyler, J.H.Hog and N.W.Larsen, J.Mol.Struct., **23** (1974) 253.

[25] N.W.Larsen, J.Mol.Struct., **51** (1979) 175.

[26] R.C.Weast and M.L.Astle, Eds., CRC Handbook of Chemistry and Physics, 60t ed. CRS Press, Boca Raton, (1979) p.E-32.

[27] R.W.G.Wyckoff, Crystal Structures, 2nd ed., Vol.6, Wiley, New York, (1969) p.14.

[28] P.Hirva and T.A.Pakkanen, Surf.Sci., **227** (1992) 389.

[29] B.A.Sexton, Surf.Sci., **88** (1978) 531.

[30] B.A.Sexton, A.E.Hughes and N.R.Avery, Surf.Sci., **155** (1985) 366.

[31] I.E.Wachs and R.J.Madix, Appl.Surf.Sci., **1** (1978) 303.

[32] K.Horn, and J.Pritchard, Surf.Sci., **52** (1975) 437.

[33] M.A.Chesters, In Analytical Applications of Spectroscopy, C.S.Creaser, and

A.M.C.Davis, Eds., Royal Society of Chemistry, London, (1988) 201.

[34] L.E.Firment and G.A.Somorjai, J.Chem Phys., **66** (1977) 2901.

[35] B.A.Sexton and A.E.Hughes, Surf.Sci., **140** (1984) 227.

[36] D.Arvanitis, K.Baberschke, L.Wenzel and U.Dobler, Phys.Rev.Lett., **57** (1986) 3175.

[37] D.Arvanitis, U.Dobler, L.Wenzel, K.Baberschke, Surf.Sci, **178** (1986) 686.

[38] O.Terasaki, J.M.Thomas and S.Ramdas, J.Chem.Soc.Chem.Commun., **216** (1984).

[39] D.H.Olson and W.O.Hagg in Catalytic Materials:Relationship Between Structure and Reactivity, (Eds. Whyte, Dalla Betta, Derouane and Baker) ACS Sym. **248** (1983) 275.

[40] L.V.C.Rees and J.Dwyer, Chem.Ind., **7** (1984) 252-269.

[41] Csicsery.S.M, Chemistry in Britain (1985) 475.

Chapter 6

A study of the adsorption of Aniline and Phenol on aluminium oxide thin film prepared under controlled conditions

The adsorption of simple organic molecules onto aluminium oxide surfaces discussed in the proceeding chapter produced some interesting results, especially with aniline and phenol. In this chapter aniline and phenol are used as probe molecules to investigate a range of aluminium oxide substrates produced at different stages of the preparation of lithographic printing plates.

6.1 Introduction

In this work, several approaches to the preparation of aluminium oxide surfaces were taken. The substrates are maintained under clean conditions to prevent contamination. The results in this chapter describe an investigation of anodic film growth on aluminium under controlled conditions in sulphuric acid at 40°C. At this temperature and under anodic polarisation, aluminium develops a duplex morphology, comprising of an inner barrier film, and an overlaying porous layer. This relates to developing an understanding of the key processes in the manufacture of lithographic printing plates, namely electrograining and anodising. A set of experiments is presented whose aim was to explore the adhesive properties of the overlaying porous layer. Other methods contained in this chapter relate to identifying changes in the observed film morphologies of each substrate, using SEM and attempting to explain these observations in terms of the fundamental processes involved. Energy Dispersive Analysis of X-rays (EDX) and Surface Mapping was used to determine the composition of individual particles on each substrate. Optical Microscopy was also used to illustrate the retention of the organic photo-coating on each sample.

Following anodising, the aluminium was immersed in the post anodic treatment bath. It is natural therefore, that the action of the PAT on the anodic film and its implications for the adhesion between substrate and photocoat is considered.

6.2 Sample Preparation

All samples were prepared using an electrolyte cell designed to simulate the conditions encountered on commercial pretreatment lines. In the experiments, use was made of four 4 litre polypropylene electrochemical cells, as shown schematically in Figure 1. In all cases, the working electrode was positioned adjacent to the counter (graphite) electrode at a distance of 1 cm. All the samples were treated at constant current density using a d.c. power supply, illustrated in Figure 2. and the current was monitored using a potentiostat.

6.3 Experimental Procedure

Initially, the aluminium printing plate received was immersed in an caustic solution to remove any impurities on the surface such as oil and dust. The plate was then rinsed with water and allowed to dry in air. The first cell simulates the graining process *(Electrograining)*. Electrograining was carried out in a HCl solution at a specific temperature and dwell time. The HCl solution is very aggressive towards aluminium and causes local breakdown of the protective oxide layer. The aluminium surface exposed to the HCl solution begins to dissolve at the breakdown sites, pits start to evolve uniformly across the surface. The second cell simulates the electrochemical process and this was carried out in an H_2SO_4 solution. This process promotes the removal of corrosion products remaining on the plate after electrograining. This has little to no effect on the substrate itself, the aluminium plate is passive when negatively polarised, and therefore the morphology remains undisturbed during this process. The third cell represents the anodising process. Anodising was carried out in sulphuric acid with dwell times of 5 and 60 seconds. Changing the immersion time in the anodising solution alters the oxide layer

and as a result increases the length of the anodic pores. The fourth cell represents the Post Anodic Treatment (PAT) process. The PAT was carried out in a phosphate solution at a temperature of 70°C with a dwell time of 60 seconds. This forms a 'precipitate' which changes the pore strucrure, significantly altering the surface morphology. Table 1. illustrates the conditions used for each preparation stage of the substrate.

The substrates prepared under laboratory conditions were:

1. Grained only.
2. Grained, electrochemically desmutted.
3. Grained, desmutted and anodised for dwell times of 5 and 60 seconds.
4. Aluminium anodised for only 30 seconds.
5. Aluminium anodised for 30 seconds and PATed for 4 minutes.

Table 1. Summary of the conditions used in the preparation of the substrates

Treatment	Conditions
Caustic Clean	Immersion in NaOH for a specific dwell time, followed by rinsing in water
Electrograin	Immersion in HCl for a specific temperature and dwell time, followed by rinsing in water
Desmut	Immersion in H_2SO_4 for a specific temperature and dwell time, followed by rinsing in water
Anodising	Immersion in H_2SO_4 for a specific temperature and dwell time, followed by rinsing in water
PAT	Immersion in a phosphate solution for a specific temperature and dwell time, followed by rinsing in water

6.3.1 Experimental Apparatus

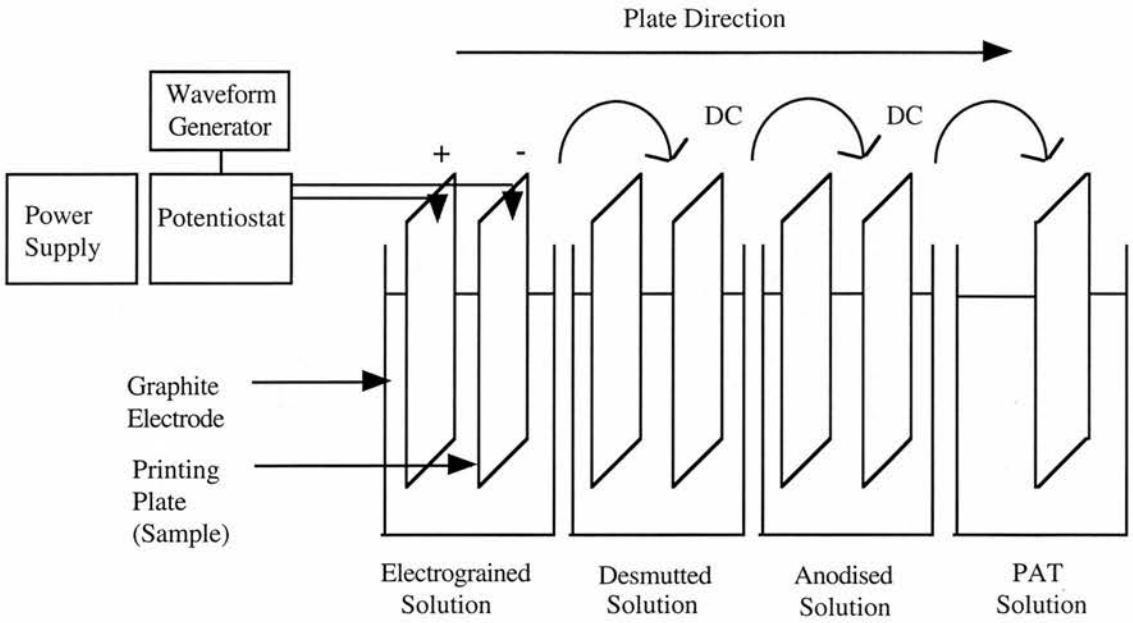

Figure 1. Schematic illustration of plate preparation.

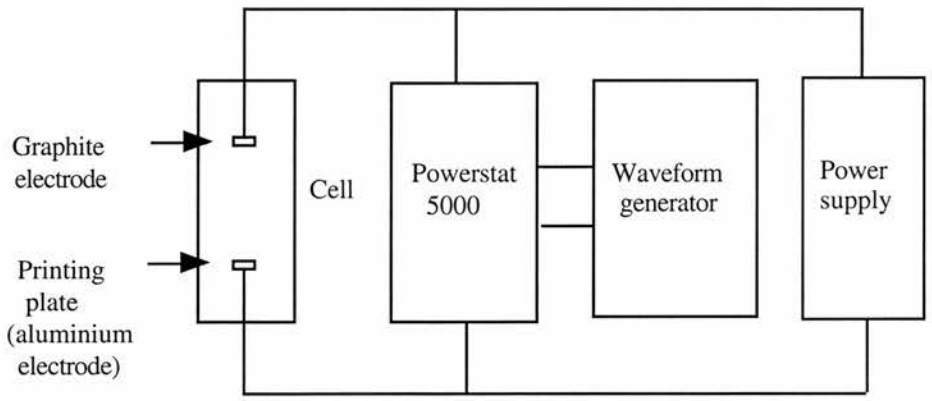

Figure 2. Circuit diagram of the apparatus.

6.4 SEM Images showing morphological differences of each surface [1]

Figure 3. Low magnification SEM image of the surface of a grained only sample before desorption.

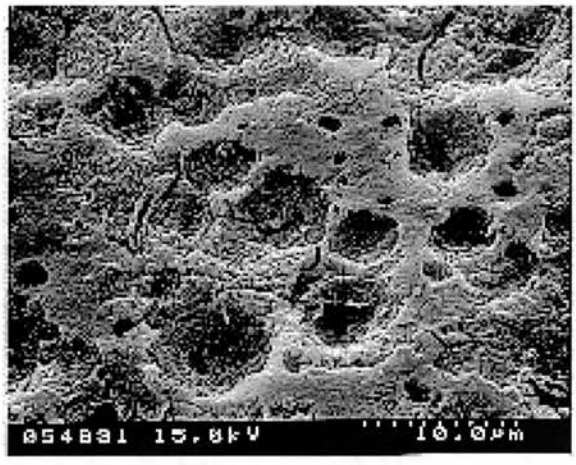

Figure 3. is a scanning electron micrograph of a grained only sample [1]. At low magnification the surface is evidently uniformly pitted, giving an apparently rough appearance. The micrograph reveals hemispherical pits, a characteristic of growth under diffusion control, ranging from 2 µm to 10 µm in diameter. Each of these "large pits" is composed of many smaller pits, ~0.2 µm in diameter. The wall of the pits have a coarse appearance and it is not possible to determine whether the pits are crystallographic in shape. The hemispherical pits are broader than they are deep. Some of the pits have sharp ridges at their rim.

Pit distribution and pit density are influenced by the metal structure and composition. Pits tend to occur preferentially at grain boundaries and at intermetallic particles. The pit density is strongly affected by grain size and grain orientation. On 99.99% purity aluminium, electrograined in hydrochloric acid, about 10^{13} pits m^{-2} are rapidly initiated. However, only a small number (10^{10} pits m^{-2}) of these pits, where the current is concentrated, develop into crystallographic, cubic shaped pits [2,4]. In addition to the creation of extensively pitted and convoluted surfaces, etch products are formed during

the early stages of the process [2]. The etch film gives a white appearance to the electrograined surface. In addition to $Al(OH)_3$ and water, Cl^- anions and metallic aluminium particles are retained in the film. EDX was used to analyse the bulk and it was found that the resultant spectra were characteristic of aluminium, oxygen and chloride ions. This is illustrated in Figure 8. The detailed morphology is masked by the presence of a non-uniform film of etch products, which develop during the graining, but can be removed when the sample is desmutted.

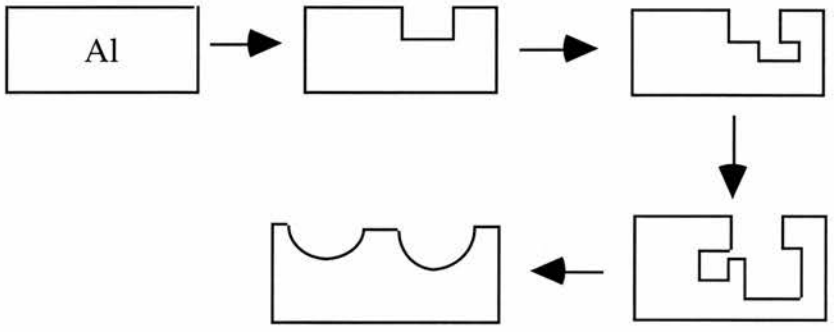

Figure 4. Illustration of the ordering of the morphological building element leading to the eventual electrograined morphology.

Previous work done [3] relating to surface treatment of aluminium at 1500 A rms m^2 at 50 HZ in 0.1 HCl at 40°C for 5 second at different frequencies showed that electrograining at low frequencies resulted in a large increase of surface area, confirming that the cubic pit networks, formed at low frequencies, penetrate deeply into the aluminium. As the frequency is increased, the surface transforms into the relatively uniformly pitted and convoluted appearance. This is shown in Figure 5.

Examination of the morphology obtained by electrograining of aluminium in hydrochloric and nitric acid reveals fundamentally different morphological building elements, leading to distinct final morphological differences. The morphology exhibited by surfaces electrograined in hydrochloric acid is built up from a fine cubic shaped pit. The pit

arrangement indicates that the dissolution of the aluminium occurs in preferred directions. Several investigators [2,3,4] showed that the cubic pits are effectively formed by intersecting [100] planes. The basic morphological element building up the morphology of aluminium surfaces electrograined in nitric acid is a small regular hemisphere. This pit shape indicates that the anodic dissolution of aluminium occurs in a random manner. The characteristic dimension of the pits decreases with increasing current density and decreasing a.c. frequency [2,3,5]. Over all, it is evident that the anodic dissolution of aluminium during graining in hydrochloric and nitric acid is controlled in fundamentally different manners [5,6].

The effect of the a.c. frequency and the current density on the electrograined morphology can be explained by their influence on the amount of charge associated with the anodic oxidation of aluminium. The amount of charge passing the surface during each anodic half period is distributed between the number of pits initiated and is given by:

$$\frac{q_{\text{period}}}{2} = \int_0^{\pi} J_{\max} \sin \omega t \, dt = -\frac{J_{\max}}{\omega} [\cos \omega t]_0^{\pi}$$

where J_{max} (Am^{-2}) is the maximum current density and $\omega = 2\pi f$ with f (Hz) the electrograining freguency. The local anodic charge is thus given by:

$$q_{pit} = \frac{q_{period/2}}{\text{number of pits}}$$

It is evident that the local anodic charge, passing for each anodic half period, increases with decreasing frequency and increasing current density. Decreasing the electrograining frequency increases the period of time in which the surface is anodically polarised, while an increase of current density enhances the amount of anodic charge for the oxidation of aluminium over a certain period of time.

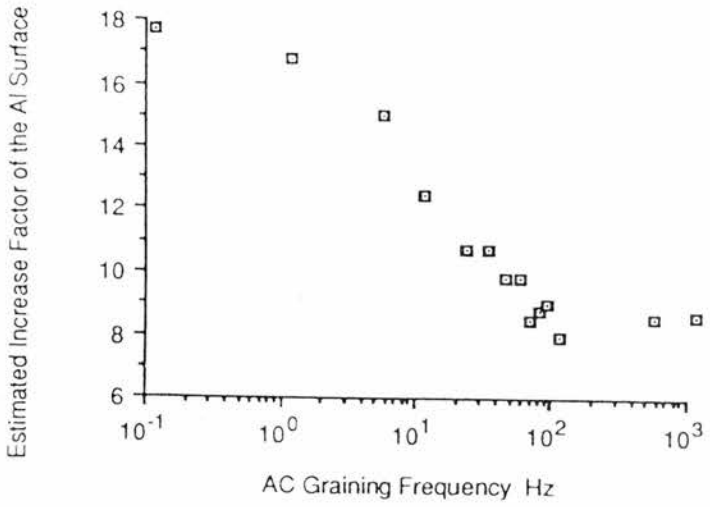

Figure 5. Variation of the specific surface area of the aluminum treated in 1500A rms m^2 at 50 Hz in 0.1 HCl at 40°C for 5 second at various frequencies: (a) 1 HZ, (b) 10 HZ, (c) 100 HZ and (d) 100 HZ.

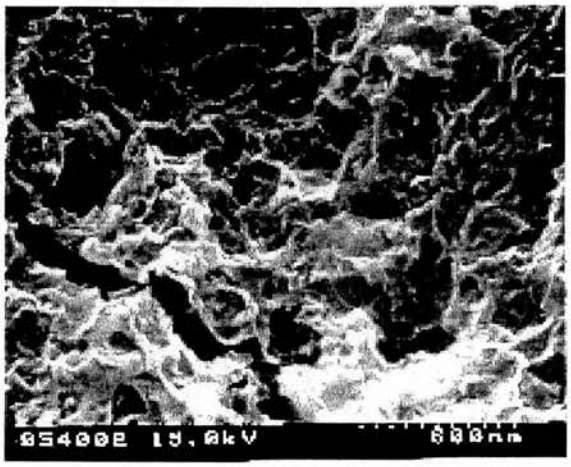

Figure 6. High magnification SEM image of the surface of a grained only sample <u>before</u> desorption.

Figure 7. High magnification SEM image showing a cross sectional view of a grained only sample <u>before</u> desorption.

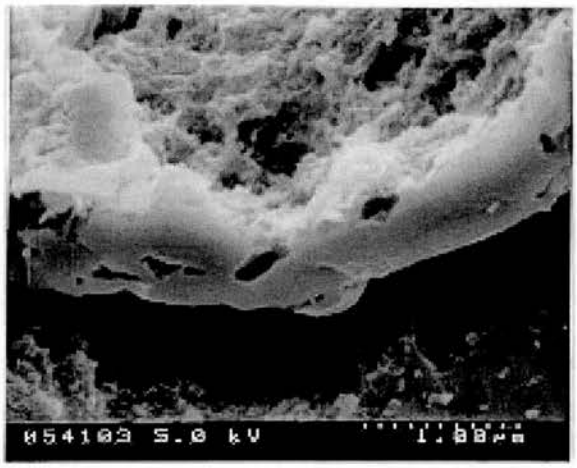

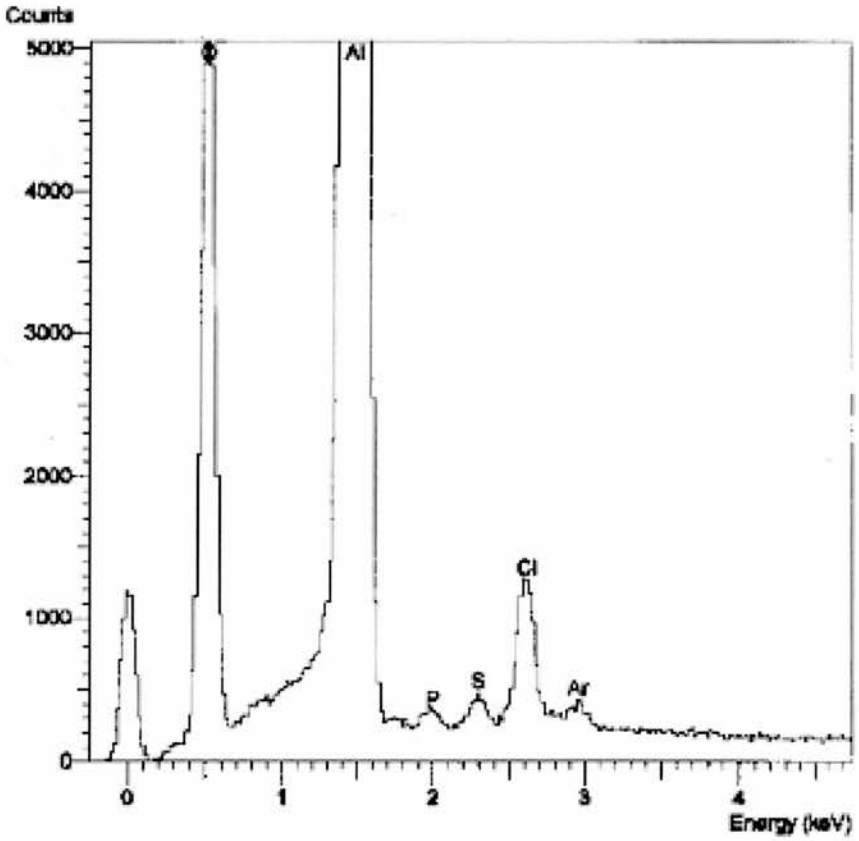

Figure 8. EDX analysis from a grain only substrate.

Figure 9. Low magnification SEM image of the surface of a grained only sample <u>after</u> desorption.

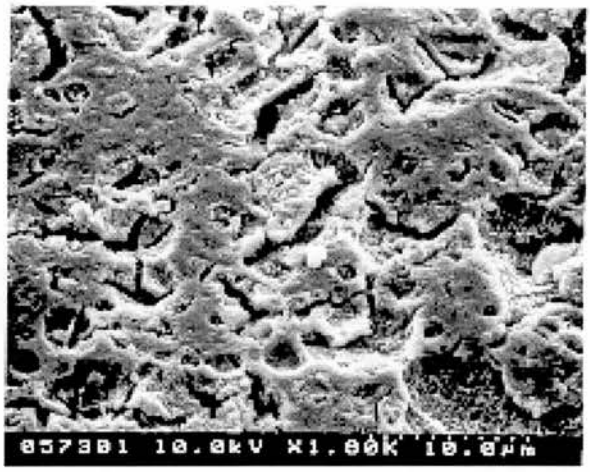

Figure 10. High magnification SEM image of the surface of a grained only sample <u>after</u> desorption.

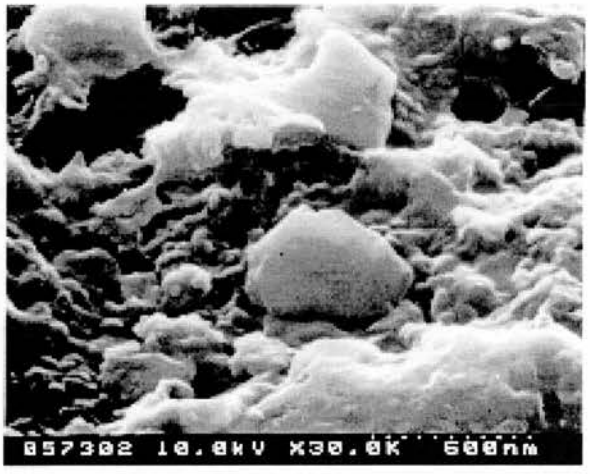

It is difficult to assess from the SEM image if there had been any structural changes to the substrate during the desorption process. Tests of the reproducibity of the results were carried out for aniline and phenol on the same sample and also on newly prepared substrates which produced the same results. From this, we can assume there to be no structural changes to the substrates induced by the desorption experiment.

Figure 11. Low magnification SEM image of the surface of a grained, desmutted sample before desorption.

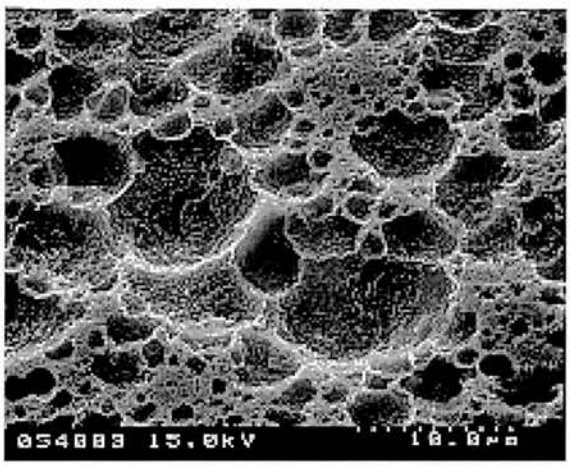

A marked difference in surface topography is observed after removing the etch film. In this figure, relatively fine featured pits are evident. The surface is composed of much larger hemispherical pits than the grained only surface covering a range of effective diameters from 1 μm to 10 μm. Although it cannot be revealed by the SEM observations within the walls of these larger pits there are a high population density of crystallographic, cubic shaped pits with a mean diameter of 0.2 μm [7]. These hemispherical pits exhibit no characteristic dimension. They are broader than they are deep and develop laterally until they merge. Some of these pits grow more rapidly, engulfing the slower developing ones.

A computer model that grew small pits over an imaginary surface has shown that the eventual surface topography is very similar to the grained desmutted surface i.e. the eventual surface is created by random nucleation and growth of 0.2 μm crystallographic pits over the aluminium surface resulting in 10 μm hemispherical pits. The etch film is a colloidal phase of fine $Al(OH)_3$ and aluminium particles in water, as well as Cl^- which covers the aluminium surface during the graining process. The desmutting process removes the etch product away from the surface. This causes the surface to be much

smoother in appearance, showing a clearer definition of the pit structure. By using EDX to analyse the bulk it was found that the peaks intensities for the aluminium and oxygen were far greater than the grained only sample. There were no chloride peaks present. Cracks are less evident on the surface.

Figure 12. High magnification SEM image of the surface of a grained, desmutted sample before desorption.

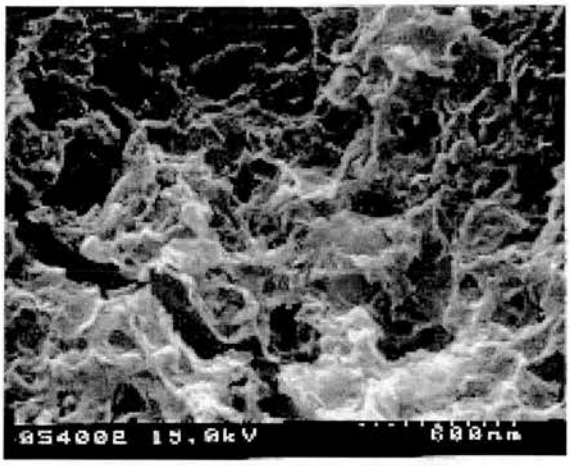

Figure 13. High magnification SEM image of cross sectional view of grained and desmutted sample before desorption.

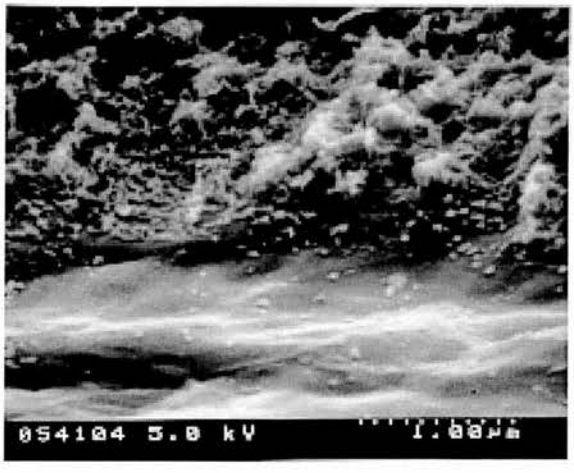

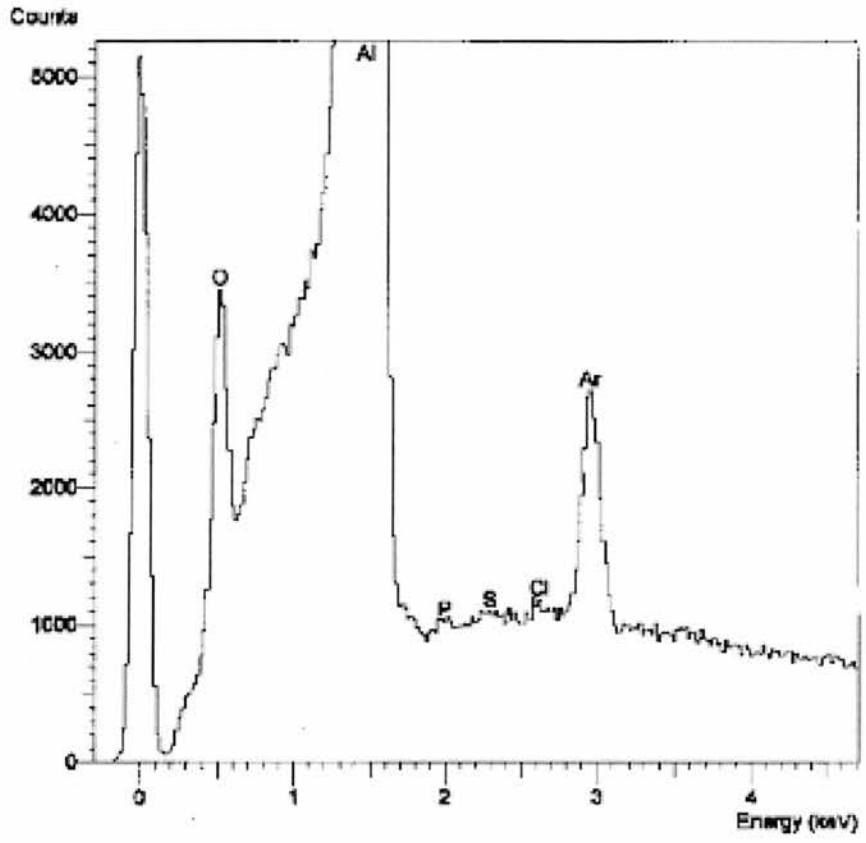

Figure 14. EDX analysis from a grained, desmutted sample.

Figure 15. Low magnification SEM image of the surface of a grained, desmutted sample <u>after</u> desorption.

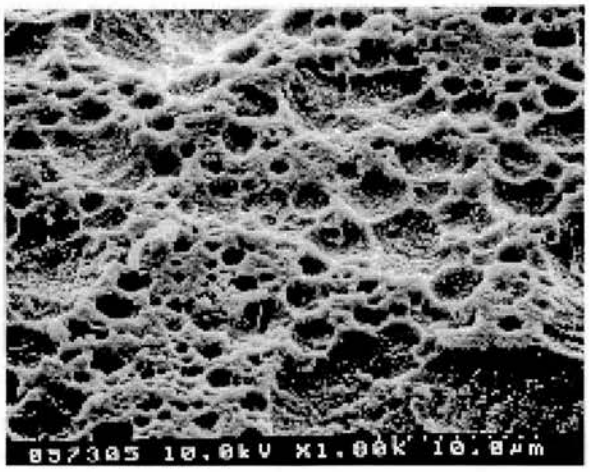

The micrograph shows the surface composed of smaller hemispherical pits. Tests of the reproducibity of the results had been carried out on the same sample and also on a new sample which produced the same results. From this we can assume there to be no structural changes to the substrates during the desorption process.

Figure 16. Low magnification SEM image of the surface of a grained, desmutted sample and anodised for 5 seconds <u>before</u> desorption.

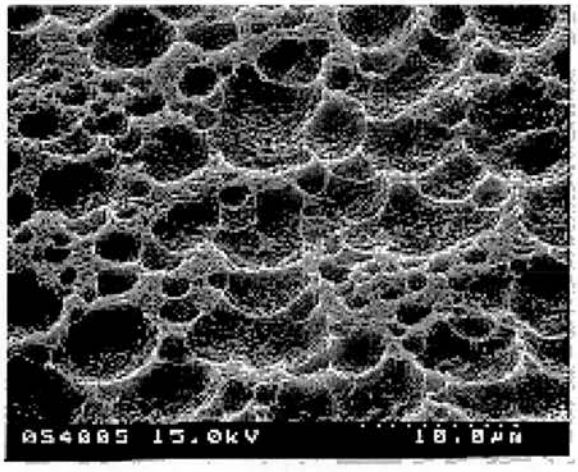

Figure 17. High magnification SEM image of the surface of a grained, desmutted sample anodised for 5 seconds <u>before</u> desorption.

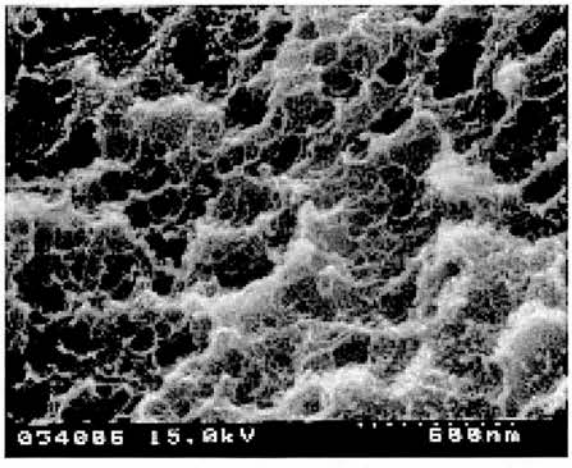

The SEM micrograph illlustrated in Figure 17. reveals a network of smaller pits known as 'micropits' scattered across the surface. This gives the anodised surface a high surface area which have been already mentioned in chapter 4.

Figure 18. High magnification SEM image of a cross sectional view of a grained, desmutted sample anodised for 5 seconds <u>before</u> desorption. The surface shows areas which have been anodised.

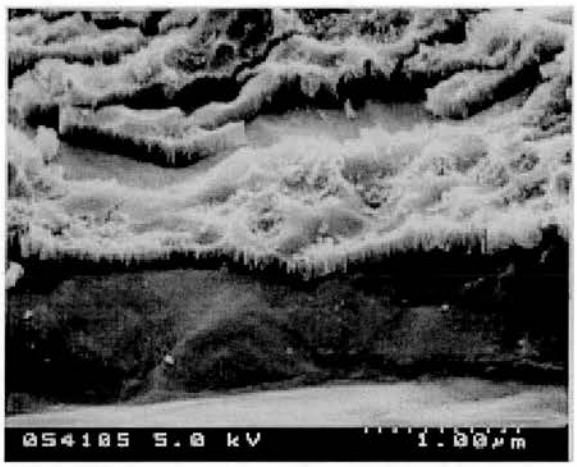

Figure 19. High magnification SEM image of anodic pores from a grained, desmutted sample anodised <u>before</u> desorption.

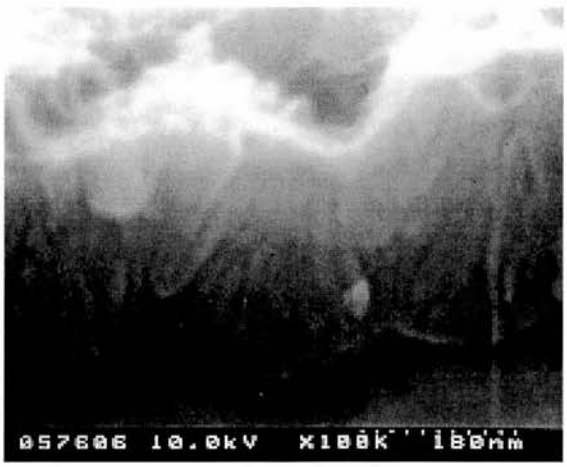

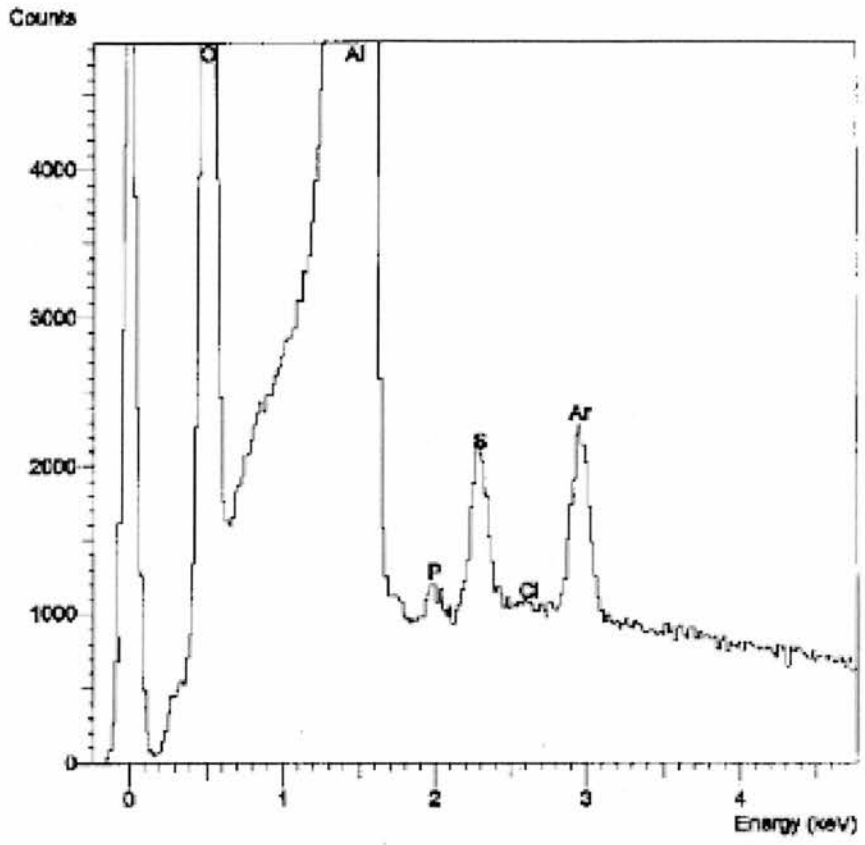

Figure 20. EDX of grained, desmutted sample anodised for 5 seconds.

Figure 21. Low magnification SEM image of the surface of a grained, desmutted sample anodised for 60 seconds <u>before</u> desorption.

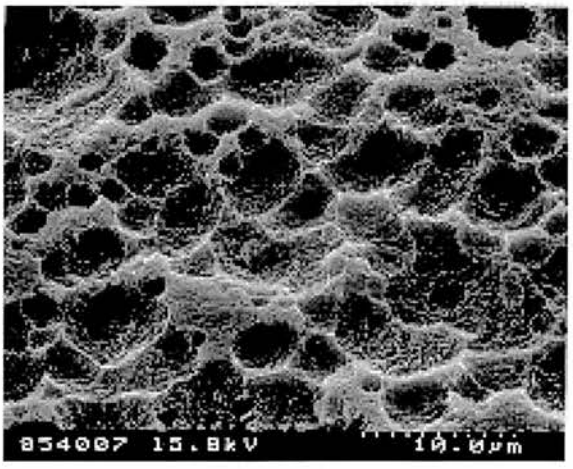

Figure 22. High magnification SEM image of the surface of a grained, desmutted sample anodised for 60 seconds <u>before</u> desorption.

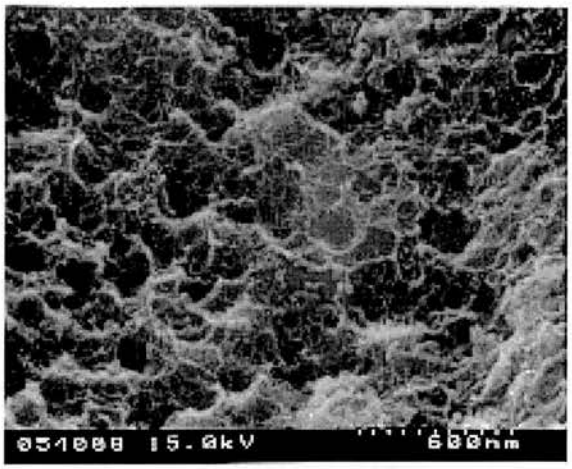

Figure 23. High magnification SEM image of a cross sectional view of a grained, desmutted sample anodised for 60 seconds <u>before</u> desorption.

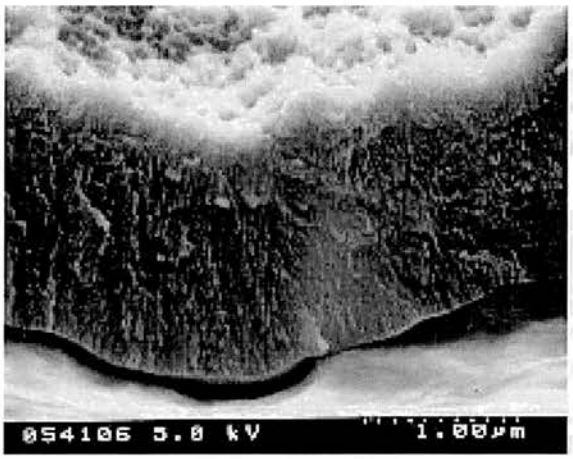

The SEM image is a cross sectional view of a grained sample desmutted and anodised. The total thickness of the film is approximately 760 nm, with the barrier layer being identifiable as the poorly resolved dark line at the bottom of the micrograph. The film overlying the barrier layer consisits of many parallel '*twisting* ' channels, the diameter ranging from 5 nm to 20 nm. Figure 26. shows a schematic illustration of the development of new pores from pore branching process.

Figure 24. High magnification SEM image of anodic pores of a grained, desmutted sample anodised for 60 seconds.

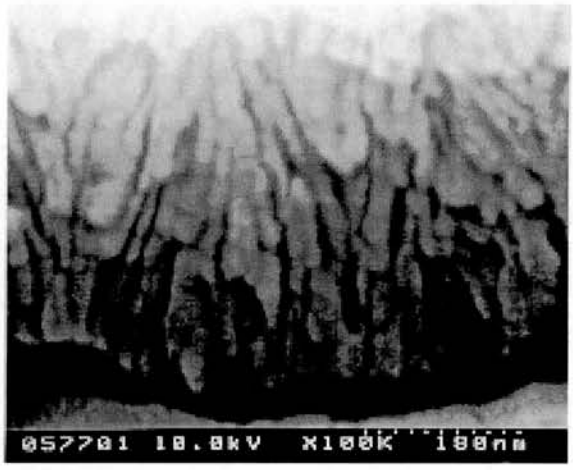

Figure 25. EDX Analysis of grained, desmutted sample anodised for 60 seconds.

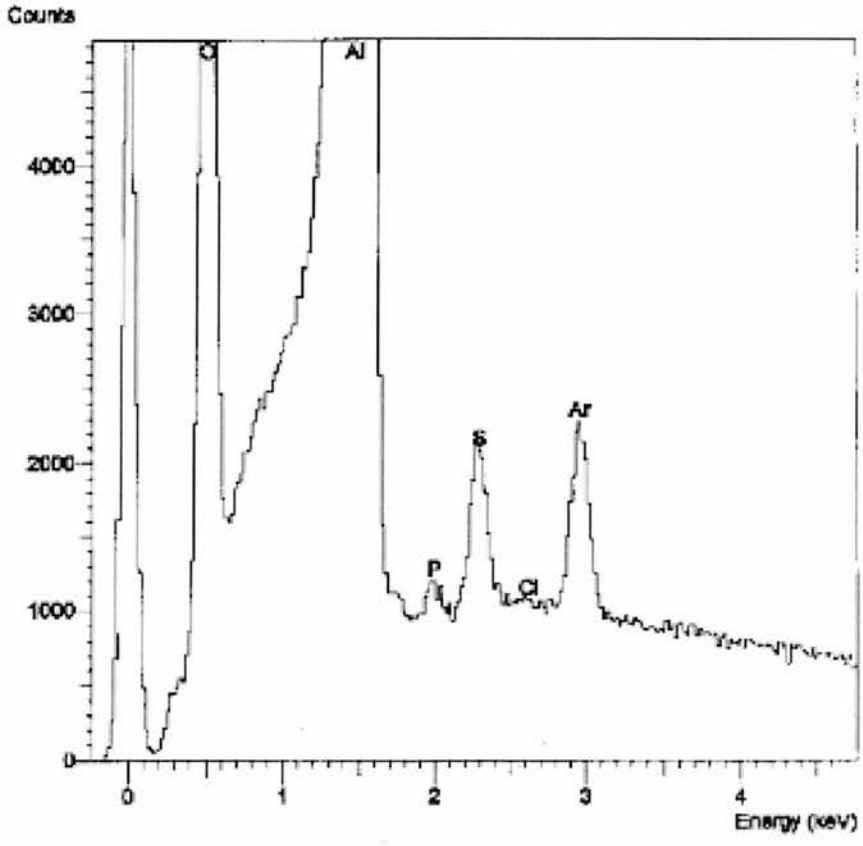

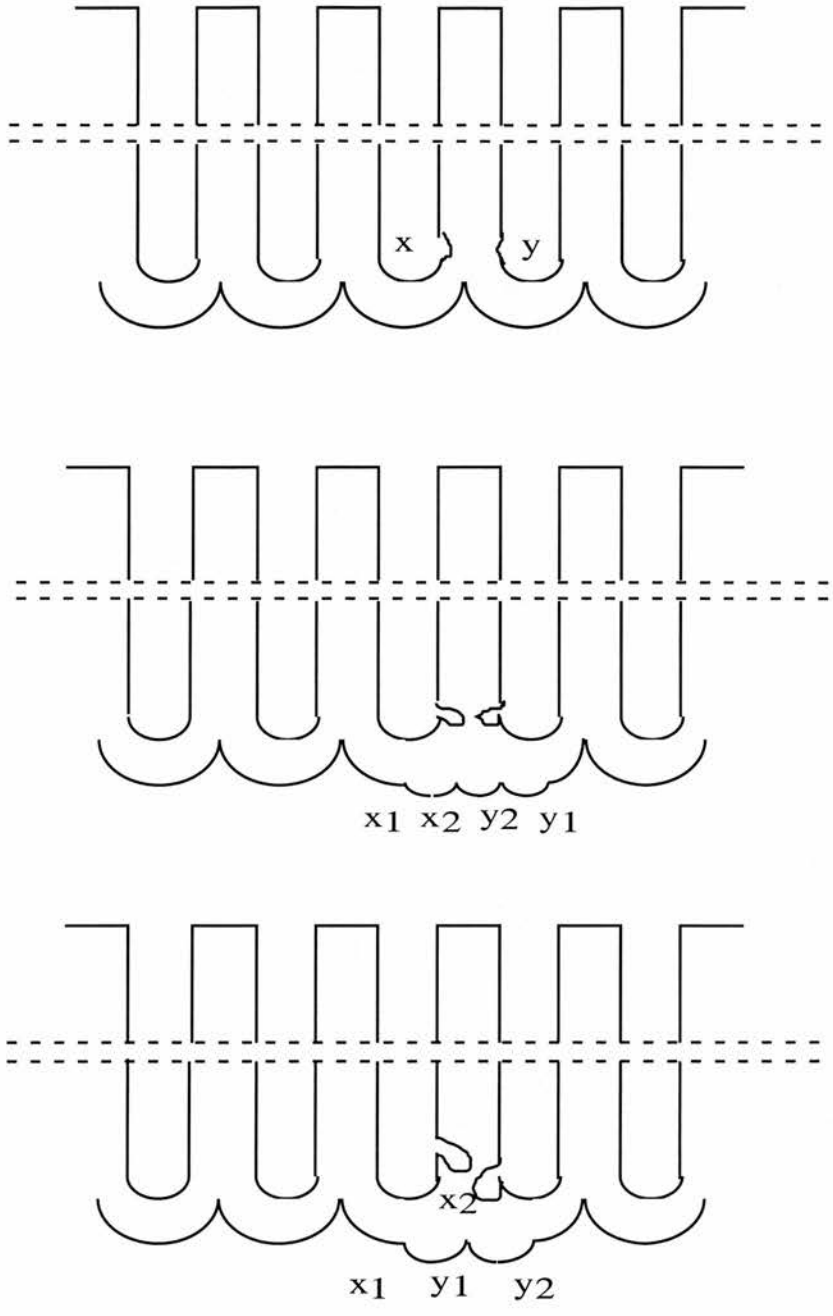

Figure 26. Schematic illustration of the development of new pores from pore branching process.

(a) shows film formation accompanied barrier layer thinning due to local field assisted dissolution at pores at x and y (b) pore branching takes place and new pores developed at the barrier layer region x_1 and y_1 (c) as anodising proceeds, pore x_2 may cease to develop further and pore y_2 may develop into a new pore.

Figure 27. Low magnification SEM image of aluminium anodised sample <u>before</u> desorption. The direction of rolling lines is clearly visable.

Figure 28. High magnification SEM image of aluminium anodised sample <u>before</u> desorption.

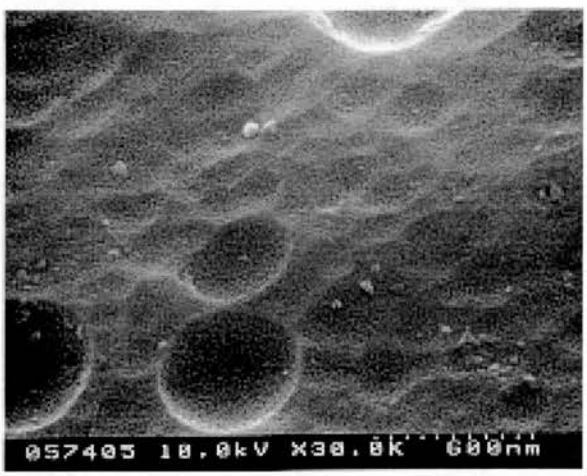

Figure 29. High magnification SEM image of a cross sectional view of aluminium anodised sample before desorption.

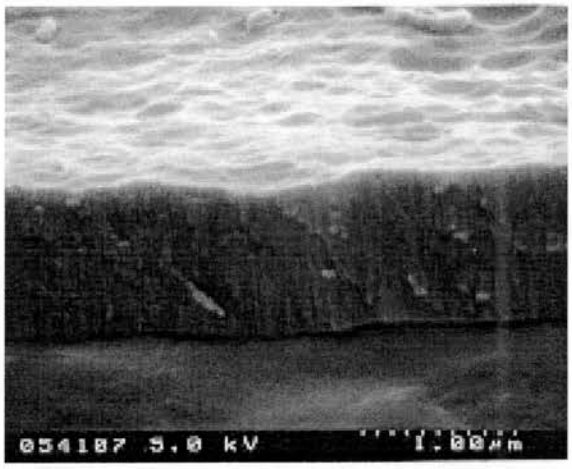

Figure 30. Higher magnification SEM image of anodic pores of aluminium anodised sample.

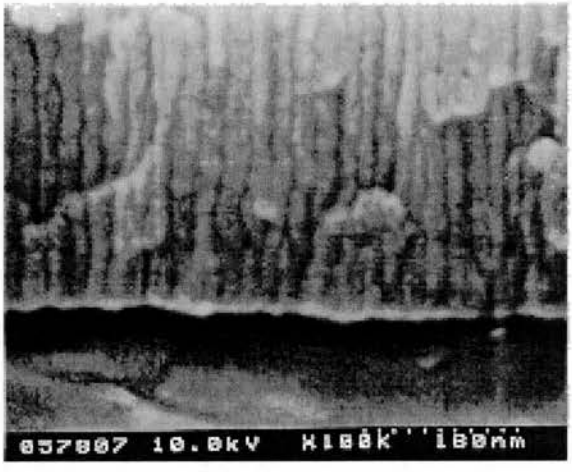

Figure 31. EDX from a aluminium sample anodised for 30 seconds.

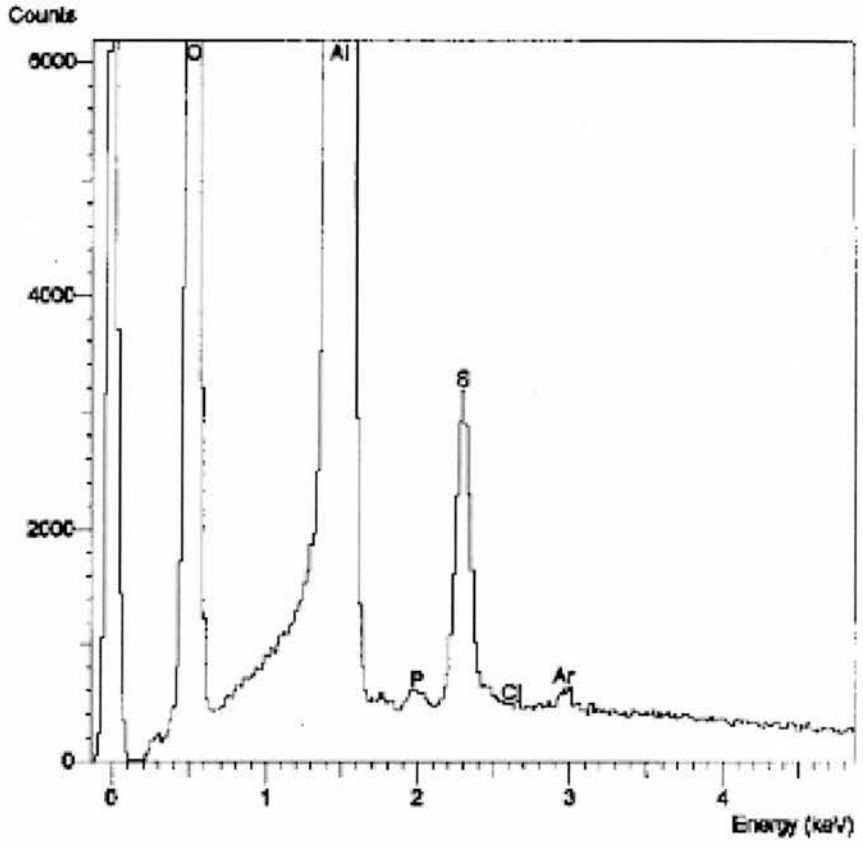

Figure 32. Low magnification SEM image of the surface of aluminium anodised sample PATed <u>before</u> desorption.

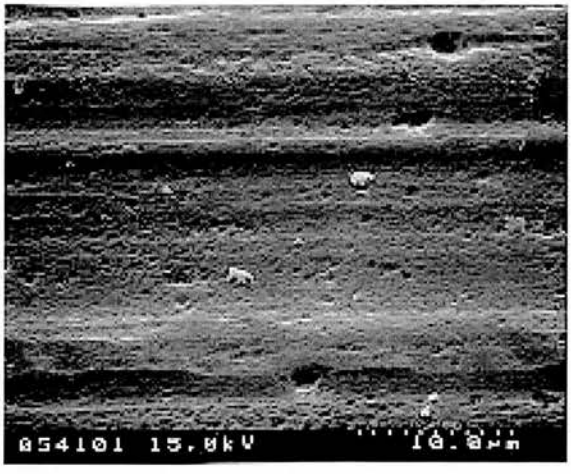

Figure 33. High magnification SEM image of the surface aluminium anodised sample PATed before desorption.

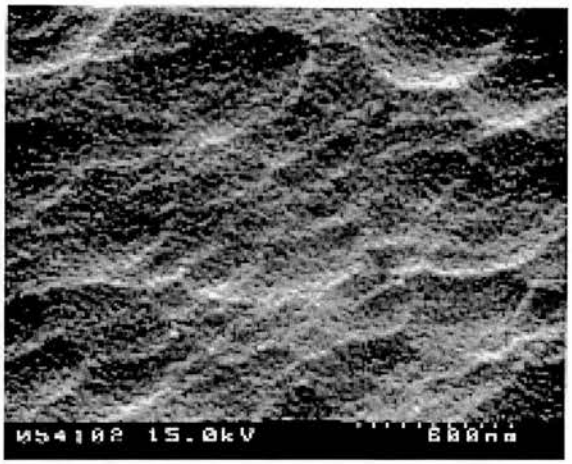

Figure 34. High magnification SEM image of a cross sectional view of aluminium anodised sample PATed for 4 minutes before desorption.

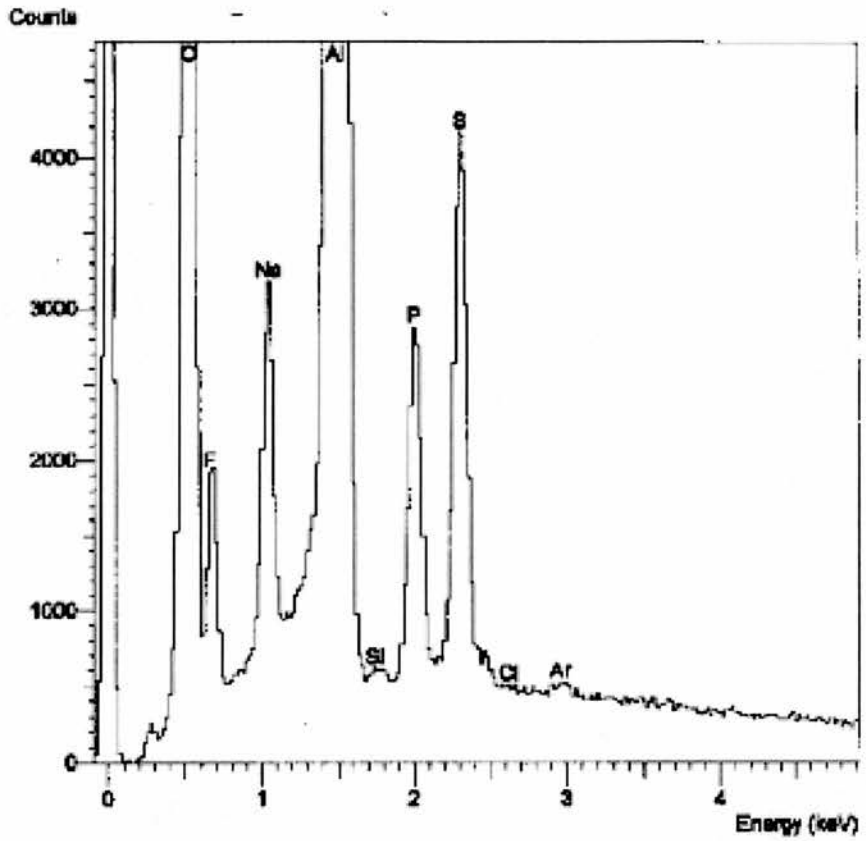

Figure 35. EDX of a aluminium anodised for 30 seconds and PATed for 4 minutes.

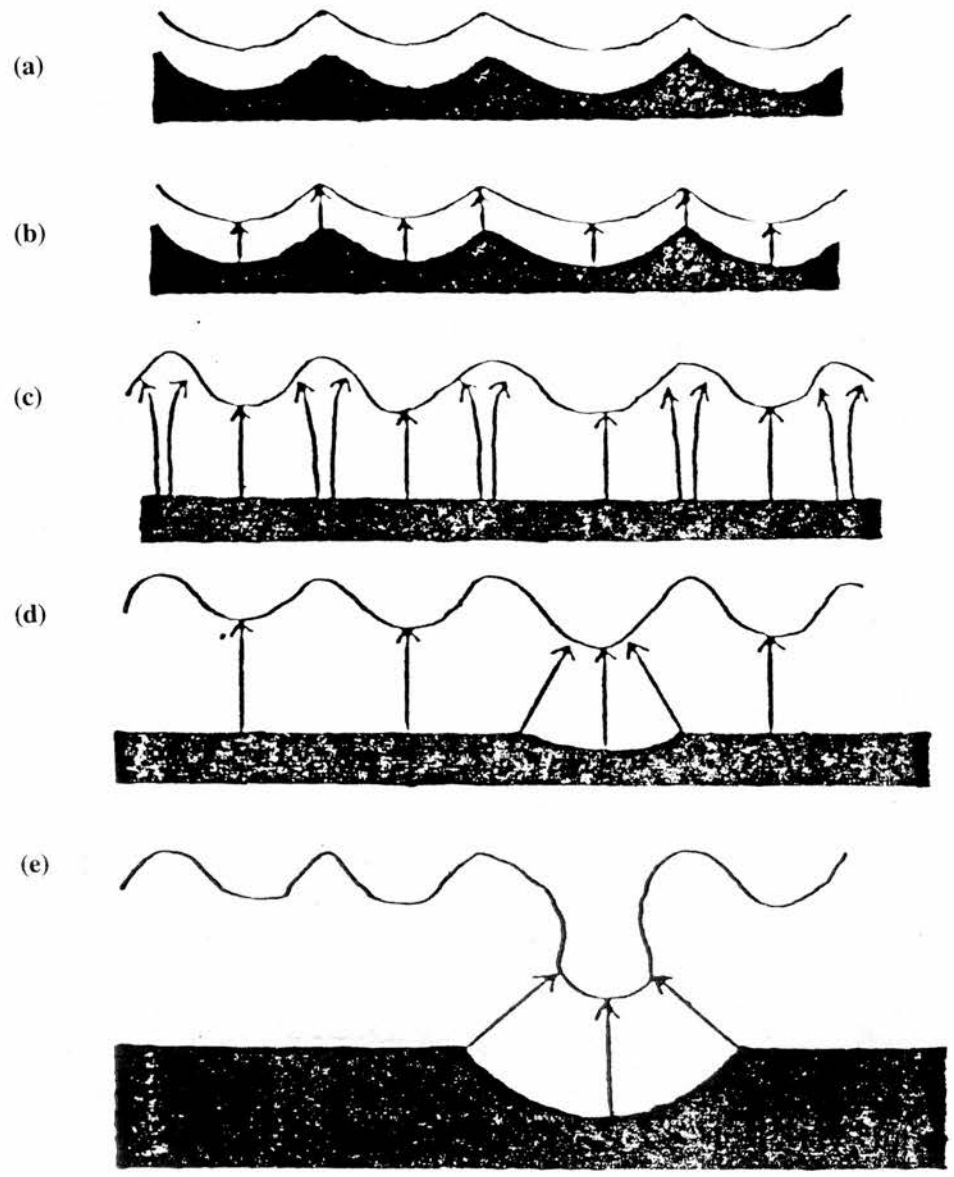

Figure 36. Schematic illustration of the film morphology growth during different stages (a) graining and (b), (c), (d) and (e) anodising process.

Table 2. Showing elemental analysis from EDX (+ means identified)

Sample	Al	O	Cl	Na	F	S	P	Ar
Grained only	+	+	+					
Grained Desmutted	+	+						+
Grained, Desmutted & Anodised for 5 seconds	+	+				+		+
Grained Desmutted, & Anodised for 60 seconds	+	+				+		
Aluminium Anodised for 30 seconds & no PAT	+	+				+		
Aluminium Anodised for 30 seconds & PATed	+	+		+	+	+	+	

6.4.1 Discussion

The SEM images shows characteristic changes in the surface morphology of each surface. The grained only surface shows uniformly pitted hemispherical pits ranging from 2 μm to 10 μm in diameter giving a rough appearance. The hemispherical depression are seen to be broader than they are deep and develop laterally until they merge. This is evident during the desmutting process. Anodising the grained, desmutted sample results in two changes; firstly, the surface is smoother in appearance and secondly, the surface oxide shows parallel porous channels intersecting the surface. Changing the time of the anodising procedure alters the length of the porous channels which is illustrated in the SEM image shown in Figures 17 and 22.

6.5 Surface Mapping

The aim of surface imaging (elemental maps) was used to determine the composition of individual particles on each substrate. The surface images were carried out at Horsell Graphics Industries.

6.5.1 Experimental Procedure

The samples were stuck on to an aluminium stub with colloidal silver electro-dag and allowed to dry. These were then coated with evaporated carbon using a solid rod of carbon in a Polaron CA508 evaporation unit. Evaporation was done in 5 bursts. Each burst lasting 1 second.

6.5.2 Surface Mapping Results

The surface mapping shows areas where there is a high concentration of the element, which is represented by the light areas on each image. The darker area shows no elemental detection.

Figure 38. Surface Images for a grained only sample.

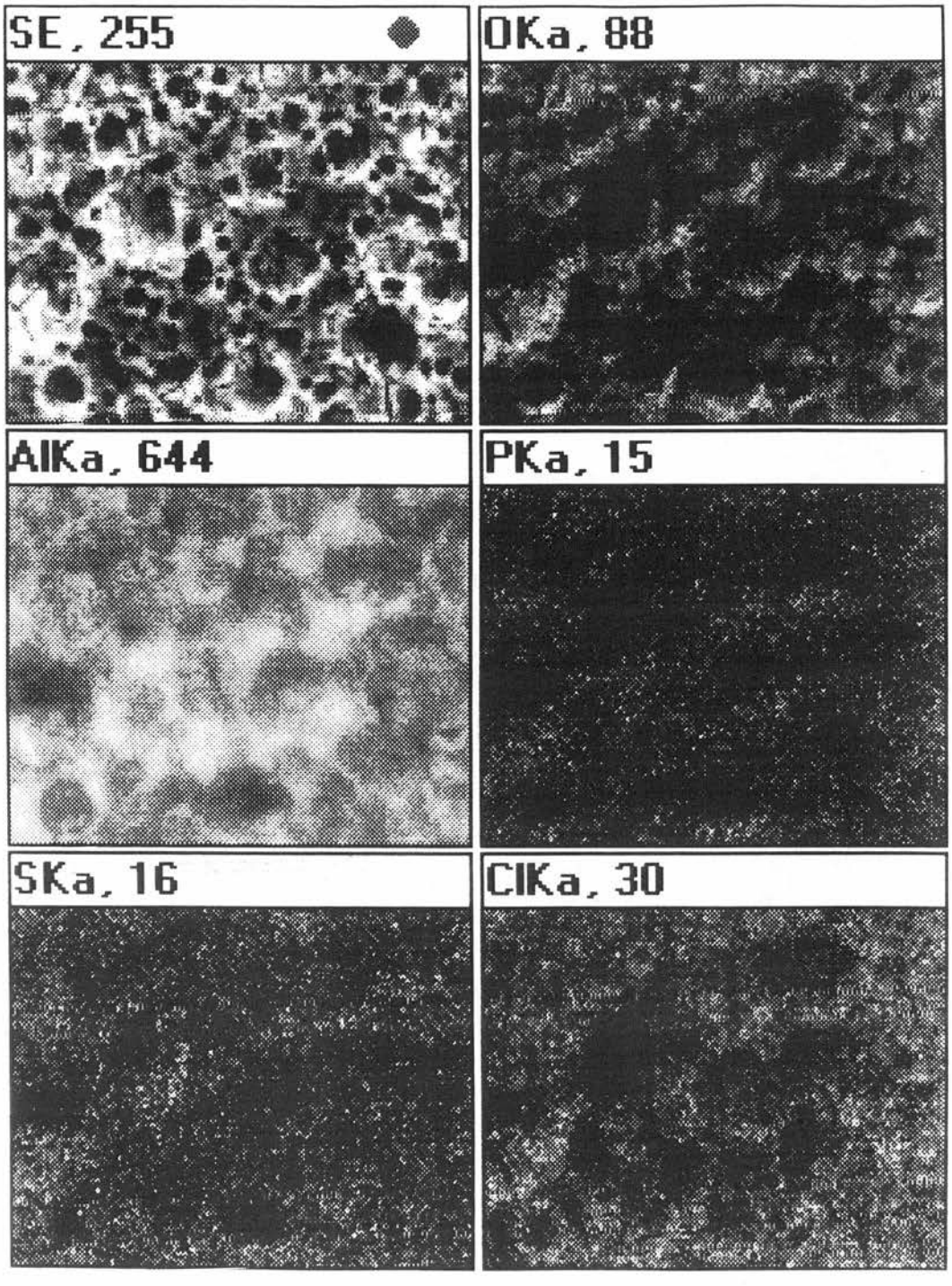

Figure 39. Surface Image for a grained, desmutted sample.

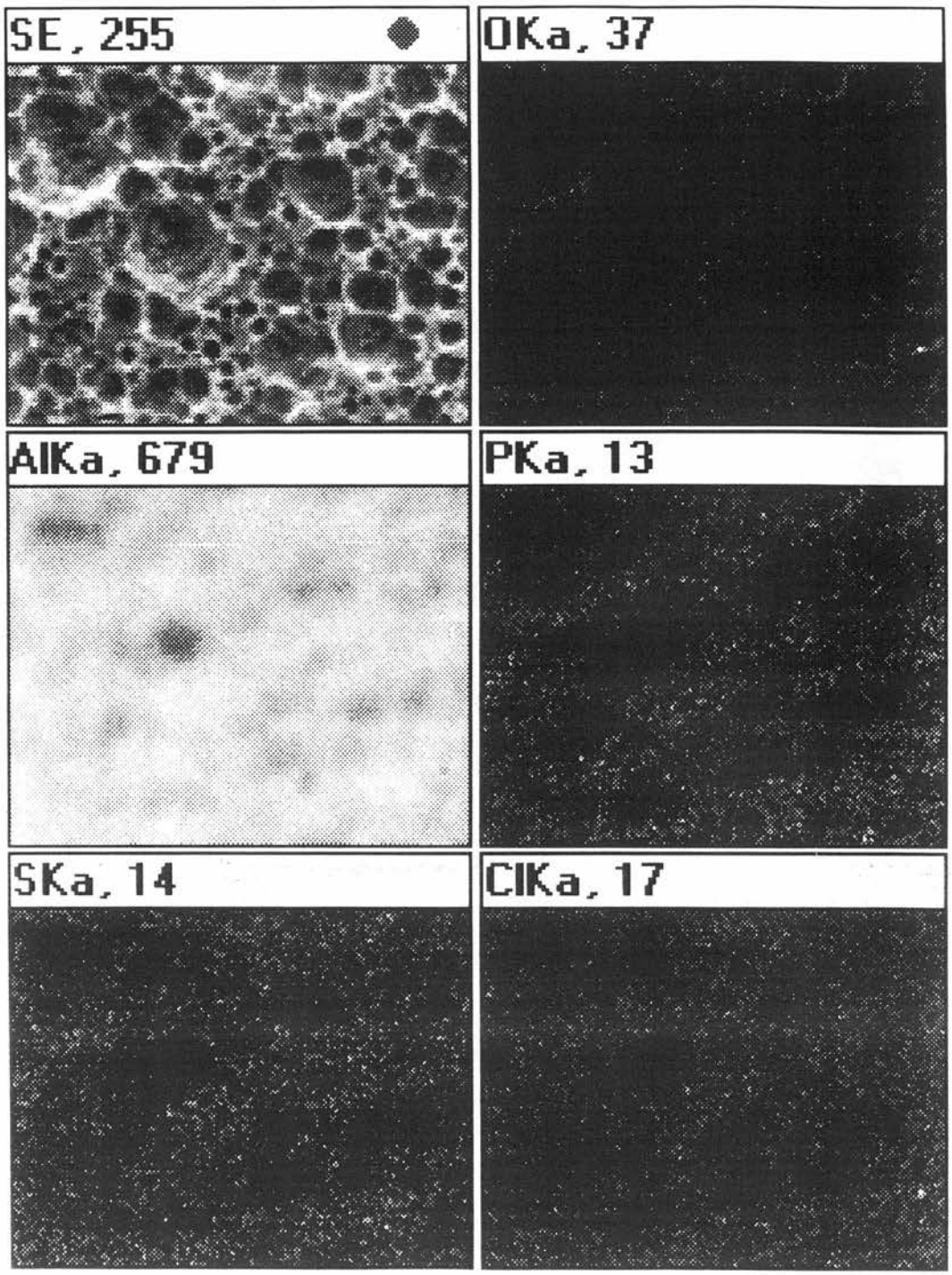

Figure 40. Surface Image for a grained, desmutted sample anodised for 5 seconds.

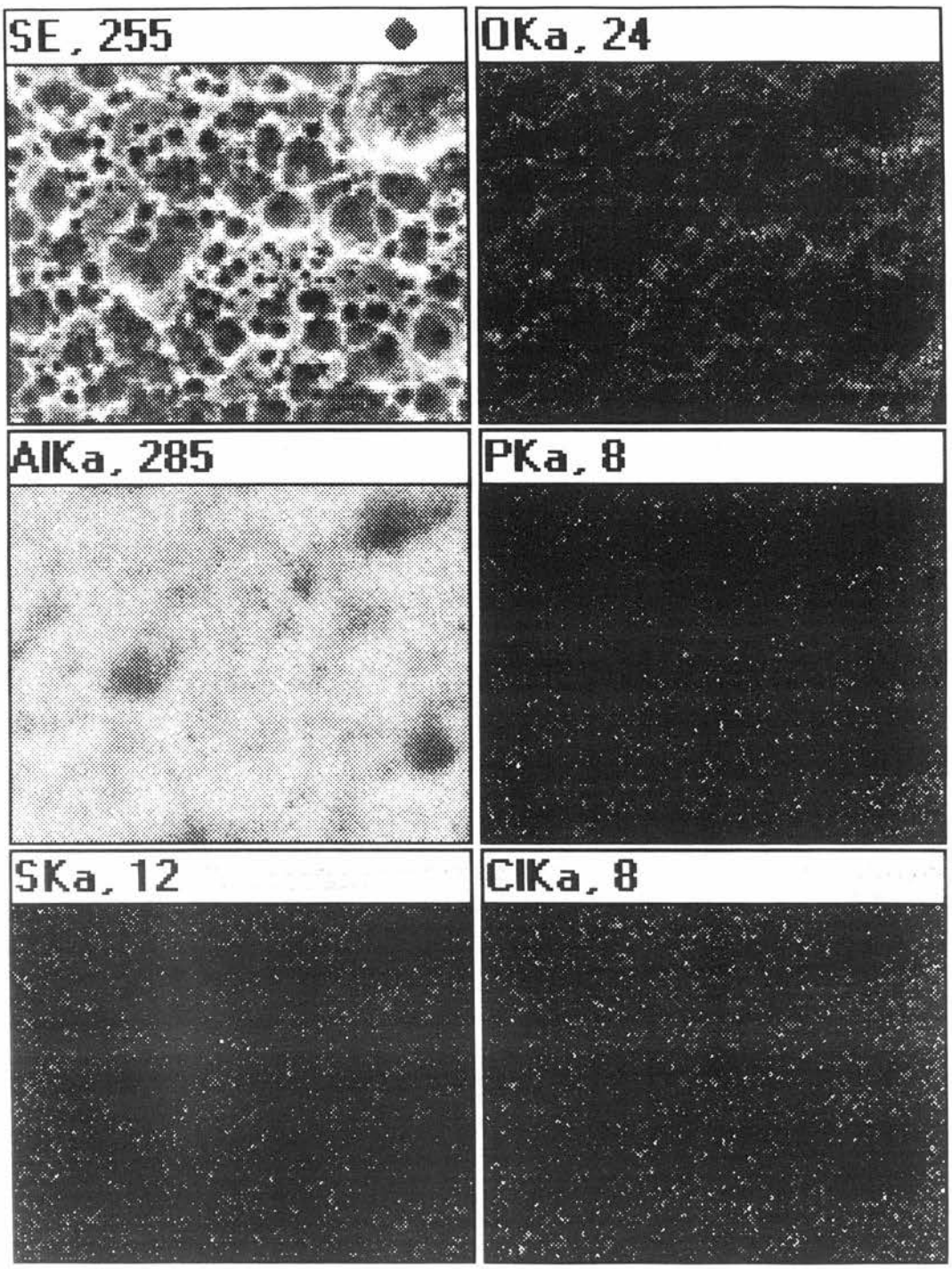

Figure 41. Surface Image for a grained, desmutted sample anodised for 60 seconds.

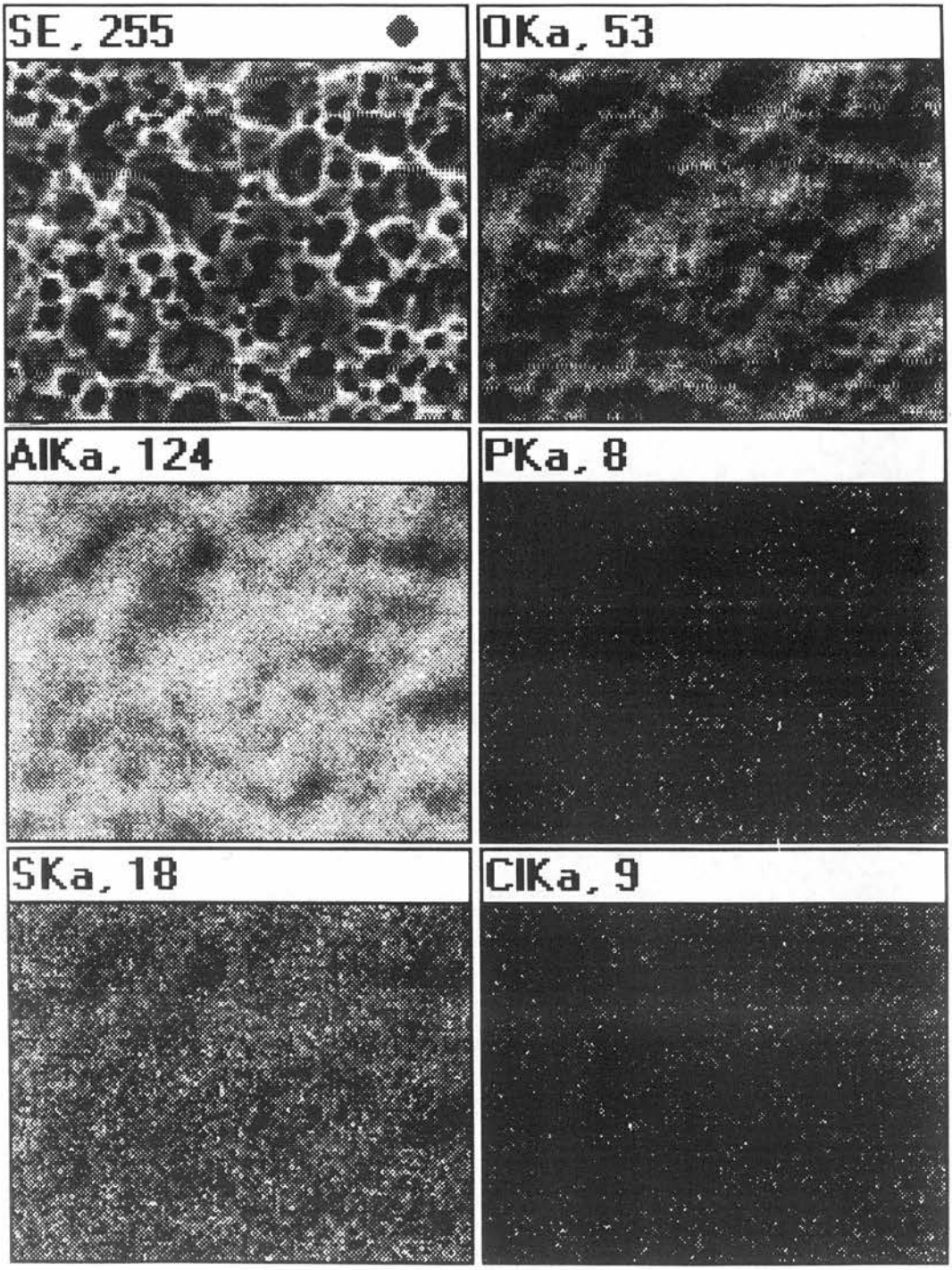

Figure 42. Surface Image for a aluminium sample anodised for 30 seconds with no PAT.

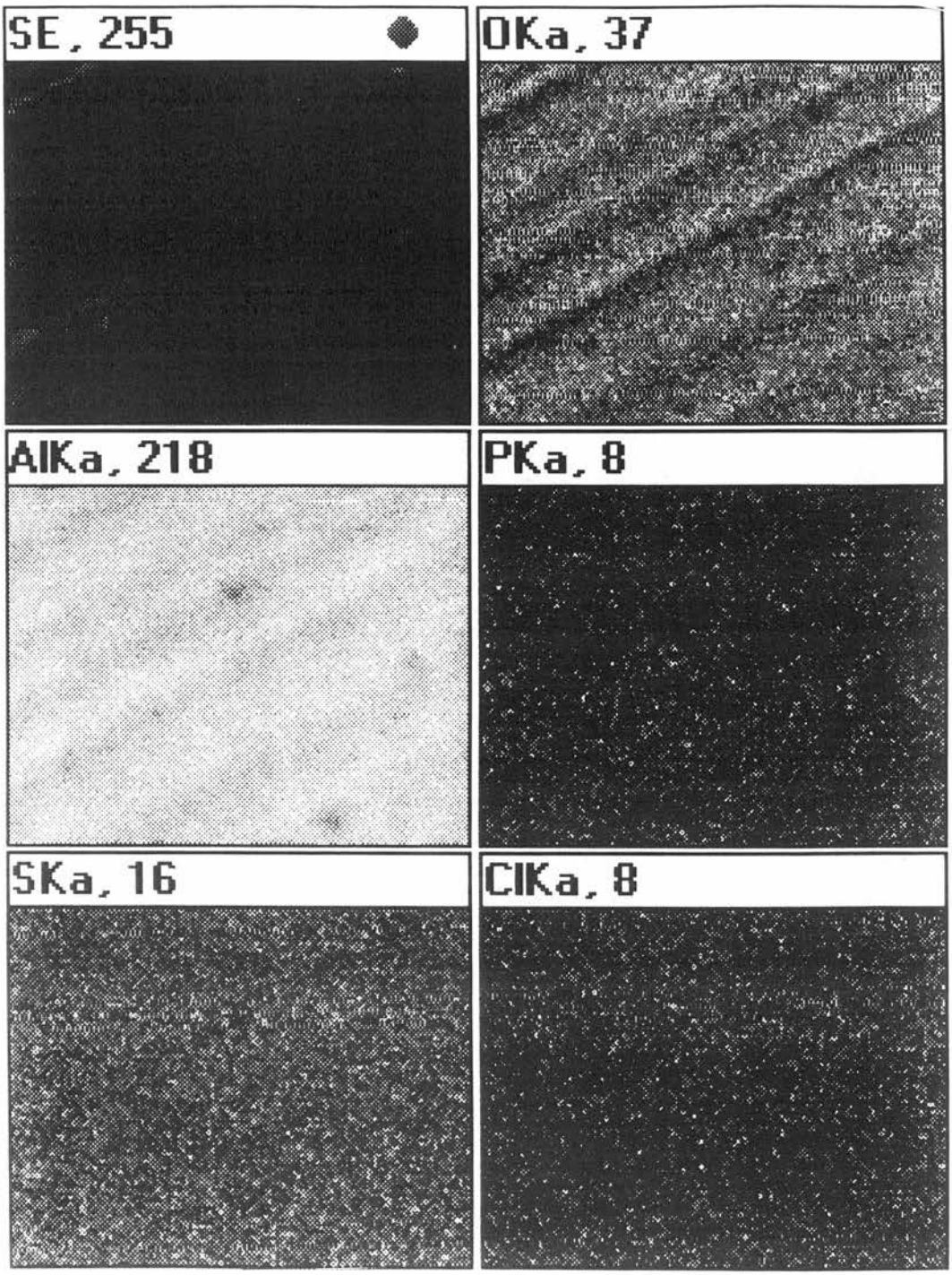

Figure 43. Surface Image for a aluminium sample anodised for 30 seconds and PAT'ed for 4 minutes.

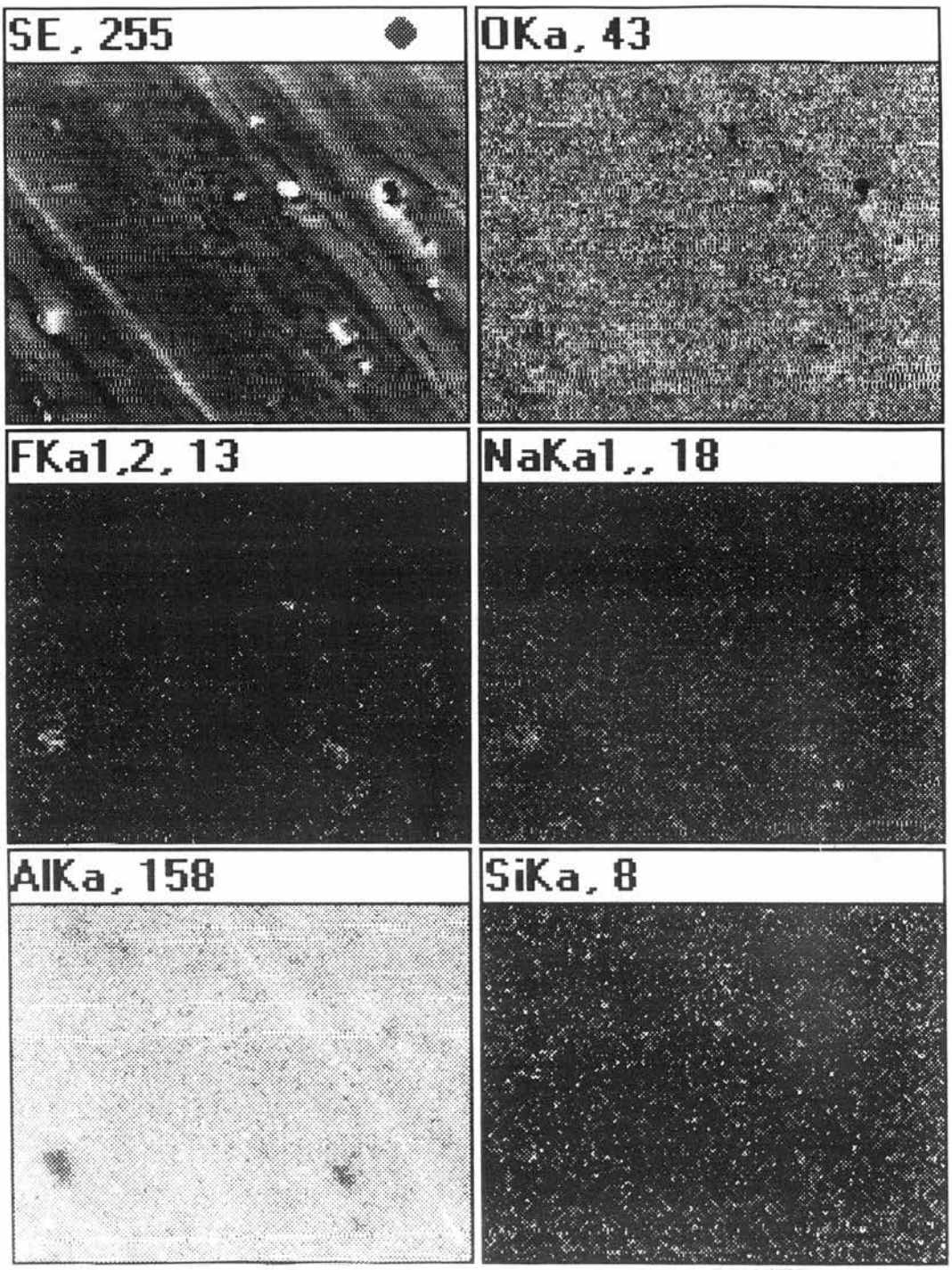

6.6 Optical Microscopy Images

Figure 44. Optical Microscopy Images for a grained only sample.

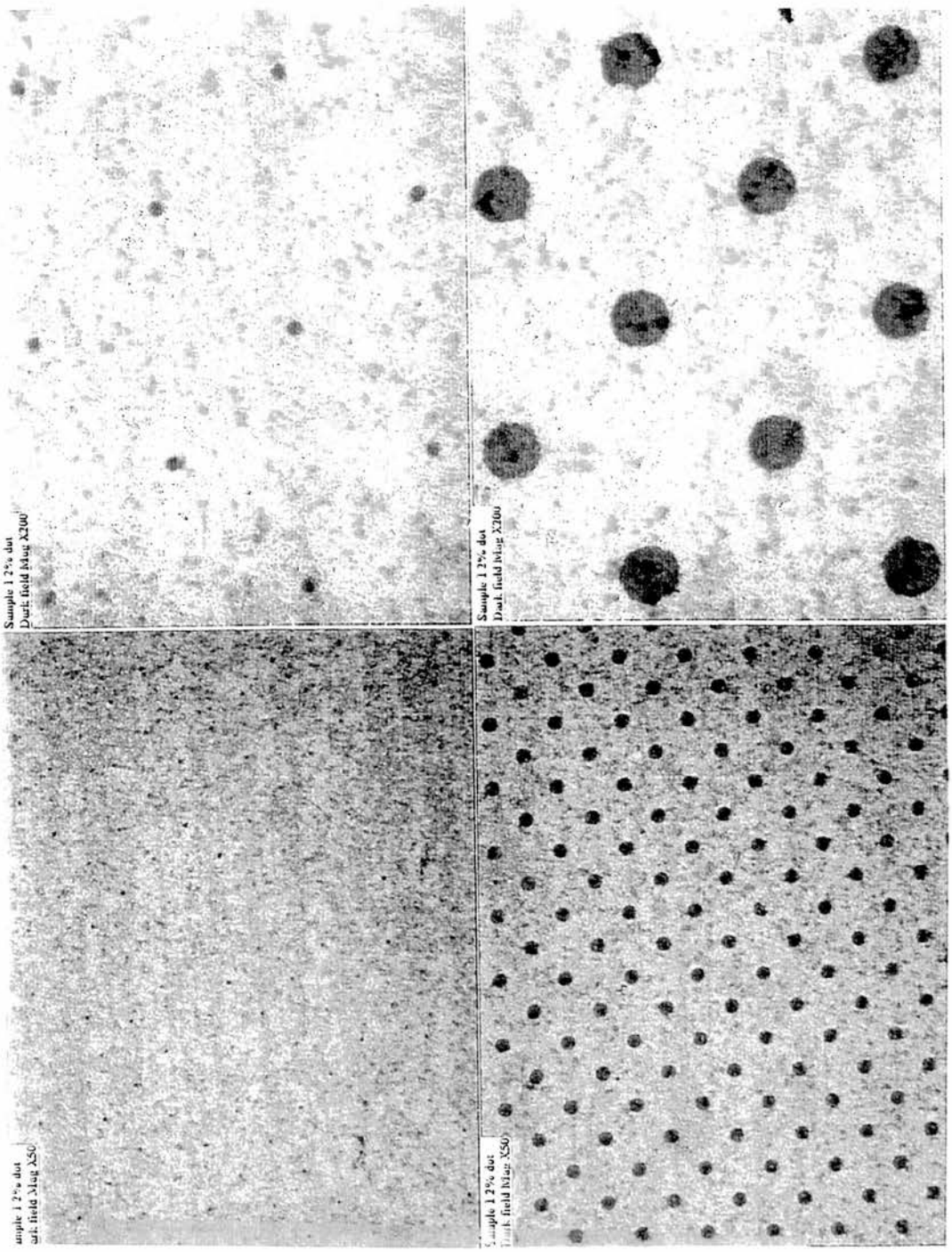

Figure 45. Optical Microscopy Images for a grained, desmutted sample.

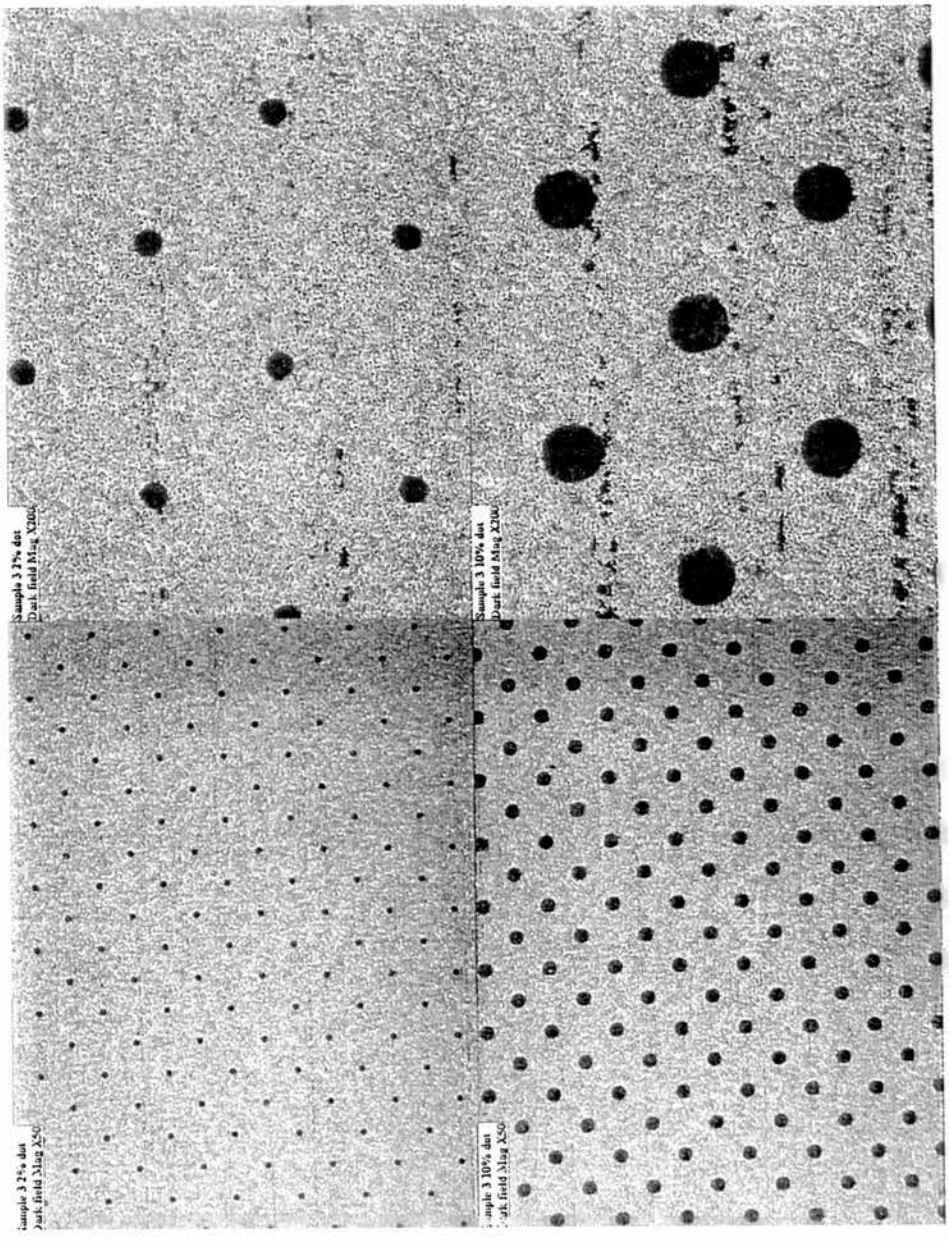

Figure 46. Optical Microscopy Images for a grained, desmutted sample anodised for 5 seconds.

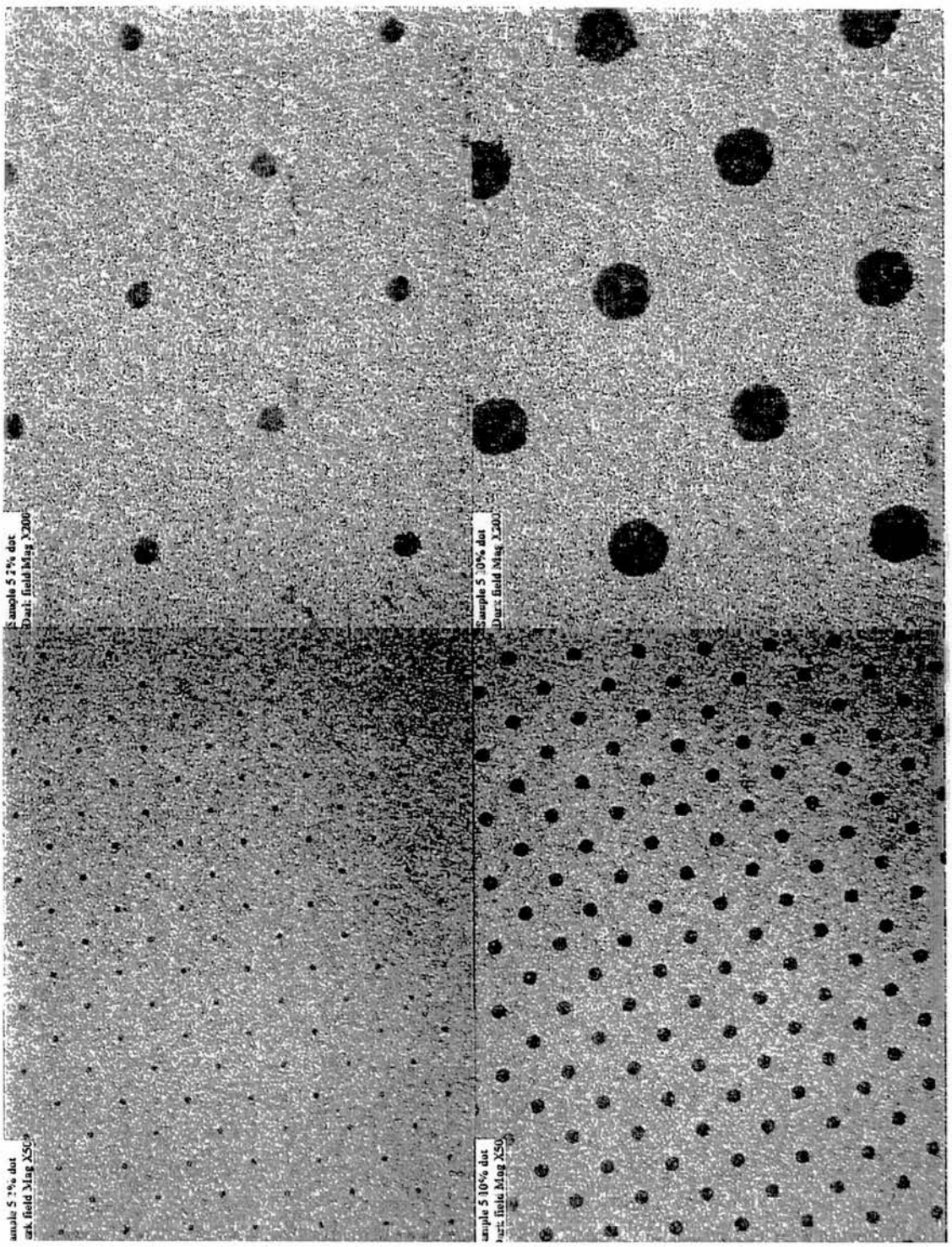

Figure 47. Optical Microscopy Images for a grained, desmutted sample anodised for 60 seconds.

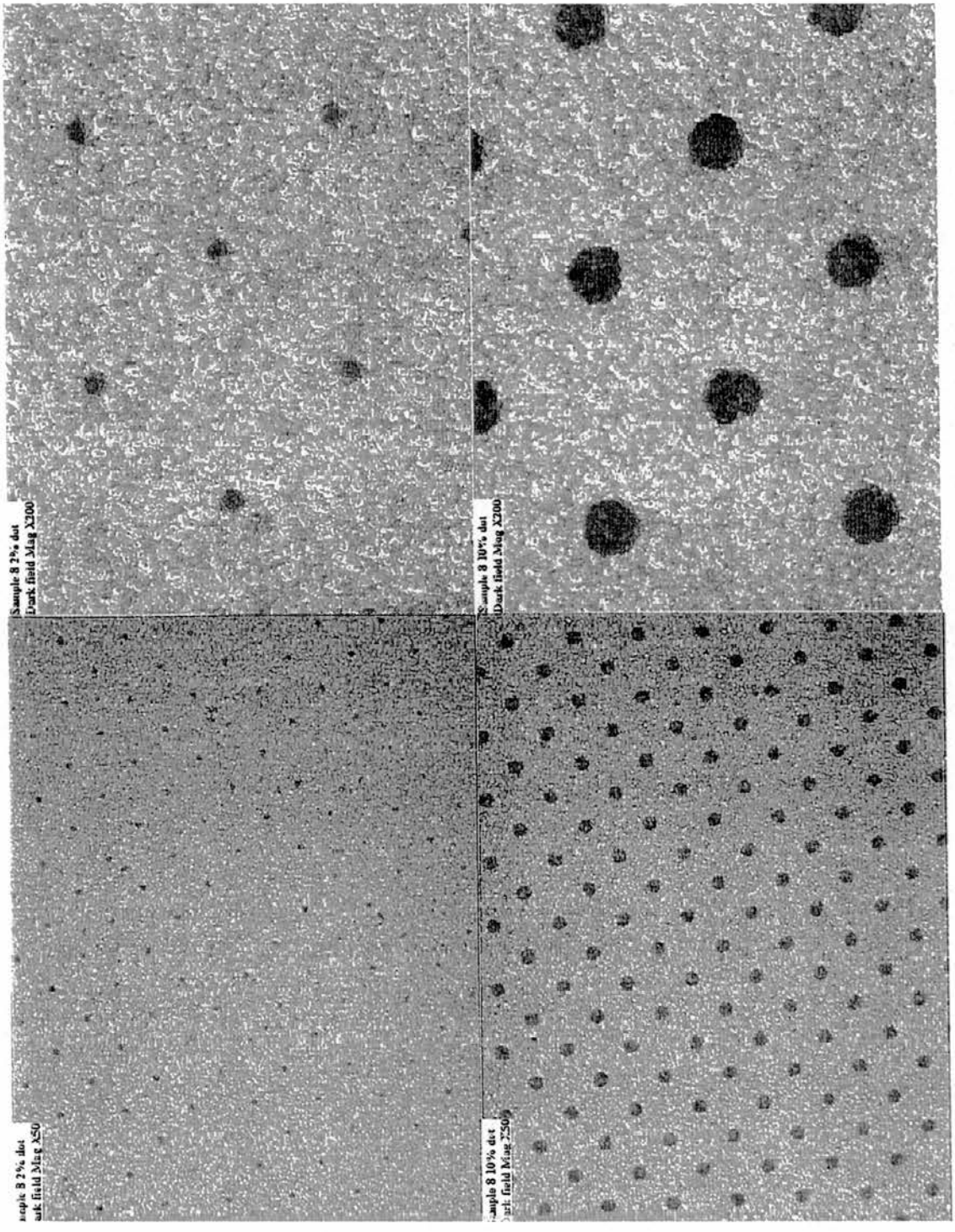

Figure 48. Optical Microscopy Images for a aluminium sample anodised for 30 seconds with <u>no</u> PAT.

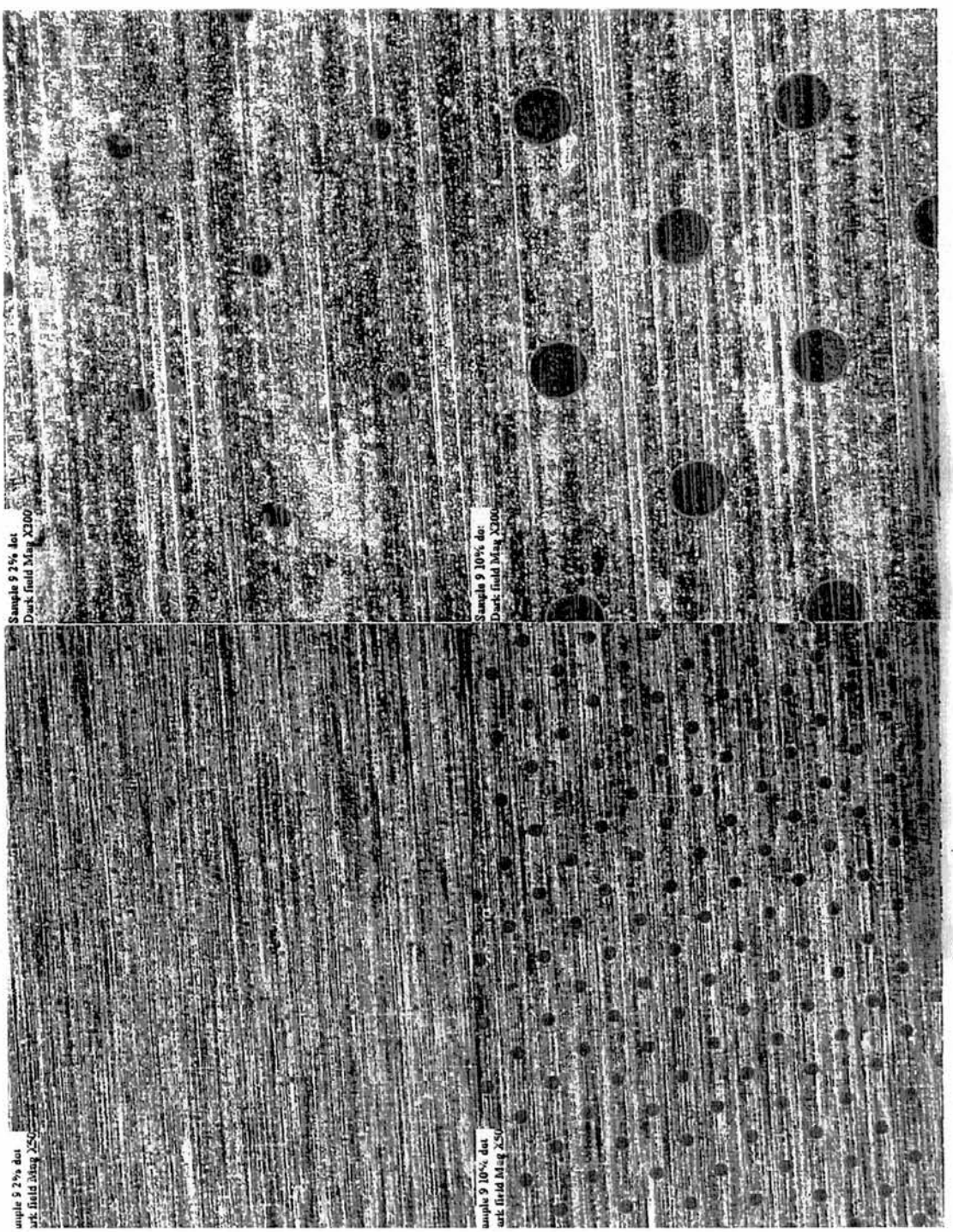

Figure 49. Optical Microscopy Images for a aluminium sample anodised for 30 seconds and PAT'ed for 4 minutes.

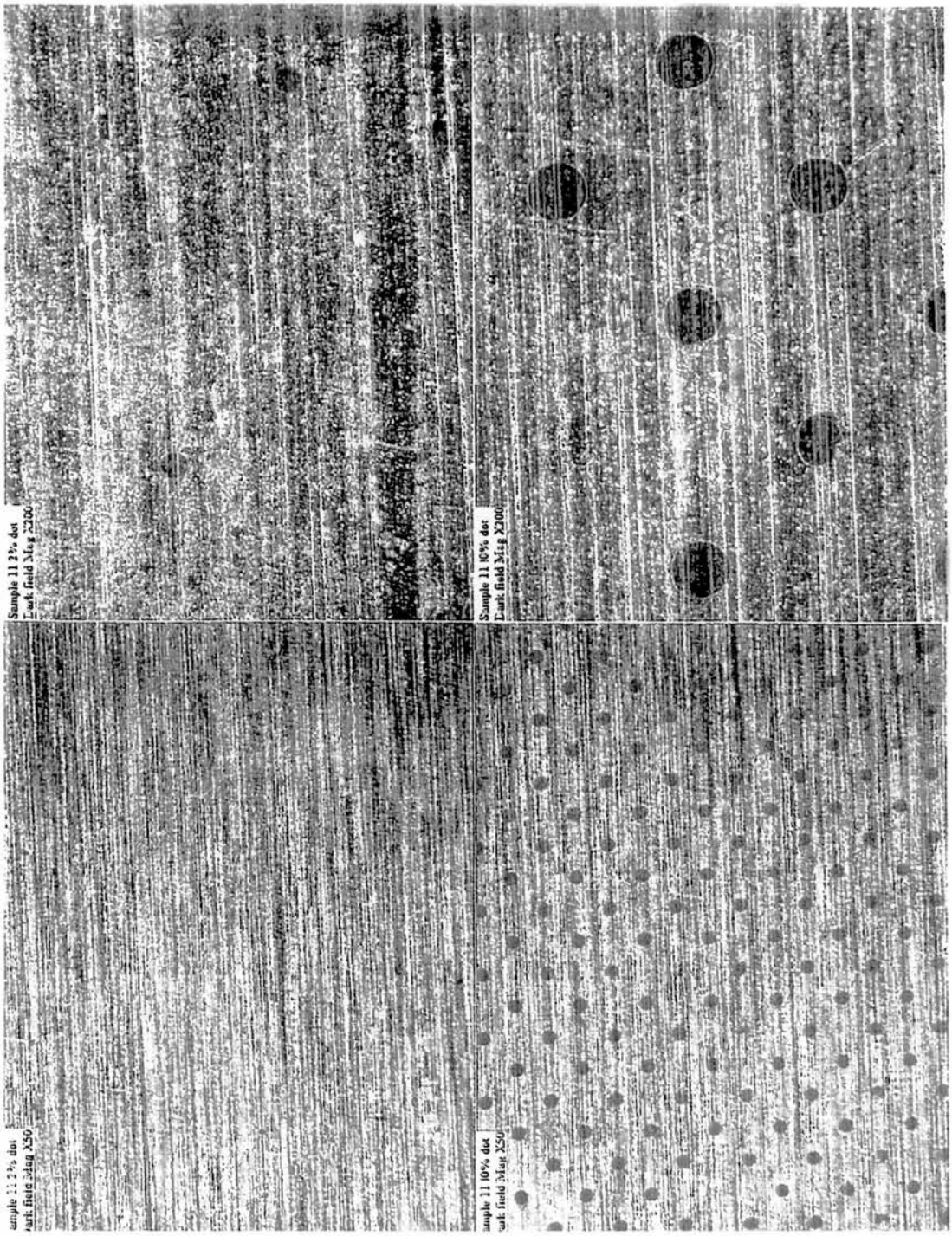

6.6.1 Discussion

Optical Microscopy images shows the retention of organic photocoating on each sample. The sharpness of the dots reveals a strong retention of the organic photocoating to the substrate, this is very important when studying the effect of adhesion of the organic polymer to substrates which have been anodised and PATed. Figure 44. illustration of a grained only sample shows a poor retention of the organic polymer. This is illustrated by the poor sharpness of the dots. Anodising for 5 and 60 seconds also shows a stronger retention to the organic polmer.

6.7 TPD Analysis of Aniline and Phenol desorption

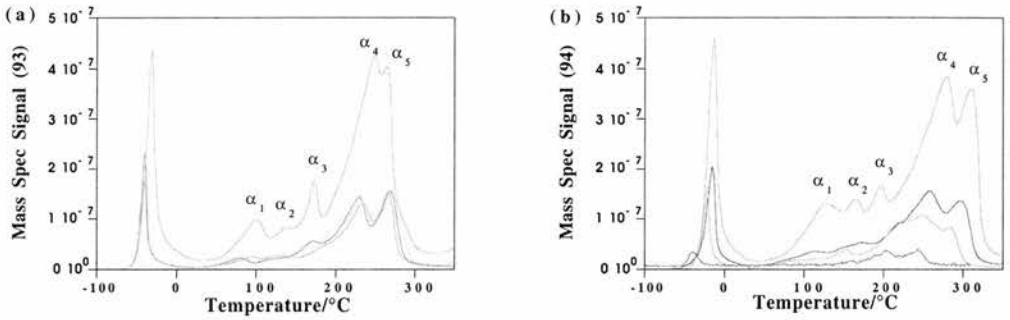

Figure 50. Desorption spectra of (a) Aniline and (b) Phenol from a grained only sample as a function of exposure.

. Aniline shows an Ice Peak temperature starting at -60°C (60 kJmol^{-1})

. Aniline shows multiple binding states ($\alpha_{1\text{-}5}$), increasing with exposure

. Aniline desorption complete by 300°C

. Phenol shows an Ice Peak temperature starting at -60°C (60 kJmol^{-1})

. Phenol shows multiple binding states ($\alpha_{1\text{-}5}$), increasing with exposure

. Phenol desorption complete by 350°C

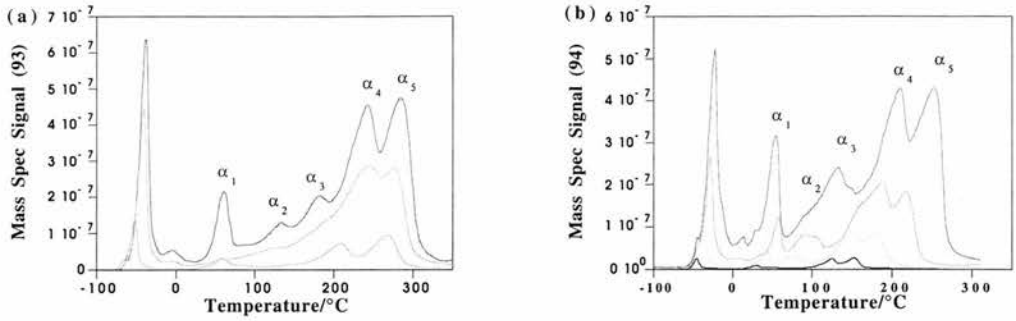

Figure 51. Desorption spectra of (a) Aniline and (b) Phenol from a grained, desmutted sample as a function of exposure.

. Aniline shows an Ice Peak temperature starting at -60°C (60 $kJmol^{-1}$)

. Aniline shows multiple binding states (α**1-5**), increasing with exposure

. Aniline desorption complete by 320°C

. Phenol shows an Ice Peak temperature starting at -60°C (60 $kJmol^{-1}$)

. Phenol shows multiple binding states (α**1-5**), increasing with exposure

. Phenol desorption complete by 300°C

The parent masses 93 and 94 amu (atomic mass unit), the strongest fragments in the cracking patterns of aniline and phenol, were followed during the desorption for both spectra. The ice peak maximum for both molecules increases in temperature in accordance to zero-order desorption kinetics. On both surfaces, the TPD spectrum showed multiple broad desorption peaks increasing in exposure, indicating that aniline and phenol exist in more than one adsorbed state with different binding energies.

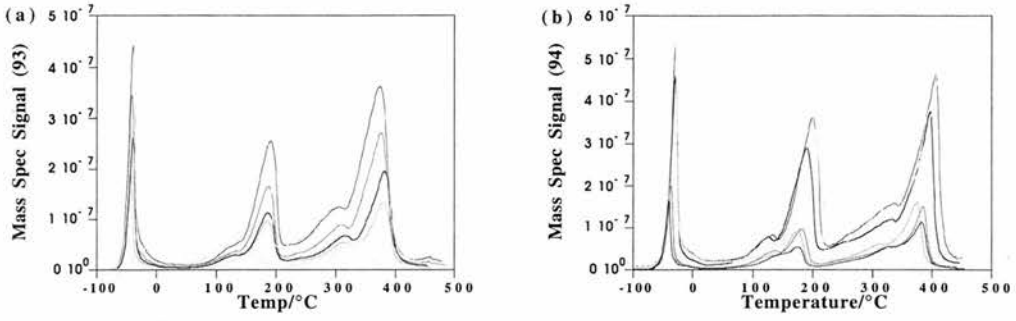

Figure 52. Desorption spectra of (a) Aniline and (b) Phenol from a grained, desmutted sample anodised for 5 seconds as a function of exposure.

. Aniline shows an Ice Peak temperature starting at -60°C (60 kJmol^{-1})

. Aniline shows two temperature desorption states starting at:

(a) Low desorption state at 100°C increasing with exposure to 180°C

(b) Higher desorption state at 200°C increasing with exposure to 370°C

. Aniline desorption complete by 400°C

. Phenol shows an Ice Peak temperature starting at -60°C (60 kJmol^{-1})

. Phenol shows two temperature desorption states starting at:

(a) Low desorption state at 100°C increasing with exposure to 180°C

(b) Higher desorption state at 200°C increasing with exposure to 380°C

. Phenol desorption complete by 450°C

Anodising the grained, desmutted sample for 5 seconds gives a characteristic change in shape of the desorption peaks. The desorption peaks are better defined. The low temperature desorption state for aniline and phenol starting at 100°C (100 kJmol^{-1}) appears to follow first-order kinetics based on the shape of the peaks. The features in the spectra shift to 150°C (120 kJmol^{-1}) with increasing exposure. The broad high temperature desorption state for aniline and phenol starting at 200°C also appears to follow first order desorption with increasing exposure. The shift of the spectra to a higher temperatures with increasing exposure suggests that the interaction between adjacent adsorbed aniline/phenol molecules is strong and attractive.

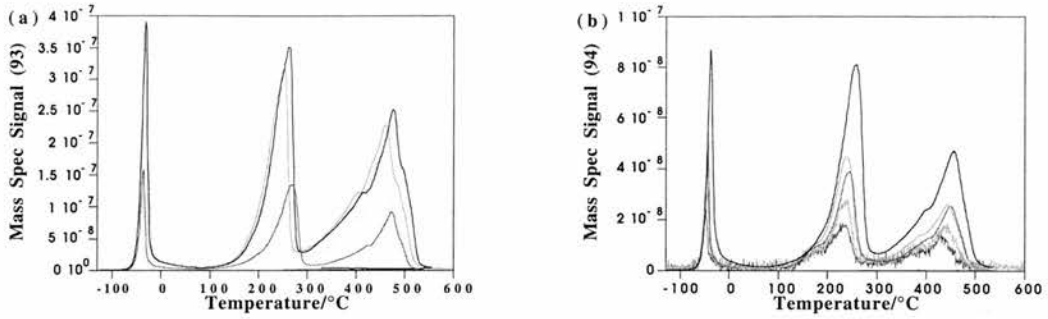

Figure 53. Desorption spectra of (a) Aniline and (b) Phenol from a grained, desmutted sample anodised for 60 seconds as a function of exposure.

. Aniline shows an Ice Peak temperture starting at -60°C (60 kJmol^{-1})

. Aniline shows two temperature desorption states starting at:

(a) Low desorption state at 100°C increasing with exposure to 250°C

(b) Higher desorption state at 300°C increasing with exposure to 450°C

. Desorption complete by 500°C

. Phenol shows an Ice Peak temperature starting at -60°C (60 kJmol^{-1})

. Phenol shows two temperature desorption states starting at:

(a) Low desorption state at 100°C increasing with exposure to 250°C

(b) Higher desorption state at 300°C increasing with exposure to 450°C

. Desorption complete by 500°C

After anodising for 60 seconds there is little change in shape of the desorption peaks. The desorption state starting at 100°C (100 kJmol^{-1}) appears to be first-order kinetics. The features in the spectra shift to higher temperature with increasing exposure. The broad high temperature desorption state at 300°C (150 kJmol^{-1}) increases with exposure and again follows first order desorption. The first aniline and phenol molecules to diffuse into the anodic pores are generally the last to finally desorb because they have the opportunity to diffuse the furthest and hence have a greater distance to travel to ultimately desorb. This may explain why the intermediate peak for the sample anodised for 60 seconds is slightly broader than that the sample anodised for 5 second, as the molecules take

different paths, and therefore different times to leave the solid.

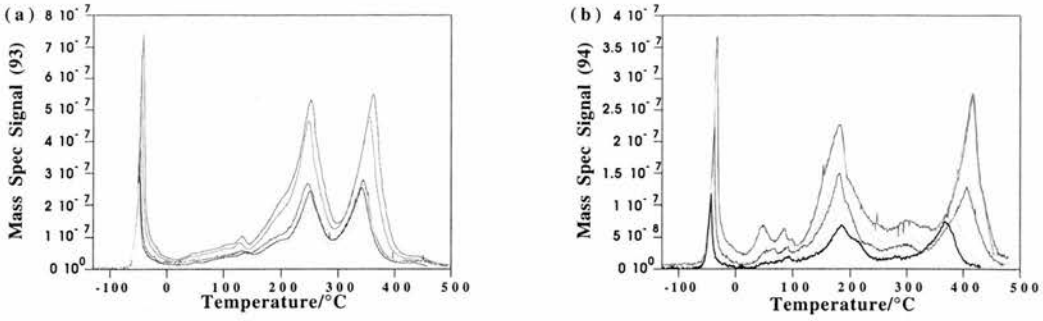

Figure 54. Desorption spectra of (a) Aniline and (b) Phenol from an aluminium sample anodised for 30 seconds with no PAT as a function of exposure.

. Aniline shows an Ice Peak temperature starting at -60°C (60 kJmol^{-1})

. Aniline shows two temperature desorption states starting at:

(a) Lower desorption state at 100°C increasing with exposure

(b) Higher desorption state at 300°C increasing with exposure

. Desorption complete by 400°C

. Phenol shows an Ice Peak temperature starting at -60°C (60 kJmol^{-1})

. Phenol shows two temperature desorption states starting at:

(a) Lower desorption state at 100°C increasing with exposure

(b) Higher desorption state at 300°C increasing with exposure

. Desorption complete by 500°C

Removing the graining and desmutting variables, the aluminium was anodised to see the effect of the anodising process alone. There are common similarities to the TPD spectra shown in Figures 52 and 53. The desorption state starting at 100°C (100 kJmol^{-1}) appears to follow first-order kinetics. The features in the spectra shift to higher temperature with increasing exposure. The broad high temperature desorption state at 300°C (150 kJmol^{-1}) increases with exposure and again follows first order desorption.

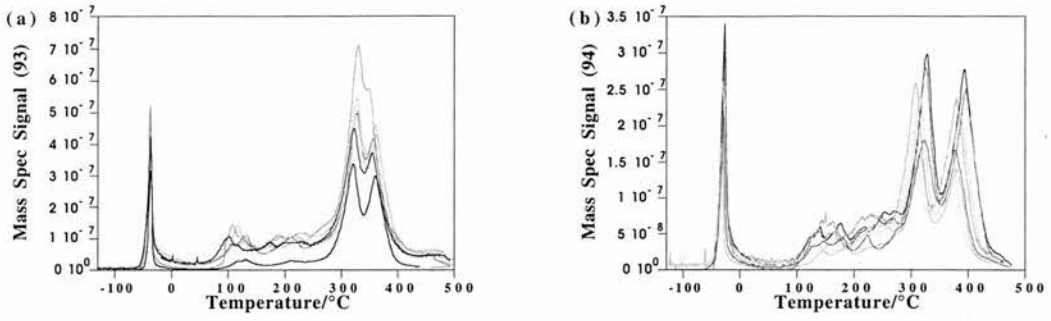

Figure 55. Desorption spectra of (a) Aniline and (b) Phenol from an aluminium sample anodised for 30 second and PATed for 4 minutes as a function of exposure.

. Aniline shows an Ice Peak temperature starting at -60°C (60 kJmol^{-1})

. Aniline shows two higher temperature desorption state starting at:

(a) Lower desorption state **absent**

(b) Higher desorption state at 350°C

. Desorption complete by 400°C

. Phenol shows an Ice Peak temperature starting at -60°C (60 kJmol^{-1})

. Phenol shows two higher temperature desorption states starting at:

(a) Lower desorption state **absent**

(b) Higher desorption state at 280°C and 350°C

. Desorption complete by 420°C

When the sample is PAT'ed the effect of PATing becomes more clear. The low temperaure desorption state for aniline and phenol is absent which may be the result of the PAT blocking the intermediate site. The broad high temperature desorption state for aniline and phenol starting at 200°C also appears to follow first order desorption increasing with exposure.

Table 3. Showing desorption temperatures of Aniline on different substrates.

Substrates	Ice Peak/ °C	Peak 1 Desorption/°C	Peak 2 Desorption/°C
Grained only	-60°C	0°C	
Grained & Desmutted	-60°C	0°C	
Grained, Desmutted & Anodised for 5 Seconds	-60°C	100°C	200°C
Grained, Desmutted & Anodised for 60 Seconds	-60°C	100°C	300°C
Aluminium, Anodised for 30 Seconds & No PAT	-60°C	100°C	300°C
Aluminium, Anodised for 30 Seconds & PATed	-60°C		350°C

Table 4. Showing desorption temperatures of Phenol on different substrates.

Substrates	Ice Peak/°C	Peak 1 Desorption/°C	Peak 2 Desorption/°C
Grained only	-60°C	0°C	
Grained & Desmutted	-60°C	0°C	
Grained, Desmutted & Anodised for 5 Seconds	-60°C	100°C	200°C
Grained, Desmutted & Anodised for 60 Seconds	-60°C	100°C	300°C
Aluminium, Anodised for 30 Seconds & No PAT	-60°C	100°C	330°C
Aluminium, Anodised for 30 Seconds & PATed	-60°C		280°C 350°C

Table 5. Relationship of aniline and phenol on different prepared substrates.

Substrates	Aniline	Phenol
Grained only	Ice Peak temperature at -60°C Multiple binding states, increasing with exposure	Ice Peak temperature at -60°C Multiple binding states, increasing with exposure
Grained Desmutted	Ice Peak temperature at -60°C Multiple binding states, increasing with exposure	Ice Peak temperature at -60°C Multiple binding states, increasing with exposure
Grained, Desmutted & Anodised for 5 seconds	Ice Peak temperature at -60°C Two temperature desorption states starting at 100°C and 180°C, increasing with exposure	Ice Peak temperature at -60°C Two temperature desorption states starting at 100°C and 180°C, increasing with exposure
Grained Desmutted & Anodised for 60 seconds	Ice Peak temperature at -60°C Two temperature desorption states starting at 100°C and 250°C, increasing with exposure	Ice Peak temperature at -60°C Two temperature desorption states starting at 100°C and 250°C, increasing with exposure
Aluminium Anodised for 30 seconds no PAT	Ice Peak temperature at -60°C Two temperature desorption states starting at 100°C and 300°C, increasing with exposure	Ice Peak temperature at -60°C Two temperature desorption states starting at 100°C and 300°C, increasing with exposure
Aluminium Anodised for 30 seconds & PATed	Ice Peak temperature at -60°C Only one temperature desorption states starting at 300°C, increasing with exposure	Ice Peak temperature at -60°C Two temperature desorption states starting at 280°C and 350°C increasing with exposure

6.8 Discussion

The morphological changes occuring on each sample has a direct influence on the shape of the desorption peaks. Anodising has a dramatic influence in the shape of the desorption states with the emergence of the intermediate state starting at 100°C, increasing in exposure. From the TPD data and the SEM images there is clear evidence that the intermediate state seen during the anodising process may be due to desorption from the anodic pores. When the surface is PAT'ed the intermediate state is absent. In general, surface reactions or even just surface heterogeneity can lead to the desorption of several different products or different binding states of the same adsorbates.

6.9 References

[1] Nick Sawyer, SEM images provided by Horsell Graphics Industries (1999).

[2] H.Terryn, J.Vereecken and G.E.Thompson, Corro.Sci., **32** (1991) 1159.

[3] H.Terryn, J.Vereecken and G.E.Thompson, Trans IMF., **66** (1988) 122.

[4] G.E.Thompson and G.C.Wood, Corro.Sci., **18** (1978) 721.

[5] P.Laevers, H.Terryn and J.Vereecken, Trans.Inst., Metal Finishing **70** (1992) 105.

[6] P.Laevers, Thesis, Vrije Universiteit Brussel (1991).

[7] V.Willard, Horsell Graphics Ltd, Internal Report (1996).

[8] F.d'Yvoire, Bull.Soc.Chim.France, (1962) 1762.

Chapter 7

A Thermal Desorption study of the adsorption of water molecules on aluminium oxide thin film

The motivation for the present study of water adsorption is to gain an understanding about the molecular adsorption of water on aluminium oxide thin film. This is extremely important in determining the ability of a substrate to take up water, giving information about the hydrophilicity of the substrate and the role of water at the interface. The experimental work described in this chapter was carried out by C.Mair using the thermal desorption instrument at Liverpool University, but the analysis is entirely my own.

7.1 Introduction

Many steps are necessary for the production of a printed image but the one under study here is the water-wetting of the printing plate. The water partitions to the hydrophilic alumina, non image areas, leaving only the hydrophobic polymer image areas to be wetted by the ink. This interaction between water and the non-image area is of crucial importance to the printing process. The substrates used to investigate water desorption were NON PAT and STD PAT aluminium oxide thin film. The preparation of these substrates is explained in chapter 3.

The interaction of water with metal oxide surfaces has been an important topic for surface scientists. The reason for this interest is because important processes like corrosion, electrochemical reactions and many heterogeneous catalytic reactions are based on the water-metal interaction. There exists a wealth of literature concerning water adsorption on solid surfaces; an excellent review has been given by Thiel and Madey [1]. A challenging adsorption system is the water-aluminium system. It is well known that water can be used to oxidise aluminium much more than oxygen. There is great deal of literature dealing with the adsorption and desorption kinetics

of water on aluminium [2,3], the geometric, electronic and vibrational structure of the adsorbed layer [2,4,5] and the oxidation kinetics of aluminium by water [6-10].

7.2 TPD analysis of water desorption

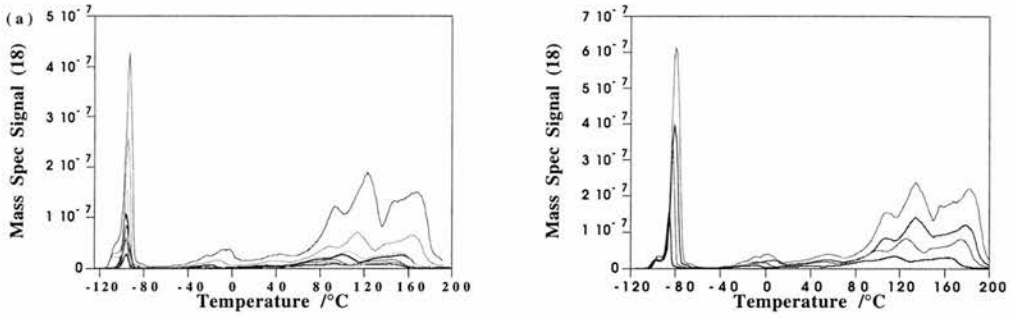

Figure 1. TPD spectra of water desorption from (a) NON PAT and (b) STD PAT substrate as a function of exposure.

Figure 1. shows TPD results from the two substrates as a function of increasing exposure. Each spectrum shows a complex fingerprint of water desorption. The spectra can be split into two distinct regions. The first desorption products give rise to a set of features extending from -105°C to -65°C. This region is characteristic of the behaviour of 'bulk ice'. It does not give information on surface bonding. The ice peak maximum increases in temperature in accordance with the zero order desorption kinetics, indicated by the common leading edge, which is typical of the desorption of weakly-bound multilayers. As the temperature of the sample is increased, the next most weakly bound states desorb, followed by the next most weakly bound states, and so on, until all the water has been desorbed from the sample. This results in the second region of the spectra which extends from -45°C to 200°C. The peak maximum for a given state shifts to higher temperature with increasing dose. This apparent increase in desorption energy, caused by increasing the amount of water on the surface, is most likely due to attractive lateral interactions between adsorbed molecules. As more water molecules adsorb on the surface, they not only form a bond with that surface, but they also interact with neighbouring molecules. If this interaction is attractive, as is the case for dipolar

water molecules, then more energy is required to remove them from the surface, because both the surface-adsorbate and adsorbate-adsorbate bonds have to be broken. The greater the surface coverage the greater the extent of attractive lateral interactions. Therefore, the features in the spectra shift to higher temperature with increasing dose.

7.2.1 Saturation Attempt

The exposure of a NON PAT surface to water was increased in an effort to saturate the surface. The surface was exposed to a pressure of $5x10^{-7}$ mbar for 10, 15, 20 and 30 minutes.

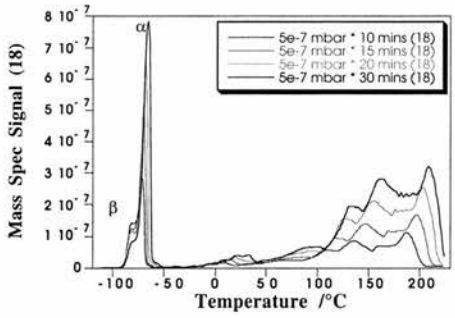

Figure 2. Saturation attempt for a NON PAT substrate as a function of exposure.

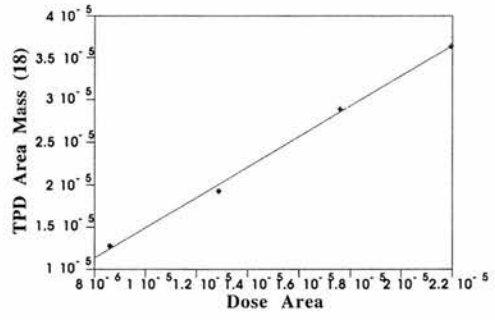

Figure 3. Linear relationship of dose area and Integrated TPD Area for 10, 15, 20 and 30 minutes H_2O exposure.

When water is adsorbed onto a surface, one might anticipate that a point will be reached when the surface cannot bond directly any more adsorbate molecules. The surface is covered by a monolayer of adsorbate and is said to be saturated. However, if the water dosing continues, the molecules are unable to bond directly with the

surface but they may bond to the monolayer of material already adsorbed. These further adsorbed layers are known as the multilayer regime. This multilayer will never saturate because, in theory, there can be an infinite number of layers which will continue to grow in a process analogous to condensation, as long as dosing continues. The bonding energy, and therefore the desorption temperature, of the water bonded directly to the substrate will be greater at least for a hydrophilic surface, than that of the water in the multilayers as they are only bonded to neighbouring water molecules. A system exhibiting this adsorption behaviour would give rise to a series of TPD spectra with increasing exposure with the following features. A peak would be seen to grow in intensity with increasing dose as the monolayer is populated until a point is reached where it will grow no more i.e. it has saturated. A second feature should then appear, at lower desorption temperature, due to the water in the multilayers. This feature in the TPD spectrum, associated with the multilayer, should not saturate with increasing dose, but continue to increase in intensity. This is indicated by the α peak. A low temperature feature in the desorption spectrum, peak marked β in Figure 2. could be due to desorption from the tantalum wires.

Work done [11] has shown that bonding of hydroxyl to aluminium at low coverage or the formation of aluminium hydroxide at high water coverage is an exothermic reaction. The excess energy can be channeled to adsorbed H atoms producing "hot" H-atoms. These atoms are able to recombine with other H atoms and lead to immediate desorption of molecular hydrogen at this low temperature. The aluminium hydroxide formed (probably gibbsite) is stable up to 300K. In this temperature range the aluminium hydroxide partially decomposes, yielding water and hydrogen. The remaining more stable aluminium hydroxide (probably diaspore) finally decomposes in the temperature range of about 650K, again leading to water and hydrogen, leaving behind a water free aluminium oxide on the surface, which might explain why the surface does not saturate.

7.3 Experiments Involving Labelled Water (D_2O)

There are many cases in the literature [12] of a phenomenon called dissociative adsorption. When this occurs, the adsorbate molecule does not bond to the surface as an intact entity but it dissociates and it is the fragments which form bonds with the surface. In the case of H_2O, it can dissociate to form $H_{(ads)}$ and $OH_{(ads)}$ species, during the desorption phase these species can recombine to form H_2O. It is suspected that this may be occurring in the case of water desorption from the alumina substrates studied here. The high temperature states indicate that strong surface bonds are being broken in the desorption process, perhaps surface-OH bonds. A series of experiments was devised, which involved dosing D_2O and H_2O onto the STD PAT and NON PAT substrates, to investigate if this is indeed the case.

H_2O dissociates to give $OH_{(ads)}$ and $H_{(ad)}$

D_2O dissociates to give $OD_{(ads)}$ and $D_{(ads)}$

Upon desorption these species can recombine in a number of possible combinations e.g.

$$OH_{(ads)} + H_{(ads)} = H_2O_{(g)}$$

$$OH_{(ads)} + D_{(ads)} = HDO_{(g)}$$

$$OD_{(ads)} + H_{(ads)} = HDO_{(g)}$$

$$OD_{(ads)} + D_{(ads)} = D_2O_{(g)}$$

If HDO is monitored as a desorption product, then cracking of the D_2O and H_2O has occurred on the surface.

7.3.1 Experimental

It was important to check the sensitivity of the mass spectrometer to D_2O, to ensure that the sensitivity was the same as for H_2O. This was achieved by moving the sample out of the path of the dosers and recording the intensity of the mass spectrometer signal for mass 18 over a range of different pressures of H_2O. This was repeated for the mass 20 signal over a range of pressures of D_2O. The mass

spectrometer sensitivity of D_2O and H_2O was found to be almost equivalent, as illustrated in Figure 4.

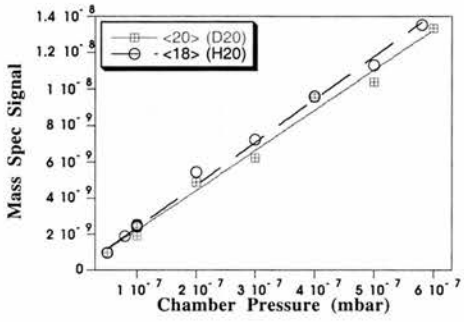

Figure 4. Mass spectrometer sensitivity to D_2O and H_2O.

Due to the geometrical differences between the two dosers, in order to provide an accurate measure of the doses, the dosers were calibrated as described below.

7.4 Doser Calibration

Calibration of the beam dosers was achieved by measuring the integrated TPD curves as a function of the integrated gas dose over a range of pressures for both D_2O and H_2O.

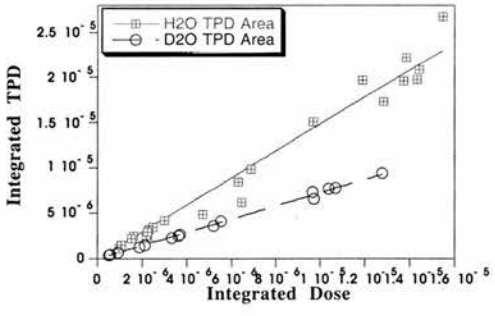

Figure 5. Calibration of D_2O and H_2O beam dosers.

The difference in flux at the sample between dosers is expressed by the ratio of the gradients of the two best fit lines, shown in Figure 5. The H_2O doser is 1.84 times more efficient than the D_2O doser, this assumes that the relative uptake ratios of H_2O and D_2O are equal. This correction factor was taken into account in D_2O/H_2O

exchange experiments to ensure that the relative amounts of D_2O and H_2O dosed onto the surface were known.

7.5 Fragment Ratios

For samples dosed with H_2O and D_2O, the fragment ratios of the ions giving rise to the signal was taken into account. The cracking patterns for H_2O and D_2O were determined over a range of pressures.

Table 1.

	Fragment Factor			
Species	Mass 20	Mass 19	Mass 18	Mass 17
D_2O	1		0.38232	
H_2O			1	0.3318
HDO		1	0.1775	0.1775

H_2O and D_2O are resolved into fragment ions at a fixed ratio (i.e fragment factors) by electron impact ionisation in the quadrupole mass spectrometer. When D_2O under goes ionisation, it is resolved into four fragment ions, D^+, O^+, OD^+ and D_2O^+. When H_2O is dosed and subsequently desorbed and detected by the mass spectrometer it has H_2O^+ as one of its parents ions. The ions OD^+ and H_2O^+ have the same mass, 18, therefore, if the thermal desorption signal due to H_2O is to be found the contribution to mass 18, from OD^+, has to be subtracted from the mass 18 signal. If HDO is produced on the surface, there is also a contribution from its OD^+ fragment ion to the mass 18 peak, which has to be subtracted. The signals due to the species of interest in this study are calculated as follows:

. [D_2O] = mass 20 signal

. [HDO] = mass 19 signal

. [H_2O] = mass 18 signal - 0.3823 x [D_2O] - 0.1775 x [HDO]

7.6 Dissociative Adsorption

To determine whether the adsorbed H_2O and D_2O molecules undergo dissociative adsorption, the correction factor was employed to ensure the STD PAT substrate was given exposures which would produce equivalent coverages of H_2O and D_2O on the sample surface.

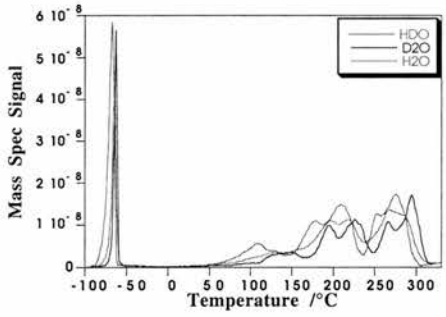

Figure 6. STD PAT substrate given equivalent coverages D_2O and H_2O.

HDO is found to desorb from the STD PAT substrate, illustrated in Figure 6, indicating that H_2O and D_2O molecules undergo dissociative adsorption. All three desorption species show similarities; however, they differ in their desorption maxima which occur at different temperatures.

7.6.1 Extent of Dissociative Adsorption

Equivalent amounts of D_2O and H_2O were dosed from separate dosers onto the STD PAT substrate for 10 minutes at a pressure of $3x10^{-7}$ mbar.

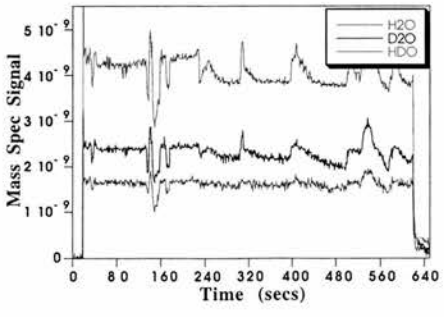

Figure 7. Mass spectrometer analysis of 50:50 D_2O:H_2O mixture.

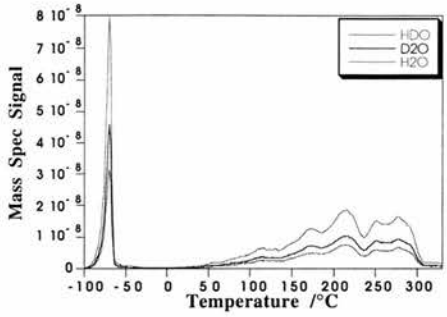

Figure 8. Thermal desorption spectra showing a 50:50 D_2O:H_2O mixture for a STD PAT substrate.

Table 2.

	% of Total Area		
	HDO	D_2O	H_2O
Dose	51	29	20
TPD	51	29	20

Equal amounts of H_2O and D_2O results in H_2O, D_2O and HDO in the ratio 1:1:2 respectively (from H_2O+ D_2O = 2HDO). Analysis of the ratio of the products in the dose mixture in Table 2. show that the ratio of H_2O:D_2O:HDO is 0.8:1.1:2. This indicates that the initial mixture was not made up of exactly 50% each of H_2O and D_2O. However, the ratio of the species desorbed from the sample are identical to those in the dose liquid. The reaction in solution has reached a dynamic equilibrium and interaction with the surface has no effect on the ratio of the products obtained. When dosing of the H_2O and D_2O was done sequentially, using separate dosers for H_2O and D_2O so that they are only able to mix on the surface, we find the following:

Table 3.

	% of Total Area		
	HDO	D_2O	H_2O
Dose	-	52	48
TPD	30	34	36

The ratio of H_2O:D_2O:HDO desorbed from the sample is 1.2:1.1:1 as shown in Table 3. This is far from the ratio of products given when the sample had been dosed with the 50:50 H_2O:D_2O mixture. This indicates that the dissociation of H_2O and D_2O, and its reaction to form HDO, has not reached equilibrium on the sample surface. Note that HDO desorption, occurring between -95°C and -55°C, as a proportion of total HDO desorption, is less for when the H_2O/D_2O was independently dosed than for the 50:50 equilibrated dose, shown in Table 4.

Table 4.

	HDO
H2O/D2O Independently Dose	48
50:50 Equilibrated Dose	36

This suggests that sites responsible for dissociation are associated with desorption temperatures greater than -55°C. Because only 13% of the total amount of HDO produced, when the sample had H_2O/D_2O independently dosed, desorbed at the low temperature region of the spectra. This means that the low temperature features may be due to molecular species, which do not undergo dissociation, and are bound molecularly to the surface. It is possible for cracking of molecules to occur within the dosing tubing and on the walls of the chamber to yield HDO. This HDO may desorb from the walls to readsorb onto the sample where it will subsequently be

detected. This wall effect may be the origin of the HDO peak, with a maximum at -65°C, in the desorption spectrum of the independently dosed case.

7.7 D_2O and H_2O Dose Order

It is not only possible to use the dosers independently of each other, but they can be used together. This enables simultaneous dosing of D_2O and H_2O. The NON PAT substrate was used to investigate the effect on the spectra of changing the order of dosing. In each case the substrate were given equivalent doses of D_2O and H_2O.

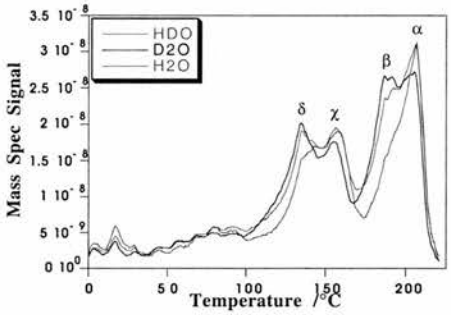

Figure 9. NON PAT substrate showing simultaneous dosing of D_2O and H_2O.

The thermal desorption results obtained when D_2O and H_2O dosing was carried out simultaneously, shown in Figure 9. shows differences in the desorption spectra for mass 18 and mass 20. Both the D_2O and the H_2O spectra showed a peak at 205°C (α). The desorption state at 190°C (β) is more intense in the D_2O spectra than in the H_2O spectra. χ at 155°C is more intense for the H_2O spectra and another at 135°C (δ) is more intense for the D_2O desorption. Even more interesting results are obtained when the sample is first dosed with H_2O followed by D_2O. The D_2O and H_2O spectra obtained are now very different from one another, shown in Figure 10.

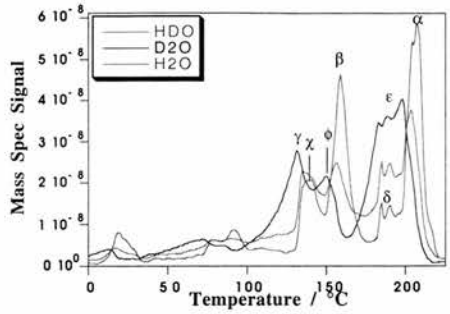

Figure 10. H_2O followed by D_2O on a NON PAT substrate.

H_2O is associated with desorption temperatures of 205°C α, 160°C β 140°C χ, a low intensity feature also occurs at 190°C δ. The main desorption temperatures for D_2O are a broad feature from 180°C to 200°C ε, and also less intense peaks at 150°C ϕ, and 135°C γ. When the dose order is reversed i.e. D_2O followed by H_2O, then again different desorption spectra were obtained, illustrated in Figure 11.

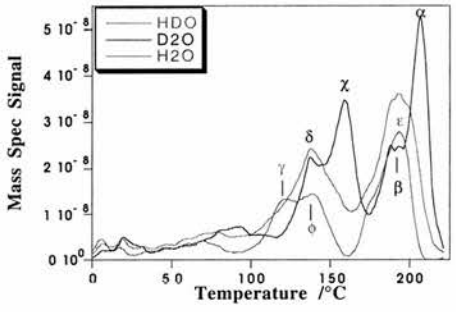

Figure 11. D_2O followed by H_2O on a NON PAT substrate.

The main desorption temperatures found for D_2O, in Figure 11. are now 205°C α , 190°C β, 155°C χ and 135°C δ. Those for H_2O are 190°C ε, 135°C ϕ and 120°C γ. These results are summarised in Table 5.

Table 5.

D_2O/H_2O		Peak Maxima (°C)				
		205	190	160/155	140/135	120
Simultaneous	H_2O	1	1	4	3	
	D_2O	1	2	3	4	
H_2O then D_2O	H_2O		1	2	3	
	D_2O	1	4	2	3	
D_2O then H_2O	H_2O	1	3	2	4	
	D_2O		1		2	3

Note

1 indicates the most intense peak in the spectrum, 4 the least intense.

When a molecule interacts with a surface, prior to bonding, it can be mobile across that surface. It is trapped by the surface but it can diffuse across it until it reaches a more reactive site with which it bonds, either as an intact molecule or as a dissociated species. When D_2O and H_2O are dosed simultaneously onto a surface, they both diffuse and compete for binding sites. Figure 9. shows that the D_2O and the H_2O have different preferred bonding sites. An H_2O peak, with a maxima at 205°C (and a broad shoulder extending to 170°C), indicates that it prefers to adsorb at a site associated with a desorption temperature of 205°C. On the other hand, the D_2O spectra shows a broad feature at 180°C to 205°C, indicating that it is able to bind to all the sites associated with these desorption temperatures. Looking next at the sequential dose data: when H_2O was dosed first, followed by D_2O shown in Figure 10. there is a time during the experiment when only H_2O is available on the surface, with no competition from D_2O for the available binding sites. In this case the H_2O occupies, almost exclusively, the sites desorbing at 205°C and 160°C. When the D_2O is dosed, it arrives at the sample to find the H_2O has occupied some sites, so the D_2O binds to the next preferred sites i.e. those desorbing at 190°C. The

H_2O may not have covered all of the sites at 205°C or the D_2O displaces some of the H_2O and occupies them itself, because there is a small intensity D_2O feature in the spectrum at 205°C. This behaviour is even more marked when the dose order is D_2O followed by H_2O shown in Figure 11. In this case the D_2O still bonds to those sites associated with desorption at 190°C but it exclusively occupies those sites at 205°C as there is very little desorption of H_2O at 205°C. The H_2O is in competition with D_2O for adsorption at the 205°C sites, but when the H_2O reaches the surface it finds that its preferred sites are occupied, therefore, it has to bond at the next most favourable one. This appears to be at 190°C as this state then grows in intensity. Note also that the D_2O occupies exclusively the state at 155°C which was favoured by H_2O when it was dosed first. The H_2O therefore has to adsorb at the 135°C site but, once that has filled, it occupies a site at 120°C. Note that when H_2O was dosed first there was no adsorption of H_2O at 120°C.

7.8 Effect of adsorption temperature on TPD curves

The effect on the desorption spectra of varying the sample temperature during dosing was investigated. The STD PAT substrate temperature was held at -120, -50 and 0°C during dosing of H_2O and for dosing of D_2O.

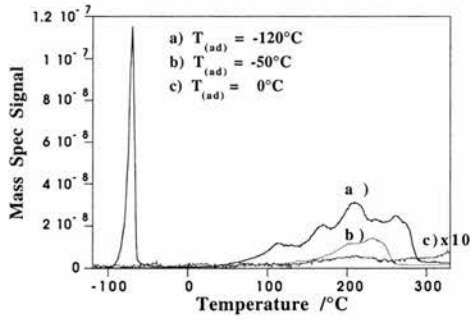

Figure 12. STD PAT substrate showing H_2O spectra for different adsorption temperatures.

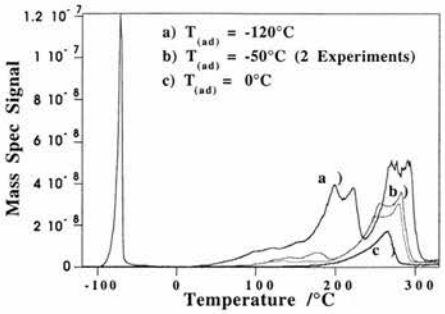

Figure 13. STD PAT substrate showing D_2O spectra for different adsorption temperatures.

H_2O dosing at -120°C produced a spectrum, shown in Figure 12a. which was the same as that obtained previously. However, when dosing was carried out at -50°C then the resulting spectrum, shown in Figure 12b. was very different; no H_2O desorption was observed below 60°C. When the dose temperature was 0°C only a small H_2O desorption spectrum could be detected, centred at 210°C, illustrated in Figure 12c. The results for D_2O show a similar trend, with adsorption at -120°C giving the same spectrum as before, shown in Figure 13a. Dosing the D_2O at -50°C, in Figure 13b. gave rise to a spectrum with no desorption below 60°C and with the features at 255°C and 280°C reduced in intensity. Adsorption at 0°C, illustrated in Figure 13c. shows a spectrum with no adsorption below a temperature of 170°C with the feature at 265°C much reduced in intensity.

Prior to adsorption at the surface site, incoming molecules are able to diffuse across the surface. As the temperature of the surface is increased there is an increasing likelihood that the molecule will desorb back into the gas phase before it has found a bonding site. This reduction in molecular residence time on the surface gives rise to a lowering in intensity of the thermal desorption signals. It is interesting to note the extent of this, e.g. when dosing D_2O at 0°C only D_2O desorbing above 170°C is detected. It appears that at the higher sample dose temperatures it is only the most strongly bound substrate-adsorbate species which can be populated. These results suggest that the states at the higher temperature end of the spectrum are populated by molecules which first enter the low temperature state at -80°C.

7.9 Constant Dose of Either D_2O or H_2O While Varying the Dose of the Other

Experiments performed in which the surface coverage of one adsorbate, D_2O or H_2O, was kept constant while the surface coverage of the other was varied. The roles for D_2O and H_2O were reversed and the experiment repeated. It was hoped that the results of these experiments would give some insight into the mechanism of the hydrogen/deuterium exchange reactions described in the previous experiment.

7.9.1 H_2O Dose Constant : D_2O Variable

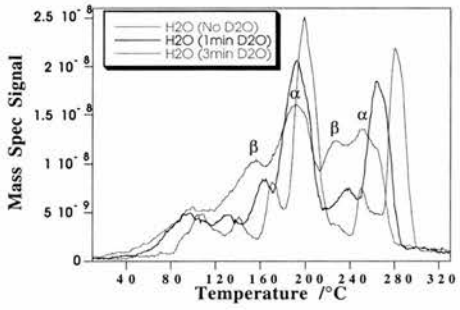

Figure 14. STD PAT substrate shows part of the desorption spectra obtained when the sample was dosed with the following:

. $5x10^{-7}$ mbar H_2O for 5 minutes.

. $5x10^{-7}$ mbar H_2O for 5 minutes then $5x10^{-7}$ mbar D_2O for 1 minute.

. $5x10^{-7}$ mbar H_2O for 5 minutes then $5x10^{-7}$ mbar D_2O for 3 minutes.

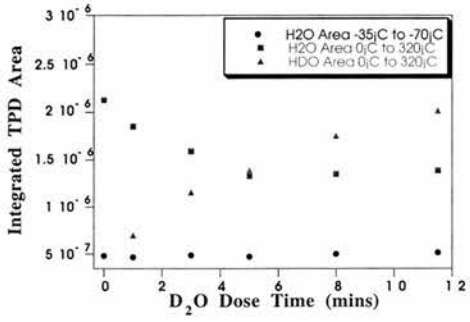

Fig 15. Area under both portions of the H_2O and HDO TPD spectra calculated for each D_2O exposure.

Figure 15. shows that the amount of H_2O desorbing between -35°C to -70°C is approximately constant over the range of D_2O doses. The amount of water desorbing in the range 0°C to 320°C decreases with increasing D_2O dose. This decrease is matched by an increase in HDO production, so it appears that the H_2O is being used up in a reaction with D_2O to form HDO. The fact that no reduction in H_2O intensity is seen in the lower temperature end of the spectrum (-35°C to -70°C) suggests that water molecules associated with it are not involved in D_2O exchange reactions. As the total concentration of the water on the surface increases there is the usual shift in peak maxima to higher desorption temperatures. The ratio of the intensity of the peaks also changes with increasing D_2O dose. The α peaks, shown in Figure 14. increase in intensity and become narrower, whereas the β peaks decrease in intensity. This indicates that addition of D_2O is either displacing H_2O from the β sites or it is removing H_2O preferentially from the surface at these sites by reaction with D_2O to form HDO. Studying the peak positions of maximum HDO adsorption should show if this is occurring.

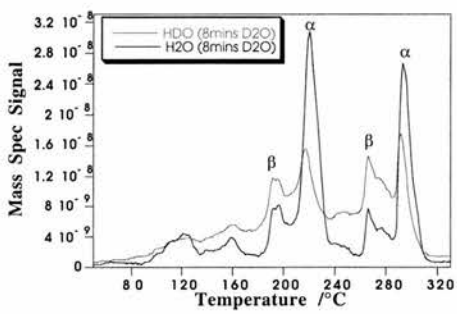

Figure 16. STD PAT substrate obtained by dosing $5x10^{-7}$mbar H_2O for 5 minutes then $5x10^{-7}$mbar D_2O for 8 minutes.

Figure 16. shows that HDO peak maxima coincide with the H_2O peak maxima and that a large proportion of HDO production occurs in the β states.

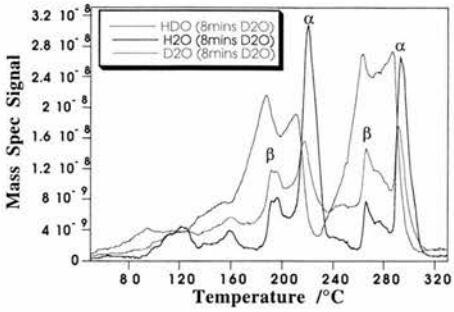

Figure 17. STD PAT substrate illustrating constant H_2O, 5mins at $5x10^{-7}$ mbar, and D_2O, 8 mins at $5x10^{-7}$ mbar.

When the D_2O signal is also plotted, as shown in Figure 17. we see that HDO desorption only occurs at temperatures where both D_2O and H_2O are found to desorb from the surface. This suggests that the H_2O states which are being reduced in intensity, including the β states, are not being reduced for any specific reason. The only requirement seems to be that both H_2O and D_2O are present on the surface at states which desorb at the same temperature.

7.9.2 D_2O Dose Constant : H_2O Variable

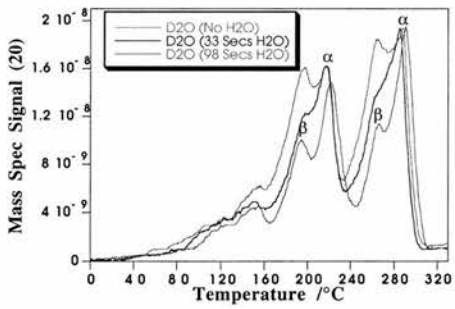

Figure 18. STD PAT substrate shows part of the desorption spectra obtained when the sample was dosed with the following:

. $5x10^{-7}$ mbar D_2O for 552 seconds

. $5x10^{-7}$ mbar D_2O for 552 seconds then $5x10^{-7}$ mbar H_2O for 33 seconds

. $5x10^{-7}$ mbar D_2O for 552 seconds then $5x10^{-7}$ mbar H_2O for 98 seconds

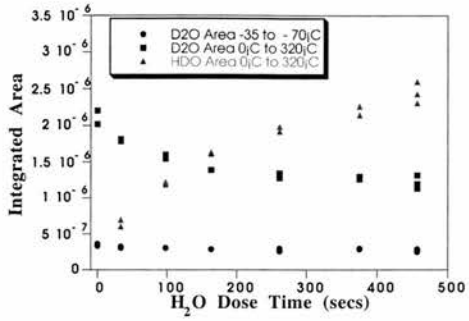

Figure 19. Area under both portions of D_2O spectrum was calculated for each H_2O exposure.

The amount of D_2O desorption in the range -35°C to -70°C is constant regardless of the H_2O dose given. The fact that no reduction in D_2O intensity is seen in the lower temperature end of the spectrum suggests that water molecules associated with it are not involved in D_2O exchange reactions. The amount of D_2O desorbing in the range 0°C to 320°C decreases with increasing H_2O dose, it appears that the D_2O adsorbed in these states is being used up in a reaction with H_2O to form HDO. The ratio of the intensity of the peaks also changes with increasing H_2O dose. As with the previous experiment, where the H_2O coverage was kept constant and the D_2O coverage varied, there is a change in the ratio of intensity of the α and β peaks. The β peaks, shown in Figure 18. show a larger decrease in intensity with increasing H_2O dose. This indicates that addition of H_2O is either displacing D_2O from the β sites or it is removing D_2O preferentially from the surface at these sites by reaction with H_2O to form HDO. Studying the peak positions of maximum HDO adsorption should show if this is occurring.

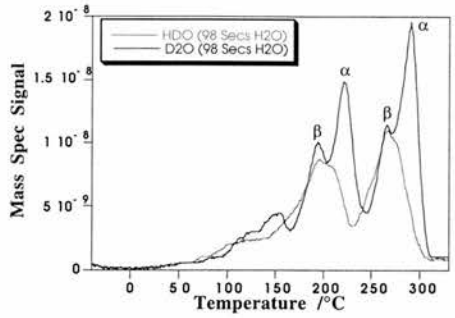

Figure 20. STD PAT substrate exposed for $5x10^{-7}$ mbar of D_2O for 9.2 minutes and then $5x10^{-7}$ mbar of H_2O for 98 seconds.

HDO desorption occurs at two peak maxima which coincide with the β D_2O peak maximum indicating that a large proportion of HDO production occurs in the β states.

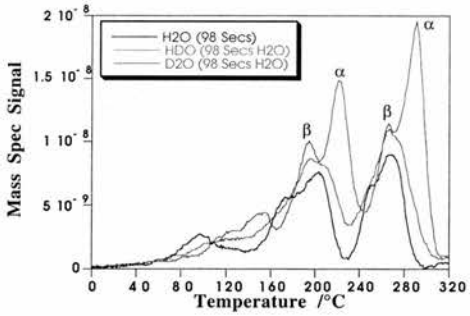

Figure 21. STD PAT substrate illustrating constant dose of D_2O for 5 minutes at $5x10^{-7}$ mbar, and H_2O for 98 seconds at $5x10^{-7}$ mbar.

However, when the H_2O TPD signal is also plotted, illustrated in Figure 21. we see that HDO desorption only occurs at temperatures which coincide with desorption maxima of both D_2O and H_2O. This suggests that the D_2O states which are being reduced in intensity, including the β states, are not being reduced for any specific reason. As before the only requirement seems to be that both D_2O and H_2O are present on the surface at states which desorb at the same temperature.

7.10 Reaction of water on other oxide surfaces

It is well known that the surface hydroxyl groups on metal oxides as TiO_2 or Al_2O_3 are removed by thermal treatment in vacuum, resulting into the formation of an activated oxide structure, as a result of the condensation of the adjacent hydroxyl groups, according to the following scheme:

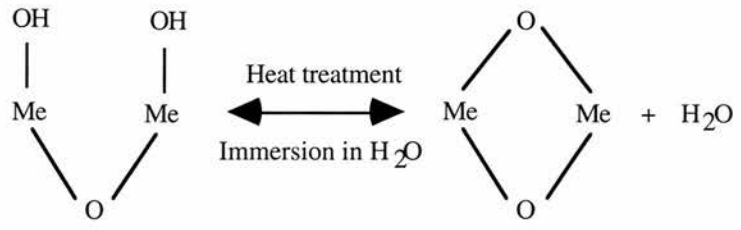

Kiselev and Lygin [13], who studied the adsorbed state of water molecules on silica by means of IR spectroscopy, concluded that a water molecule was adsorbed on two surface hydroxyl groups through the formation of a hydrogen bond between the oxygen atom of the water molecule and two hydrogen atoms of the neighbouring hydroxyl groups. Hallabaugh and Chessick [14] drew a similar conclusion from the fact that the cross section area of the water molecule in the TiO_2 (rutile) was extremely large, i.e. 23.5 $Å^2$. Also Morimoto *et al* [15] arrived at a similar conclusion in their analysis of water adsorption isotherm on rutile. They proposed the following scheme for the secondary adsorption:

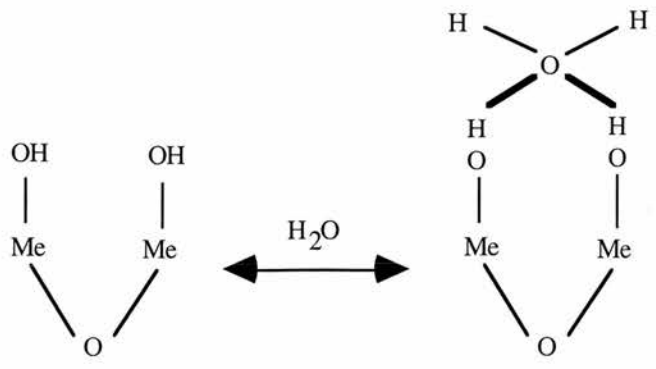

Exactly the same picture can be found in the work by McCafferty and Zettlemoyer [16] on water adsorption on Fe_2O_3. On the contrary, an IR study of water adsorbed on titanium oxides has brought Primet [17] to the conclusion that the secondary adsorption of water should be represented by the following scheme:

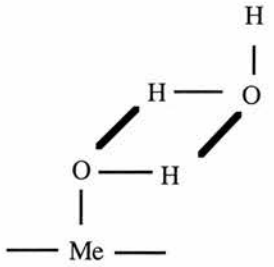

Griffiths and Fuerstenau [18] argued that the formation of the secondary adsorbed molecules proceeded as follows:

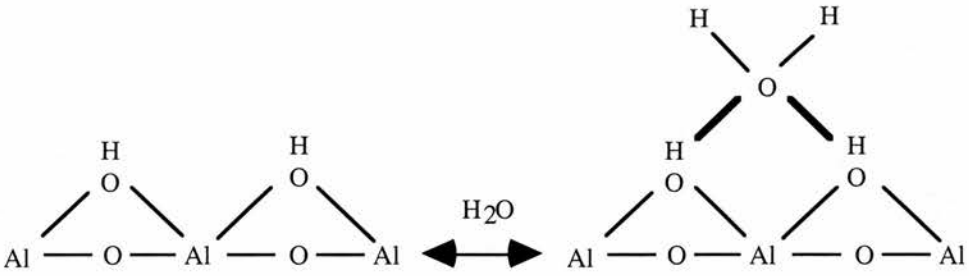

and led finally to an iceberg structure near a solid surface. Doremieux-Morin *et al* [19] carried out an NMR study of water adsorbed on rutile and amorphous titanium oxide. On that basis they postulated that, in addition to the Primet's mechanism, further water molecules could be adsorbed in three different ways:

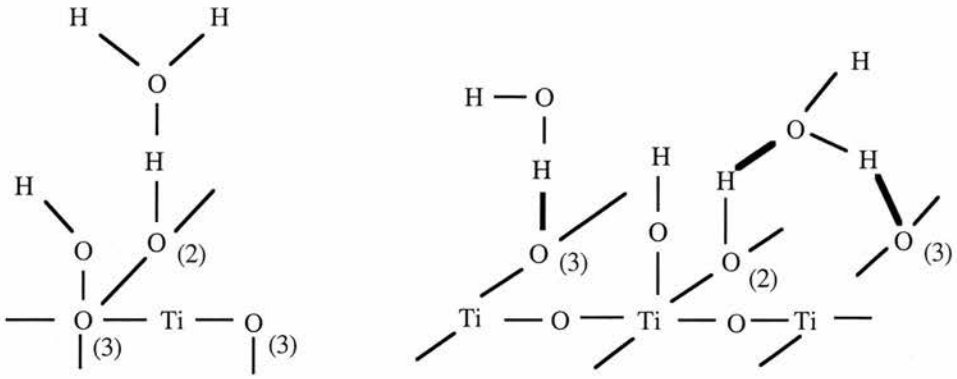

where (2) and (3) denote the co-ordination number of oxygen atoms.

7.11 Interaction of water with alumino-phosphate zeolite

VPI-5 is an aluminophosphate framework with one-dimensional pores defined by 18-member ring [20]. VPI-5 has three crystallographically distinct Al and P sites. The interaction of water with each of the Al sites was studied. The interaction of water is more favourable for the Al_1 site rather than the Al_2 and Al_3 sites. The incoming water molecule can approach the Al_1 site through three planes, namely, 413, 412 and 312. Out of these three modes, the approach of water along the 413 plane, where the O-Al-O angle is a maximum of 169°C, is the most favourable mode of adsorption. The hydrogen atom of the water molecules lies parallel to the O_3-Al_1-O_4 bonds. The experimental position of the water molecules shows that there are simultaneously two water molecules present leading to octahedral coordination at Al_1 as shown in Figure 22.

Experiments had been carried out [21] to study the interaction between the water molecules and the three crystallograpically distinct P sites. The interaction of water was more favourable for the P_2 site than the P_1 and P_3 sites.

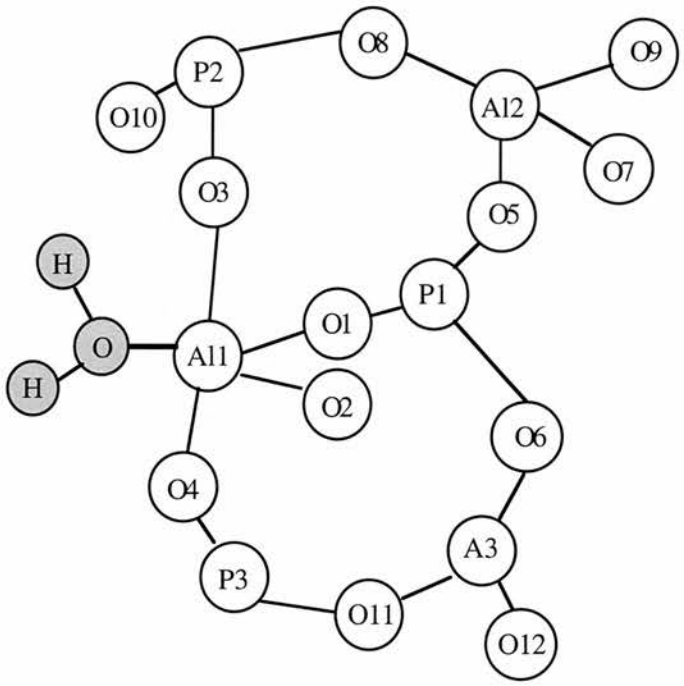

Figure 22. Energetically favourable mode of adsorption of water molecule over Al_1 site leading to octahedral coordination [22].

7.12 Computer simulation of adsorption-desorption on modelled aluminium oxide surface

A computer model has been written to simulate the behaviour of the water TPD peaks on the aluminium oxide substrates [23]. Several criteria had to be filled in order for the model to simulate the behaviour accurately.

1. The overall shape of the desorption curves.
2. The shift to higher temperatures of the desorption states as a function of surface coverage.
3. The effect of adsorption temperature on the desorption peak intensity.

The sublimation of ice is classically a zero order reaction. This can be expressed as:

$$\text{Rate} = A * \exp - (E_a/RT) \quad \ldots\ldots\ldots \quad 0^{th} \text{ order}$$

The main feature of a zero order reaction is a common leading edge, the desorption accelerates until all the reactant has been consumed and then comes to an abrupt end.

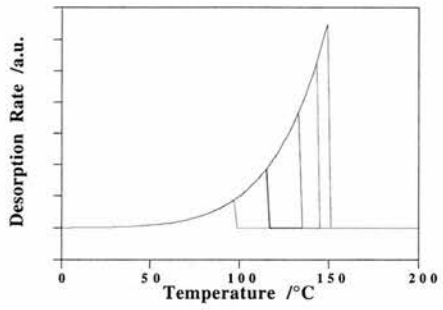

Figure 23. Simulated thermal desorption spectra for zero order desorption. Parameter values: E_a=50 kJmol^{-1} and A=10^{23} sec^{-1}. The exposure used was 600 seconds at: (i) 1.0x10^{-7} mbar, (ii) 2.5x10^{-7} mbar, (iii) 5.0x10^{-7} mbar, (iv) 7.5x10^{-7} mbar and (v) 1.0x10^{-6} mbar.

The shape of the higher temperature desorption states can be either first or second order reactions of the form:

$$\text{Rate} = [C]*A*\exp - (E_a/RT) \quad \ldots\ldots\ldots \quad 1^{st} \text{ order}$$

$$\text{Rate} = [C]*[C]*A*\exp - (E_a/RT) \quad \ldots\ldots\ldots \quad 2^{nd} \text{ order}$$

For the 1st order desorption the peak temperature is maintained with increasing coverage but, for 2nd order desorption, the peak temperature falls with increasing coverage. Clearly, there are two parameters that needed to be fitted, the pre-exponential factor A and the activation energy E_a. The effect of the pre-exponential factor and the activation energy for desorption can be seen in Figures 24 and 25.

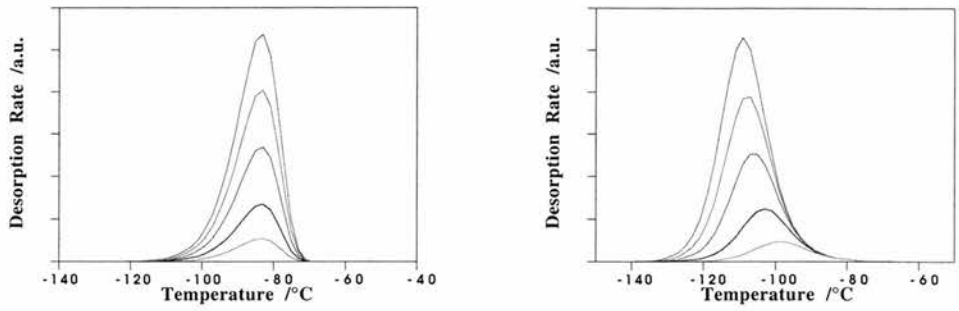

Figure 24. Simulated thermal desorption spectra for 1st order (left) kinetics: Parameter values: E_a = 50 kJ mol^{-1} and A = 10^{23} s^{-1} and 2nd order (right) kinetics. Parameter values: E_a = 50 kJ mol^{-1} and A = 10^{-3} s^{-1}.

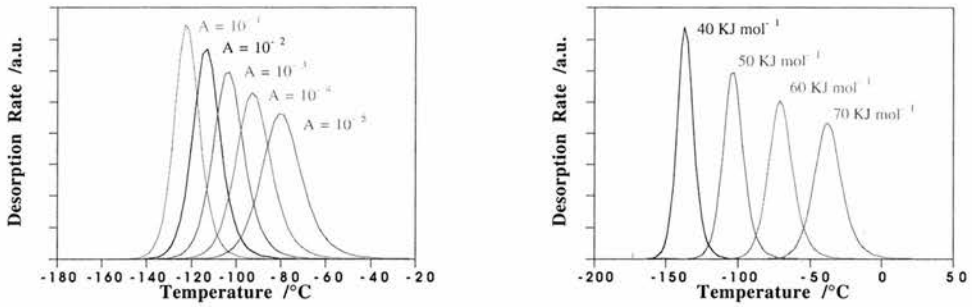

Figure 25. Effect of the pre-exponential factor (left) and the effect of activation energy (right) on a 2nd order desorption. Parameter values: E_a = 50 kJ mol^{-1} and A = 10^{-3} s^{-1}.

In order to simulate the increase in peak temperature as a function of coverage a coverage dependent activation energy was used. This simulates attractive interaction between molecules on the surface. To simulate the behaviour of the TPD peaks as a function of adsorption temperature it was found that not only should all adsorption proceed via the physisorption state but also that the chemisorption states must be in equilibrium with the physisorption state. The model [23] is shown schematically in Figure 26.

The computer simulation is designed to mimic the experiment. The adsorption process is run for 600 seconds at a given pressure (flux), the system was allowed to equlibrilate for 43 minutes and then the temperature is raised at 1 Ksec^{-1} until the desorption is complete. The concentrations in the gas phase and the three chosen

desorption states are continously calculated at each step of the reaction. Desorption and diffusion are taken into account throughout the calculation, and the rates of reaction are monitored. It is the rate of reaction that is measured in the TPD experiments and therefore it is this that is of primary interest. A typical profile is shown in Figure 27.

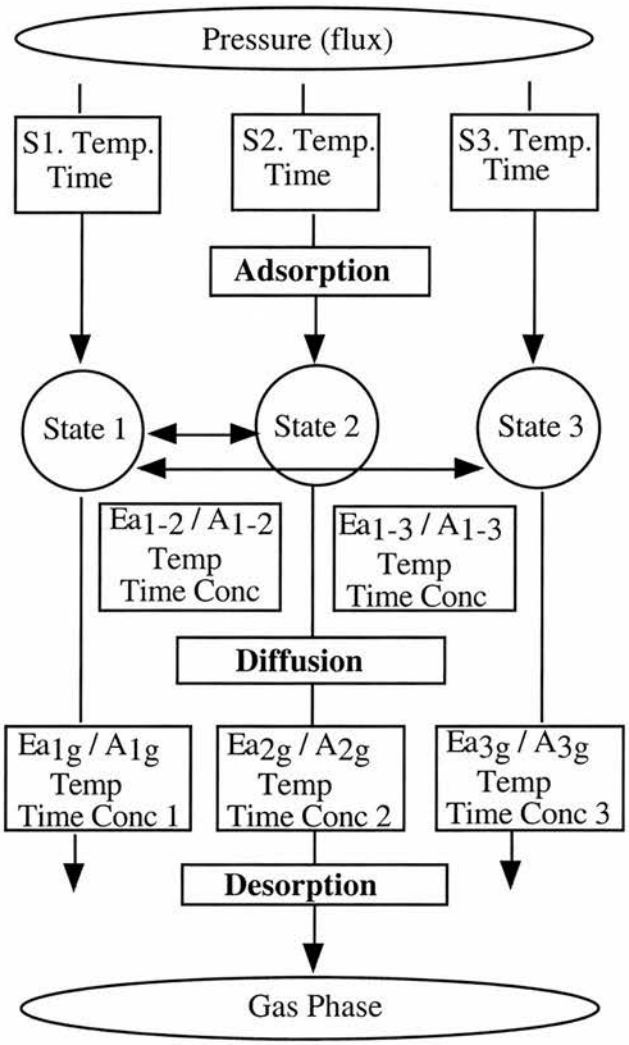

Figure 26. Schematic diagram of the model used for the computer simulation [23].

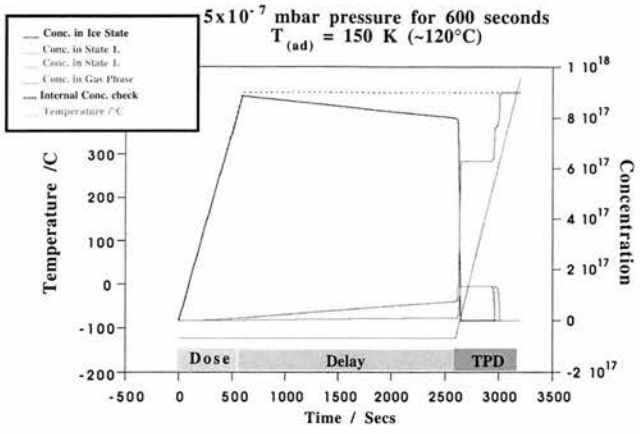

Figure 27. A typical reaction profile.

The rate of reaction (TPD spectrum) is the differential of the concentration curve and a typical simulated TPD spectrum is shown in Figure 28. Typical values for the parameters are Ice Peak, E_a = 50 kJmol^{-1}, A= 10^{23} molecules sec^{-1}. For the higher temperature peaks the range for E_a = 120-180 kJmol^{-1} with an A value of 10^{-13} sec^{-1}.

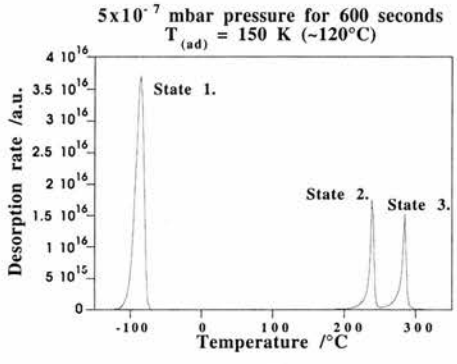

Figure 28. A typical TPD spectrum generated by the computer model.

If the transfer by diffusion/reaction is allowed from the ice state to the higher temperature states a plot of integrated peak intensity versus adsorption temperature can be drawn, shown in Figure 29. This is obviously incorrect as it predicts that the peak intensity in the higher temperature state increases as the adsorption temperature is raised. This is due to enhanced transfer into the chemisorption states and the higher states are maintained in an equilibrium the same plot yields Figure 30. It is

clearly seen from this graph that increasing the adsorption temperature by only a small amount has a dramatic effect on the intensity of the higher temperature peak. Desorption via the physisorbed states becomes favourite and accounts for this loss in intensity.

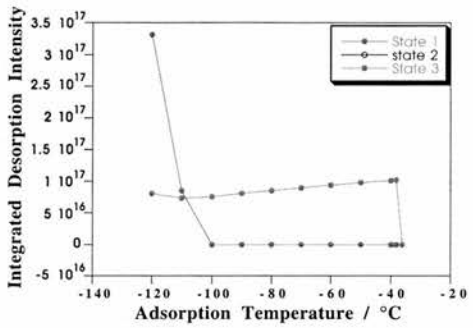

Figure 29. Integrated peak intensity as a function of adsorption temperature with no equilibrium. This shows the wrong trend in the peak intensity.

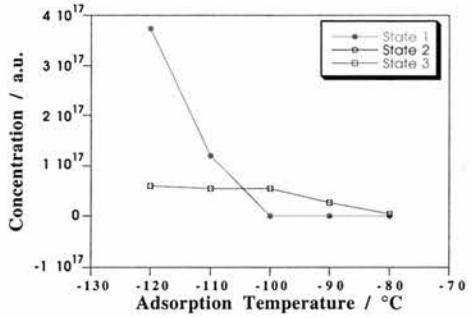

Figure 30. Integrated peak intensity as a function of adsorption temperature with the equilibrium. This shows the correct trend in the peak intensity as a function of adsorption temperature.

7.13 Discussion

The model can successfully describe the behaviour of both the ice peak and the higher temperaure peaks, solely from the adsorption into state 1, with transfer from state 1 to higher states. The inclusion of a coverage dependent E_a for states 2 and 3 models the increase in desorption temperature with coverage. A pseudo-equilibrium between state 1 and the higher temperature states, the decrease in population of these states as a function of adsorption temperature can be modelled successfully.

7.14 References

[1] P.A.Thiel and T.E.Madey, Surf.Sci., Rep.**7** (1987) 211.

[2] F.P.Netzer and T.E.Madey, Surf.Sci., **127** (1983) L102.

[3] U.Memmert, S.J.Bushby and P.R.Norton, Surf.Sci., **219** (1989) 327.

[4] J.E.Crowell, J.G.Chen, D.M.Hercules and J.T.Yates, Jr., Surf.Sci., **86** (1987) 5804.

[5] P.B.Smith and S.L.Bernasek, J.Electron Spectrosc.Relat.Phenom., **49** (1989) 149.

[6] J.C.Fuggle, L.M.Watson, D.J.Fabian and S.Affrossman, Surf.Sci., **49** (1975) 61.

[7] W.Eberhard and C.Kunz, Surf.Sci., **75** (1978) 709.

[8] F.Szalkowski, J.Chem. Phys., **77** (1982) 5224.

[9] E.R.Wouters, D.J.O' Connor, J.F.van der Veen, P.M.Zagwijn, J.Vrijmoeth, W. Slijkerman and J.W.M.Frenken, Surf.Sci., **296** (1993) 141.

[10] H.D.Ebinger and J.T.Yates, Jr., Surf.Sci., **412/413** (1998) 1.

[11] H.Polzl, F.Zinka, D.Gleispach and A.Winkler, Surf.Sci., (1999).

[12] V.E.Henrich and P.A.Cox, The Surface Science of Metal Oxides, Cambridge University Press, Cambridge (1994).

[13] A.V.Kiselev, V.I.Lygin, Kolloid. Zhurn., **21** (1959) 561.

[14] C.M.Hallabaugh, J.J.Chessick, J.Phys.Chem., **65** (1961) 109.

[15] T.Morimoto, M.Nagao and F.Tokuda, J.Phys.Chem., **73** (1969) 243.

[16] E.McCafferty and C.Zettlemoyer, J.Colloid Interface Sci., **34** (1970) 452.

[17] M.Primet, PhD Thesis, Lyon No. **640** (1970).

[18] D.A. Griffiths and D.W.Fuerstenau, J.Colloid Interface Sci., **80** (1981) 271.

[19] C.Doremieux-Morin, M.A.Enriquez, J.Sanz and J.Fraissard, J.Colloid Interface Sci., **95** (1983) 502.

[20] W.Rudzinski, R.Charms, S.Partyka and J.Y.Bottero, Langmuir, **9** (1993) 2641.

[21] S.Prasad, S.B.Liu and R.Vetrivel, Stud.Surf Sci. Catal., **90** (1994) 291.

[22] V.A.Bakaev and O.V.Chelnokova. Surf.Sci., **215** (1989) 521.

[23] S.M.Francis, University of St. Andrews, Internal Report (1999).

Chapter 8

General Conclusion

The work described in this thesis has considered important stages in the development of a lithographic printing plate namely, graining, anodising and post anodic treatment. This chapter briefly summaries the conclusions from chapter 4-7. Although the general theme is the interaction of organic molecules and water on aluminium oxide thin film, it is necessary to split the discussion into three parts. The first section deals with the structure/morphology of aluminium oxide thin film. The second section discusses the thermal desorption spectra in relation to surface structure and the final section suggests future work.

In the process of quantifying the alumina surface, SEM along with SIMS, TEM and XPS produced excellent results illustrating the key differences between the STD PAT and NON PAT substrate. Anodising in sulphuric acid led to the development of a duplex film comprising an inner barrier film and overlying layer. TEM showed the total thickness of the oxide film to be ~760 nm, with the barrier layer ~10nm thick. The film overlying the barrier layer consisits of many parallel porous twisting channels, the diameter ranging from 5 nm to 20 nm. Earlier work [1] with anodised alumina in sulphuric acid and phosphoric acid showed the pore shape to be circular or elongated holes arranged in pentagonal or hexagonal packing. A mechanism for PAT has been proposed [2].

The deposition of the PAT has a great impact upon smaller surface structures such as the anodic pores than the macropits. Changes in the substrate surface areas, volume and chemistry brought about by the PAT had a direct affect on the adhesive nature of the substrate. Adhesion is thought to be reduced through:

(i) A reduction in interfacial interactions (active sites) due to the reduction in the surface area.

(ii) A reduction in mechanical interlock brought about by a reduction in surface area and volume. Physical or mechanical keying of the photocoat to substrate plays an important part in adhesion. Deposition of PAT reduces mechanical interlocking by applying phosphate which penetrates the porous anodic and micropit surface. A non porous outer surface is formed compared to the porous anodic and micropit surface with which the photocoat can no longer interlock.

(iii) Changes in the surface chemistry alters the interactions which can occur between the substrate and photocoat. The adsorption of aniline and phenol (aromatic molecules) showed to be the most favoured probe molecules showing very similar but important differences. The chemical identity of aniline and phenol in the chemisorb state is uncertain. However, since no water is observed to adsorbed on the surface, it appears that no N-H and O-H bonds are broken and we can only assume aniline and phenol molecules remains intact on the surface. The shift of the spectra to a higher temperature with increasing exposures suggests that the interactions between adsorbed molecules are attractive. An attractive interaction could be due to the hydrogen bond between adsorbed molecules. The morphological changes occuring on each sample has a direct influence on the shape of the desorption peaks. Anodising results in the emergence of an intermediate state, increasing in exposure. From the TPD data there is clear evidence that the intermediate state seen during the anodising process may be due to molecules desorbing from the anodic pores. When the surface is PATed the intermediate state is absent. It would seem the PAT process has preferentially blocked the intermediate adsorption site.

The high temperature features seen with water is the result of multilayer water diffusing into the pores of the porous alumina (and ultimately adsorbing on the interior pore wall) in competition with desorption into the vacuum. Simultaneous dosing of H_2O and D_2O yield high temperature desorption features that are largely isotope independent and exhibit extensive H/D exchange. H_2O followed by D_2O yields more complex desorption with strong isotope effects and reduced H/D exchange. D_2O desorption proceeds H_2O desorption with HDO features appearing

as a superposition of the non-exchange features. The first molecules to diffuse into the pores are generally the last to finally desorb because they have the opportunity to diffuse the farthest and hence have a greater distance travel to ultimately desorb. Clearly, this simple minded model does not explain the multi-peaked nature of the high temperature features. This probably is determined by the strength of the interaction of the molecules with the solid surface of the pore. Multiple binding sites give rise to multiple peaks, the highest binding energy sites are normally filled first. In general, surface reactions or even just surface heterogeneity can lead to the desorption of several different products or different binding states of the same adsorbates. When modelling the adsorption-desorption behaviour the direct adsorption path into the high temperature adsorption states was set to zero and all molecules forced to pass through the physisorption state before chemisorption. With this constraint within the model the effect of adsorption temperature could be modelled very successfully.

The work described in this thesis has enabled graining, anodising and post anodic treatment to be defined sucessfully by thermal desorption. Future work should consider desorption of similar small molecules from other support materials such as Polyester Osprey plates. A detailed examination of the effects of morphology on desorption can also be investigated. Also interesting is to consider how the presence of a phosphate layer modifies coating adhesion and developability. In this way, insight is provided into the role of PAT in determining the performance of the finished lithographic plate.

8.1 References

[1] S.H.Tan, PhD Thesis, UMIST, Manchester (1982).

[2] J.F.Pye, PhD Thesis, University of Cambridge (1997).

[3] D.R.Lide and H.H.P.R.FrederikseHandbook of Chemistry and Physics, eds. 74th Edition, CRC Press (1993).